UNIVERSITY OF CALIFORNIA SAN DIEGO

Shelf Width Variability Controls Sediment Dispersal on Active Margins

A dissertation submitted in partial satisfaction of the
requirements for the degree
Doctor of Philosophy

in

Earth Sciences

by

Emily Ann-Yi Wei

Committee in charge:

Professor Neal Driscoll, Chair
Professor Chris Charles
Professor Sarah Giddings
Professor Tara Hutchinson
Professor Miriam Kastner

2019

The dissertation of Emily Ann-Yi Wei is approved, and it is acceptable in quality and form for publication on microfilm and electronically:

_____

_____

_____

_____

_____

Chair

University of California San Diego

2019

DEDICATION

To my amazing mom.

EPIGRAPH

I learned to make my mind large, as the universe is large,

so that there is room for paradoxes.

—Maxine Hong Kingston

TABLE OF CONTENTS

LIST OF FIGURES

LIST OF TABLES

ACKNOWLEDGEMENTS

This work would not have been possible without the guidance of my advisor, Neal Driscoll, who provided me with incredible opportunities. Additionally, he taught me so much about the field of stratigraphy, patiently critiqued my presentations and papers, and always knew how to cheer me up with a good joke. Most importantly, he taught me how to view stratigraphy through a processed-oriented lens and a through a tectonic framework; this has changed the way that I see the Earth. I would also like to thank my committee and especially Miriam, for teaching me how to prepare clay mineralogy samples in her lab and guiding me with insights on geochemistry. I thank Pat and Tom Manley, my advisors at Middlebury College, for getting me hooked on marine geology and teaching me the fundamentals of the scientific method. I also thank them for mentoring me throughout graduate school.

My labmates were also very instrumental to this process and I learned so much from Shannon, James, Valerie, Hector, Jillian, Brian, Boe, and Lana. I could always turn to them for life advice and they have become incredible friends. I had many valuable discussions on clay mineralogy and geochemistry with Robert Rex, Brian Oller, and James Day. Heather Webb and Joan Kimbrough at San Diego State University taught me so much about running XRD samples. Alex Hangsterfer helped immensely with anything related to sediment cores and is always a joy to talk to. Mackenzie Roberts, Leanne Hirsch, and Lana Graves did an incredible amount of work picking foraminifera from Inner California Borderland sediment cores. Alistair Harding helped immensely with the re-processing of USGS sparker seismic profiles.

I would like to thank the amazing friends at Scripps. Lauren, Abby, and Jess have always been by my side and I cherish the amazing adventures we've been on. Finally, my family has supported me through all of the ups and downs. Thank you, mom, dad and Jeremy.

Chapter 2, in full, is a reprint of the material as it appears in Marine Geology 2019. Wei, E.A., Driscoll, N.W., Slingerland, R.L. The dissertation author was the primary investigator and author of this paper.

Chapter 3, in full, is currently accepted for publication of the material as it appears in Sedimentology. Wei, E.A. and Driscoll, N.W. The dissertation author was the primary investigator and author of this paper.

Chapter 4, in part is currently being prepared for submission for publication of the material. Wei, E.A. and Driscoll, N.W. The dissertation author was the primary investigator and author of this paper.

Chapter 5, in part is currently submitted for publication of the material. Wei, E.A., Holmes, J.J., Driscoll, N.W. The dissertation author was the primary investigator and author of this paper.

Appendix A, in full, is a reprint of the material as it appears in Marine Geology 2019. Marcuson, R., Gee, J., Wei, E.A., and Driscoll, N.W. The dissertation author was a co-author of this paper.

VITA

2013	B. A. in Geology *cum laude*, Middlebury College
2014	M. S. in Earth Sciences, University of California, San Diego
2014-2019	Graduate Student Researcher, University of California, San Diego
2019	Ph. D. in Earth Sciences, University of California, San Diego

PUBLICATIONS

Wei, E.A., Driscoll, N.W., Slingerland, R.L., 2019. "Oceanographic currents, differential subsidence, and physiography control three-dimensional clinothem growth in the Gulf of Papua, Papua New Guinea." *Marine Geology*, 407, 164-180.

Wei, E.A. and Driscoll, N.W., Accepted. "Clay Mineralogy of Gulf of Papua shelf and Pandora Trough deposits constrains sediment source and routing during the last sea-level cycle", *Sedimentology*.

Marcuson, R., Gee, J., Wei, E.A., Driscoll, N.W., 2019. "A 2000 year geomagnetic field record from the Gulf of Papua." *Marine Geology*, 408, 48-66.

Seidenstein, J.L., Cronin, T.M., Gemery, L., Keigwin, L.D., Peace, C., Jakobsson, M., Coxall, H., Wei, E.A., Driscoll, N.W., 2018. "Late Holocene paleoceanography in the Chukchi and Beaufort Seas, Arctic Ocean, based on benthic foraminifera and ostracodes." *arktos*, 4(1), 23.

ABSTRACT OF THE DISSERTATION

Shelf Width Variability Controls Sediment Dispersal on Active Margins

by

Emily Ann-Yi Wei

Doctor of Philosophy in Earth Sciences

University of California San Diego, 2019

Professor Neal Driscoll, Chair

High-resolution CHIRP and multi-channel seismic data paired with sediment cores provide an unprecedented view of forcing functions on continental margin deposits. Serving as reservoirs for hydrocarbons, sand, and aquifers, continental margin deposits have societal and scientific relevance. Traditionally, relative sea-level and sediment supply are considered the dominant controls on the geometry of continental shelf deposits. On active margins studied in this dissertation, tectonic deformation plays a large role in controlling shelf geometry, as deformation is at high angles to the shoreline. Sediment storage and dispersal are modified further by energetic oceanographic currents and climate. In the Gulf of Papua (GoP), clinothem architecture and surfaces of lap are not dependent on eustatic sea level changes. As a result of foreland basin

tectonics, subsidence in the northeast GoP engenders aggradational Holocene clinoforms whereas peripheral bulge uplift in the southwest GoP causes toplap. Along-margin currents build the clinothem obliquely to the northeast. Downcore clay mineralogy constrain contributions of the Fly and Purari rivers to the GoP clinothem and lowstand deep-water basin deposits. Results suggest that sediment source and routing changed through a sea level cycle. Fly River sediment may have bypassed the inner mid-shelf clinothem during intermediate lowstands due to narrower shelf widths that allow for the establishment of incised valleys. Depocenters of post-glacial shelf deposits offshore of the Oceano Dunes State Vehicular Reservation in Central California are influenced by eustatic sea-level changes in the cross-shore direction and uplift of the San Luis Block and subsidence of the Santa Maria Basin in the along-margin direction. The timing and emplacement of turbidite deposits from submarine canyon systems offshore of San Onofre (SO) and Dana Point (DP) may be controlled primarily by shelf width. Wide shelves offshore of SO were formed by transpression along a left jog on the right-lateral Newport-Inglewood/Rose Canyon Fault Zone. Turbidites offshore of SO were deposited during and prior to the last sea-level lowstand, whereas turbidites were deposited offshore DP during the sea-level lowstand, transgression, and highstand. Second-order controls on local turbidite emplacement include small synclines and anticlines that engender deposition or promote sediment bypass.

Chapter 1

Introduction

1.1 Continental Margins and Sequence Stratigraphy

Source to sink studies investigate the transport of sediment from land, to transfer zones in delta plains and continental shelves, to the deep-sea sink. In many cases, the erosion of sediment at the source originates from climatic (e.g., intensification of El Niño, intensification of monsoon, onset of glacial activity, shifting of Intertropical Convergence Zone) or tectonic events (e.g., uplift, earthquakes). As sediment propagates through the system, timescales of transfer and storage in delta plains and continental shelves differ in various tectonic and basin settings. This dissertation focuses on the storage of sediment in continental shelves and ultimate transfer to the deep sea. On many margins worldwide, continental shelf, continental slope, and basin slope deposits with high accumulation rates potentially record past sea-level changes, tectonic deformation, oceanographic regimes, and climate.

Understanding the processes that build continental margins has both societal and scientific relevance. Sediment dispersal at continental margins has the potential to influence navigation, algae productivity, fisheries, and engineering close to the continental margin. The study of margin architecture using reflection seismic surveying and sediment cores is called sequence stratigraphy

or seismic stratigraphy (e.g., Vail et al., 1977). Seismic reflection surveys resolve the geometry of clinothems, which are stacks of sigmoidal-shaped sediment units that are considered the building blocks of ancient and modern continental margins. Clinothem geometry has been considered in the classic sequence-stratigraphy studies to reflect the balance of the rate of sediment supply and the rate of creation of accommodation (e.g., Mitchum Jr et al., 1977; Christie-Blick & Driscoll, 1995). Accommodation can be created by changes in sea level and tectonic deformation (i.e., uplift or subsidence). In theory, interpreting continental margin geometry could provide insight on past changes in relative sea-level or sediment supply. Despite much research on clinothems and continental margins, it remains difficult to invert continental margin stratigraphy for the factors responsible for their formation. This is because other factors operating in the along-margin geometry may complicate continental margin formation, such as tectonic deformation, oceanographic currents, and climate. Source-to-sink studies require evaluation of the whole continental margin including focused studies on continental shelves, continental slopes, and basin floor deposits.

The continental margins described in this dissertation are located on active margins where tectonic deformation is at high angles to the shoreline. In active margin settings where deformation is parallel to eustatic sea-level changes, tectonic deformation is often viewed as a secondary control that amplifies or diminishes the effects of sea-level (e.g., Posamentier & Vail, 1988). Nevertheless, when tectonic deformation operates at high angles, it creates along-margin variability in shelf width and accommodation (e.g., Le Dantec et al., 2010; Hogarth et al., 2012; Klotsko et al., 2015). Such geometries of tectonic deformation and eustatic sea-level changes permits these two signals to be disentangled. The Gulf of Papua in Papua New Guinea is located in a foreland basin and as a result has wide shelves and differential accommodation. Block uplift north of the Oceano Dunes destroys accommodation, whereas subsidence of the Santa Maria Basin serves as a depocenter for sand. Narrow shelves in the Inner California Borderlands facilitates the rapid transfer of sediment from source to sink; however, increased shelf width

offshore of San Onofre inhibits sediment transfer to the deep-sea during sea-level highstands.

To study these processes, geological and geophysical data are used to image continental margin architecture. Seismic reflection datasets were used to image subsurface layers, which provide insight on the sediment dispersal systems on differing scales. In Chapters 2, 3, and 4, high-resolution Compressed High Intensity Radar Pulse (CHIRP) seismic reflection data penetrated the seafloor to depths of 50 m and imaged sediment layers at sub-decimeter vertical scales. In chapters 4 and 5, sparker multi-channel seismic reflection data with lower resolution was used to image sediment layers at meter vertical scales to depths of 600-1300 m. Combining high- and low-resolution seismic data provides an unprecedented view of margin morphology. High-resolution CHIRP data constrain active processes within the upper 50 m of the seafloor, whereas low-resolution sparker data are deeper penetrating and elucidate the margin's long-term tectonic evolution. High-resolution multibeam bathymetry was used to map the nearshore region offshore of the Oceano Dunes. To ground truth our seismic datasets, we examined large diameter gravity and jumbo piston cores to constrain sediment properties, grain size, age of the sediment, and geochemistry in the Gulf of Papua and Inner California Borderlands. Offshore of the Oceano Dunes, surficial sediment grabs were collected along seismic profiles.

1.2 Outline of the Thesis

Chapter 2 examines the growth of three-dimensional clinothems in the Gulf of Papua (GoP). Thirty-nine new radiocarbon ages from sediment cores reveal that inner mid-shelf clinothem architecture and surfaces of lap are less dependent on eustatic sea-level and instead are controlled by foreland basin subsidence, strong along-margin currents that build the clinothem obliquely to the northeast, and inherited physiography. Foreland basin subsidence creates more accommodation in the northeast GoP and engenders deposition of thick, aggradational sediment units. Uplift of the peripheral bulge in the southwest GoP destroys accommodation and may cause

sediment bypass. Along-margin stratigraphy and radiocarbon ages suggest that strong northeast bottom currents have prevailed for at least the past 2000 years. This could have implications for future Holocene oceanographic or climate studies.

Chapter 3 uses clay mineralogy to track the fate of Fly and Purari river sediment to the inner mid-shelf clinothem and Pandora Trough throughout a sea-level cycle (last 120 kyr). By integrating the records from the inner mid-shelf and deep-sea Pandora Trough, this study suggests that narrow shelves offshore of the Fly River enable three incised valleys to funnel sediment to the deep sea during intermediate lowstands such as Marine Isotope Stage (MIS) 3. Such valleys do not exist offshore of the Purari River because of deeper shelves and basin subsidence. Therefore, during MIS 3, the inner mid-shelf clinothem was built by sediment sourced from the Purari River.

Chapter 4 presents new CHIRP seismic, multibeam bathymetry, and surficial sediment grab data from the margin offshore of the Oceano Dunes State Vehicular Reservation, which is one of the few areas that allow motorists to drive on the beach. To aid in our understanding of sediment budgets and anthropogenic impacts, seismic surveys reveal that sediment depocenters are located in the center of the basin and seaward of the shoreline cutoff. The shoreline cutoff was formed before Meltwater Pulse 1A when the rate of sea-level rise slowed. The northern end of the basin has decreased accommodation due to uplift of the San Luis block. Based on the tilt of the transgressive surface, we calculated uplift rates of 0.3-0.6 mm/yr, which are three times greater than previously-published rates. This along-margin gradient in accommodation influences reworking of sediment by oceanographic currents, as deposits in uplifted regions exhibit extensive reworking.

Chapter 5 presents new sediment core chronology in order to examine the influence of shelf width on turbidite emplacement by two end-member canyons in the Inner California Borderlands (ICB). One end member is the Dana Point Canyon, which is disconnected from San Juan Creek by a narrow 2-km shelf and has limited tectonic deformation on the continental slope. This is compared to the San Onofre North and South (SON and SOS) canyons, which are

separated from San Juan Creek by 10 km and traverse a tectonically deformed slope with ponded basins.

In summary, shelf width plays an important role on modulating sediment storage and transfer from the source to the sink on active margins. Tectonic signals on these margins can be distinguished from sea-level changes, as deformation is at high angles to the shoreline. As a result, rates of uplift and subsidence can be calculated and used in future seismic models. Understanding the factors that control sediment depocenters have implications for coastal dune sediment supply, carbon sequestration, and aquifers.

Chapter 2

Oceanographic currents, differential subsidence, and physiography control three-dimensional clinothem growth in the Gulf of Papua, Papua New Guinea

2.1 Abstract

A regional high-resolution CHIRP seismic survey in the Gulf of Papua (GoP) extends the geographic scope of previous studies by 125 km and reveals that the Holocene clinothem along-margin geometries, surfaces of lap, and steepness of foreset slopes appear less dependent on eustatic sea level changes and sediment supply than previously suggested. Clinothems imaged by CHIRP profiles and sampled by sediment cores include two older, relict clinothems and a younger Holocene clinothem divided into three units by two surfaces of lap. New radiocarbon ages from this study establish that depositional timing is more recent than previously proposed for the transgressive deposits, the Holocene clinothem units, and surfaces of lap. While previous

ages suggested that observed stratal relationships could coincide with meltwater pulses or sea level stillstands, the younger ages from this study question these results and suggest the dominant control on Holocene clinothem architecture may be inherited physiography, SW-NE differential subsidence, along-margin currents, and seasonal variations in wave energy. Inherited physiography underlying the Holocene clinothem consists of valleys incised during re- lative lowstands of Marine Isotope Stages (MIS) 4 and 2. Valleys in the relict clinothem potentially served as across-margin conduits for an older Holocene clinothem unit. After the older Holocene unit filled valleys and accommodation, younger Holocene units preferentially grew along- rather than across-margin as bottom shear stresses increased. Relict clinothems have undergone differential subsidence since deposition due to foreland basin loading, which has engendered more accommodation in the northeast GoP that systematically decreases toward the southwest. Areas with less accommodation are more likely to experience toplap as they are exposed to increased shear stresses. Therefore, the surfaces of lap are caused by interactions between accommodation and oceanographic currents. Examining stratal relationships along the Holocene clinothem has broad implications for sequence stratigraphy, as many clinothems exhibit a three-dimensional stacking pattern. Measurements of seafloor slopes yield complicated results, illustrating that seafloor steepness within lobes is influenced by a complex interplay of accommodation, sediment supply, underlying physiography, and oceanographic currents. This suggests that clinothem architecture in the GoP cannot simply be interpreted as a rate-related problem between rates of sediment supply and relative sea level.

2.2 Introduction

In recent years, stratigraphic studies of modern and ancient clin- othems have focused increasingly on the three-dimensional processes that form them. The Gulf of Papua (GoP; Fig. 2.1) is an ideal locale to study three-dimensional clinothem development in a high-energy

setting because of its rapid sediment accumulation, active foreland basin tectonics, and seasonal oceanographic currents. Despite much research on clinothem geometry worldwide, transport mechanisms of sediment across and along clinothems are still not well understood. The GoP clinothem is a mid-shelf clinothem with three-dimensional lobate geometry suggestive of a high-energy environment (Driscoll & Karner, 1999; Slingerland et al., 2008,b). Its downdip geometry has well-defined topsets, foresets, and bottomsets, with the highest accumulation rates occurring on the foresets (Harris et al., 1993; Walsh et al., 2004). In classic-sequence stratigraphy studies (e.g. Mitchum Jr et al., 1977; Christie-Blick & Driscoll, 1995), the geometries and evolution of the clinothems are viewed as a rate-related problem balancing the rate of sediment supply and the rate of creation of accommodation. Accommodation can be created by changes in sea level and tectonic deformation (i.e., uplift or subsidence). Though clinothem growth is often characterized by its across-margin geometry, along-margin growth controls many aspects of clinothem geometry. Numerous modeling studies (e.g., Driscoll & Karner, 1999; Ritchie et al., 2004) have shown that processes that drive modern clinothem growth include oblique and along-shelf transport from wind-driven flows, wave-orbital flows, buoyant plumes, and surf-zone processes (Nittrouer & Wright, 1994). This concept is reinforced by clinothems that grow and extend downdrift of major river systems on margins such as the Rio de Janeiro (Reis et al., 2013), the Adriatic Sea (Cattaneo & Steel, 2003; Cattaneo et al., 2007), the Yangtze (Xu et al., 2009), the Ganges-Brahmaputra (Kuehl et al., 1997), and the Mekong River (Nguyen et al., 2000). Along-margin transport regimes may exhibit a more regional role in the development of coastal and nearshore areas than previously considered, as along-margin currents can transport up to 30–40% of fluvially dis- charged sediment along the shore far from the river mouth (Liu et al., 2009). When interpreting seismic profiles that image the along-margin geometry of clinothems, challenges still exist in inverting clinothem geometry to fingerprint the process or combinations of processes that build them.

Previous sedimentological work on the GoP clinothem focused on the across-margin

geometry and chronostratigraphy of relict clinothems (Harris et al., 1996; Slingerland et al., 2008) as described in Section 2.2. This paper describes a larger area spanning ∼285 km along the GoP margin, whereas the Harris et al. (1996) study area is located to the south and farther offshore and the Slingerland et al. (2008a) study area is a subset of the MARGINS survey spanning ∼60 km along-margin in the Central Lobe northeast of the Fly River and offshore of the Bamu and Turama rivers (See white seismic track lines in Fig. 2.1). Radiocarbon ages from the Slingerland et al. (2008a) study were limited and out of chronostratigraphic order and thus more constraints on depositional timing were required. The geometry of the Holocene and relict clinothems were explained largely by eustatic sea level changes and sediment supply by Slingerland et al. (2008a). Expanded scope of the study area and new radiocarbon ages allow us to investigate other regional tectonic and oceanographic processes that contribute to the formation of the Holocene clinothem and builds on the previous results.

2.3 Regional setting

The GoP is a semi-circular embayment with shelf widths that progressively narrow from the southwest to the northeast, with southwest shelf widths of 72km and northeast widths of 10km (Fig. 2.1). The southwest edge of the basin is characterized by shallow bathymetry with reef systems and Halimeda banks bordering the distal edge (i.e. peripheral bulge) of the foreland basin filled with Miocene sediment (Fig. 2.1; Davies et al., 1989; Pigram et al., 1989; Davies, 2012). Conversely, the northeast GoP is bordered by high mountains associated with numerous fold-and-thrust belts. Mountain building events initiated during the Mid Oligocene uplifted the Finisterre, Owen Stanley, and the New Guinea Highlands mountain ranges and formed a foreland basin to the south (Pigram & Symonds, 1991). The onset of loading heralded the transition from passive margin to a foreland basin environment as well as a transition from carbonate to detrital siliciclastic sediment deposition (Pigram et al., 1989; Tcherepanov et al., 2008). At present, the

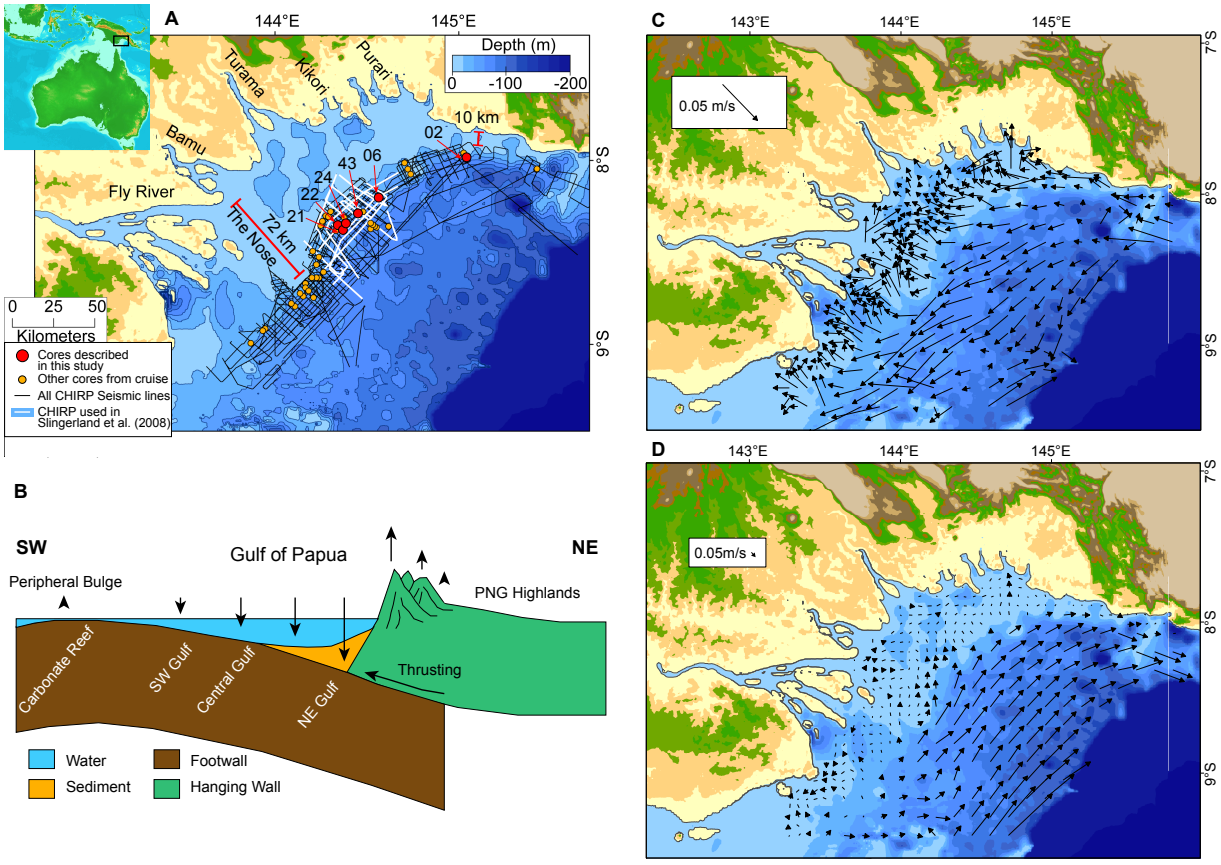

Figure 2.1: A) The study area focuses on the inner shelf of the Gulf of Papua (GoP), which is highlighted by the black box in the inset. Yellow circles show the location of the 54 sediment cores. Larger red circles indicate location of cores described in this study. Black lines show the location of CHIRP seismic profiles in the entire seismic survey. A subset of these lines is highlighted in white as the seismic lines studied in Slingerland et al. (2008a). Relative shelf width decreases to the northeast, as shown by the red lines. B) Schematic cross section of the foreland basin in the Gulf of Papua. Figure modified from Christie-Blick and Driscoll (1995). C) Bottom currents during the quiescent Monsoon season. Figures C and D are modified from Slingerland et al. (2008b). D) Bottom currents during the Trade Wind season. Note different scales for Monsoon and Trade wind season bottom currents.

foreland basin subsides with regional rates estimated at $\sim$1 mm/a (Slingerland et al., 2008a).

Five rivers (the Fly, Bamu, Turama, Kikori, and Purari rivers) collectively discharge approximately 15000 $m^3\ s^{-1}$ of freshwater (Wolanski et al., 1995; Fig. 1) and 365 Mt. of sediment (Milliman, 1995; Slingerland et al., 2008a) into the GoP. Discharging an average of 6500 $m^3\ s^{-1}$ of water to the GoP, the Fly River has the broadest floodplain. Despite the Fly River having the largest freshwater discharge, 40% of the Fly River sediment load is captured in its floodplain (Day et al., 2008). Although river discharge can have minor seasonal variations (Warrick et al., 2004), the largest fluctuations in discharge result from El Niño climatic conditions, which decrease rainfall, reducing water and sediment discharge (Dietrich et al., 1999; Ogston et al., 2008). When sediment discharge from the rivers is hyperpycnal, it moves as fluid muds by gravity flows that travel from the river mouth, are temporarily deposited on the clinothem topset and subsequent reworking advects it downslope to the foreset and bottomset. Conversely, hypopycnal flows carry sediment in suspension, where the sediment is advected by wind-driven and baroclinic currents and eventually deposited when energy decreases (Wolanski & Alongi, 1995; Wolanski et al., 1995; Harris et al., 1993; Walsh et al., 2004; Keen et al., 2006; Ogston et al., 2008).

2.3.1 Oceanographic setting

Circulation in the Gulf of Papua modulates the location of erosion and deposition as well as influences the along- and across-shelf transport of sediment. GoP circulation is complex and spatially heterogeneous due to baroclinic currents, wind-driven currents, and the region's variable morphology (Slingerland et al., 2008).

In general, the main forces that resuspend noncohesive mud are spring-neap tidal currents and seasonal bottom currents, as the conditions that allow for sediment resuspension and the generation of gravity flows are peak spring tides during the trade wind season (Martin et al., 2008; Slingerland et al., 2008b). Tides in the GoP have a strong spring-neap variation, are directed

across-shelf, and amplified on topsets (Slingerland et al., 2008b). Near-bed tidal currents can reach 0.76 m/s on the clinothem topset, whereas upper foreset currents can reach 0.64 m/s during spring tides (Slingerland et al., 2008b). As a result, spring tides can produce shear stresses capable of resuspending fine sand and noncohesive mud (Walsh et al., 2004).

The largest control on circulation is seasonal changes in energy (i.e., monsoon versus trade wind). Shifting wind patterns can create gyres that can cause subsequent shifting of currents on timescales of hours, weeks, and seasons (Slingerland et al., 2008b). During the winter Monsoon season (December to March), northwest winds on the order of 1–2 m/s generate a persistent eddy in the north GoP and a clockwise gyre over the gulf (Fig. 2.1C; Slingerland et al., 2008b). These conditions generate weak landward bottom currents that reach a peak of 0.04 m/s during spring tides whereas net conditions are 0.02 m/s (Slingerland et al., 2008b). The quiescent Monsoon season allows for temporary sediment storage on the shallow topset bed at depths < 10 m (Walsh et al., 2004). Conversely, the stronger and sustained southeast Trade Winds (prevalent from May through October), with velocities $\sim$4–5 m/s, cause a convergence of flow north of the clinothem that then results in a counterclockwise gyre (Slingerland et al., 2008b). Trade wind conditions generate near-bed currents that are weaker (0.01–0.03 m/s) over the topset and increase to 0.05–0.1 m/s at the foreset; even though in general bottom currents during the trade wind season are stronger than those during the monsoon season (Fig. 2.1D; Slingerland et al., 2008b). Bottom currents over the foreset during the trade wind season may be responsible for the advection of illite-rich Fly River sediment to the northeast (Slingerland et al., 2008b).

In the GoP as well as many delta-scale subaqueous clinoforms (e.g., the Amazon, the Adriatic Sea, and the Atchafalaya) around the world, sediment accumulation is largely focused on the foreset with little deposition on the topset and bottomset (Kuehl et al., 1986; Walsh et al., 2004; Neill & Allison, 2005; Puig et al., 2007; Patruno & Helland-Hansen, 2018). Traditionally, clinothem topsets are expected to experience higher energy conditions than the foreset or bottomset, where the clinothem rollover indicates the limit below which wave-current shear

stresses decreases (Cattaneo et al., 2007; Nittrouer et al., 1986; Kuehl et al., 1986; Walsh et al., 2004). Elevated near-bed shear stresses at the topset beds may result in bypass caused by resuspension of topset sediment that is advected to the foreset (Nittrouer & DeMaster, 1996). Such is the case in the Gulf of Papua, where sediment on topset beds are eroded and winnowed during the trade wind season (Walsh et al., 2004; Slingerland et al., 2008b). The mechanisms that resuspend and mobilize sediment are a combination of spring tidal currents, waves, and storm surges acting in concert with strong bottom currents during the trade wind season (Harris et al., 2004; Ogston et al., 2008; Slingerland et al., 2008b). Once these currents generate the necessary shear-strength to resuspend sediment, mobilized sediment in concentrations $>$10 mg l^{-1} may form fluid muds that move down the clinothem foreset until halted by drag (Slingerland et al., 2008b). Although peak spring tide conditions during the trade wind season are the most effective at transporting bottom sediment along and across margin, these transport regimes are episodic and spatially heterogeneous (Slingerland et al., 2008b). As bottom currents are not directed seaward during either the trade wind or monsoon season (Fig. 2.1C and D), deposition on the clinothem foreset occurs via downslope movement of fluid mud (Slingerland et al., 2008b) and appear similar to fluid mud processes that built the Amazon subaqueous clinothem (Kineke et al., 1996). Similar temporary sediment storage and advection on the topset is observed in the Atchafalaya clinothem in the Gulf of Mexico where the passage of occasional cyclonic storms resuspends topset sediment and supplies it to the foreset (Neill and Allison, 2005).

2.3.2 Previous studies on the GoP inner shelf clinothem

Stratigraphy in the GoP inner shelf clinothem has been previously described by Harris et al. (1996) and Slingerland et al. (2008a). Here we summarize the findings of previous research in the GoP. Although the Slingerland et al. (2008a) study referred to sediment units as colors, we prefer to name the units alphanumerically as A1, A2, A3, B1, B2, C, and D because this practice has become more standard in recent seismic stratigraphy studies (e.g., McHugh et al.,

2010; Hogarth et al., 2012). To relate nomenclature from Slingerland et al. (2008a) to this study, please refer to Table 2.1. Interpretations from Slingerland et al. (2008a) were confined to an area that they defined as the "central lobe." To maintain consistency and to orient the reader, we will refer to this central area as the Central lobe and will refer to the adjacent areas as the Southern and Northern lobes.

Three distinct clinothems are observed in the Gulf of Papua (Figs. 2.2 and 2.3 from this study). Although the geometry and morphology of the margin is largely influenced by the most recent Holocene clinothem, the two underlying relict clinothems exert important controls on the ar- chitecture of the Holocene clinothem. As described by Harris et al. (1996) and Slingerland et al. (2008a), the margin consists of stacks of two relict and eroded clinothems and a smooth younger clinothem. The two older clinothems are herein referred to as separate units; however, the smooth, youngest clinothem was divided into three units by Slingerland et al. (2008a). The three clinothems are separated by two prominent regional unconformities. The older and deeper regional unconformity truncates prograding reflectors and separates the basal unit from an overlying unit with horizontal reflectors. The unit with prograding reflectors, herein referred to as Unit D, is the most basal unit observed in this survey and is separated from the overlying Unit C by a regional unconformity. Horizontal reflectors in Unit C are truncated by a younger regional unconformity that separates Unit C from Unit B, which also has horizontal reflectors that infill topographic lows (Slingerland et al., 2008a). Within the Holocene clinothem are two bounding surfaces that separate it into three units.

Unit D is shown in an uninterpreted dip profile from the southwest portion of the survey and is characterized by tangential oblique clino- forms (see Fig. 4a from Slingerland et al., 2008a; Mitchum Jr et al., 1977). Based on the prograding geometry, this unit is inferred to have been deposited during MIS 4 (Slingerland et al., 2008a; Fig. 2.3). This basal unit is mantled by Unit C and is separated by an angular unconformity (Fig. 2.3; Slingerland et al., 2008a). Unit C (shown in blue) is interpreted to have been deposited during MIS 3 and is characterized by aggrading

reflectors and an erosional upper boundary that truncates reflectors (Figs. 2.2 and 2.3; Slingerland et al., 2008a). This erosional surface has created the so-called corrugated "Mesa topography" (Harris et al., 1996), on top of which the Holocene clinothem has been deposited. In order to have accommodation sufficient to create aggradational beds at this time, the gulf required regional subsidence rates on the order of $\sim$ 1 mm/a (Slingerland et al., 2008a).

Sedimentary deposits between the Unit C and the Holocene clinothem are characterized by two facies (Harris et al., 1996). The younger facies contains abundant benthic foraminifers, molluscs, echinoid fragments, bryozoan, and Halimeda and was dated to $\sim$6160 years BP (Harris et al., 1996). The older facies is a peat bed dated to $\sim$ 16,750 years BP (Harris et al., 1996). Based on the dates and facies descriptions, these deposits were interpreted to have been deposited during the post-glacial sea level rise and we will refer to them as Unit B1. Unit B1 is not continuous but rather is localized in topographic lows incised into Units C and D. The boundary between Unit B1 and the overlying Holocene clinothem is defined by downlap of Holocene clinothem sediment onto horizontal beds in Unit B1 (Slingerland et al., 2008a).

Downlapping onto Units B1 and C is the Holocene clinothem, which is separated into three units by two surfaces of lap defined as the older S1 and younger S2 (Fig. 2.2; Slingerland et al., 2008a). S1 and S2 were identified as surfaces that terminate underlying units through top- or offlap (Slingerland et al., 2008a). Overlying units may exhibit on- or downlap onto the S1 or S2 surfaces. The S1 surface was interpreted by Slingerland et al. (2008a) to represent an erosional unconformity or a surface of bypass. Although these Holocene units were referred to by their color (Yellow, Orange, and Red) by Slingerland et al. (2008a), we will refer to them as Units A3, A2, and A1, respectively (Table 2.1). The oldest Unit A3 (Yellow in Fig. 2.2) is separated from the overlying Unit A2 (Orange in Fig. 2.2) by S1. Radiocarbon ages from bivalves above and below the S1 surface constrain the surface between 2.41 and 5.2 ka (Slingerland et al., 2008a). Given this time interval has no rapid rises in sea level, the authors speculated that S1 was caused by a decline in sediment supply (Slingerland et al., 2008a). The most recent package

A1 (Red in Fig. 2.2) drapes the clinothem, has nearly uniform thickness, and is characterized by three aggrading high-frequency low-amplitude reflectors (Fig. 2.2). It is separated from the underlying package by S2, another surface of lap (Slingerland et al., 2008a). Slingerland et al. (2008a) do not provide a hypothesis for the formation of the S2 surface of lap. Isopach maps of Units A2 and A1 show that sediment is generally thicker on topographic highs and pinches out in valleys (Slingerland et al., 2008a). The thickness variability mapped through Units A3, A2, and A1 suggest that the growth of the Holocene clinothem was via along-shelf oblique transport in a northeast-southwest-trending direction, consistent with northeast-directed bottom currents during the Trade-Wind season (Slingerland et al., 2008a,b). Predominant northeast advection also explains patterns of clay mineralogy, with high illite:smectite ratios proximal to the Fly River, a mixing zone of intermediate values, and low illite:smectite ratios proximal to the northeastern rivers (Slingerland et al., 2008a).

Table 2.1: Units described by Slingerland et al. (2008a) and this study.

Name (Slingerland et al. (2008)	Unit color in seismic profiles	Unit name (this study)	Upper bounding surface	Relative age (Slingerland et al. (2008)	Relative Age (this study)
Red	Red	Unit A1	Seafloor	$<$ 1.6 ka	$<$ 112 years BP
Orange	Orange	Unit A2	Surface of lap S2		112-1570 years BP
Yellow	Yellow	Unit A3	Surface of lap S1	$>$ 2.41 ka or $>$ 5.2 ka	3835-1570 years BP
	Green	Unit B1			3835-6561 years BP
	Cyan	Unit B2	Undulatory boundary		9.5 - 10.3 ka
Relict clinothem	Blue	Unit C	Erosional surface	Marine Isotope Stage (MIS) 3	MIS 3
Relict oblique clinothem	Pink	Unit D	Erosional surface	MIS 4	MIS 5a-4

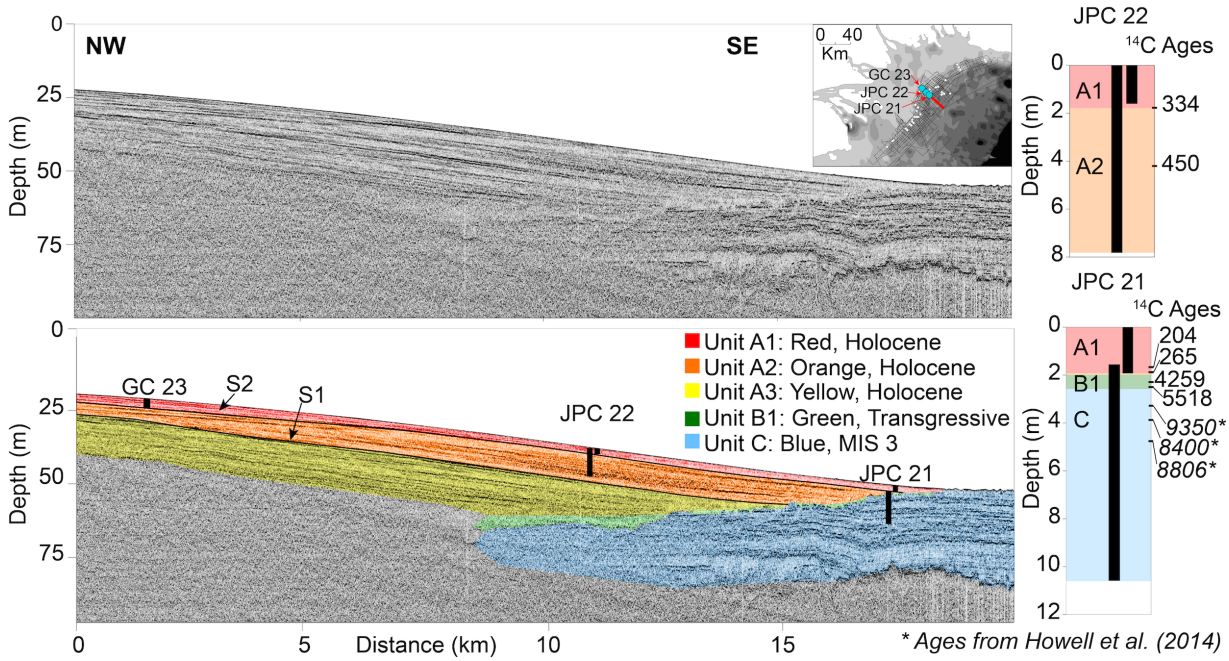

Figure 2.2: CHIRP seismic dip profile images the four main sediment packages formed along the margin. The bottommost sequence in this profile, Unit C (blue), has horizontal reflectors. This is overlain by thin deposits of Unit B1 (green). Units A3, A2, and A1 (yellow, orange, and red) comprise the Holocene clinothem. Three reflectors (Yellow, Blue, and Lime green) within A2 are correlated to sediment cores. The locations of three sediment cores, GC23, JPC22, and JPC21 are shown as topset, foreset, and bottomset cores, respectively. For JPCs 21 and 22, both the trigger and piston cores are projected onto the seismic line. Inset shows location of the seismic line (highlighted in red) and cores GC23, JPC 22, and JPC 21 (highlighted in blue). At right, an expanded view of the cores shows corrected radiocarbon ages relative to depth in the core.

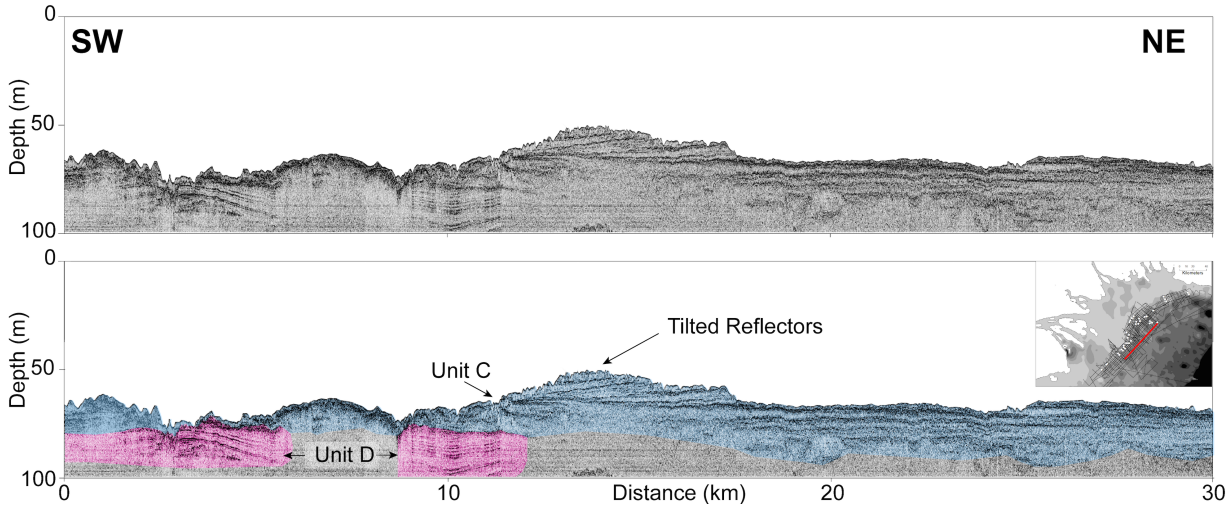

Figure 2.3: A strike line of the so-called "Mesa" topography comprised of Unit C and underlying Unit D. Horizontal beds in Unit C are overlain in some locations by tilted reflectors. The upper boundary of Unit C is eroded with marked truncation. Unit D exhibits across-margin dipping geometry, and in strike profiles, the northeast dip is the consequence of three-dimensional clinothem growth. Inset shows location of the seismic line (highlighted in red).

2.4 Materials and Methods

2.4.1 CHIRP seismic data

Between September 2003 and March 2004, 6800 km of Compressed High Intensity Radar Pulse (CHIRP) data were collected onboard the R/ V Melville as part of the NSF MARGINS Initiative (Fig. 2.1). Of these lines, 2300 km were collected with the Scripps Institution of Oceanography surface-towed Edgetech profiler with a 500Hz–6kHz signal and a 50 ms sweep and navigation of the surface-towed CHIRP was derived from comparing the fish depth and winch cable payout relative to the ship topside DGPS receivers. In addition, 4500 km of data were acquired with a Knudsen hull-mounted profiler with a 3.5 kHz center frequency. For both systems, vertical resolution is submeter to depths of 50 m. Cruise track spacing was designed to provide dip line coverage of clinothem geometry as well as detailed strike-line coverage of along- shelf variability (Fig. 2.1A). Although no new seismic data were acquired in the GoP since Slingerland et al. (2008a), that study used only a subset of Edgetech profiler seismic lines located in the

Central GoP, whereas this study uses Edgetech profiler and Knudsen profiler lines across the entire GoP (Fig. 2.1A).

Initial processing, including ship heave removal and gain adjust- ment were performed using SIOSEIS (Henkart, 2003) and Seismic Unix (Cohen & Stockwell Jr, 2001). Lines were then imported into Kingdom Software, where basic sequence stratigraphic principle, that is identi- fying changes in stratal geometry (e.g., Mitchum Jr et al., 1977,b; Vail et al., 1977; Christie-Blick & Driscoll, 1995) were employed to identify and interpret sediment packages as well as trace strong re- flectors in the Holocene units. Once interpreted, Kingdom Software aided in determining depths to interpreted surfaces by converting two-way travel time to depth in meters (See Section 3.4.2). Depths of lower surfaces were subtracted from upper surfaces to compute thicknesses of intervening units. Data points with thickness values were converted into interpolated grid surfaces using a continuous curvature surface algorithm with an interior tension of 0.60 in Generic Mapping Tools (GMT; gmt.soest.hawaii.edu). Interpreted seismic profiles and their corresponding navigation were loaded into Fledermaus Software by Interactive Visualization Systems to create three-dimensional perspective views.

2.4.2 Sediment Cores

CHIRP subbottom profiles were used to select the locations of 27 jumbo piston core (JPC) and 21 gravity core (GC) locations across the shelf during the MARGINS campaign (Fig. 2.1A). Trigger cores (TC) were deployed with the JPCs. In some cases, drift in ship position caused the cores to be offset from the profiles, in which case the core locations were projected orthogonally onto the profile. On board, whole intact cores were scanned for magnetic susceptibility, gamma density, P-wave velocity, and resistivity using a GeoTek Core-logger. Cores were split and observations of colour, grain size, sediment structures, and general lithology were recorded. The entire suite of cores collected during the 2004 MARGINS campaign were analyzed and described in this study. Detailed description and sampling are presented for JPCs 01, 02, 06, 17, 21, 22, 24,

and 43. Slingerland et al. (2008a) presented results from JPCs 40 and 43 and Howell et al. (2014) examined JPCs 01, 13, 21, and 48.

A total of 39 samples were collected for radiocarbon dating, preferentially from benthic foraminifera (asterotalia), as planktonic for- aminifera abundance was insufficient for radiocarbon dating. The samples were analyzed at the Center for Accelerator Mass Spectrometry at Lawrence Livermore Laboratory and produced an age using the Libby half-life of 5568years and following the convention of Stuiver & Polach (1977). The ^{14}C ages were converted using the IntCal13 program (Reimer et al., 2013) with a δ R value of 10.

Radiocarbon dates of the top of the piston core and the bottom of the trigger core indicate that some of the piston cores overpenetrated the sediment during deployment, which was the result of sampling in shallow water ($<$ 200 m) that limited the rebound of the trawl wire when the piston core was triggered. Though modern radiocarbon ages of the tops of the trigger core indicate that they recovered surficial sediment, ages older than one hundred years suggest that many of the piston cores did not recover surficial sediment. Offset between the trigger and piston cores were calculated in the following manner. Sedimentation rates between the bottom and top of the trigger core were calculated. This rate was multiplied by the age of the top of the JPC to find its true depth. JPC 22 and 24 were found to have no offset between the trigger and piston cores. However, JPCs 02, 06, 17, 21, and 43 had offsets ranging from 1.6 to 4.26 m (this study; Marcuson et al., 2014).

To correlate the cores to the seismic profiles, two-way travel times were converted to depth using a sound velocity of 1300 m/s in contrast to the 1750 m/s used by Slingerland et al. (2008a). We first estimated the sound velocity of the sediment by averaging P-wave velocity measurements from the GeoTek Core logger to obtain a value of $\sim$1350 m/ s. Downcore P-wave velocity reveals that muddy sediments have P-wave velocities averaging $\sim$1500 m/s and sandy layers have average P- wave velocities $\sim$1000 m/s. We verified the sound velocity by matching the distinct shift in core facies to seismic profile unconformities between the MIS 3 unit and the

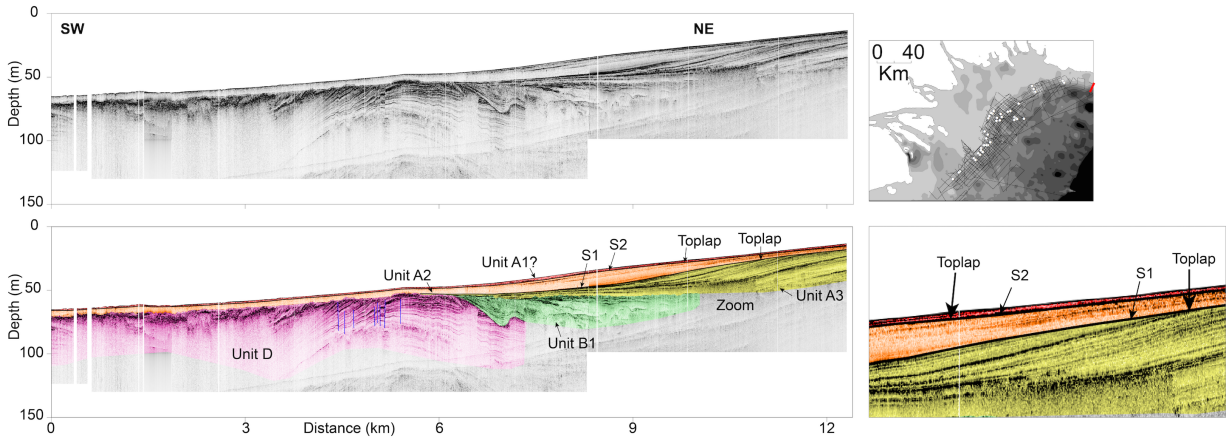

Figure 2.4: Deformation is observed in Unit D and the overlying channel deposit (green). An E-W trending antiform is crosscut by numerous vertical faults. The Holocene clinothem sediment (Units A3, A2, and A1) downlaps the anticline and exhibits little to no deformation. White striping represent data gaps. Map inset shows location of the seismic line highlighted in red. Below this, a section on the clinothem foreset is enlarged to show toplapping reflectors at the S2 and S1 surfaces.

overlying transgressive and Holocene units and found a sound velocity of 1300m/s matched the facies boundaries to the seismic profiles better than a sound velocity of 1350 m/s. Though 1300 m/s is low compared to average velocities of 1500 m/s in the literature, lower values for velocity have been determined in Fallen Leaf Lake to match reflector depths to identifiable core features (Maloney et al., 2013). Recently measured P-wave velocities from the Beaufort margin yield velocities of $\sim$1333 m/s in fine-grained sediment (Keigwin et al., 2018). As the P-wave velocity is inversely related to density, in some shallow sedimentary environments, especially fine-grained sediments, the density increases more than the bulk modulus. As such the velocity of the shallow sediments can be lower than seawater.

2.5 Results

Interpretations of clinothem sequences by Slingerland et al. (2008a) were built upon and extended as the extent of their interpretations was limited to an area offshore of the Bamu and Turama rivers highlighted by white seismic track lines in Fig. 2.1. Here we extend these

interpretations 75 km to the southwest and 50 km to the northeast to constrain the regional architecture of the clinothems in light of the different source rivers (e.g., Fig. 2.1). Units are defined by bounding unconformities and surfaces of lap defined by Harris et al. (1996) and Slingerland et al. (2008a) and summarized in Section 2.3.2. We briefly describe new observations in each unit before focusing on internal ar- chitecture and surfaces of lap within the Holocene units, architecture of the Southern, Central, and Northern lobes, facies descriptions, and Holocene chronology.

2.5.1 Basal sequence: Unit D (pink)

Gas wipeout obscures the internal reflectors of Unit D in many places, namely the Central and Northern lobes of the GoP clinothem. In the Southern lobe, high-amplitude reflectors that abruptly terminate due to gas wipeout are observed in Unit D (Fig. 2.3). Despite the domi- nant dip of reflectors to the east, the dips are variable along-margin. Unit D is highly deformed in the northeastern-most section of the GoP with increased deformation proximal to the thrust front (Fig. 2.4). A prominent antiform-synform pair in Unit D is imaged in the profile with faulting occurring mostly along the fold axis.

2.5.2 Unit C (blue)

Where Unit D is observed, it is mantled by Unit C. Most of Unit C is characterized by aggradational beds; however, in some regions, an increase in dip in the upper portions of the unit is observed (Fig. 2.3). Dipping beds are not observed regionally in the upper section of Unit C because of marked differential erosion. Where this dipping package is imaged, progradation in the along-margin direction is steeper ($\sim 2.5°$) than in the across-margin direction ($\sim 0.1°$). Note the marked increase in rugosity of the seafloor in regions where Unit C is exposed (Figs. 2.2 and 2.3).

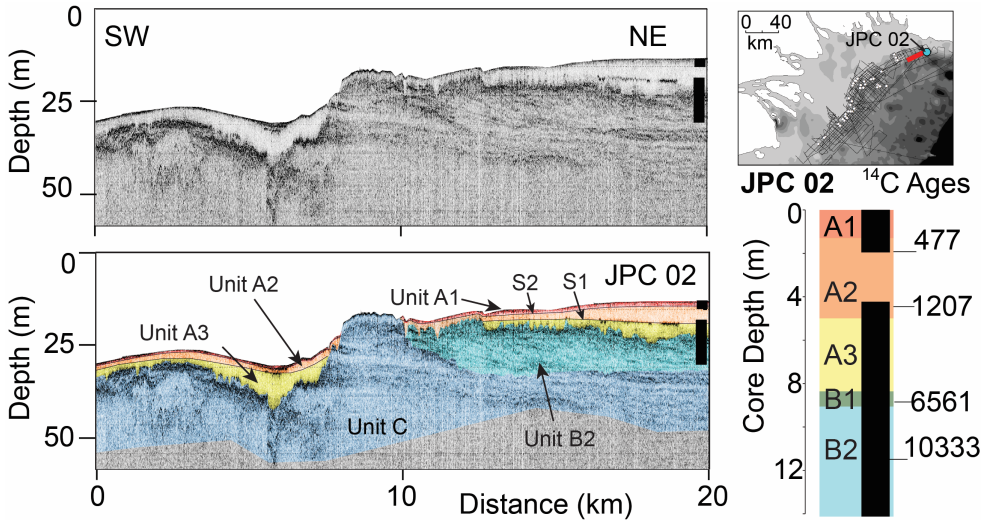

Figure 2.5: Deformation is observed in Unit D and the overlying channel deposit (green). An E-W trending antiform is crosscut by numerous vertical faults. The Holocene clinothem sediment (Units A3, A2, and A1) downlaps the anticline and exhibits little to no deformation. White striping represent data gaps. Map inset shows location of the seismic line highlighted in red. Below this, a section on the clinothem foreset is enlarged to show toplapping reflectors at the S2 and S1 surfaces.

2.5.3 Unit B2 (cyan)

Unit B2 is observed only in the northeast GoP and it exhibits subtle oblique prograding reflectors to the northeast that downlap onto Unit C (Shown as Cyan in Fig. 2.5). The reflectors in this deposit are tightly spaced and have lower acoustic amplitudes than the reflectors in Unit C. The upper boundary of this prograding deposit is undulatory and is ∼19 m below sea level, whereas the bottom boundary of the deposit is erosional and located at ∼34 m below sea level.

2.5.4 Unit B1 (green)

Unit B1 infills the erosional relief on the upper surface of Unit C (Fig. 2.2) and its thickness is predominantly controlled by the highs and lows in Unit C. In the valleys and channels, these deposits are the thickest. In the intervening highs, the deposits thin and pinch out by onlap. As described in Section 4.7, the thickness of many of the infilling deposits is close to 1 m, which approaches the imaging capability of the CHIRP system to resolve acoustic horizons. In seismic

profiles, the reflectors of this deposit exhibit a variety of acoustic character. In Fig. 2.2, Unit B1 is acoustically transparent whereas in Fig. 2.4, basal reflectors in Unit B1 mimic underlying topography and upper reflectors are wavy and discontinuous. The top of this deposit is roughly horizontal; however, in localized areas, such as the northeast GoP, this deposit is deformed (Fig. 2.4).

2.5.5 Holocene clinothem: surfaces S1 and S2, Units A1, A2, and A3

Units A1, A2, and A3 are defined by the S1 and S2 bounding surfaces. The S1 and S2 surfaces of lap are by reflectors in the underlying unit exhibiting toplap against the surface of lap. Toplap is not observed in all profiles, as in the case of the dip profile in Fig. 2.2. Where toplap is observed, Unit A3 originates at the upper boundary of Unit C or B1 and terminates where reflectors are truncated or offlap at S1. The base of Unit A2 reflectors contact S1 by onlap or downlap and are terminated at the top of the unit by S2. Unit A1 is defined by parallel reflectors that mimic S2 with the upper boundary of Unit A1 being the seafloor.

In dip profiles where toplap is observed, toplap against S1 and/or S2 can be observed on both the clinoform topset and foreset. In Fig. 2.4, prograding Unit A3 reflectors exhibit toplap against the S1 surface and to the southwest, Unit A2 a prograding reflector is truncated by the S2 surface. In the southern survey area, Unit A3 exhibits toplap against S1 on the clinothem foreset (Fig. 2.6; Line 03, Zoom 1). In strike profiles, toplap is commonly observed on the transition from topographic high to topographic low (Fig. 2.6). Near the 7.4 km marker of Line 01 is a topographic high in Unit C above which the overlying Holocene units thin (Fig. 2.6). On the flanks of this topographic high, Unit A2 thickens and reflectors within A2 prograde to the southwest and northeast (Fig. 2.6). These prograding reflectors exhibit toplap against S2, as shown in Fig. 2.8, zooms 2 and 3. Additional examples of NE-SW prograding reflectors that exhibit toplap are shown in Fig. 2.6, zooms 4 and 5, where Units A3 and A2 prograde and thicken into the topographic low. The upper boundary of these prograding reflectors are terminated by

the S1 and S2 surfaces, respectively (Fig. 2.6).

Shingling and toplap are more pronounced on clinothem topsets, as demonstrated in Line 06 from the Central Lobe (Fig. 2.7). In Zoom 1, a mounded feature in Unit A3 is truncated by the S1 surface. Above the mounded feature, reflectors in Unit A2 pinch out and shingle into the topographic low (Fig. 2.7). In Zoom 2, hummocky reflectors within Unit A3 are suggestive of a slump and bulge downward into a topographic low (Fig. 2.7). Where this feature mounds, the high-amplitude reflectors in Unit A3 appear to terminate up dip at the S1 surface (Fig. 2.7). Above the mound of Unit A3 sediment, reflectors in Unit A2 pinch out and exhibit shingling (Fig. 2.7). Similar patterns of toplap are observed in the topset line of the Northern lobe, where reflectors within Unit A2 are truncated by the S2 surface (Fig. 2.8). Unit A2 displays great variability in thickness in the Northern lobe and is likely controlled by highs and lows formed in the underlying Unit A3 deposits (Fig. 2.8). In the Northern lobe, hummocky reflectors within Unit A3 that build into topographic lows are observed and are interpreted as potential slumps (Fig. 2.8).

2.5.6 Holocene clinothem lobe architecture

The Holocene clinothem has three lobes, the Southern, Central, and Northern lobes that are defined by stratal geometry (Fig. 2.9), Holocene sediment thickness (Fig. 2.10A and B), and the bathymetric highs and incised valleys in Unit C (Fig. 2.10C). The northern edge of the Southern lobe is a promontory referred to as “the Nose” (Fig. 2.1) and located offshore of the northern tributary of the Fly River delta. The Central and Northern lobes are separated by a broad topographic low that is infilled with Holocene deposits thick enough to obscure the underlying Units C and D. Within the Northern and Southern lobes are valleys incised into Unit C that have not been completely infilled by Holocene sediments, creating lows in the modern day bathymetry with intervening bathy- metric highs. There are two bathymetric highs (BH) in the Southern lobe and two in the Northern lobe. In contrast, valleys incised into Unit C in the Central lobe have

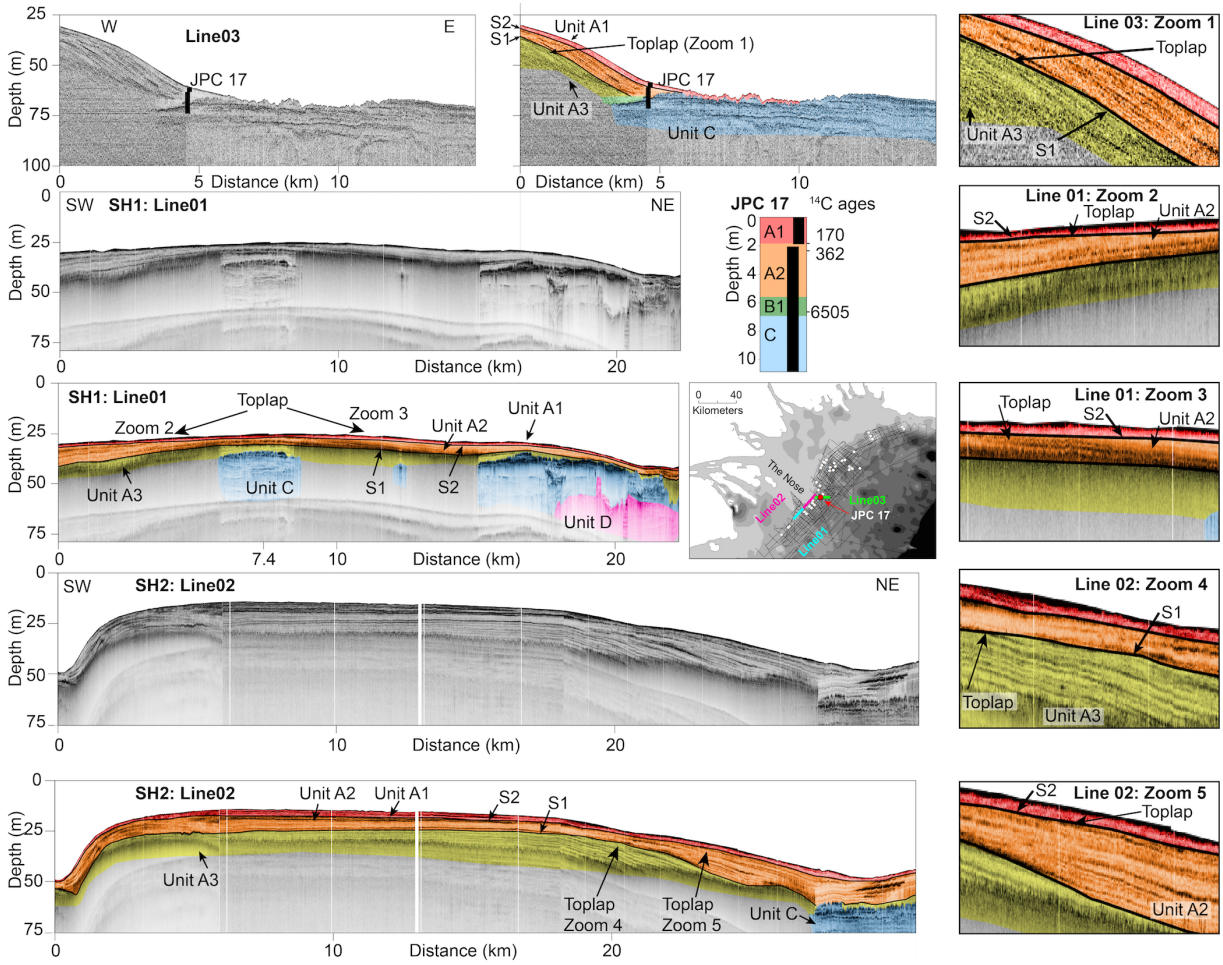

Figure 2.6: Seismic profiles in the Southern Lobe exhibit toplap. Top: line 03 shows toplap in Unit A3. Bottomsets of A3, A2, and A1 are sampled by JPC 17. Corrected radiocarbon dates are shown on units identified in the seismic profiles. Middle: Holocene clinothem is thinner across sublobe SH1. Toplap is observed in Unit A2 on line 1. Bottom: Holocene clinothem is thicker to the north in SH2 with pronounced toplap in Units A3 and A2. Inset map locates seismic profiles. At right are enlargements of areas that exhibit toplap against the S1 and S2 surfaces.

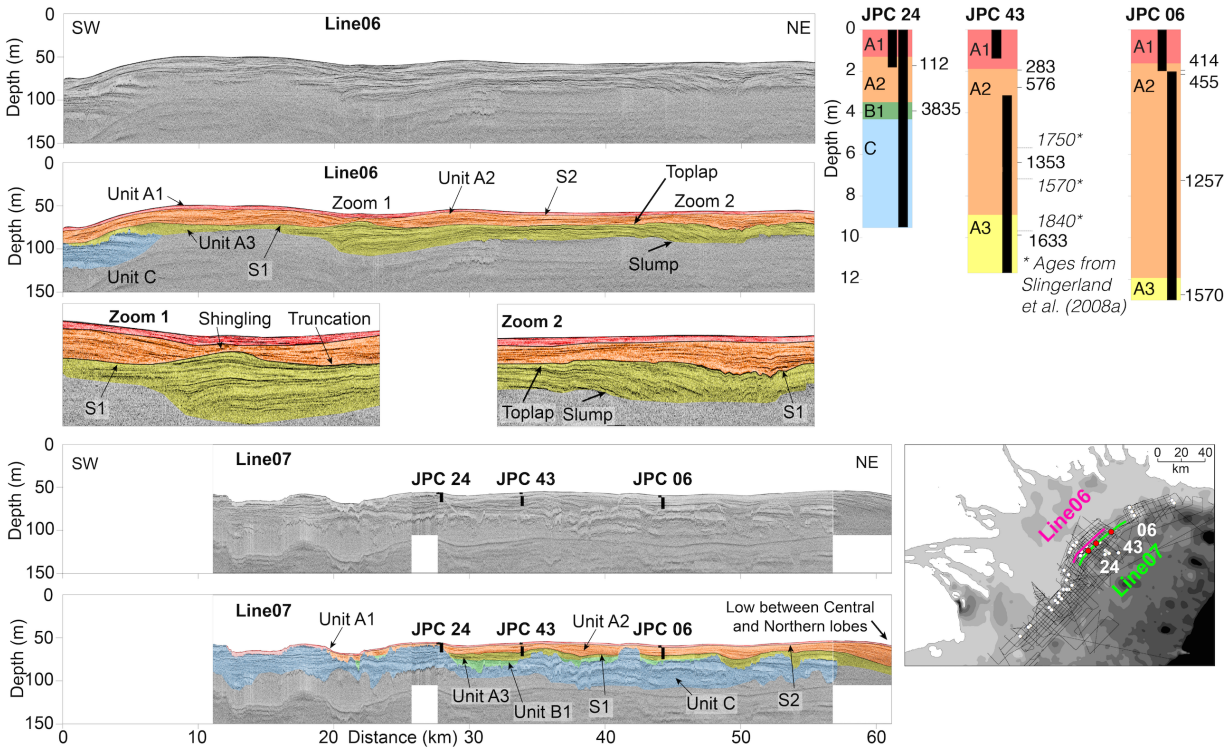

Figure 2.7: Strike profiles from the Central Lobe. Top: line 06 across the foreset illustrates aggradational Units A3 and A2. Reflectors in Unit A2 exhibit no toplap. Below the seismic profile, two zooms enlarge areas that exhibit shingling, truncation, toplap, or slumping. The area of enlargement is labeled on the seismic profile. Bottom: Line 07 acquired across the bottomset images valleys incised into Unit C with aggrading infill. JPCs 24, 43, and 06 are located on this line. Corrected radiocarbon dates are shown on units identified in the seismic profiles. JPC 43 also shows radiocarbon ages from Slingerland et al. (2008a). Below, map locates the two seismic profiles and three cores.

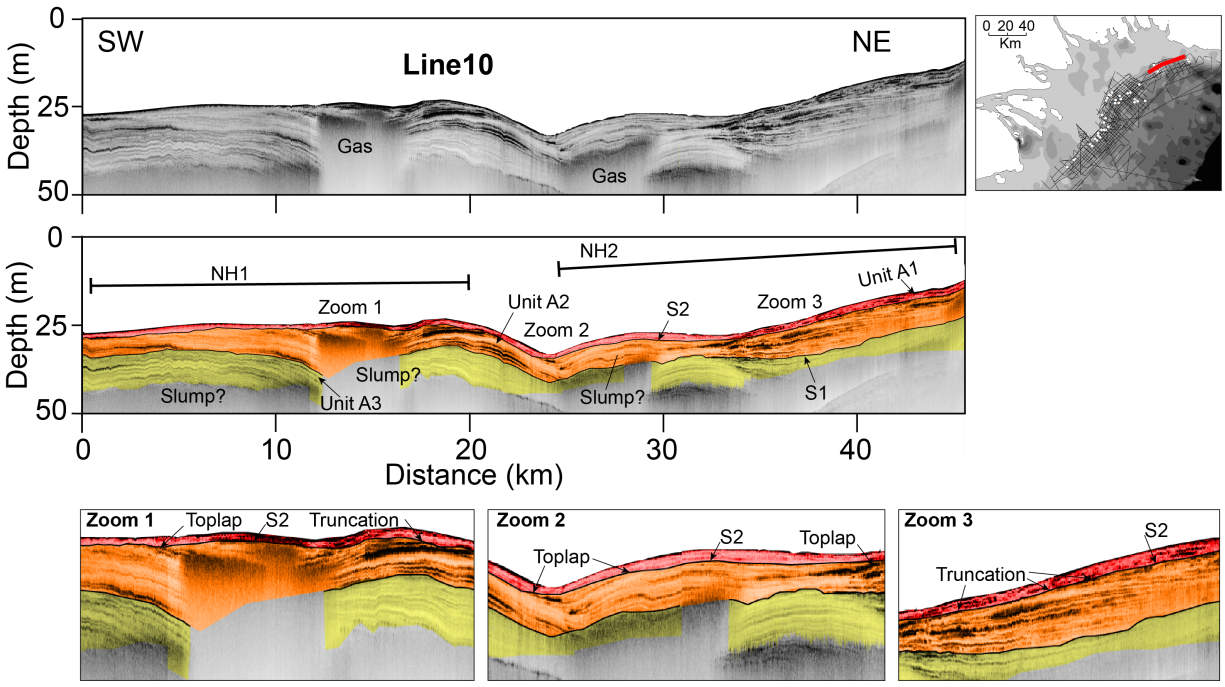

Figure 2.8: Strike line 10 located on the upper foreset of the Northern lobe. Unit A3 and A2 exhibit internal deformation characteristic of a slump deposit. Note thick deposits and gas wipeout obscure underlying Unit C. Inset at right: red line shows the location of strike profile. Below, three enlargements of areas that exhibit toplap. The area of enlargement is labeled on the seismic profile.

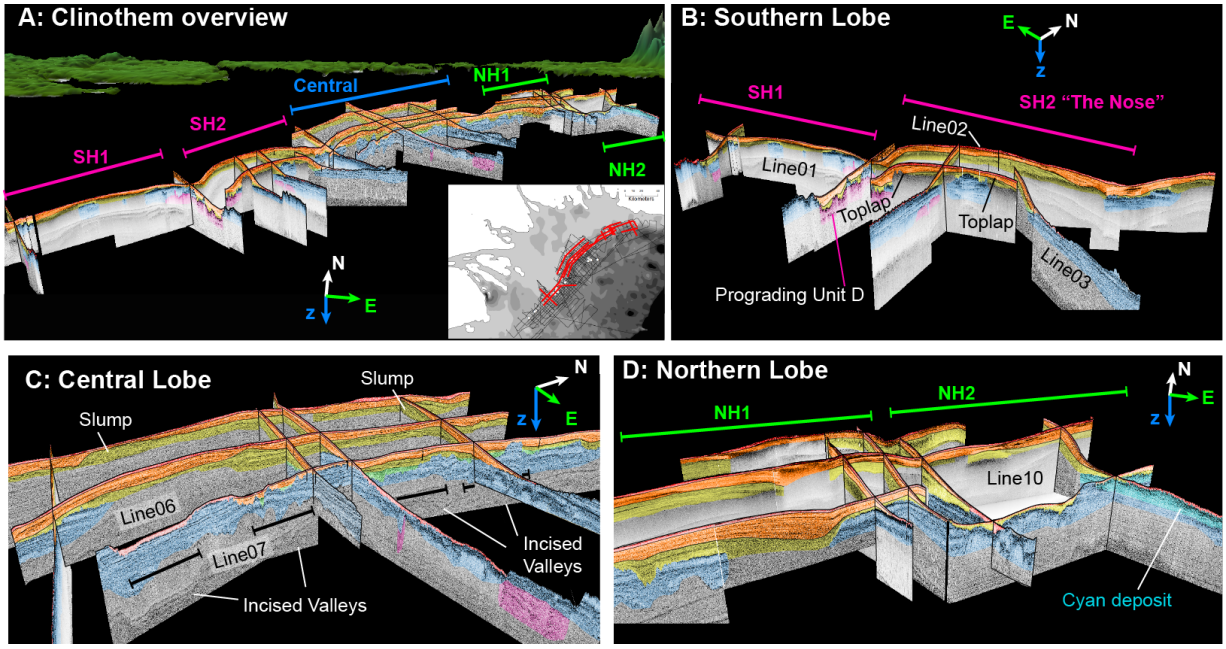

Figure 2.9: A) Fence diagram of the GoP clinothem shows the three main lobes and their sublobes. Inset: red lines show location of fence diagram. B) Fence diagram of the Southern Lobe and its bathymetric highs SH1 and 2. Lines 01, 02, and 03 are shown in Fig. 2.6. C) Fence diagram of the Central Lobe shows incised valleys are filled by aggradational deposits. Two deformed regions are observed in the southwest and northeast and are interpreted to be slump deposits. Lines 06 and 07 are shown in Fig. 2.7. D) Fence diagram of the Northern Lobe and its two bathymetric highs NH1 and 2. Unit B2 (cyan) is located on the northeast edge of NH2. Line 10 is shown in Fig. 2.8.

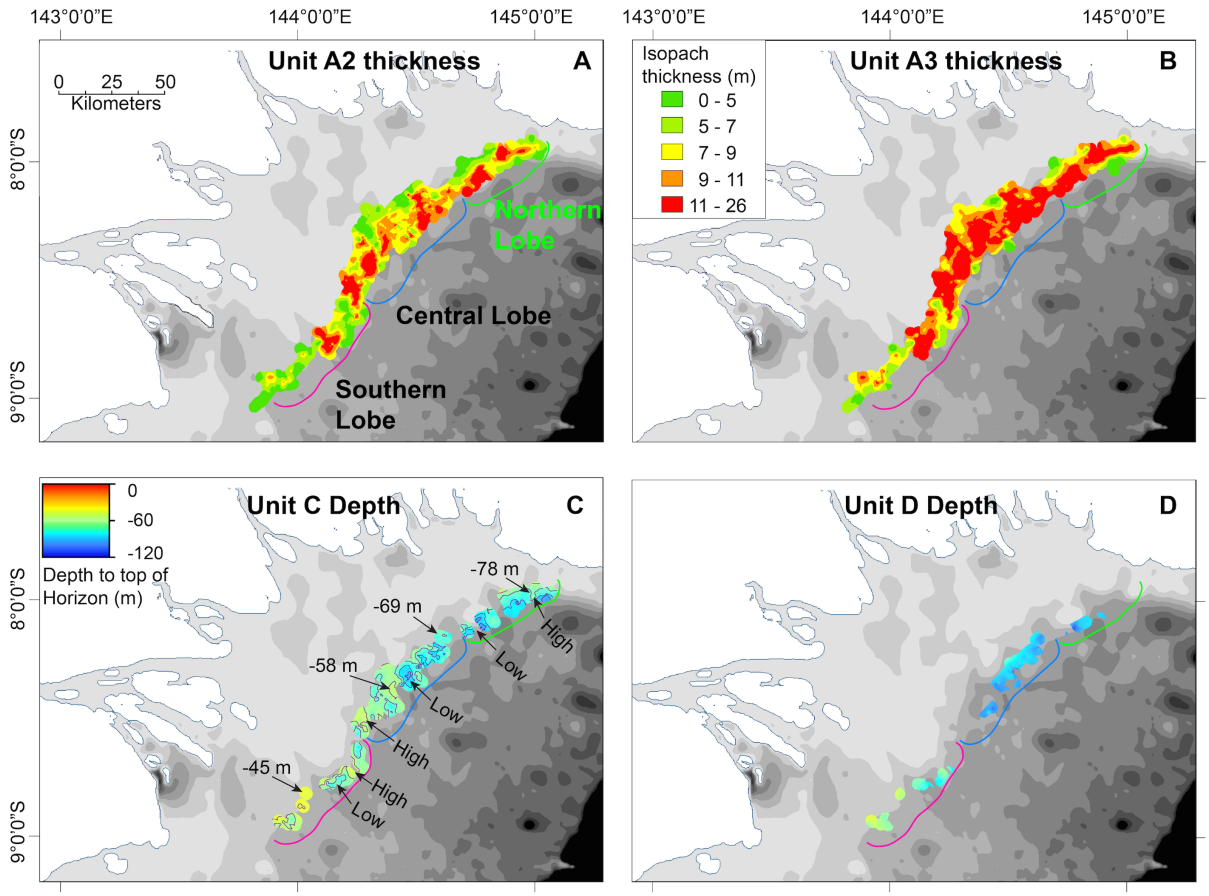

Figure 2.10: Isopach maps of sediment thickness; map A shows Unit A2 (orange) and Map B shows yellow Unit A3 packages. Note the thickness of Unit A3 is greater than A2 and is more uniformly distributed, whereas the thickness in Unit A2 is more localized because sediment is prograding off the topographic highs. On the bottom are structure contour maps of the surfaces of the (C) Unit C and (D) Unit D sequences. The depth to Units C and D systematically increase to the northeast.

been infilled almost completely by thick Holocene sediments.

In the Southern lobe, the southernmost bathymetric high (Line 01, SH1) shoals to a minimum depth of 23.6 m. Moving north, the adacent BH (Line 02, SH2) shoals to $\sim$12 m, which is the shallowest bathymetric high along the entire margin and creates a shallow promontory (i.e., the Nose; Figs. 2.1 and 2.6). Holocene sediment cover is thin on the SH1 promontory. Conversely, across the SH2 promontory, Unit A3 thickens. Unit A2 does not thicken on topographic highs but instead exhibits oblique progradation into the adjacent topographic lows, such as along the southwest flank of SH1 and the northeast flank of SH2. Unit A2 displays along-margin thickness variability and toplap at the highs of both bathymetric highs beneath the S2 boundary (Fig. 2.6 middle and bottom, Fig. 2.9B).

Due to infilling of incised valleys in Unit C by thick Holocene sediment cover, the Central lobe has only one bathymetric high (Figs. 2.7 and 9C). Infilling of valleys by Unit A3 is predominantly aggradational in strike lines (Fig. 2.7). Northeast of the Central lobe, A3 and A2 thicken and prograde into the low separating the Central and Northern lobes (Fig. 2.7). On topographic highs, there is no observed toplap in Unit A2 against the S2 boundary. Two regions of deformed sediment within Unit A3 are observed in the southwest and northeast portions of the Central lobe. An antiform-shaped feature with discontinuous, wavy reflectors is observed in the southwest (Fig. 2.9C). The upper reflectors in the antiform are truncated by the S1 surface. On top of this surface of lap lies a thin veneer of aggrading Unit A2.

The Northern lobe is composed of two bathymetric highs: NH1 in the southwest and NH2 in the northeast (Figs. 2.8 and 2.9D). No toplap is observed in Unit A3. The reflectors within Unit A2 aggrade on NH1 and prograde into the low between NH1 and NH2 (Fig. 2.8). Where Unit A2 progrades into the low, it exhibits toplap, as the Blue and Lime green internal reflectors are truncated by the S2 surface (km 20 in Fig. 2.10). Thick deposits and gas wipeout limit the imaging of the Unit C in the Northern lobe.

2.5.7 Holocene clinothem dip variability along the margin

The slopes of the upper boundaries of Units A3, A2, and A1 exhibit along-margin variability throughout the clinothem foresets (Table 2.2; Fig. 2.11). Note that the upper boundary of Unit A1 is the seafloor, the upper boundary of A2 is S2, and the upper boundary of A3 is S1. Foreset slopes are the steepest at the seafloor and systematically diminish downsection to the upper surface of Unit A3. Slopes from Table 2.2 reveal that slopes are steepest within the Southern and Northern lobes, with the lowest slopes located within the Central lobe. Given the lobate geometry of the GoP clinothem, we measured slopes on profiles that were located near the center of the bathymetric high and within a bathymetric low. The Southern lobe exhibits the largest difference in slope between bathymetric highs and lows (0.154° for the seafloor), whereas the Northern and Central lobes have lower differences between bathymetric highs and lows (0.025° and 0.005° for respective seafloor slopes). Our range of seafloor slopes are comparable to those measured in the high-energy Amazon subaqueous clinothem that reported a range of slopes between 0.06° and 1.15° with an average of 0.29° (Nittrouer and Demaster, 1996). Steeper seafloor slopes were reported in the shallow-water Atchafalaya subaqueous delta of 0.10–0.11° (Neill & Allison, 2005). Seafloor foreset slopes in the GoP are lower than the global average of foreset slopes of muddy delta-scale subaqueous deltas at $\sim 0.76°$ but are within the global range of 0.03–6° (Patruno et al., 2015).

2.5.8 Core facies

Unit D was recovered only in JPC 36, where the sediment facies is homogenous mud interbedded with sand lenses that are ∼0.5–1cm thick (Fig. 2.12A). Cores recovered from Unit C consist of a mud matrix with interbedded sand lenses and this unit was recovered at the bottom of JPCs 17, 21 and 24. In JPC 21, this sequence consists of 0.5–1 cm thick sand lenses separated by layers of mud 20–30 cm thick (Fig. 2.12B). In JPC24, Unit C is dominated by a mud matrix with

Table 2.2: The slopes of the upper surfaces of Units A1, A2, and A3.

Line	Seafloor (A1) foreset(°)	A2 foreset(°)	A3 foreset(°)	Lobe	Bathymetric High/Low
Line04	0.446	0.421	0.370	Southern	High
Line05	0.292	0.257	0.153	Southern	Low
Line08	0.182	0.144	0.121	Central	High
Line09	0.187	0.198	0.173	Central	Low
Line12	0.262	0.250	0.184	Northern	High
Line 11	0.287	0.260	0.219	Northern	Low

centimeter-thick sand lenses separated by tens of centimeters of mud (Fig. 2.12C). In this core, the sand lenses are medium-grained sand.

Unit B2 sediment is markedly different from those in Unit C and was recovered only at the base of JPC02. This deposit has dominantly dark sands and mud lenses at intervals of 1–2 cm. The matrix sand is dark colored (7.5R3/0) and has higher magnetic susceptibility (MS) values of 60 to 200 E^{-8} SI (m^3/kg) in comparison to Unit C MS values in the range of 20 to 80 E^{-8} SI (m^3/kg).

Unit B1 was recovered in cores JPC02, JPC17, JPC21, and JPC24. In all of these cores, this deposit is represented by mud with coarse- grained sands containing shell fragments (Fig. 2.12E, F). In cores, the thickness of Unit B1 ranges from 0.70m in the Northern lobe, 0.3–0.62 m in the Central lobe, and 0.26–1.13 m in the Southern lobe. Based on the cores, Unit B exhibits little variation in sediment thickness along the margin across topographic highs or within lows; however, more cores recovered B1 deposits in the Southern lobe than in the Central and Northern lobes. The boundary between Unit B1 and A3 is transitional from more abundant sand and shell lag deposits in B1 to less abundant sand and shell material in Unit A3. This transition can be up to a few decimeters thick.

Holocene units A1, A2, and A3 are distinct in seismic profiles; however, they do not appear to correlate with any observed grain size differences in the cores. Instead, facies and grain

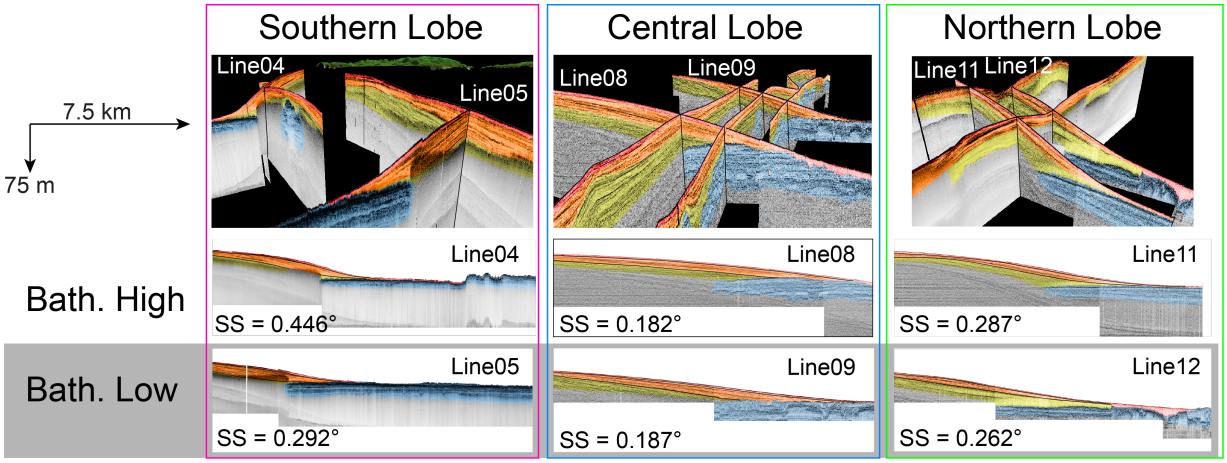

Figure 2.11: Selected dip lines from the topographic highs and lows for the Southern, Central, and Northern lobes. In the Southern and Northern lobes, the dip profiles across the topographic highs have steeper seafloor slopes (SS) than the profiles across the topograhic lows. In contrast, the Central lobe exhibits little change in dip across the topographic high and low. The steepest seafloor slopes are observed in the Southern lobe and the most gentle slopes observed in the Central lobe. Scale shown is for all dip profiles.

size variability within the Holocene units appear more dependent on core location, whether it be on the topset, foreset, or bottomset. Topset facies are characterized by more abundant sand lenses, whereas foreset and bottomset facies have few sand stringers. The topset cores GC31 and GC23 are composed of a mud matrix with abundant 0.5–1 cm thick sand lenses (Fig. 2.12G, H). In contrast, foreset cores JPC02 and JPC22 contain mostly silty mud with sparse sand lenses (Fig. 2.12J, K). The bounding surfaces of lap S1 and S2 do not correlate with detectable changes in grain size or facies.

2.5.9 Chronostratigraphy and sedimentation rates of Units B2, B1, and Holocene sequences

Benthic foraminifera were sampled from Units B2, B1, A3, A2, and A1 and were radiocarbon dated. Corrected and uncorrected ages, depth in core, and sediment unit are described in Table 2.3. Only one sample from Unit B2 was recovered, yielding an age of 10.33 ka (Table 2.3; Fig. 2.5). Ages of Unit B1 range from the youngest at 3835 years BP to the oldest at 6561

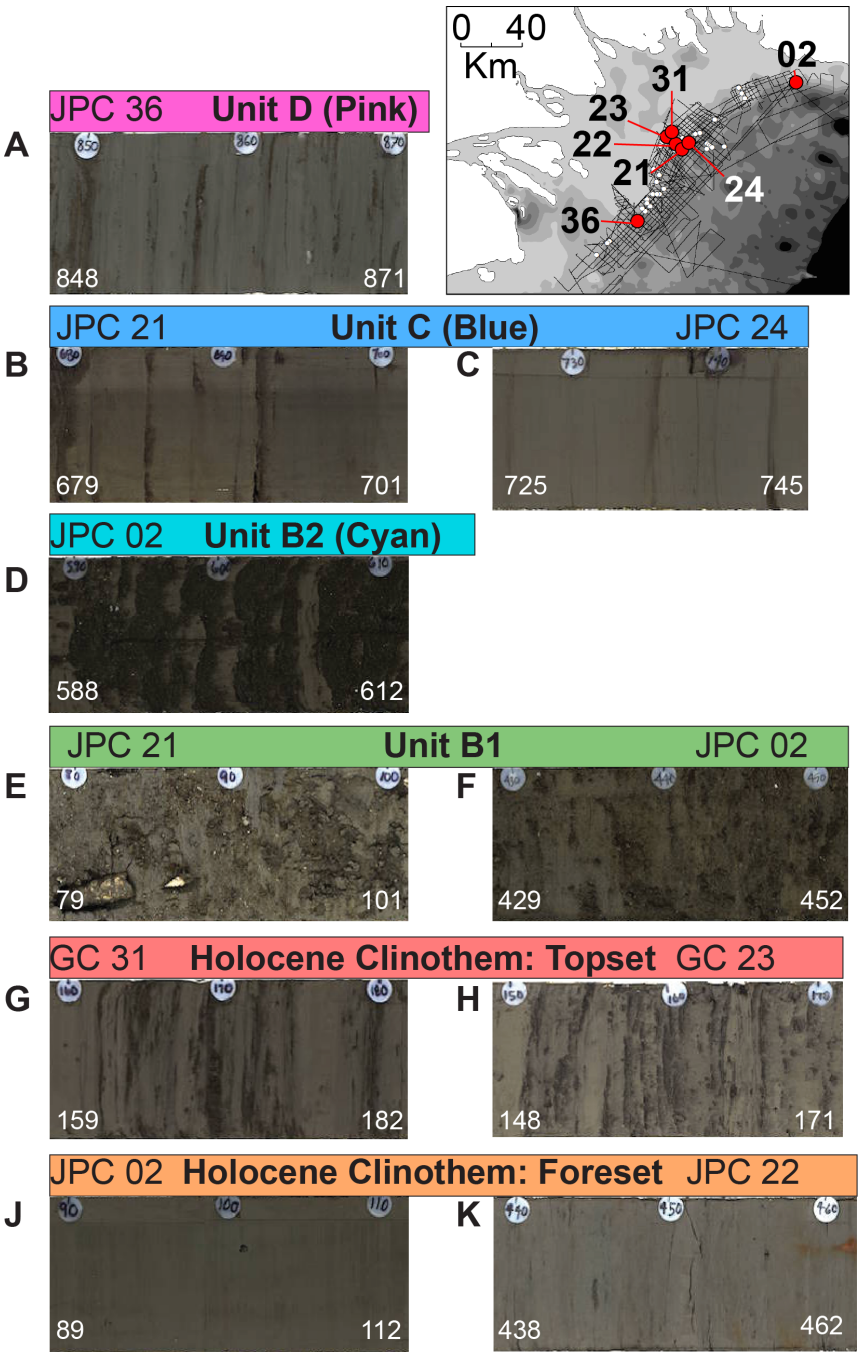

Figure 2.12: Photos of facies observed in cores. Plastic circles mark 10-centimeter intervals in the core. Photo intervals are annotated at the bottom corners of each photo. Sand stringers interspersed with mud layers are observed in Unit D, Unit C, and the Holocene clinothem topset (A, B, C, G and H). The Holocene clinothem foreset is characterized by only occasional sand stringers (J, K). The transgressive gravel and shell lag of Unit B1 separates Unit C from the Holocene clinothem (E, F). Next to A, the inset map shows the locations of the cores.

years BP (Table 2.3; Figs. 2.2, 2.5, 2.6, and 2.7).

The Holocene sequence has ages spanning from modern sediment at the sediment surface to the oldest collected age of 1633 years BP. No ages were recovered in the uppermost Unit A1. An age of 170 years BP is located just below the A1 and A2 boundary (S2) in JPC 17 (Table 2.3; Fig. 2.6). In JPC 24, the youngest date in Unit A2 is dated at 112 years BP (Table 2.3, Fig. 2.7). The boundary between Units A2 and A3, or the S1 surface, is dated between 1353 and 1570 years BP.

Sedimentation rates were calculated for units that had two or more ages and no rates were calculated across package boundaries. Sedimentation rates for Unit A2 in bottomset cores (all except for JPC 22) range from 2.83–6.36 mm/yr. Downcore sedimentation rates in A2 from JPCs 06 and 43 are higher than those upsection (Table 2.3). Radiocarbon dates from JPC 22 reveal that sedimentation rates for Unit A2 are an order of magnitude higher than other rates for the same package; however, it is the only dated core located on the clinothem foreset. The only sedimentation rate calculated for Unit B1 is in JPC 21 and is an order of magnitude lower than rates determined for Unit A2.

2.6 Discussion

We present a conceptual model for the timing of Units B2, B1, A3, A2, and A1. In light of the revised chronostratigraphic framework for deposits in the GoP, we will focus on parameters that control the architecture of the Holocene clinothem, such as tectonic deformation, sediment supply, and oceanographic forcing.

Table 2.3: Radiocarbon ages shown with their sequence or package. Sedimentation rates were calculated within packages. Ages denoted with a single asterisk (*) were published by Slingerland et al. (2008a). Listed ages with two asterisks (**) were published by Howell et al. (2014).

Core	Depth (mbsf)	Corrected ^{14}C age	Uncorrected ^{14}C age	Error ± (year BP)	Unit	Sediment-ation rate (mm/yr)
JPC 02	1.85	477	860	43	A2	3.58
	4.46	1207	1655	38	A2	
	8.86	6561	6140	54	B1	
	13.66	10,333	9480	100	B2	
JPC 06	1.95	414	785	21	A2	3.90
	2.11	455	830	27	A2	6.36
	7.21	1257	1710	46	A2	
	12.71	1570	2015	40	A3	
JPC 17	1.83	170	550	30	A1/A2	2.71
	2.35	362	725	16	A2	
	6.65	6505	6090	46	B1	
JPC 21	1.64	204	585	35	A2	3.44
	1.85	265	630	37	A2	
	2.27	4259	4185	30	B1	0.18
	2.50	5518	5165	30	B1	
	2.90	9350**	8820		C	
	3.50	8400**	8070		C	
	4.40	8806**	8250		C	
JPC 22	1.80	334	690	30	A2	20.69
	4.20	450	825	35	A2	
JPC 24	1.73	112	500	13	A2	
	3.87	3835	3880	46	B1	
JPC 43	1.95	283	645	38	A2	2.83
	2.78	576	995	27	A2	4.63
	5.68	1750*			A2	
	6.38	1353	1820	30	A2	
	7.18	1570*			A2	
	9.68	1840*			A3	
	9.88	1633	2070	35	A3	

2.6.1 Updated chronostratigraphy

By using radiocarbon dates and a balance between sediment supply and eustatic sea level changes, we develop a relative stratigraphy for Unit C. We also agree with the relative depositional timing of Unit D proposed by Slingerland et al. (2008a). We also agree with the depositional timing proposed by Harris et al. (1996) and Slingerland et al. (2008a) for Unit C; however, their age estimates are significantly older than published ages from Howell et al. (2014) from Unit C. Previous radiocarbon age determinations for Unit C exhibit quite a wide range in ages, with Harris et al. (1996) dating an intact bivalve (articulated) to yield an age of 26,900 years BP and Howell et al. (2014) dating mollusk fragments and ooids to yield inverted ages in the core ranging from 8400 to 9350 years BP (Fig. 2.2). The ages from Howell et al. (2014) may not be reliable because the vital effects of molluscs are poorly known and ooids have concentric growth rings. In light of these considerations, we prefer the interpretations from Harris et al. (1996) and Slingerland et al. (2008a) that Unit C was formed during MIS 3.

For the Holocene units, core sampling and radiocarbon dates provide a more quantitative age model. Unit B2 mantles Unit C and is beneath the maximum flooding surface. Thus, we postulate that Unit B2 was deposited during the sea level transgression after MIS 2. Radiocarbon ages from Table 2.3 and an age of 9500yearsBP from Slingerland et al. (2008a) lead us to propose that Unit B2 was deposited during Holocene sea level rise around 10.3–9.5 ka (Fig. 2.13).

The chronostratigraphy of Unit B1 was first discussed by Harris et al. (1996), who acquired uncorrected radiocarbon ages from this deposit ranging from 16,750–7290 years BP. These ages are much older than the uncorrected radiocarbon ages reported here, and the older ages could reflect redeposition of older peat deposits. Radiocarbon dating constrains the timing of deposition for Unit B1 to be between 3835 and 6561 years BP. Slingerland et al. (2008a) reported a 5.21 ka age measured on a bivalve sample recovered from the overlying Holocene Unit A3. Given the age is older than determined for the underlying Unit B, we propose that the bivalve may be sourced from re- worked material older than the age of deposition. The ages reported

here are from benthic foraminifera, which are more likely to be closer to the depositional age. Based on the younger radiocarbon ages, we propose that Unit B1 is younger than 6.5 ka and that the overlying Holocene sequence is younger than 3.8 ka (Fig. 2.13).

We propose a younger depositional age for the Holocene sequence, as our ages are younger than those acquired by Slingerland et al. (2008a) on bulk carbonate samples for JPC 43 consisting of shelf fragments, ooids, and other material (Fig. 2.9). In all likelihood, they represent reworked debris, which would explain the older ages than the benthic foraminifera ages reported in this study. Our refined chronostratigraphy dates the S1 surface (Units A3–A2) between 1353 and 1570 years BP. This surface of lap was not likely caused by sea level, given there are no meltwater pulses or stillstands during this time period.

2.6.2 Transgressive deposits

The shell lag and coarse sand within Unit B1 was likely eroded from tidal deposits from an inner estuary, as suggested by Harris et al. (1996). The mixture of this material within a matrix of silts and clays suggests that Unit B1 is a lag deposit derived from wavebase erosion and reworking of upslope material. As Unit B1 was deposited between 3.8 and 6.5 ka when sea level rose following MIS 2, this unit is interpreted as a transgressive lag. Overlying Unit B1 is the transgressive surface that separates subaerially exposed sediments below from marine sediments above. In seismic profiles, horizontal reflectors in Unit B1 are observed below the transgressive surface and above it Unit A3 reflectors exhibit downlap. In sediment cores, the transgressive surface appears as a gradual grain size and shell abundance transition as described in Section 2.5.8.

Given Unit B2's localized deposition in the northeast GoP, we pos- tulate that Unit B2 could be tidal channel fill in an inner estuary environment. Tidal channels can have high sedimentation rates, are composed of medium-grained cross-bedded sand with mud, and have cross-bedded laminae due to undulatory tidal flow (Allen & Posamentier, 1994). Similar se-

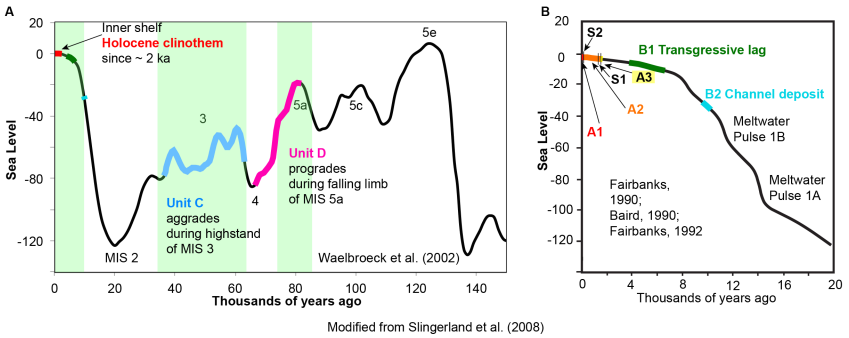

Figure 2.13: Two sea level curves are shown for the last 150 kyr (A) and the last 20 kyr (B). Depositional timing based off sequence stratigraphic principles is shown for the Units C and D. Based off new radiocarbon ages, the depositional timing is shown for Units B2, B1, A3, A2, A1, S2, and S1.

quences of estuarine facies onlapping onto tidal channel facies have been documented in boreholes and seismic profiles in the Sabine River Valley (Thomas & Anderson, 1994), the Gironde River Estuary (Allen & Posamentier, 1994), the Guadiana Estuary (Lobo et al., 2003), and the Eel margin (Hogarth et al., 2012). We hypothesize that the undulatory upper boundary of Unit B2 likely represents sediment waves, which could be formed by bidirectional tidal flow. Differences in depositional environments cause resulting disparities in lithologies and thicknesses between the two transgressive deposits. Unit B2 infilled existing physiography whereas B1 is formed by transport of reworked material seaward.

2.6.3 Holocene clinothem architecture

Growth of the older Holocene A3 unit was likely controlled by changes in thickness of the underlying Unit C and thus water depth. Our observations that Unit C exerts controls on the overlying Holocene clinothem is consistent with the concept of a foundation surface (or "depositional foundation") that stresses the importance of the surface morphology onto which a clinoform is emplaced (Helland-Hansen & Gjelberg, 1994; Helland-Hansen & Martinsen, 1996; Cattaneo et al., 2007). The foundation surface concept introduces two factors relevant in the GoP that may influence younger deposition: 1) the importance of the depth of the surface onto which

the progradational wedge advances and 2) that preexisting depressions may be preferentially filled com- pared to adjacent zones (Cattaneo et al., 2007). Units A3 and A2 are very much influenced by the depth of the foundation surface, as more shingling and toplap occurs in the Southern lobe with a shallower foundation surface and more aggradation occurs in the Northern lobe with a deeper foundation surface. The isopach map of Unit A3 (Fig. 2.10B) reveals that thick A3 deposits exist in both topographic lows and highs and are connected across the corrugated topography (Fig. 2.10B). As Unit A3 is first deposited, it preferentially infills pre-existing depressions into Unit C, and thus is consistent with the foun- dation surface concept (Helland-Hansen and Gjelberg, 1994; Helland-Hansen and Martinsen, 1996; Cattaneo et al., 2007). Preferential infilling into local depressions is also observed on the Adriatic margin (Cattaneo et al., 2007). Once these incised valleys were preferentially filled, fluid-mud processes may have acted on these recent Unit A3 deposits and allowed for across-margin progradation of A3 sediment across the foreset. The across-margin orientation of these conduits could have caused Unit A3 to prograde preferably across- rather than along-margin. After Unit A3 infilled these across-margin valleys, across-margin fluid-mud transport for Unit A2 may not have been as effective. As a result, Unit A2 does not prograde seaward much farther than A3.

Unit A2 thickens into the topographic lows creating bullseye pat- terns of discontinuous thick deposits in topographic lows (Fig. 10A). Note differences in the isopach maps between continuous Unit A3 deposits and patchy A2 deposits. Minimal seaward progradation of A2 could result from oceanographic processes that prograde A2 obliquely northeast, as described in Section 2.6.3.

Oceanographic controls on along-margin geometries

Along-margin profiles of the Holocene clinothem throughout the entire GoP reveal oblique growth in the northeast-southwest direction as observed in Unit A2 (Figs. 2.6, 2.7, and 2.8). Our stratigraphic observations agree with hydrographic interpretations from Walsh et al. (2004)

and Slingerland et al. (2008b). Aggradation and temporary deposition of sediment on topographic highs likely occurs during the Monsoon season, which has lower energy bottom currents. Strengthening of near-bed currents during the Trade wind season winnows and reworks sediment on the topographic highs. Northeast bottom currents active during the Trade wind season advect sediment, causing it to prograde into topographic lows. The net sediment transport shifts the topo- graphic highs to the northeast, as a result building the clinothem obliquely (Fig. 2.10A). Oblique progradation of A2 off the preexisting highs into the corrugated morphology controls the bulls-eye patterns observed in the isopachs by thinning deposits on the topographic highs. Thus, the current seasonal circulation patterns in the Gulf of Papua have likely persisted since inception of Unit A2.

Convergence of flow localizes sedimentation in SH2 (Slingerland et al., 2008b) and may be responsible for creating a depocenter at SH2 or "the Nose". Flow convergence may cause further feedbacks where sediment deposition causes features to grow and shoal, thus altering local circulation and allowing for the persistence of gyres (Figs. 2.6 and 2.10A).

Foreland basin subsidence, accommodation, and surfaces of lap

Subsidence of the northern GoP and peripheral bulge uplift of the southern GoP have influenced Holocene clinothem growth since they engender more accommodation in the north and less in the south. These tectonic processes may modulate the depth of the foundation surface, which in turn can exert influences on depositional regimes of the overlying Holocene clinothem, as shallower foundation surfaces are exposed to higher shear stresses than deeper foundation surfaces (Cattaneo et al., 2007). Deformation of GoP sediment by foreland basin subsidence is evidenced in Fig. 2.4, where faults cross-cut reflectors in Unit D (Fig. 2.4). Another line of evidence for foreland basin subsidence is that depth to the upper surface of Units D and C are deeper in the Northern lobe than in the Southern and Central lobes (Fig 2.10C and D). Unit C is observed at depths of 45 m in the Southern lobe and at depths of 78 m in the Northern lobe (Fig. 2.10C).

Unit C beds are horizontal to sub-horizontal throughout the margin, suggesting that subsidence occurred after deposition. The observed deepening of Units C and D may record footwall loading associated with GoP foreland basin subsidence in the northern GoP, whereas the southwest GoP is located closer to the peripheral bulge and is thus undergoing less subsidence (Fig. 2.1; Pigram et al., 1989). As tectonic deformation and dif- ferential subsidence are orthogonal to the eustatic plane, the eustatic and tectonic signals can be deconvolved. The difference in depth between the Southern and Northern lobes suggests that since the LGM, the topography has undergone differential subsidence of $\sim$33 m, yielding an average subsidence rate of 1.65 mm/a. This is comparable to the rate calculated from Slingerland et al. (2008a). In contrast, subsidence rates during the Pliocene calculated from stratigraphic thicknesses from DSDP Site 209 are an order of magnitude larger (Davies et al., 1989). Additional research and deeper imaging seismic reflection data are required to understand the decrease in subsidence rates since the Pliocene.

Differential subsidence of the foreland basin creates more accommodation in the northeast than in the southwest and as a result it influences reflector geometry in the Holocene clinothem. In the Southern lobe, with the least amount of accommodation, Units A3 and A2 exhibit toplap in SH1 and SH2 (Fig. 2.6). SH2 is shallower than SH1, and thus SH2 is exposed to higher bottom stresses and exhibits more toplap. In contrast, the Central and Northern lobes have deeper Unit C, with the reflectors in the Holocene clinothem characterized predominantly by aggrading reflectors in their sublobes (Figs. 2.7 and 2.8). In the Central lobe, toplap is observed only in Unit A3 truncating the upper reflectors of slumped deposits (Figs. 2.7 and 2.10C). Farther north, toplap is only exhibited in the topset of NH1 within Unit A2 of the Northern lobe (Fig. 2.8).

Seismic strike profiles through the topset exhibit more toplap than those in the foreset or bottomset. Toplap is evidence of a nondepositional hiatus (likely due to bypass) caused by a lack of accommodation to permit aggradation (Mitchum et al., 1977a; Christie-Blick and Driscoll, 1995). It is likely that toplap is more prevalent on topsets because of reduced accommodation, increased exposure to wave energy, and larger bed shear stresses. As a result, suspended sediment

concentration above the bed is higher on the topsets than on the foresets (Walsh et al., 2004). Suspended sediment above the topset beds could form fluid mud, which under high bed shear stresses could be remobilized, bypass the topset, and be deposited farther downslope. This process may cause toplapping reflectors to pinch out upsection (Christie-Blick and Driscoll, 1995). Sediment bypass at topset beds was also suggested by Walsh et al. (2004), who observed that topset cores have reduced sediment accumulation rates. Gradients in energy regimes from the topset to the bottomset affect the accumulation of sediment, downdip variations in reflector thickness, and physical sediment properties.

Surfaces of lap observed throughout the survey area are recognized mainly in seismic profiles and are not discernable in sediment cores. As truncation of underlying layers by S1 and S2 is most commonly ob- served on clinothem topsets, it is likely that the S1 and S2 surfaces represent erosive boundaries rather than flooding surfaces. Based off radiocarbon dates of the S1 and S2 surfaces, Slingerland et al. (2008a) proposed that S1 was caused by a decline in sediment supply. Given the S1 surface is dated between 1353 and 1570 years BP, a time of no sea level stillstands (Fig. 2.13), we propose that S1 in the Southern lobe is due to the local interplay between decreased paleowater depths and increased bottom stresses. In the Central lobe, thick Unit A3 slump deposits (Figs. 2.7 and 2.9C) could have filled available water depth, thus preventing further sediment accumulation and promoting bypass. Since the S2 surface separating Units A2 and A1 is younger than at least 112 years BP, this surface is not likely a result of decreased sediment supply as was proposed by Slingerland et al. (2008a), since sediment accumulation during this period likely increased as a result of anthropogenic impacts (Haberle, 1998). Instead, the S2 surface is also likely formed by decreased paleowater depths and increased bottom stresses.

Interpreting S1 and S2 as margin-wide surfaces of lap caused by sea level and sediment supply is difficult, as the S1 and S2 surfaces are not continuous surfaces found throughout the GoP Holocene clinothem. Toplap against the S1 and S2 surfaces where observed appear to separate

Holocene packages; however, such geometry is not observed throughout the Holocene clinothem. When examining the different lobes of the Holocene clinothem and toplap geometry, it appears to record a local interplay between paleowater depths and oceanographic currents.

Implications: relationship of along-margin and across-margin geometry

Slopes of the upper boundary of Units A3, A2, and A1 exhibit variations along the GoP (Table 2.2, Fig. 2.11). Cross-sectional clinothem dips may be controlled by a number of complex factors including grain size, clinothem height, oceanographic energy and sediment dispersal regimes, and basin physiography (Pirmez et al., 1998; Driscoll and Karner, 1999; Cattaneo et al., 2003, 2007; Swenson et al., 2005; Patruno et al., 2015). The variability in the GoP may reflect a number of factors, including the location of the profile, location within a bathymetric high or low, accommodation created by foreland basin subsidence, sediment supply, and the dispersal of sediment by oceanographic currents. In the Central lobe, across-margin clinothem profiles have the shallowest slopes, whereas the steepest across-margin slopes are observed in the Southern lobe (Table 2.2; Fig. 2.11). The Central Lobe is located at the depocenter of the margin-wide clinothem where accumulation rates are the highest (Walsh et al., 2004; Slingerland et al., 2008a,b). Thick sediment deposits in the Central lobe diminish the relief of the underlying physiography. As a result, differences in slope between the topographic highs and lows are minimal (0.005° difference in the seafloor slopes). In the Northern lobe, clinothem slopes appear to be steeper than those in the Central lobe. Steeper slopes may be a consequence of topset aggradation in the Northern lobe that is enabled by more accommodation. Model simulations from Driscoll and Karner (1999) reveal that when the rate of sediment supply is subordinate to the rate of new accommodation, clinothems aggrade faster than prograde, thus causing downslope thinning and the steepening of each successive clinothem. Such is the case with clinothems in the Northern lobe that exhibit thinning near the bottomset (Line 12, Fig. 2.11). As a result of deeper clinothem rollovers in the Northern lobe, Northern lobe topsets may be deeper than the wave-base

and as a result may not experience the shear stresses necessary for sediment resuspension, as evidenced by aggradational topsets in Lines 11 and 12 (Fig. 2.11). Sediment normally supplied to the foreset via fluid-mud may be diminished in the Northern lobe. Thus, vertically aggrading topsets and diminished foreset progradation may be the cause of steeper clinothem slopes in the Northern lobe.

Large differences in slope between the topographic highs and lows in the Southern lobe reflect interplays between lower sediment supply and the convergence of currents around the Nose (SH2). Low sediment supply to this region (Walsh et al., 2004; Palinkas et al., 2006) is unable to infill uneven topography, creating large height differences between the topographic highs and lows. Sediment that is supplied to this region is redirected to SH2 instead of SH1 due to the convergence of currents. As a result, these currents build a localized depocenter at SH2 and engender large height differences between SH1, SH2, and the topographic low between them. This illustrates that in the Southern lobe, steep slopes are likely caused by uneven topography dividing the two sublobes and variable sediment distribution due to the convergence of currents toward SH2.

The balance between sediment supply, accommodation, and the influence of the underlying Unit C controls Holocene clinothem slopes. Steepness and geometry of clinothems change with along-margin transport processes, and thus down-slope clinothem geometry can be misinterpreted as changes in sediment supply or relative sea level. Thus, the traditional two-dimensional approach to interpreting clinothems as a rate-related geometry between accommodation and sediment supply needs to incorporate additional processes that alter three-dimensional clinothem geometry.

2.7 Summary and conclusions

Analysis of modern clinothem stratal architecture illustrates the importance of circulation, preexisting physiography, and differential subsidence in their development.

1. Chronology of several units was redefined from those of Slingerland et al. (2008a) by extensive radiocarbon dating within Units B1, B2, and the Holocene clinothem. Depositional timing of the Holocene clinothem was found to be younger than reported in previous studies because material sampled (e.g., shell fragments, bivalves, peat, wood) by Slingerland et al. (2008a) appear to have been reworked when compared to dates derived from benthic foraminifera. As the ages of surfaces of lap are not coincident with sea level stillstands or meltwater pulses, these surfaces are not likely caused by eustatic sea level changes, as was previously suggested.

2. The basal Unit D (Pink) has been subject to deformation, such as folding and faulting, associated with foreland basin tectonics. Valleys incised into Unit C affect the flow of bottom currents on the shelf and also create localized increases in paleowater depth in the intervening lows. Subsidence of Units C and D has created more accommodation in the northeast and less in the southwest. Toplap is more extensive in the shallow Southern lobe and in topset beds, which are to be subjected to higher bed shear stresses (Walsh et al., 2004) and may experience more bypass or non-deposition.

3. Thicknesses and geometries of Holocene units may be influenced by interplays between the corrugated topography and oceanographic currents. Isopach maps of Unit A3 show that depocenters are more interconnected, as there were large paleowater depths in the topographic lows. Thus A3 maintains topography with slightly more deposition in the topographic lows. Elevated topographic highs constructed by A3 increase bottom shear stresses such that Unit A2 progrades to the northeast, infilling the adjacent topographic lows.

Unit A2 preferentially infills the topographic lows and is winnowed off the topographic highs, creating a bullseye appearance in the isopach map.

4. Though the S1 and S2 surfaces of lap are identified by toplap, toplap is not universally present throughout the Holocene clinothem. As such, toplap probably is not caused by margin-wide processes such as sea level stillstands or decreased sediment supply but is rather influenced by local interplays between paleowater depths and oceanographic currents.

5. Downdip clinothem slopes are shallowest in the Central Lobe and show the greatest difference between topographic highs and lows in the Southern Lobe. The traditional rate-related problem of interpreting clinothem geometry is further complicated in settings with current-controlled sediment advection. In these locations, along-margin controls on sediment dispersal need to be considered.

Controls exerted by tectonic deformation, bottom currents, and inherited physiography can be isolated in the GoP because the deformation and currents are normal to eustatic sea level changes. However, this configuration is not observed at many margins. As mentioned above, there are many instances of clinothems extending downdrift in response to along-margin currents, such as in Rio de Janeiro (Reis et al., 2013), the Adriatic Sea (Cattaneo & Steel, 2003), and offshore of the Yangtze River (Xu et al., 2009). Additionally, some margins exhibit along-margin tectonic deformation, such as the case of offshore La Jolla, California (Hogarth et al., 2007; Le Dantec et al., 2010) and the Eel Margin in northern California (Hogarth et al., 2012). Clinothem growth should be analyzed in three-dimensions on continental margins and could be further aided by three-dimensional modeling studies (e.g., Driscoll & Karner, 1999).

2.8 Acknowledgements

This work is published in **Wei, E.A., Driscoll, N.W., Slingerland, R.L., 2019. Oceanographic currents, differential subsidence, and physiography control three- dimensional clinothem growth in the Gulf of Papua, Papua New Guinea.** ***Marine Geology*** **407, 164-180**. The dissertation author was the primary investigator and author of this material. This research was funded by the National Science Foundation awards 0305699, 0305779, and 0305607 under the MARGINS Source to Sink program. Special thanks to the crew of the R/V Melville as their efforts allow scientists access to the sea. Craig Fulthorpe, Claudio Pellegrini, Hector Perea, and two anonymous reviewers provided salient and helpful reviews that improved the quality of the manuscript. Rachel Marcuson and Ana Martini aided in sampling benthic foraminifera for radiocarbon dating. GMT was used to construct isopach and structural contour maps.

Chapter 3

Clay Mineralogy of Gulf of Papua Shelf and Pandora Trough Deposits Constrains Sediment Source and Routing During the Last Sea-Level Cycle

3.1 Abstract

The Gulf of Papua (GoP) inner mid-shelf clinothem and lowstand deposits in Pandora Trough (PT) record sediment source and routing through the last sea-level cycle on 20-kyr cyclicities. Clay mineralogy tracked dispersal of sediment from the two types of rivers (wide versus narrow floodplains) to constrain the contributions of river systems to the GoP clinothem and PT deposits. Fly River sediment has higher illite:smectite than clays from small mountainous rivers (Bamu, Turama, Kiokori, and Purari rivers) that drain regions with more limestones. X-Ray Diffraction shows high illite:smectite proximal to the Fly River delta that decrease towards the northeast. Downcore mineralogy of inner mid-shelf cores reveals that the largest shifts in

illite:smectite correspond to changes in sediment units. The relict clinothem emplaced on the GoP shelf during Marine Isotope Stage (MIS) 3 has lower illite:smectite than the Holocene clinothem that has been building since 2 ka and the MIS 5a relict clinothem. In the inner mid-shelf, downcore decreases in illite:smectite during MIS 3 suggest that this region received less clay from the Fly River and more contributions from small mountainous rivers. During MIS 3, the exposed physiography and narrower shelf in this region may have deflected Fly River sediment more southeastward where it bypassed the inner shelf via the Kiwai, Purutu, and Umuda valleys and deposited in PT. The Fly River may have been more susceptible to valley incision because of its limited shelf accommodation and higher ratio of water:sediment discharge. Such bypass of the inner mid-shelf by Fly River sediment during sea-level lowstands (MIS 2) is recorded in PT deposits with high illite:smectite ratios. Inner mid-shelf clinothems with compositional shifts on the order of 20-kyr may be influenced by shelf physiography, accommodation and the variable incision by small and large rivers.

3.2 Introduction

Source-to-sink studies investigate the propagation of signals from the source, through transfer zones, and to the ultimate sink (e.g., Romans et al., 2016 and references therein). In many areas and in the Gulf of Papua (GoP), continental shelves serve as transfer zones and stratigraphic recorders of preserved highstand signals. This paper investigates the stratigraphy and clay mineralogy of the GoP inner shelf, the transfer zone, and Pandora Trough, considered the sink. The two main rivers investigated in this study, the Fly and Purari rivers, can be considered intermediate and large transfer subsystems (river length >300 km), as their lengths are 744 and 630 km respectively (Pickup, 1983; Métivier & Gaudemer, 1999; Castelltort & Van Den Driessche, 2003; Milliman & Farnsworth, 2011). As such, the timescales for sediment to transfer from the source to PT is on the order of intermediate timescales of 102-106 years (Allen, 2008; Romans

et al., 2016). This study demonstrates that storage on the inner mid-shelf clinothem is dependent on location along the margin and sea-level; thus, routing between the source, transfer zone, and sink, is more complicated than previously proposed.

Previous studies have investigated the clay mineralogy of shelf deposits (e.g. Slingerland et al., 2008; Szczuciński et al., 2013; Villaseñor et al., 2015) or basin deposits (e.g., Howell et al., 2014; Huang et al., 2016) though few studies have investigated both areas. Clay mineralogy is an effective tool for discerning sediment provenance (e.g., Vital et al., 1999) including river switching (Heroy et al., 2003), changes in climatic, precipitation, and weathering regimes (e.g., Wan et al., 2007; Montero-Serrano et al., 2010; Wu et al., 2012; Huang et al., 2016), or modern and past sediment transport by oceanographic currents and rivers (e.g., Varela et al., 2013; Andrews & Vogt, 2014). Additionally, shelf and basin deposits may record the erosion of older sediments that were previously stored in floodplains (Johnsson & Meade, 1990).

The goal of this study is to investigate the apparent roles of eustasy, basin physiography, and the response of large and small rivers to eustatic changes (i.e., incision versus floodplain aggradation) on the formation of 20-kyr sequences in the GoP clinothem. On margins worldwide, sequences formed during 100-kyr sea-level cycles are formed by the amalgamation of regressive units during a longer-term sea-level fall that is punctuated by 20-kyr high frequency changes in sea-level (Lobo & Ridente, 2014). While some margins, such as the Canterbury (Villaseñor et al., 2015) and New Jersey (McHugh et al., 2017) are composed of sequences of 100-kyr periodicity, margins with very high sedimentation rates such as the GoP exhibit a 20-kyr cyclicity (Harris et al., 1996; Kolla et al., 2000; Slingerland et al., 2008; Lobo & Ridente, 2014). It is postulated that 20-kyr successions reflect the interplay between eustasy and local processes such as river response and basin physiography in the sedimentary environment (Lobo & Ridente, 2014). As such, this study proposes that inherited physiography and differential shelf accommodation for the Fly and Purari rivers control the variable responses of these rivers to eustatic sea-level changes. There is less accommodation on the shelf offshore of the Fly River than the shelf offshore of the

Purari River during sea-level highstands such as Marine Isotope Stages (MIS) 5a and 1. This study proposes that differences in shelf accommodation are greater during intermediate sea-level highstands such as MIS 3. This study compares rivers of different sizes within the same basin, similar to studies from the Gulf of Mexico (Anderson et al., 2016), the Adriatic (Harris et al., 2008), and the South Yellow Sea (Xu et al., 2012; Hu et al., 2018). The transport of fine-grained sediment through river systems to the clinothem and basin floor has implications for carbon storage; as the GoP inner mid-shelf clinothem is observed to be far more effective at sequestering organic carbon than Fly River floodplain sediment (Goñi et al., 2014).

3.3 Geologic Setting

Receiving freshwater input from five major rivers, the GoP is an ideal setting to study Source-to-sink processes because of high uplift rates and tropical climates, leading to high erosion and high sediment flux. The five rivers listed from southwest to northeast are the Fly, Bamu, Turama, Kikori, and Purari rivers (Figs. 3.1 and 3.2). This study will focus on the differing geomorphology of the Fly River versus the other four small mountainous rivers. The Fly River has a wide floodplain, is a classic tide-dominated delta, and its lower floodplain is composed of low-gradient topography with slopes estimated at 6.3×10^{-5} (Lauer et al., 2008). The Fly River is a confluence of the Ok Tedi, Fly, and Strickland rivers (3.2) and is composed of a network of tie and tributary channels in its floodplain that exceed 900 km in length (Dietrich et al., 1999; Day et al., 2008; Bolton et al., 2008). Conversely, the Bamu, Turama, Kikori, and Purari are considered small mountainous rivers with narrow floodplains; in large part, their river catchments are characterized by steep mountainous terrain, with the average slope of the Purari calculated as 5.9×10^{-3} (data from Pickup, 1983; Milliman & Farnsworth, 2011).

Predicting the past sediment flux from the Fly River is complicated, as previous studies show that the Fly River can store or transfer sediment differently during various stages of sea-level

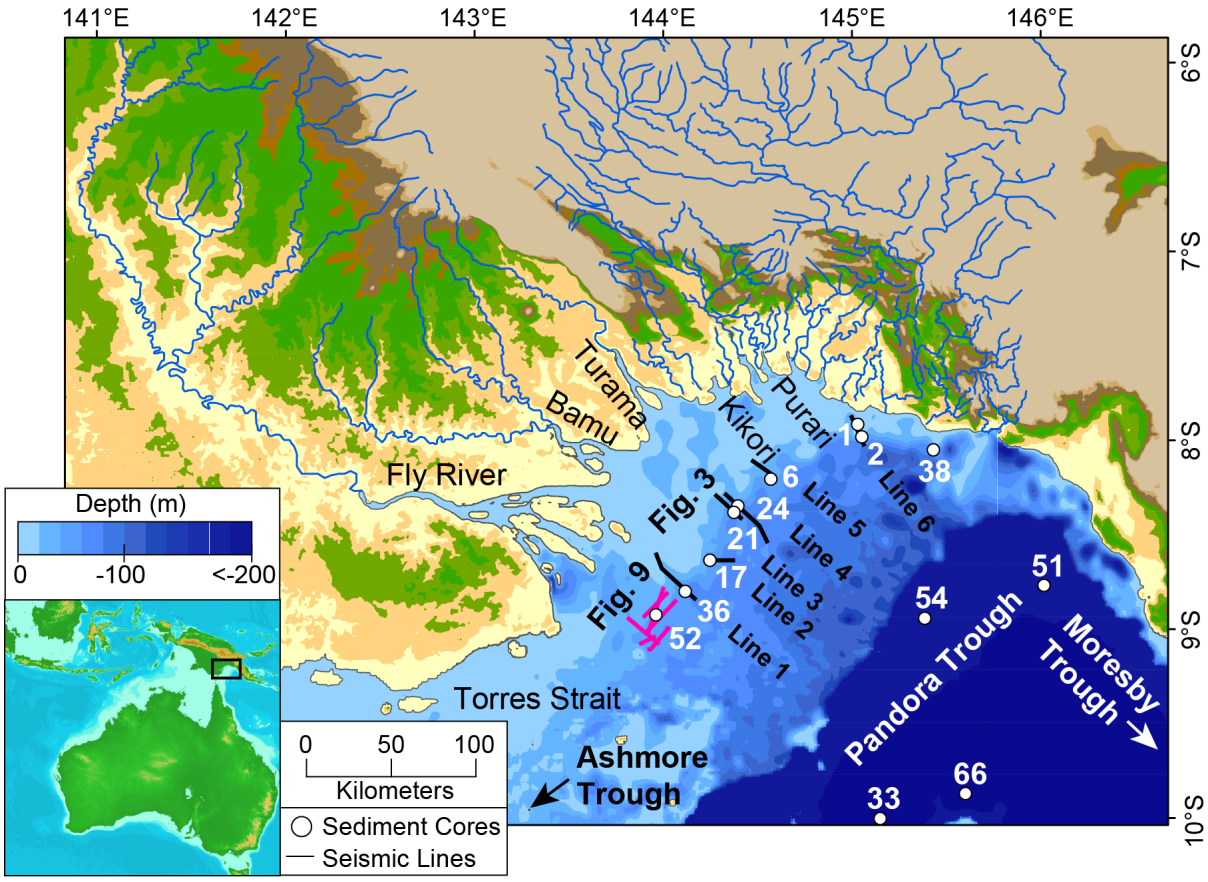

Figure 3.1: Map of the GoP. The study area focuses on the Gulf of Papua (GoP), which is highlighted by the black box in the inset. Sampled cores are shown by the white circles and core names are in white. Solid black lines represent CHIRP seismic dip profiles shown in Figure 3.3. Pink lines represent the CHIRP seismic fence diagram shown in Figure 3.9. River catchments, Torres Strait, and Pandora, Ashmore, and Moresby troughs are also shown.

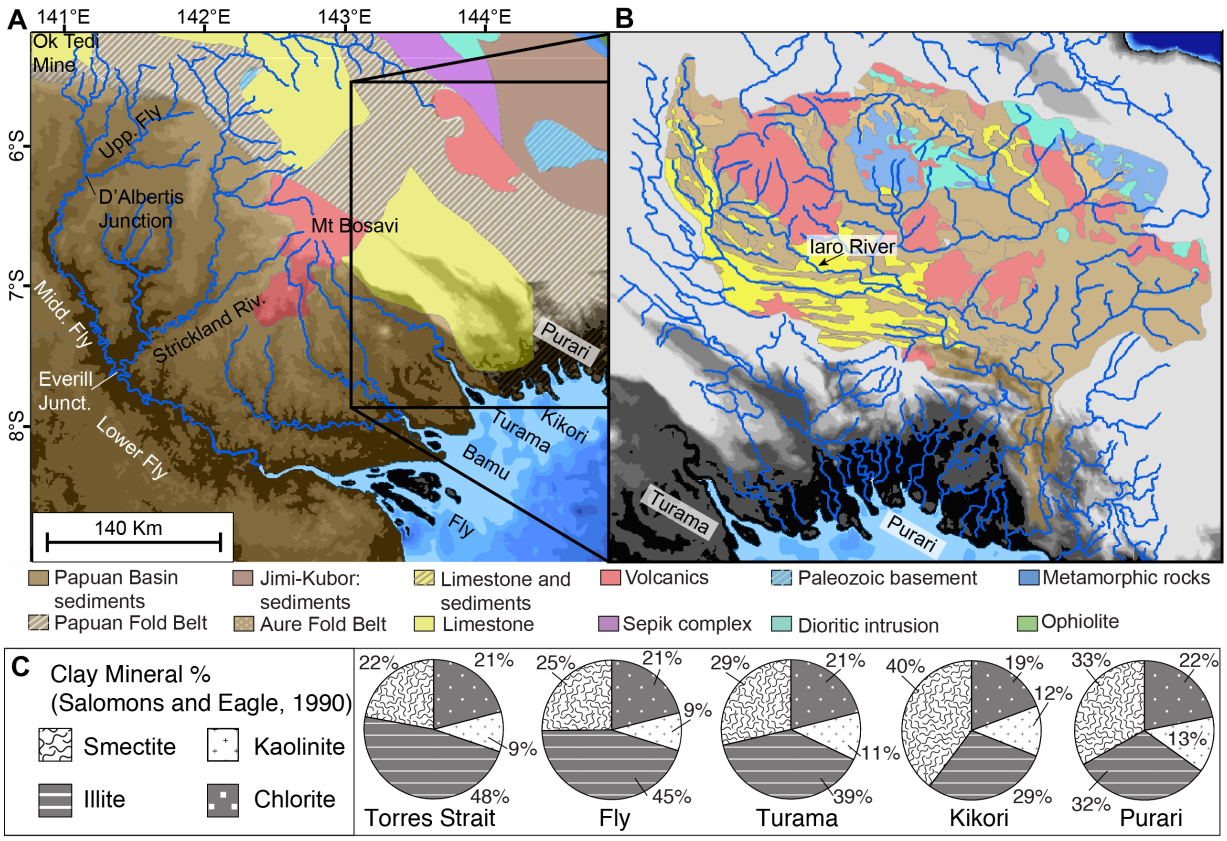

Figure 3.2: Geology and clay mineralogy of GoP rivers. A) geologic formations (after Davies, 2012) in the Fly River catchment compared to B) detailed geology of the Purari River catchment east of the Fly River (Pain, 1983). C) shows the clay mineralogy measured from suspended river sediments from Salomons & Eagle (1990). See Figure 3.1 for the location of Torres Strait.

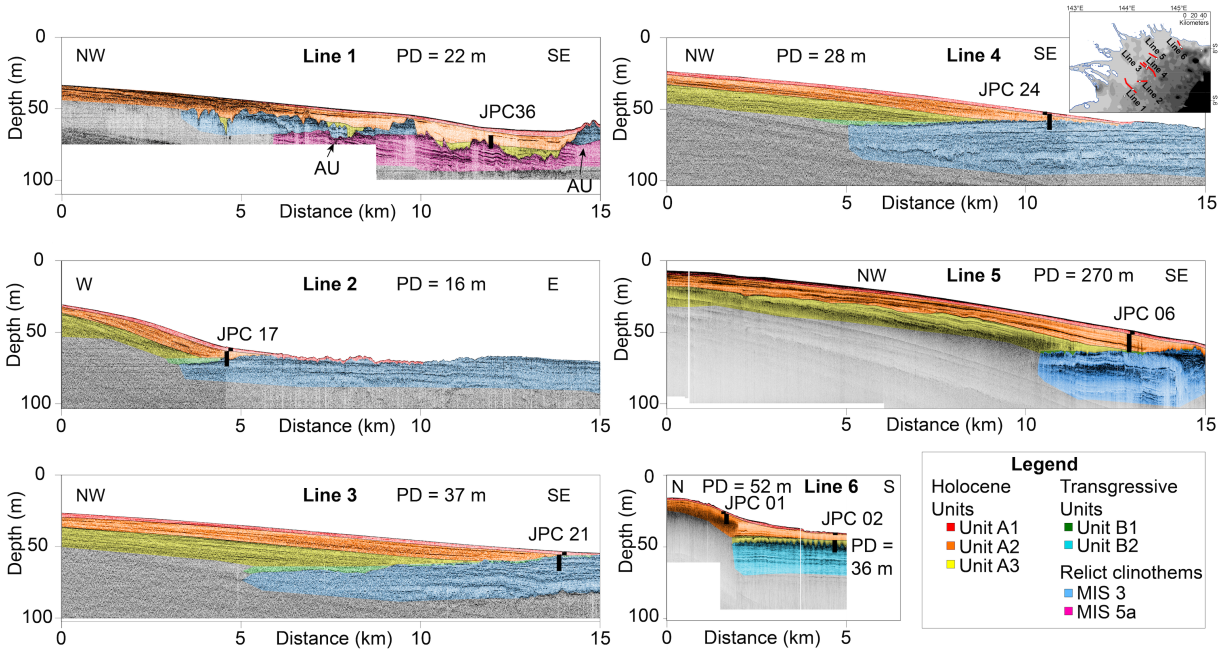

Figure 3.3: Trigger and jumbo piston cores in this study are projected onto CHIRP seismic dip profiles and are shown in black. Locations of the seismic profiles and cores are shown in the inset on the upper right and in Figure 3.1. JPCs 17, 21, and 24 recovered sediment from the MIS 3 clinothem as well as the Holocene clinothem. JPC 36 recovered sediment from the Holocene clinothem in addition to the MIS 5a and 3 clinothems. JPCs 01 and 06 recovered sediment only from Holocene clinothem Units A1, A2, and A3. JPC 02 recovered Holocene clinothem units and the thick transgressive Unit B2.

cycles (Dietrich et al., 1999; Day et al., 2008; Aalto et al., 2008; Swanson et al., 2008; Lauer et al., 2008). During marine transgression following the Last Glacial Maximum (LGM), sediment in the Fly River aggraded rapidly; however, accumulation slowed down during the past 5 kyr (Aalto et al., 2014; Aalto, 2015). Even though sediment cores, ^{210}Pb accumulation rates (Aalto et al., 2008), geochemical tracers (Swanson et al., 2008), and models (Lauer et al., 2008), have made significant contributions to understanding storage in the river floodplain, it remains difficult to quantify and predict floodplain aggradation and erosion throughout the last sea-level cycle ($\sim$120 kyr to the present).

Deposition on the inner mid-shelf occurs during relative highstands in sea-level, which are delineated by the odd-numbered Marine Isotope Stages (Harris et al., 1996; Slingerland et al., 2008; Wei et al., 2019). The inner mid-shelf is constructed of clinothems, or coarsening-

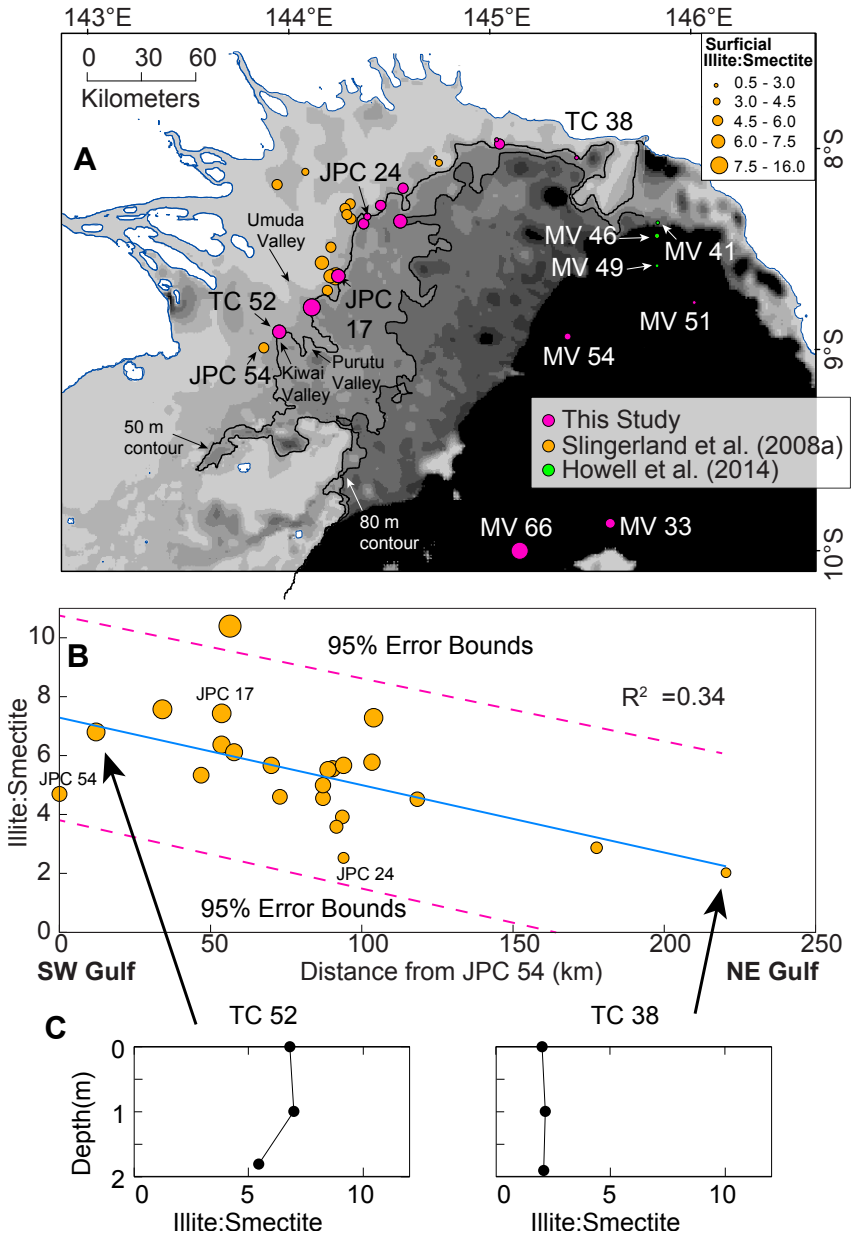

Figure 3.4: Surficial and shallow mineralogy of inner mid-shelf and PT cores. A) Map of surficial illite:smectite ratios. Surficial samples from this study are shown in pink, from Slingerland et al. (2008a) are shown in yellow, and from Howell et al. (2014) in green. Bold black lines highlight the 50 and 80 m depth contours. The locations of the Kiwai, Purutu, and Umuda valleys are shown. B) Plot shows illite:smectite ratios plotted against distance from JPC 54, the southwestern-most core on the inner mid-shelf. C) Illite:smectite ratios for the upper 2 m of TCs (trigger cores) 52 and 38 are shown.

upward sediment packages separated by erosional unconformities or maximum flooding surfaces (Mitchum Jr et al., 1977; Harris et al., 1996; Slingerland et al., 2008; Lobo & Ridente, 2014). In the GoP inner mid-shelf, these clinothems generally exhibit 20-kyr cyclicities (Harris et al., 1996; Slingerland et al., 2008). Sediment units and seismic stratigraphy from the inner mid-shelf will be explored further in Section 2.3. Cores on the inner shelf recover sediment extending back to Marine Isotope Stage (MIS) 5a at the bottomset of the Holocene clinothem (Fig. 3.3; Slingerland et al., 2008). Deposits since the late Holocene are thick; however, underlying deposits from MIS 3 and 5a are thin and characterized by erosional tops and truncated reflectors (Harris et al., 1996; Slingerland et al., 2008; Wei et al., 2019). In contrast, during relative sea-level lowstands, deposition is primarily in Pandora (PT) and Moresby troughs (MT; Fig. 3.1; Jorry et al., 2008; Muhammad et al., 2008; Howell et al., 2014). As the GoP has a distinct shelf-slope break, three well-developed incised valleys offshore the Fly River (Incised valleys shown in Fig. 3.4; Crockett et al., 2008) and other small valleys (Milliman et al., 2004) engender sediment bypass and deposition of basin-floor turbidites (e.g., Posamentier & Vail, 1988; Ritchie et al., 2004). Much of this deposition to PT and MT is via turbidites (Patterson, 2006; Jorry et al., 2008; Septama et al., 2016). Intervals between turbidites record off-shelf transport of neritic carbonates and hemi-pelagic sediment (Febo et al., 2008; Jorry et al., 2008; Septama et al., 2016). During sea-level lowstands such as MIS 2 and 4, inner shelf sediment was subaerially exposed, and as a result, channels incised and eroded relict clinothems (Harris et al., 1996; Slingerland et al., 2008), which is consistent with sequence stratigraphic principles (Mitchum Jr et al., 1977; Vail et al., 1977; Christie-Blick & Driscoll, 1995).

3.3.1 Bedrock Geology

The river catchments for the Fly River lie within the Papuan Basin, a foreland basin located in southern Papua New Guinea (PNG) (Fig. 3.2A). The foreland basin is infilled by a sequence of sediments, which have a composition from oldest to youngest with the following

ages: (1) Mesozoic synrift shelf sediments, (2) Eocene to mid-Miocene carbonate sediments, and (3) molasses-type sedimentation during the Miocene to Quaternary derived from the emerging mountains and subaerial volcanic eruptions (Davies, 2012). The Fly and Strickland river catchments drain Papuan Basin sediment as well as limestone and volcanic rocks (Fig. 3.2A; Davies, 2012). Limestone deposits of the Eocene to mid-Miocene are comprised of 600 m of siltstone overlain by 200 m of limestone (Davies, 2012). Volcanics of K-rich basalt and andesite composition were emplaced during the Quaternary; however, they are not currently active.

Conversely, the river catchments for the Bamu, Turama, Kikori, and Purari drain rocks from the Papuan Fold Belt (PFB), limestones from the Eocene to mid-Miocene, and Quaternary volcanics (3.2B; Pain, 1983; Davies, 2012). The PFB is underlain by a Proterozoic basement that appears in the upper Purari River catchment (Pain, 1983; Hill et al., 2004). Thick sedimentary sequences on the order of 2-5 km were deposited and unconformably overlain by Miocene limestones and marine sediment of 1-2 km thickness (Hill et al., 2004). The sedimentary succession in the PFB is a combination of plastic shales and thick competent units (Hill et al., 2004). The main differences in lithology between Fly and Purari river catchments are that limestone and volcanic deposits are thicker and cover a larger areal extent in the Purari River catchment than the Fly River catchment (Pain, 1983; Davies, 2012; Fig. 3.2). Furthermore, limestone and volcanic deposits are located in the lower Purari River catchment and are not confined to the upper catchment, as is the case with the Fly River (Pain, 1983; Davies, 2012; Fig. 3.2). As mapping by Pain (1983) defined lithologic boundaries on smaller scales than Davies (2012), the lithologic boundaries between Figs. 3.2A and B do not match completely.

3.3.2 Previous Studies on Clay Mineralogy in Papua New Guinea

Suspended sediment sampling at Torres Strait in addition to the mouths of the Fly, Turama, Kikori, and Purari Rivers reveal that Torres Strait and the Fly River are characterized by higher percentages of illite (45-48%) and lower percentages of smectite (22-25%; Salomons & Eagle,

1990; Fig. 3.2C) whereas the Kikori and Purari Rivers have 29-32% illite and 33-40% smectite (Salomons & Eagle, 1990). Among these rivers, kaolinite and chlorite percentages do not exhibit wide variability, ranging from 9-13% kaolinite and 19-22% chlorite.

The clay mineralogy in the Fly-Strickland River system varies from the headlands to the delta. In the headlands and Upper Fly River, there are equal amounts of interlayered illite-smectite, chlorite, and mica (Bolton et al., 2008) such that the headwaters have a similar clay mineralogy to that of the Kikori and Purari rivers. Along the middle Fly, clay mineralogy consists of $\sim$50% smectite, 25% illite, 13% kaolinite, and 14% chlorite (Salomons & Eagle, 1990). Inputs from the Strickland River into the Fly River at Everill Junction changes the clay mineralogy of the suspended sediment because the Strickland River has a composition of $\sim$19% smectite and 48% illite. Therefore the Strickland River plays an important role in controlling the clay mineralogy of the river system, as $\sim$80% of the fine fraction of sediment is composed of material with origins in the Strickland River (Salomons & Eagle, 1990). Since the 1979 commencement of mining in the Ok Tedi copper mine in the upper catchment of the Fly River (Shown in Fig. 3.2A), Cu, Ag, Cd, Pb, Se, Zn, Mn, and S concentrations have increased in river-deposited sediment (Bolton et al., 2008). Mining has also affected Fly River clay mineralogy. After mining began, the dominant mineral in suspended sediment in the Upper and Middle Fly changed from smectite to illite, whereas in the Lower Fly River, the dominant mineral changed from illite to chlorite (Bolton et al., 2008). The cause of these changes remains unclear (Bolton et al., 2008). Higher percentages of smectite and lower percentages of illite in the Purari River can be attributed to weathering of uplifted limestones and marine sediment in its catchment (Irion & Petr, 1983; Pain, 1983). As an example, the Iaro River in the Purari catchment has abundant limestone and fine-grained marine sediment in its catchment and carries sediment with high concentrations of montmorillonite (Fig. 3.2A; Irion & Petr, 1983). High percentages of kaolinite in the Purari River watershed is attributed to the presence of tephras in the catchment (Pain & Blong, 1976; Irion & Petr, 1983).

3.3.3 Inner Shelf Clinothem Dynamics and Sediment Core Facies

The inner mid-shelf clinothem in the GoP is composed of a smooth clinothem deposited during the late Holocene (3.8 ka - present) stacked on top of relict clinothems dating from MIS 3 and MIS 5a (Harris et al., 1996; Slingerland et al., 2008; Wei et al., 2019). At present, transport, deposition, and erosion of sediment at the inner mid-shelf clinothem is influenced by heterogeneous baroclinic currents, wind-driven currents, waves, and tides (Slingerland et al., 2008). Spring tides can produce shear stresses capable of resuspending fine sand and noncohesive mud and these shear stresses are amplified on clinothem topsets (Walsh et al., 2004; Slingerland et al., 2008b). Seasonal shifts in wind patterns allow for temporary storage of fine-grained sediment on topset beds during the quiescent Monsoon season in the winter and advection and erosion of the stored sediment during the more energetic Trade wind season (Walsh et al., 2004; Slingerland et al., 2008b). Thus, spring tidal currents, waves, and storm surges act in concert with strong bottom currents during the Trade wind season to resuspend and mobilize sediment (Harris et al., 2004; Ogston et al., 2008; Slingerland et al., 2008b). Mobilized sediment can move down the clinothem foreset as fluid mud until halted by drag (Slingerland et al., 2008b). Along- and across-clinothem stratigraphy suggests that the Holocene inner mid-shelf clinothem grows obliquely in the northeast-southwest direction and generally agrees with hydrographic interpretations from Walsh et al. (2004) and Slingerland et al. (2008b; Wei et al., 2019). During the Monsoon season, aggradation occurs on bathymetric highs, and during the Trade wind season, sediment on the bathymetric high is winnowed, advected to the northeast, and progrades into topographic lows (Wei et al., 2019). The net sediment transport shifts bathymetric highs to the northeast and builds the Holocene inner mid-shelf clinothem obliquely (Wei et al., 2019).

Five facies were identified in inner shelf cores and are correlated to acoustic units imaged in CHIRP seismic profiles (Fig. 3.3; Slingerland et al., 2008a; Wei et al., 2019). The uppermost facies A consists of homogenous mud with some black laminations. Depending on whether the cores were acquired on the clinothem foreset or bottomset, facies A can range from 5-20

m thick. Beneath facies A, facies B1 grain size and physical character changes markedly, as it is characterized by a mud matrix with coarse sand and shell fragments. Facies B1 ranges in thickness from 0.3-1.1 m and is present in all cores that recover the lower boundary of facies A. On the contrary, facies B2 is recovered only in JPC 02 from the northeast GoP and is characterized by interbedded dark sands and mud lenses with thicknesses of 1-2 cm with higher magnetic susceptibility than facies B1 (Wei et al., 2019). In JPC02, facies B2 is 4 m thick. The underlying facies C is characterized by olive-green homogenous mud with sand lenses. The sand lenses are characterized by medium-fine sand and many lithic fragments including pyroxene, amphibole, garnet, biotite, and muscovite. Only the mud fraction from Unit C was sampled for XRD analysis. The thickness of Unit C is difficult to constrain, as most of the cores did not recover the bottom of the unit. The bottommost facies D was recovered only by JPC 36 and consists of homogenous mud interbedded with sand lenses that are $\sim$0.5-1 cm thick. Facies C and D are distinguished by a color change from olive-green in facies C to blue-gray in facies D (Wei et al., 2019). Additionally, sand lenses within facies C are coarse, whereas sand lenses with facies D are fine-medium sands.

Projecting the cores onto the seismic lines allows for the correlation of sediment facies to acoustic packages imaged across and along the clinothem (Fig. 3.3). For cores on the inner mid-shelf clinothem, Wei et al. (2019) described the correlation of facies with sediment units and Marcuson et al. (2019) explored the correlation of cores using seismic reflectors. The homogenous mud in the upper section of the core corresponds to Units A1, 2, and 3 (shown by Red, Yellow and Orange), which comprise the Holocene clinothem. The most recent deposits were divided into three units, Units A1, A2, and A3, based on reflector geometry and sequence-stratigraphic interpretations from Slingerland et al. (2008) and Wei et al. (2019). Facies B1, B2, C, and D, correspond to sediment units interpreted from seismic profiles, and are referred to as facies in cores and units on seismic profiles. Beneath the Holocene clinothem, the sandy and shelly layer corresponds to the transgressive lag (Unit B1, shown in Green). The thick sandy unit observed in JPC 02 also was deposited during the transgressive systems tract (9.5-10.3 ka) and is identified as

Unit B2, shown in Cyan (Wei et al., 2019). The interlayered sand and mud correspond to topset beds from the MIS 3 clinothem (Unit C, shown in Blue; Slingerland et al., 2008a; Wei et al., 2019). One radiocarbon date within Unit C dates this deposit to 33.9 ka (Harris et al., 1996). The basal most layer, Unit D (shown in Pink), was recovered only in JPC 36 and corresponds to dipping foresets of the MIS 5a clinothem (Slingerland et al., 2008a; Wei et al., 2019). Even though facies D was recovered only in JPC 36, Unit D is imaged in seismic profiles in the southwest GoP and is characterized by prograding beds that are truncated at their upper boundary and onlapped by sub-horizontal beds in Unit C (Slingerland et al., 2008a; Wei et al., 2019). As Unit D is radiocarbon dead, the age of the unit was determined by sequence stratigraphic principles and its relationship to Unit C as discussed in Slingerland et al. (2008a).

Offset coring based on CHIRP seismic profiles allowed for the sampling of a number of sediment facies from the clinothem topset, foreset, and bottomset as well as the different lobes along the margin (i.e., Southern, Central, and Northern lobes). For this study, only bottomset cores were sampled (with the exception of JPC 01) because Unit A was condensed in these cores, and the older facies (Units B1 through D) could be recovered. Variable thickness of Units A1-A3 along the inner mid-shelf influenced the recovery of Units B1 through D. Though JPC 06 was the longest core recovered in this study, it recovered only sediment from Holocene Units A1-3 from the Central lobe, the depocenter of the Holocene clinothem (Harris et al., 1996; Walsh et al., 2004; Slingerland et al., 2008a). In contrast, the Southern lobe has thinnest Holocene clinothem deposits due to limited accommodation, and as a result Unit D was only recovered in JPC 36 proximal to the Fly River (Wei et al., 2019). Accommodation in the southwest GoP is less than in the northeast due to differential subsidenced caused by foreland basin tectonics (Pigram et al., 1989; Pigram & Symonds, 1991; Wei et al., 2019). The GoP clinothem and PT deposits are viewed as sediment sinks; however, both deposits are subject to post-depositional reworking (Nittrouer et al., 2007), with the Eel, Po, and Waipaoa deposits exhibiting biological reworking to depths $>$5 cm over the span of a few years (Wheatcroft et al., 2007; Walsh et al., 2014).

3.3.4 Pandora Trough (PT) Cores

Deposits in PT were examined to test whether the Fly and Purari rivers maintain a connection to PT throughout sea-level cycles. During sea-level lowstands, sediment that bypassed the inner mid-shelf could be deposited in Ashmore, Pandora, and Moresby troughs, which were formed by rifting of the Coral Sea Basin from the Early Cretaceous to the Paleocene (Davies et al., 1989; Pigram et al., 1989). PT is a southwest-northeast trending basin. The SW end is a 1700 m deep semi-enclosed basin without a modern outlet. The northeast end is connected to Moresby Trough (MT) at 2000 m water depth (Francis et al., 2008). Southern PT is the site of extensive mass-wasting and mass-transport. The intra-slope basin floor is relatively smooth and filled with extensive turbidites (Jorry et al., 2008). The north PT shelf is characterized by prograding clinoforms and a sediment wedge (Francis et al., 2008; Howell et al., 2014). MT is in the eastern GoP and is separated from the Papuan Peninsula by a narrow shelf (Fig. 3.1; Francis et al., 2008). Ashmore Trough (AT) is located in the southwest GoP (Fig. 3.1), is the smallest and shallowest of the intraslope basins, and is rimmed by active carbonate reefs (Francis et al., 2008). Of these troughs, PT and specifically northern PT have the highest recent ($<$100 years) accumulation rates and it is estimated from ^{210}Pb inventories that 7-14 Mt of sediment is liberated from the shelf and deposited in PT annually (Muhammad et al., 2008). AT has less sediment accumulation because its geomorphology is dominated by carbonate platforms, siliciclastic sediment supply is lower than in PT, and sedimentation consists of a uniformly thin pelagic and hemipelagic drape of mostly carbonate composition (Francis et al., 2008; Muhammad et al., 2008). Sediment accumulation rates in PT are estimated to have been an order of magnitude larger than in MT during MIS 2 and 1 (Septama et al., 2016).

Clay mineralogy was previously sampled by Howell et al. (2014) in northeast PT JPCs MV 41, MV 46, and MV 49 proximal to the Papuan Peninsula (MV = Melville; locations shown in Fig. 4). To avoid confusion between inner mid-shelf cores and PT cores, JPCs in PT will be referred to as MV, per the convention of Howell et al. (2014) and Septama & Bentley (2017). MV

41, located on the outer shelf, records low illite:smectite signatures (∼0.1-1.0) during the post-glacial transgression when clays may have been sourced from the Papuan Peninsula (Howell et al., 2014). The deeper slope wedge cores MV 46 and MV 49 record slightly elevated illite:smectite signatures (∼1-3.2) as these cores were supplied by turbidites that may have been sourced from the Fly River. Howell et al. (2014) suggest that during the sea-level transgression, Fly River sediment may have bypassed the shelf and deposited turbidites with high illite:smectite signatures along the deeper slope wedge. Another provenancing study in PT by Septama & Bentley (2017) examined heavy minerals in turbidite deposits from multiple cores. Before MIS 2, PT and MT received sediment from different sources, with MT turbidite sands originated from the Papuan Peninsula and PT turbidite sands sourced from felsic plutonic, sedimentary, and metasedimentary source rocks of the Papuan orogeny (Septama & Bentley, 2017). As the sea-level fall approached MIS 2, cores within PT and MT exhibited more geochemical variability (Septama & Bentley, 2017). The authors suggested that the migration and incision of rivers across the coastal plain may have resulted in the repartitioning of sediment sources to create depocenters with distinct geochemical compositions (Septama & Bentley, 2017). After MIS 2, delivery of sandy sediment to PT and MT decreased markedly (Jorry et al., 2008; Howell et al., 2014; Septama & Bentley, 2017).

Cores sampled in PT include previously studied cores MV 33 (Jorry et al., 2008; Septama et al., 2016; Septama & Bentley, 2017), MV 51 (Febo et al., 2008), MV 54 (Febo et al., 2008; Septama et al., 2016; Septama & Bentley, 2017), and MV 66 (Patterson, 2006; Jorry et al., 2008; Septama et al., 2016; Septama & Bentley, 2017). MV 33 and MV 66 are located in the intra-slope basin floor with a nearly flat floor. Sediment input to the region is predominantly from turbidites (Francis et al., 2008; Jorry et al., 2008). Lower parts of the MV 33 and MV 66 predating 12.5 ka consist of siliciclastic sandy and muddy turbidites, which are not observed in the Holocene (Jorry et al., 2008). The siliciclastic turbidites contain dark sand-dominated layers that are 1-10 cm thick, containing well-preserved wood and plant fragments, with some erosional bases (Jorry

et al., 2008). Thin section analysis revealed that the sands are predominantly quartzofeldspathic with >50% sand and ∼20% of heavy and mafic minerals, such as amphibole, pyroxene, zircon, and apatite (Patterson, 2006; Jorry et al., 2008). Intervals of sandy and muddy turbidites are separated by intervals rich in pelagic carbonates. Holocene sediments consist largely of pelagic and hemipelagic carbonate-rich sediment and calciturbidites (Jorry et al., 2008). The upper 160 and 130 cm of MV 33 and MV 66 respectively contain a fining-upward calciturbidites, consisting of skeletal fragments at the base and planktic foraminifers at the top that are hypothesized to have originated from the Eastern Fields Atoll (Jorry et al., 2008).

MV 51 was collected from a narrow shelf along north PT on top of a northwest-southeast-trending tectonic ridge that forms a local topographic high (Fig. 3.1). This ridge elevated MV 51 enough so that it is not inundated directly by gravity flows and may have lowered accumulation rates at this site (Febo et al., 2008). Sediment dated to 18.4-20.4 ka and at 28 ka contains high total organic carbon (TOC) that was suggested to have derived from land-plant debris. The section of the core deeper than 10 m and older than 32 ka is interpreted to have received input of volcaniclastic material from central and eastern PNG and possibly from the Papuan Peninsula (Febo et al., 2008). MV 54 was collected at a similar depth as MV 51; however, MV 54 was collected on the slope seaward of the broad shelf that borders central PT (Febo et al., 2008). MV 54 is characterized by low calcium carbonate percentages ∼3% and low overall TOC except for four TOC maxima that correspond to maxima in magnetic susceptibility and in the sand-size fraction. Other features of this core are two coarse-grained fining-upward organic-rich intervals at depths of 1.5-1.9 m and 6.1-6.3 mbsf. Additionally, between the depths of 6.1-6.3 mbsf, sediment lamina are inclined by 45°, suggesting mass flow deposition (Febo et al., 2008). Radiocarbon ages within MV 54 span only 15-18 ka, at which time sea-level was at approximately ∼110 mbsl (Waelbroeck et al., 2002) and the Fly, Turama, and Kikori rivers could deposit sediment closer to the shelf edge (Milliman et al., 2004; Febo et al., 2008). Rapid deposition on the order of 6 m in <1000 years may be due to mass failure of upslope deposits (Febo et al., 2008). At ∼16

ka, sediment in MV 54 is characterized by increasing sandy material that ceases abruptly at 15 ka (Septama & Bentley, 2017). After 15 ka, sediment accumulation rates in MV 51 and MV 54 diminished markedly and may be due to flooding of the outer shelf at that time (Howell et al., 2014; Septama & Bentley, 2017) or development of a coralgal ridge at the shelf edge from 14.5-12 ka, which may have served as a barricade of sediment (Droxler, Mallarino, Francis, Dickens, Beaufort, Bentley, Peterson & Opdyke, Droxler et al.; Febo et al., 2008).

3.4 Materials and Methods

3.4.1 CHIRP seismic data

Between September 2003 and March 2004, 6800 km of Compressed High Intensity Radar Pulse (CHIRP) data were collected aboard the R/V Melville as part of the NSF MARGINS Initiative (Driscoll & Milliman, 2004a; Driscoll & Milliman, 2004b). Of these lines, 2300 km were collected with the Scripps Institution of Oceanography surface-towed Edgetech with profiler with 1 – 6 kHz CHIRP signal with a 50 ms sweep and 4500 km were collected with a Knudsen hull-mounted profiler centered on 3.5 kHz frequency. Navigation of the surface-towed CHIRP was derived from comparing the fish depth and winch cable payout relative to the ship topside DGPS receivers. The cruise track spacing was designed to provide dip line coverage of the clinothem geometry as well as detailed strike-line coverage of along-shelf variability (Fig. 3.1). This coverage allowed for submeter vertical resolution to depths up to 50 m in areas where underlying stratigraphy was not obscured by gas wipeout.

Processing steps such as ship heave removal and gain adjustment were performed using SIOSEIS (Henkart, 2003) and Seismic Unix (Cohen & Stockwell Jr, 2001). Processed lines were imported into IHS Kingdom Software and sequence stratigraphic principles were employed to identify changes in stratal geometry (e.g., Mitchum Jr et al., 1977; Vail et al., 1977; Christie-Blick & Driscoll, 1995). Interpreted seismic profiles and their corresponding navigation were

loaded into Fledermaus Software by Interactive Visualization Systems to create three-dimensional perspective views.

Table 3.1: Radiocarbon ages, Analytical Errors, the study that published the ages, and sampled material. Studies cited are: I) Marcuson et al., 2019; II) Wei et al., 2019; III) Jorry et al., 2008; IV) Septama et al., 2016; V) Febo et al., 2008; VI) Patterson, 2006. *Calendar ages were calculated by Septama et al. (2016) using the Marine09 curve for marine samples and Intcal09 curve for wood samples. MBF = Mixed benthic foraminifera, PF = Planktonic foraminifera, and PT = Pandora Trough.

Core	Depth (mbsf)	Corrected ^{14}C age	Uncorrected ^{14}C age	Error ± (year BP)	Study	Location in GoP	Material
JPC 01	2.03	715	1175	40	I	Inner Mid-Shelf	MBF
	2.25	753	1220	30	I		MBF
	6.01	979	1440	30	I		MBF
	9.94	1361	1825	40	I		MBF
JPC 02	1.85	477	860	43	I, II	Inner Mid-Shelf	MBF
	4.46	1207	1655	38	I, II		MBF
	8.86	6561	6140	54	I, II		MBF
	13.66	10333	9480	100	I, II		MBF
JPC 06	1.95	414	785	21	I, II	Inner Mid-Shelf	MBF
	2.11	455	830	27	I, II		MBF
	7.21	1257	1710	46	I, II		MBF
	12.71	1570	2015	40	I, II		MBF

Table 3.1 (continued): Radiocarbon ages

Core	Depth (mbsf)	Corrected ^{14}C age	Uncorrected ^{14}C age	Error ± (year BP)	Study	Location in GoP	Material
JPC 17	1.83	170	550	30	I, II	Inner Mid-Shelf	MBF
	2.35	362	725	16	I, II		MBF
	6.65	6505	6090	46	I, II		MBF
JPC 21	1.64	204	585	35	I, II		MBF
	1.85	265	630	37	I, II		MBF
	2.27	4259	4185	30	I, II		MBF
JPC 21	2.50	5518	5165	30	I, II		MBF
JPC 24	1.73	112	500	13	I, II		MBF
	3.87	3835	3880	46	I, II		MBF
MV 33	1.55	11805*	10625	40	III	Pandora Trough	MBF
	3.32	12765*	11325	25	III		MBF
	12.15	22815	19560	70	IV		Bulk sediment
MV 51	1.2	18600	15565	50	V	East Pandora Trough	Wood
	1.34	18405	15390	100	V		Wood

Table 3.1 (continued): Radiocarbon ages

Core	Depth (mbsf)	Corrected ^{14}C age	Uncorrected ^{14}C age	Error ± (year BP)	Study	Location in GoP	Material
MV 51	3.51	20405	20400	90	V		Wood
	7.40	28017	29500	220	V		MBF
	10.00	32617	34100	250	V		MBF
MV 54	1.90	16385*	13320	25	V	Pandora Trough	Wood
MV 54	4.75	17230*	14160	35	V		Wood
	8.30	17250*	14175	40	V		Wood
	9.94	18100*	14810	80	V		Wood
MV 66	0.63	8722	8390	10	III	Pandora Trough	PF
	1.28	12033	10730	25	III		PF
	2.22	14776	13040	80	III		PF
	8.37	19563	16450	45	VI		Wood
	9.55	20272	17100	40	VI		Wood

3.4.2 Sediment Cores

The CHIRP subbottom profiles were used to identify the locations of 27 jumbo piston (JPC) and 21 gravity core (GC) locations across the shelf (Fig. 3.1). Trigger cores (TC) were deployed with the JPCs. In some cases, drift in the ship position caused the cores to be offset

from the profiles. The core locations in these situations are correlated with the subbottom profiles by projecting the core location orthogonally onto the plane of the subbottom profile and noting on the profile the projecting distance. To correlate the cores to the seismic profiles, the two-way travel time was converted to depth using a sound velocity of 1300 m/s which is discussed in Wei et al. (2019) and Marcuson et al. (2019). Cores were split in half vertically and then observations of color, grain size, sediment structures, and general lithology were recorded. Radiocarbon ages of inner mid-shelf JPCs 01, 02, 06, 17, 21, and 24 and PT cores MV 33, 51, 54, and 66 are previously published and summarized in Table 3.1. (Patterson, 2006; Febo et al., 2008; Jorry et al., 2008; Septama et al., 2016; Marcuson et al., 2019; Wei et al., 2019).

Age models for the PT cores were constructed using the "Bacon" package in R Studio from Blaauw & Christen (2011), as they are well-dated. JPCs from the inner mid-shelf are not suitable for this analysis, as they contain unconformities and do not have radiocarbon ages in Units C and D. Calibration within the Bacon package was done using the Marine 13 and IntCal 13 curve depending on the sample's composition (foraminifera or wood; see Table 3.1). Age models were used to plot downcore variations in illite:smectite in PT cores with respect to age.

3.4.3 X-ray Diffraction (XRD)

On the inner shelf, seven JPCs and two TCs were selected for downcore XRD analysis based on an along-margin transect from southwest to northeast and their recovery of older underlying sediment facies. JPCs 01 and 21 in this study had published data on XRD analysis by Howell et al. (2014). In addition to sampling at the same depths in order to reproduce their results, JPC 21 was sampled at additional depths based on facies boundaries. Within PT cores, sampling depths were selected based on their previously published chronology and lithostratigraphy.

While riverine and surficial XRD was measured by Salomons & Eagle (1990), Slingerland et al., (2008a), and Howell et al., (2014), few studies have investigated the major and trace element concentration of suspended river sediment. Furthermore, few of these studies have measured

these signatures for all of the rivers discharging into the GoP. One these studies, Irion & Petr (1983), measured major elements of suspended sediment from the Fly and Purari rivers such as Zn, Ti, Cu, Mn, Cr, Pb, K, Mg, and Ca; however, none of these signatures are diagnostic of different source material and the concentration of mobile elements could be masked by tropical weathering signatures (Irion & Petr, 1983; Moore, 2011). As there is little knowledge of the major and trace element geochemistry of suspended river sediment, this study will instead use clay mineralogy as a provenance tool as it has been established in multiple studies in the GoP.

Sediment samples were first washed, centrifuged and decanted several times, and tested with silver nitrate until there was no salt left in the sample. These samples were separated into the clay size fraction (<2 μm) according to Stokes Law and the clay-sized fraction was concentrated using centrifugation. Clay-sized material was transferred to a glass slide using an eyedropper following methods described in Moore & Reynolds (1989). For each slide, air-dried and ethylene glycol-solvated XRD runs were conducted at the Philips X'Pert XRD at San Diego State University with Cu-K alpha radiation and Ni filter at a voltage of 40 kV and a current of 40 mA. Each run was performed at a 2 theta-scan step of 0.02° through a range of 4-36°. Peaks were identified with the MacDiff software (Petschick, 2000) and semi-quantative analysis of the peak area of clay minerals was conducted using the intensity factors from Biscaye (1965) and following the methods of Xu et al. (2012) and Howell et al. (2014). Hierarchical cluster analysis was conducted by constructing dendrogram plots using the statistical toolbox in MATLAB®. The default mode measured Euclidean distance between samples. Due to the size of the clay mineralogy dataset, facies in each core were averaged instead of using discrete samples to calculate the dendrogram.

3.5 Results

3.5.1 Surficial Sediment Mineralogy of Shelf Sediment

Surficial sediment samples from sediment cores sampled in this study expand upon previous work conducted by Slingerland et al. (2008) and Howell et al. (2014). Mapped illite:smectite ratios reveal that samples located closest to the Fly River delta in the southwest have larger illite:smectite ratios (illite:smectite of JPC 54 ∼4.7) than those in the northeast farther from the Fly River (illite:smectite of TC 38 ∼2.0; Fig. 3.4A). When distance from JPC 54 (the southwestern-most core) is plotted vs. illite:smectite ratios, there is a linear trend with an R^2 value of 0.34 (Fig. 3.4B) and a correlation factor of -0.59. TC 52 located near the mouth of the Fly River, has surficial illite:smectite values of 6.8 that decrease downcore to values of 5.5 at the base (Fig. 3.4C). The most northeasterly core, TC38, has surficial illite:smectite ratios of 2.0 and shows no significant increases or decreases downsection.

3.5.2 Downcore Sediment Mineralogy of Inner Mid-Shelf Sediment

Downcore sediment mineralogy paired with 14C dates from the inner mid-shelf reveal that clay mineralogy changes with facies (Fig. 3.5). Variability in the downcore composition was investigated by Howell et al. (2014), though changes were not related to seismic stratigraphy. As TCs 52 and 38 were too short and recovered only Unit A sediment, their downcore composition shows little variability. Likewise, JPC 01 and JPC 06 penetrated only Units A1-A3 and hence their downcore composition shows little variability with smectite fluctuating between 7-17% in JPC 01 and 11-16% in JPC 06. Nevertheless, JPCs 02, 17, 21, 24 and 36 exhibit compositional changes that correspond to facies.

JPCs 17, 21, 24, and 36 recovered sediment from Units A, B1, and C. This transition from Unit A to B1 occurs below 6 m for JPC 17, below 2 m for JPC 21, and below 5 m for JPC 24. Above this transition, these three cores are characterized by low smectite (9-14%), high

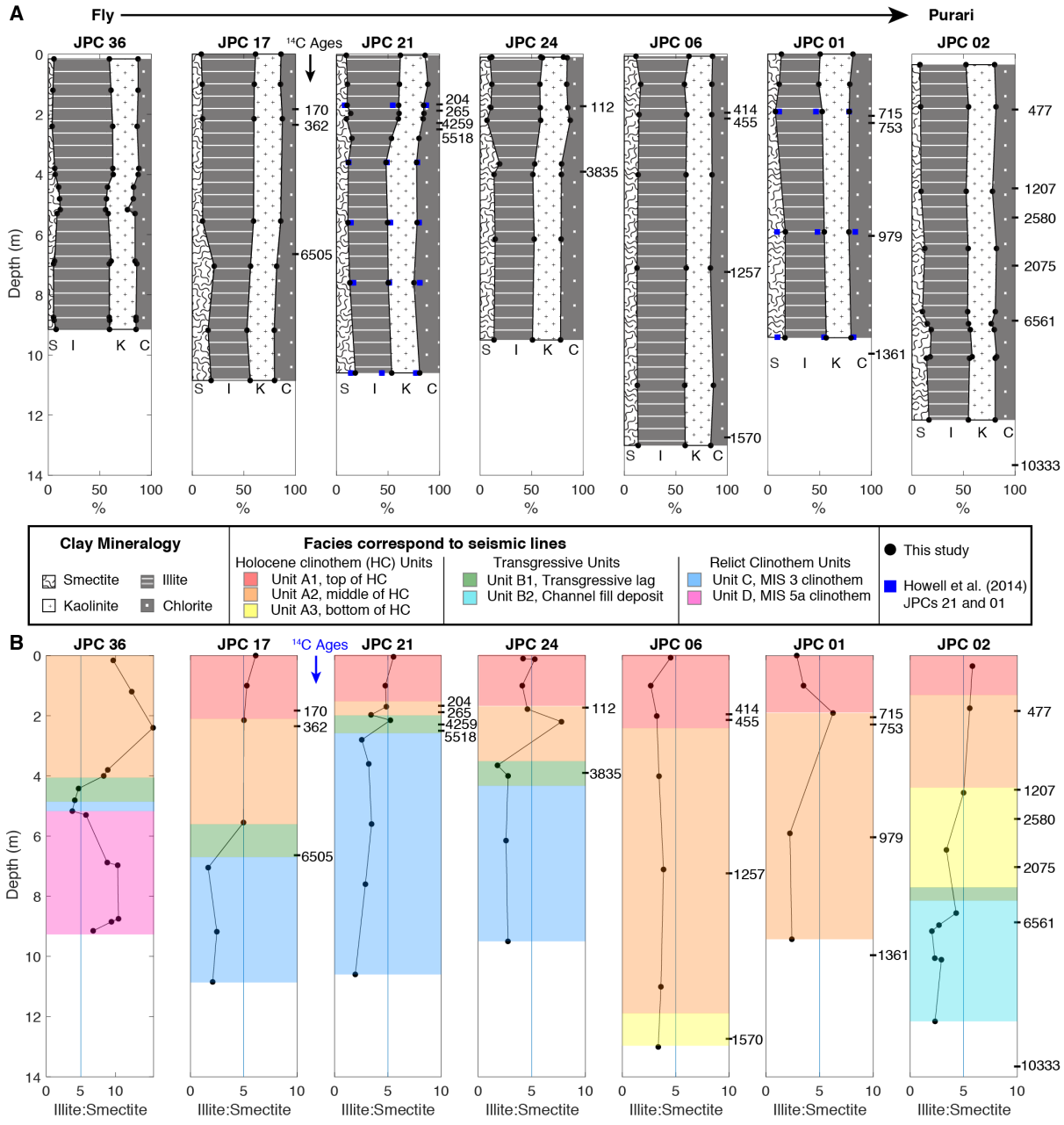

Figure 3.5: Downcore mineralogy for inner mid-shelf clinothem cores. A) Percent mineralogy is plotted downcore. Corrected radiocarbon ages (yr BP) are plotted on the right side of the core. The cores are arranged from SW to NE, with JPC 36 proximal to the Fly River and JPC 02 proximal to the Purari River. Downcore plots of JPCs 21 and 01 also plot the percent mineralogy measured by Howell et al., (2014) shown as blue squares. B) Illite:smectite ratios are plotted downcore. Vertical color changes correspond to sediment units. Corrected radiocarbon ages are plotted to the right of the core. Note the marked variation in illite:smectite ratios across the transgressive surface (Unit B1, green).

illite (47-61%), and kaolinite in the range of 24-28% (Fig. 3.6). Unit B1 in these four JPCs typically has slightly increased smectite (6-18%), slightly decreased illite (34-50%), and kaolinite ranges similar to those from Unit A (24-28%). Below this transition, the composition of the three minerals changes to 13-19% smectite, 34-39% illite, and 24-30% kaolinite. Slight changes in percent smectite and percent illite are highlighted by examining downcore illite:smectite ratios (Fig. 3.5B).

JPCs 36 and 02 contain facies not recovered in other cores, as JPC 36 is the only core to recover Unit D and JPC 02 is the only core to recover Unit B2. JPC 36 recovered Unit A in the upper 4 m and it is characterized by very high illite:smectite values around 10. Below this, Unit B1 decreases in illite:smectite to values of around 4.1-4.6 (Fig. 3.5B). A thin veneer of Unit C exhibits decreases in illite:smectite to values $\sim$3.8. Below this, Unit D illite:smectite increases from 5.7 at the top of the unit to maximum values of 10.3 at $\sim$ 7-9 m (Fig. 3.5B). JPC 02 recovered Unit A in the upper sections of the core, a thin veneer of Unit B1, and Unit B2 at the base of the core. Mineralogy of Unit A in JPC02 are comparable to mineral compositions of other Unit A sediment recovered from the northeast GoP, for example, JPC 01. Above the Unit B1 transgressive deposit in JPC 02, illite:smectite ratios are $>$4 and below Unit B1, Unit B2 illite:smectite ratios decrease to 2-2.9 (Fig. 3.5B).

Downcore percent mineralogy of JPCs 21 and 01 from this study are generally in agreement with measurements from Howell et al., (2014). In JPC 01, percent smectite in this study deviates from the measurements of Howell et al., (2014) by 3-8% and this study's percent illite deviates from Howell et al., (2014) by 1-10%, with the greatest deviation at 1.9 m (Fig. 3.5A). This study's mineralogy measurements in JPC 21 exhibit more similarity to measurements of JPC 21 from Howell et al., (2014), with percent smectite deviating by 0-4% and percent illite deviating by 0-5% (Fig. 3.5A).

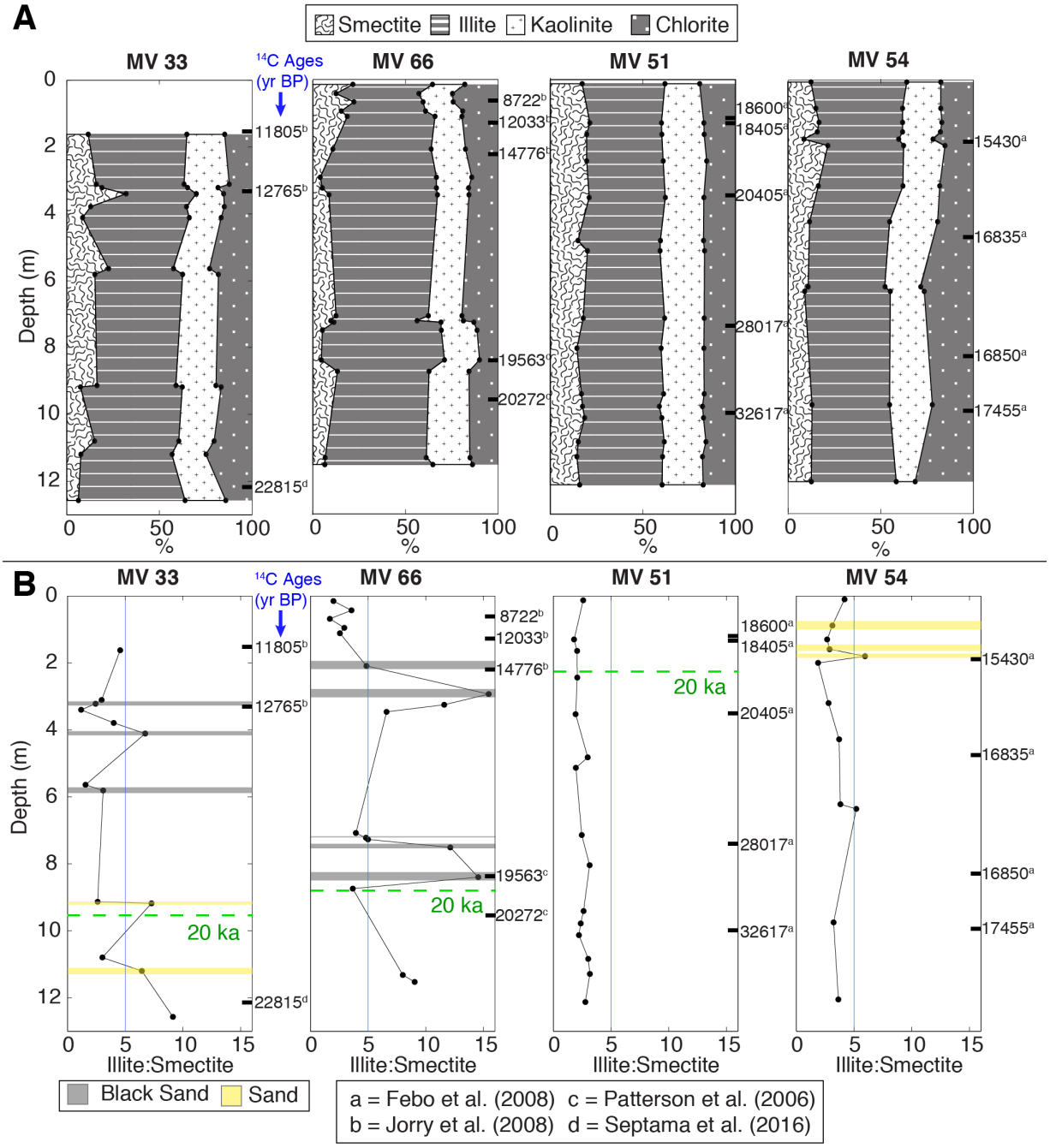

Figure 3.6: Downcore mineralogy for Pandora Trough cores. A) Percent mineralogy is plotted downcore. Corrected radiocarbon ages (yr BP) are plotted on the right side of the core for A and B. The sources of those ages are shown in the legend at bottom. B) Illite:smectite is plotted downcore. Grey horizontal bars indicate black sand layers, yellow horizontal bars indicate sandy turbidite layers, and dashed green lines mark sediment dating to 20 kyr BP.

3.5.3 Mineralogy of Pandora Trough Cores

The mineralogy of MV 51 located near the Papuan peninsula exhibits little downcore variability (Fig. 3.6A). Variations at around 5 m depth are the result of a slight decrease in smectite at the expense of slightly increasing illite. MV 54 also displays very little downcore variability except at the sand layer younger than 15.4 ka, during which smectite decreases at the expense of illite. MV 54 shows an increasing trend downcore in kaolinite at the expense of chlorite. The peak in illite:smectite ratios in MV 54 corresponds to the sandy interval with coarse-grained fining-upward material that is younger than 15.4 ka.

The greatest variations in Pandora Trough cores are observed in the sawtooth patterns of MVs 33 and 66. Increases in illite at the expense of decreasing smectite generally correspond to sediment older than 20 kyr or sandy layers (Fig. 3.6B). Muddy intervals in MV 33 exhibit low illite:smectite ratios of $\sim$3 from 6-10.8 m, which corresponds to an estimated time period from 15.9-21.5 ka from the Bacon age model. Below 10.8 m, illite:smectite sampled from a muddy interval increases to $\sim$9, which corresponds to an age older than 22.8 ka (Septama et al., 2016). Sandy layers in MV 33 have lower illite:smectite ratios than those in MV 66 and exhibit illite:smectite ranges of 6.7-7.2 (Fig. 3.6B). In MV 66, illite:smectite ratios reach peak values of 14.5-15 in sandy layers at 2.93 m (estimated age $\sim$15 ka) and at 8.4 m (estimated age $\sim$19.7 ka). Below 11.3 m in MV 66, illite:smectite ratios of muddy sediment increase to 8-9 and have estimated ages between 22.4-22.7 ka (Fig. 3.6B).

3.5.4 Hierarchical Cluster Analysis

Hierarchical Cluster Analysis, or dendrogram analysis from the MATLAB® Toolbox was used to statistically group similar samples based on their clay mineralogy (Fig. 3.7). Within each facies/unit of a sediment core, clay mineralogy data points were averaged because the clay mineralogy dataset contained 122 samples that could not be displayed on the dendrogram.

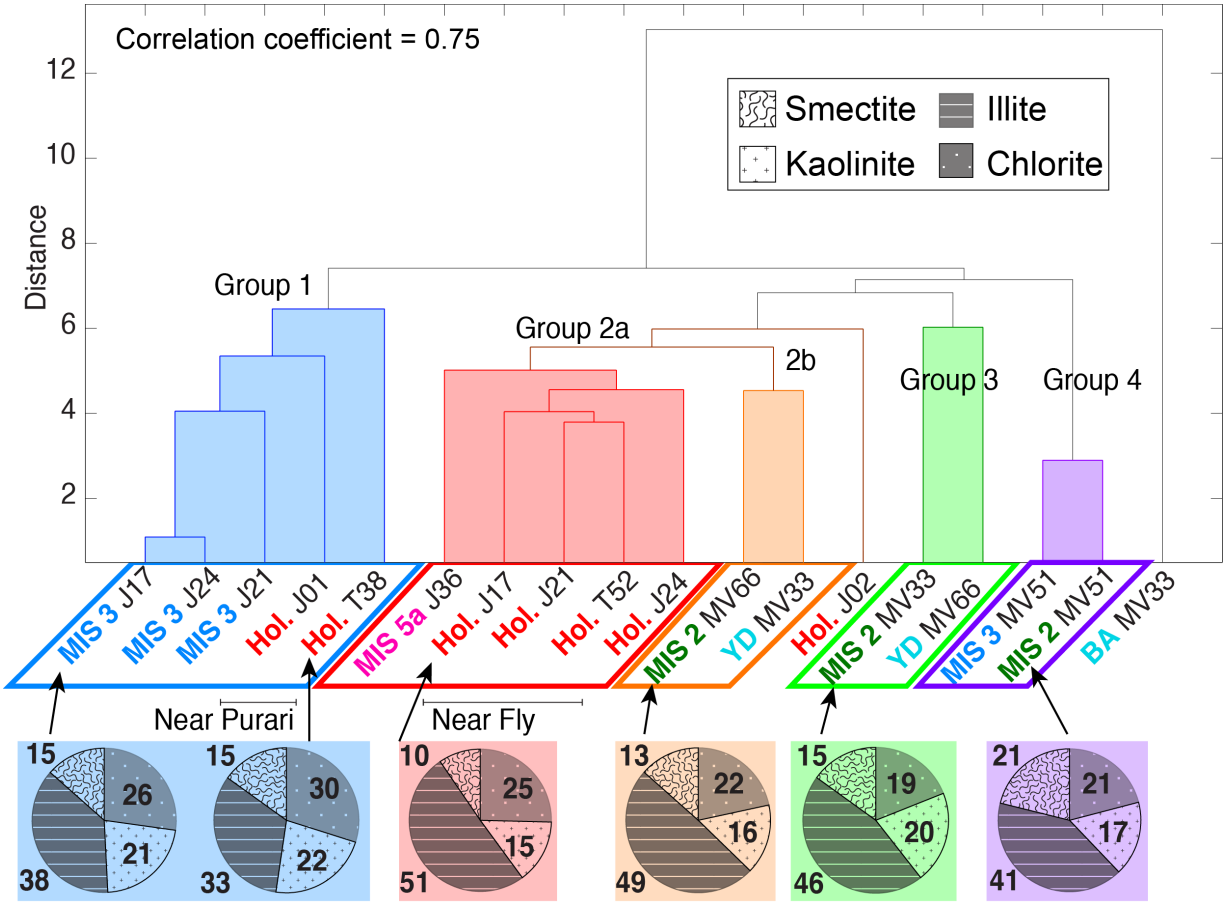

Figure 3.7: Dendrogram analysis based on clay mineralogy reveals four main groups. Smaller Ward's Distances correspond to similar assemblages. Below, pie diagrams for representative average samples are shown.

Smaller Ward's distances correspond to similar assemblages. Since the maximum distance between Groups 1-4 is only 6, the assemblages are not largely different. From dendrogram analysis, four main groups and two outlier samples were recognized. Group 1 consists of samples with illite:smectite ratios less than 5, whereas Group 2 consists of samples with ratios generally greater than 5. Thus, dendrogram analysis statistically groups modern-day Purari sediment with inner shelf MIS 3 sediment in Group 1 and in Group 2, MIS 5a sediment is statistically related to Holocene clinothem sediment proximal to the Fly River. Groups 2b and 3 are composed of sediment from PT MVs 33 and 66. Their signature is distinguished from that of Group 2 by slightly lower concentrations of illite, and higher concentrations of smectite at the expense of decreasing chlorite. Holocene sediment from JPC 02 is distantly related to Group 2 with intermediate illite:smectite values, as it lies within the zone of mixing between the Fly and Purari rivers. Group 4 contains samples only from MV 51. MV 33 sediment dating to the Bolling-Allerød period is not statistically related to any of the four groups and is separated from them by a distance greater than 12.

3.6 Discussion

Clay mineralogy potentially tracks the sediment from the Fly and small mountainous rivers to assess temporary storage on the inner shelf, recycling of inner shelf sediment, as well as transport and deposition in Pandora Trough. Cores from the inner mid-shelf are not continuous records, as there are unconformities between units and facies on 20-kyr cyclicities that are identifiable by abrupt transitions in sediment cores and by package boundaries in seismic profiles (e.g., Harris et al., 1996; Slingerland et al., 2008; Wei et al., 2019). Illite:smectite ratios in inner mid-shelf cores display little variability within package boundaries and exhibit the largest changes with facies. Changes in clay mineralogy with 20-kyr cyclicities in the inner mid-shelf and PT may be caused by the variable response of rivers to eustasy and basin physiography.

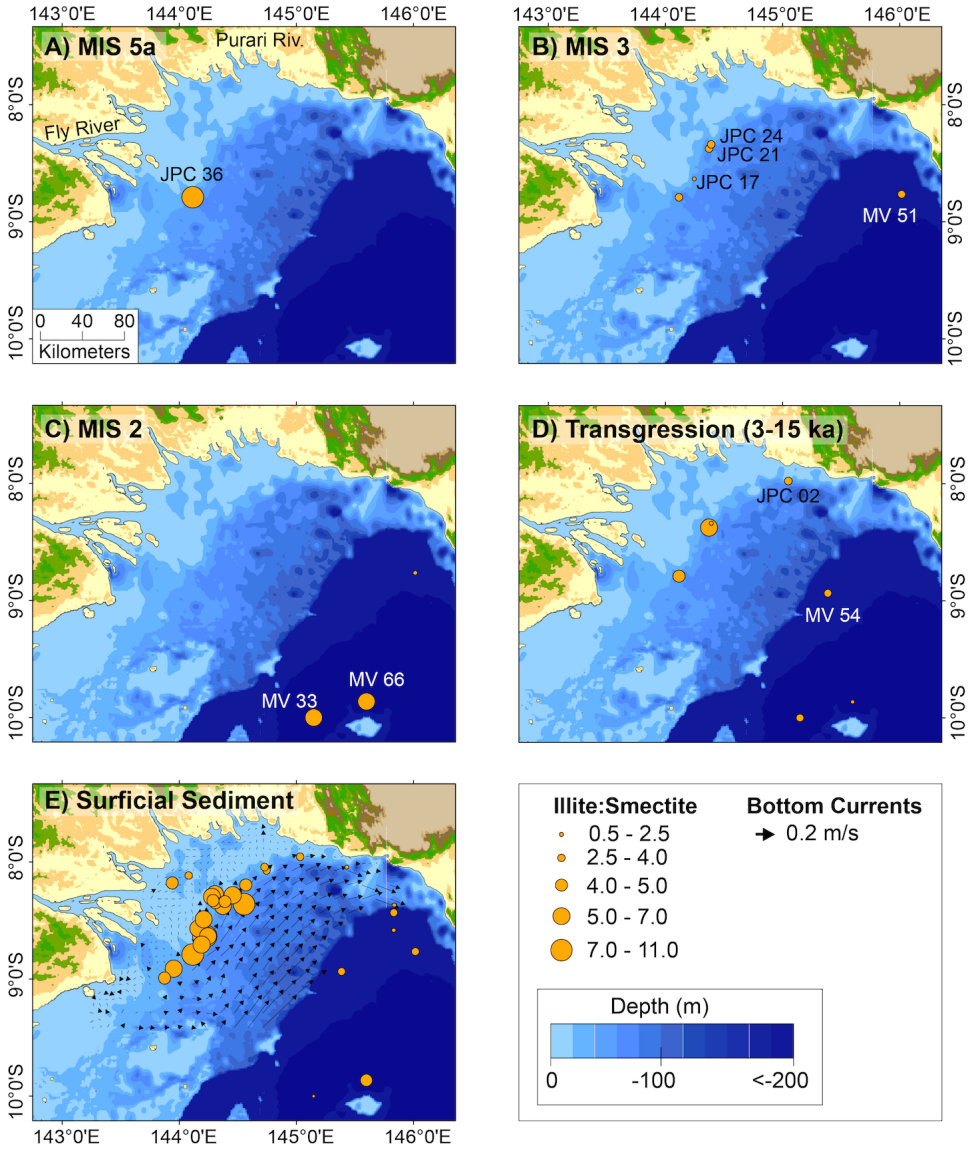

Figure 3.8: Average illite:smectite values are shown through space and time. Larger circles correspond to higher illite:smectite; legend is shown at bottom right. A) Sediment from the MIS 5a inner mid-shelf clinothem recovered in JPC 36 has high illite:smectite ∼10. B) MIS 3 inner mid-shelf clinothem sediment and sediment dating to MIS 3 in MV 51 have low illite:smectite ∼2. C) MVs 33 and 66 have high illite:smectite for MIS 2, whereas MV 51 has low illite:smectite. D) The post-glacial transgression is characterized by high illite:smectite in the inner mid-shelf clinothem and low illite:smectite in PT. E) Surficial sediment illite:smectite is juxtaposed with bottom currents during the Trade Wind season from Slingerland et al. (2008a). High illite:smectite persists proximal to the Fly River and decreases towards the Purari River.

3.6.1 Subsurface Illite:Smectite Ratios Reflect Oceanographic Transport Processes

Surficial sediment maps of illite:smectite reveal that samples located closest to the Fly River delta have high illite:smectite ratios (illite:smectite of inner mid-shelf JPC 54 ∼4.7), and samples located in the NE Gulf have lower ratios (illite:smectite of TC 38 ∼2.0; Figs. 4A and 4B). In between the two is a zone of mixing with intermediate illite:smectite ratios. The illite:smectite ratios have a generally linear trend with a low R^2 value (Fig. 3.4B), which is expected because mixing along oceanographic currents is not a linear process. These results are consistent with previous observations from suspended sediment from rivers measured by Salomons & Eagle (1990) as well as from surficial sediment samples measured by Harris et al., (1993), Slingerland et al., (2008a), and Howell et al., (2014; Fig. 3.4A). Such illite:smectite patterns are consistent with observed seasonal currents (Walsh et al., 2004) and strong bottom currents that advect sediment to the northeast GoP during the Trade wind season that are predicted by the Navy Coastal Ocean Model (Fig. 3.8E; Slingerland et al., 2008a; Slingerland et al., 2008b). Along-margin mineralogy results from this study, Slingerland et al. (2008), and Howell et al. (2014) suggest that sediment is likely temporarily stored on bathymetric highs during the quiescent monsoon season and advected to the northeast during the trade wind season (Walsh et al., 2004). The mixed assemblage on the shelf likely represents bottom currents advecting sediment to the northeast that build the Holocene clinothem obliquely (Fig. 3.8E; Slingerland et al., 2008a; Slingerland et al., 2008b; Wei et al., 2019).

3.6.2 Downcore Changes Reflect Changes in River Sources

Downcore increases in smectite (4-5%), decreases in illite (11-13%), and increases in chlorite (2-11%) on the inner mid-shelf are attributed to facies changes. Cores from the inner mid-shelf clinothem do not appear to show downfacies gradients and this relative uniformity

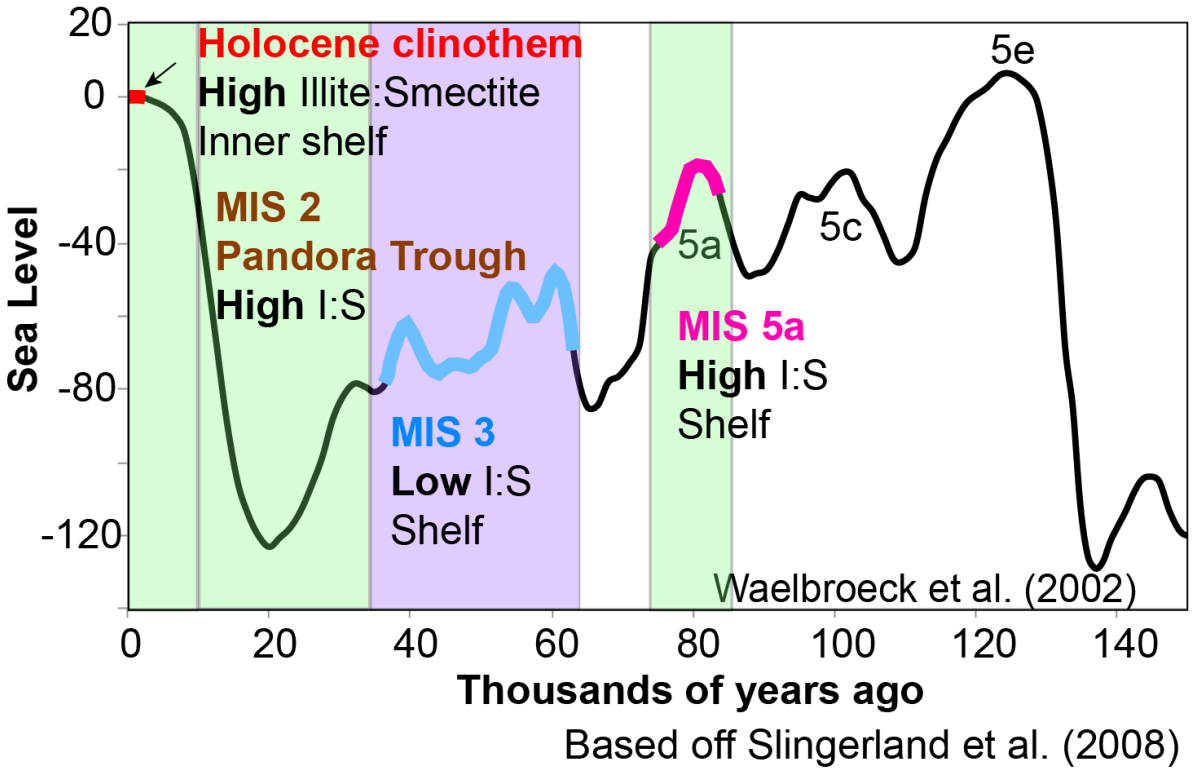

Figure 3.9: Intervals of low and high illite:smectite are plotted on the sea-level curve for the past 120 kyr (Waelbroeck et al., 2002). High Illite:Smectite (shown in green) is observed on the inner shelf during the Holocene, in Pandora Trough during MIS 2, and on the inner shelf during MIS 5a. Low illite:smectite (shown in purple) is observed on the inner shelf during MIS 3.

could reflect that the dominant control on illite:smectite ratios is sediment source and reworking of clinothem sediment by bottom currents or bioturbation. Alteration due to weathering and subaerial exposure appears to be minimal. Lower illite:smectite ratios during MIS 3 are likely not caused by short-term changes in paleoclimate (1000s to 10,000s of years), as changes in soil mineralogy caused by climatic changes require time scales of at least 1 million years (Thiry, 2000). As such, these changes likely reflect changes in source material. Changes in source material and sediment supply from rivers to the shelf can be preserved in sequences with 20 kyr cycities (e.g., Lobo & Ridente, 2014).

Intervals of high and low illite:smectite ratios are plotted with respect to time and the sea-level curve from Waelbroeck et al. (2002; Fig. 3.9) and are shown spatially while stepping through time in Fig. 3.8. High illite:smectite sediments are observed on the inner mid-shelf clinothem proximal to the Fly River during the Holocene and MIS 5a (Figs. 3.8 and 3.9). During the MIS 2 lowstand and in turbidite deposits, high illite:smectite ratios are observed offshore in Pandora Trough (Figs. 3.6, 3.8, and 3.9). Low illite:smectite signatures are observed proximal to the Purari River during the Holocene and throughout the entire inner mid-shelf clinothem during MIS 3 (Figs. 3.5B, 3.8, and 3.9).

In PT cores, a notable change in clay mineralogy is higher percent chlorite in MVs 33 and 54 during MIS 2 that decreases during the post-glacial transgression (Fig. 3.6). Upsection decreases in chlorite in these cores are accompanied by increases in illite (Fig. 3.6). Increases in chlorite have been attributed to physical weathering processes (Vital et al., 1999); as such, it is possible that cold climates and glacial processes during MIS 2 may have increased chlorite. Around 12.7 ka, increases in smectite at the expense of illite are observed in MV 33 (Fig. 3.6) and this mineralogical signature is separated from all other samples by the greatest distance on the dendrogram (Fig. 3.7). At similar sampling depths in MV 33, Septama & Bentley (2017) observed elevated K_2O and suggested that this may be caused by pumice fragments and volcanic ash. This explains the increase in smectite during this period in MV 33, as smectite can form by

alteration of volcanic ash (Varela et al., 2013).

3.6.3 Sources of Low Illite:Smectite During MIS 3

Clustering of downcore clay mineralogy suggests that MIS 3 sediment from JPCs 17, 21, and 24 are more compositionally similar to sediment proximal to the Purari River sampled in TC 38, as shown in the dendrogram in Fig. 3.7. This study proposes that the compositional shift in illite:smectite signatures observed in the MIS 3 deposit reflects many complex processes that favor the deposition of 20-kyr sequences in the GoP inner mid-shelf clinothem. Preservation of sequences with 20-kyr cyclicities is favored on margins with subsidence that creates ample accommodation, rivers with incised valleys that develop over sea-level cycles (e.g., Anderson et al., 2016), and variable sediment dispersal during different sea-level stages (e.g., Ridente et al., 2009; Lobo & Ridente, 2014). This study proposes that the low illite:smectite signature that is observed in the MIS 3 clinothem (Unit C) could be caused by decreased contribution of Fly River sediment to the inner mid-shelf clinothem at this time, which may have amplified the low illite:smectite Purari signature on the inner mid-shelf clinothem. Low illite:smectite signatures during MIS 3 contrasts with MIS 5a clinothem sediment that has high illite:smectite values similar to the Fly River sediments. Even though MIS 5a and MIS 3 were both times of relative highstands, MIS 3 sea-level was between 50-80 mbsl and MIS 5a level was 20 mbsl (Waelbroeck et al., 2002; Septama & Bentley, 2017; Fig. 3.9). The 30 m difference between these two relative highstands could have exposed different physiography that may have diverted Fly River sediment.

Three potential hypotheses may explain the low illite:smectite ratios observed in the MIS 3 inner mid-shelf clinothem. First, Fly River sediment could have bypassed the inner-midshelf clinothem and could have been transported through three incised valleys formed during the lowstand of MIS 4 or MIS 6 (Fig. 3.10). A complex interplay of basin and river properties could have created conditions favorable for Fly River sediment bypass through incised valleys, such as limited accommodation proximal to the Fly River and higher water discharge that favors incision

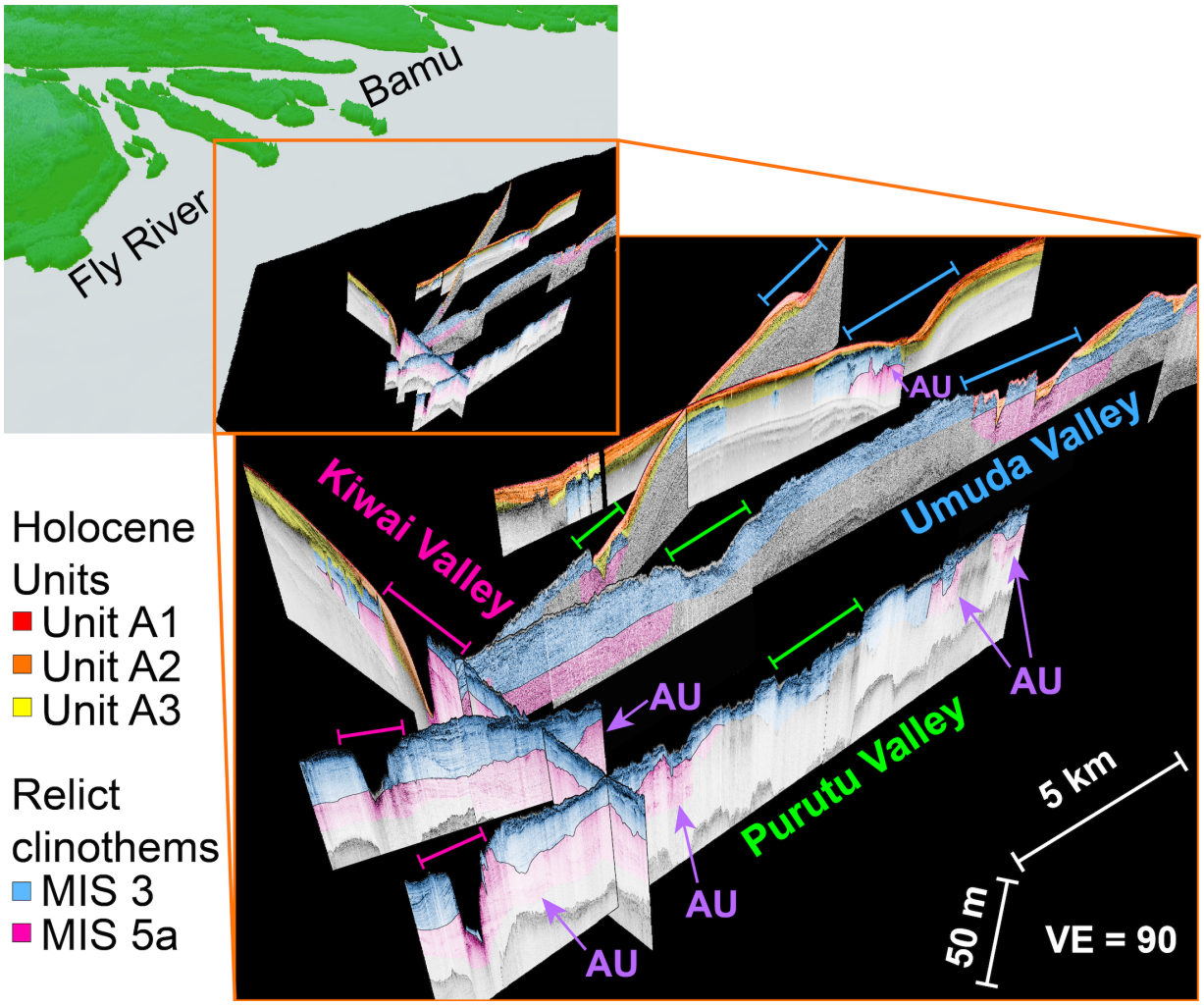

Figure 3.10: Seismic fence diagram offshore of the Fly River shows the Kiwai, Purutu, and Umuda valleys that were described by Crockett et al. (2008). Small inset in the upper left corner shows the location of the seismic fence diagram. These valleys possibly served as conduits that transported Fly River sediment downslope to Pandora Trough.

over deposition. Second, the relative highstand of MIS 3 could have caused aggradation in the large Fly River floodplain, with little sediment escaping to the inner shelf clinothem. In contrast, the small mountainous rivers may have sequestered less sediment and they could have continued to supply sediment to the inner mid-shelf. Lastly, Blake & Ollier (1969) hypothesized that the Fly River once flowed towards the southwest into Torres Strait and hence sediment with high illite:smectite signatures bypassed the inner mid-shelf.

Geomorphology of incised valleys offshore of the Fly River, depositional patterns during intermediate sea-level stages, and flume experiments that simulate canyon incision and bypass support the first hypothesis, that during MIS 3, Fly River sediment was funneled down incised valleys and bypassed the inner mid-shelf clinothem. Seismic profiles and multibeam bathymetry offshore of the Fly River delta reveal three incised valleys, the Kiwai, Umuda, and Purutu, from southwest to northeast (Fig. 3.10; Crockett et al., 2008). The Kiwai valley is the narrowest and deepest valley that generally remains underfilled, whereas Umuda and Purutu valleys are shallower, broader, and are partially infilled by Holocene sediment (Fig. 3.10; Crockett et al., 2008). Seismic profiles reveal that the valleys incise the MIS 5a and MIS 3 clinothems, with the greatest incision in the MIS 3 clinothem. The timing of initial formation of the Kiwai, Umuda, and Purutu valleys remain uncertain, as incised valleys may have been formed during the MIS 4 relative lowstand and were likely overprinted by the MIS 2 lowstand (Crockett et al., 2008; Slingerland et al., 2008). Nevertheless, angular unconformities between the MIS 5a clinothem and the MIS 3 clinothem are observed in the seismic fence diagram between the valleys (AU in Fig. 3.9). Additionally, angular unconformities between these two relict clinothems are also observed in Line 1, which is also located offshore of the Fly River (AU in Line 1, Fig. 3.3). Thus, preserved angular unconformities adjacent to the valleys suggest widespread erosion of MIS 5a deposits offshore of the Fly River during the MIS 4 lowstand.

Even though these valleys had the most direct connection to the deep sea during the maximum lowstand of MIS 2, stratigraphic evidence from PT suggests that these valleys acted

to route sediment through intermediate lowstands between MIS 2-1, MIS 4, and MIS 3. These valleys appear to have served as conduits for Fly River sediment during the MIS 2 maximum lowstand, as evidenced by PT MVs 33 and 66 that exhibit high accumulation rates, numerous sand layers, and high illite:smectite ratios (Jorry et al., 2008; Septama et al., 2016). In addition to high terrigenous influx during MIS 2, sedimentation rates in MVs 33 and 66 may also be high due to confinement by a narrow intra-slope basin (Septama et al., 2016). Observations from this study and previous studies suggest that routing of Fly River sediment to Pandora Trough is not limited to just lowstands but may have continued until as recently as 8 ka (Fig. 3.6B; Jorry et al., 2008; Septama et al., 2016). This finding is significant because sea-level at 8 ka was higher than sea-level during MIS 3 (Waelbroeck et al., 2002), suggesting that if Fly River sediment bypassed the inner shelf at 8 ka, it is plausible that Fly River sediment could bypass the inner shelf during MIS 3. Not only is this study's hypothesis supported by sea-level and our provenance studies, but it is also supported by studies on the Adriatic margin that observe poor development of MIS 3 deposits on the inner and outer shelves (Ridente et al., 2009; Lobo & Ridente, 2014).

The intermediate sea-level during MIS 3 may have reduced accommodation on margins worldwide and affected sediment-dispersal, as evidenced in the Adriatic margin (e.g., Ridente et al., 2009; Lobo & Ridente, 2014). The Adriatic margin draws parallels with the GoP in that it has energetic oceanographic circulation that controls sediment thickness (Ridente et al., 2009). In the Adriatic margin, the MIS 3 interstadial unit represents a departure from the general pattern of progradation (Ridente et al., 2009; Lobo & Ridente, 2014). Throughout the Adriatic margin, the MIS 3 deposit is poorly developed on the shelf and outer slope or is amalgamated with MIS 4 and MIS 2 deposits (Ridente et al., 2009; Lobo & Ridente, 2014). The authors hypothesize that MIS 3 deposits are poorly developed on this margin because the relative highstand was not able to significantly flood the shelf and establish shore-parallel dispersal patterns, which are important for the development of elongate clinoforms on this margin (Ridente et al., 2009; Lobo & Ridente, 2014).

Similar changes in accommodation and sediment dispersal may have occurred in the GoP, where paleo water depths affect whether sediment is dispersed by oceanographic currents or whether it bypasses through incised valleys. Foreland basin tectonics engender ongoing differential subsidence in the GoP and as a result, the GoP inner mid-shelf is narrowest in the southwest proximal to the Fly River and widest and deepest in the northeast proximal to the Purari River (Pigram et al., 1989; Pigram & Symonds, 1991; Harris et al., 1996; Slingerland et al., 2008; Wei et al., 2019). During MIS 3, sea-level is estimated to have ranged from 50-80 mbsl (Fig. 3.7; Waelbroeck et al., 2002; Slingerland et al., 2008; Septama & Bentley, 2017) and at this time the northeast GoP may have had more accommodation (see 50 and 80 m contours in Fig. 3.4). As the heads of the Kiwai, Purutu, and Umuda valleys offshore of the Fly River are located at depths between 50-70 mbsl (Crockett et al., 2008), it is possible that during MIS 3, the heads of these submarine valleys were subaerially exposed or in shallow water and the Fly River discharge may have been routed directly to the heads of the submarine valleys (Fig. 3.4). In contrast, enough of the shelf is flooded during the present sea-level highstand to establish strong oceanographic circulation, similar to the Adriatic Margin (Slingerland et al., 2008; Ridente et al., 2009). During the present sea-level highstand, sediment accumulation rates in the incised valleys have a maximum of 2 cm a^{-1} since the main modes of canyon infilling are hemipelagic sedimentation, gravity flows, and progradation of inner mid-shelf clinothems into valley heads (Crockett et al., 2008). Instead of traversing down the incised valleys, much of the Fly River sediment is advected by energetic bottom currents during the Trade Wind season to the northeast (Walsh et al., 2004; Slingerland et al., 2008a; Slingerland et al., 2008b). Thus, interactions between shelf physiography and sea-level exert controls on the exposure of the incised valleys and the advecting power of oceanographic currents.

Shelf physiography may have played the most important control on the incision of valleys offshore of the Fly River. Additionally, hydrologic factors could influence the development of incised valleys offshore of the Fly River. Larger rivers such as the Fly River may preferentially

incise into margins if their water discharge (Q_w) is greater than their sediment discharge (Q_s), as modeled by global flume experiments that simulated the influence of water discharge on canyon incision over glacio-eustatic sea-level cycles (Bijkerk et al., 2016). Although these experiments were not designed for the GoP, the importance of Qw:Qs on river incision has global implications and can be applied to the GoP. Higher Q_w:Q_s resulted in less concave profiles and formation of incised valleys (Bijkerk et al., 2016), and in the GoP, the Fly River has Q_w:Q_s values of ∼563 compared to the Purari Q_w:Q_s values of ∼322 (Wolanski et al., 1995; Slingerland et al., 2008). After valley incision, nearly all discharge is funneled through the incised valley and erosion migrates upstream until the following sea-level highstand (Bijkerk et al., 2016). This may explain why three prominent incised valleys, the Kiwai, Umuda, and Purutu valleys, are observed offshore of the Fly River delta (Crockett et al., 2008) and not offshore of the Bamu, Turama, Kikori, and Purari rivers.

Another potential explanation for diminished contribution of the Fly River to the MIS 3 inner mid-shelf clinothem is that during the relative highstand, Fly River sediment could have aggraded in the floodplain instead of accumulating in the inner shelf clinothem. This explanation has some validity since the modern-day Fly River floodplain stores about 40% of its sediment in the depositional web through overbank deposition, levee breach, or tie channels (Day et al., 2008). Despite the efficiency of the Fly River's modern-day floodplain at trapping sediment, high illite:smectite sediment sourced from the Fly River is still preserved in Holocene inner mid-shelf clinothem deposits (Units A1-A3). The Fly River floodplain likely aggraded sediment during MIS 3; however, aggradation in the floodplain likely was not sufficient enough to prevent deposition on the inner shelf. Furthermore, aggradation in the Fly River floodplain during MIS 3 likely did not exceed aggradation during the formation of the Holocene clinothem. For these reasons, aggradation in the Fly River floodplain is not likely the cause for decreasing illite:smectite in the inner mid-shelf clinothem during MIS 3.

The third hypothesis proposed by Blake & Ollier (1969) suggests that the Fly River

previously flowed southward and deposited into Torres Strait. The current course of the lower Fly River is postulated to have existed only as far back as 36 ka, since tectonic forcing caused a rearrangement of the lower reaches Blake & Ollier (1969). Nevertheless, geomorphic evidence of tectonic movement in the catchment and MIS 3 sediment deposits from the Fly River in Torres Strait or the Gulf of Carpentaria (GoC) are lacking (Dietrich et al., 1999; Reeves et al., 2008). Torgersen et al. (1988) postulated that prior to 36 ka, the Fly River flowed south into the Gulf of Carpentaria, since brackish fauna in the GoC dating to MIS 3 were interpreted to originate from Fly River dilution of marine conditions. Long cores from six locations in the GoC and analyzed by Reeves et al. (2008), however, refute this evidence. Reeves et al. (2008) instead propose that dilution to brackish conditions in the GoC could have occurred by wetter conditions during MIS 3. In the estuarine facies recovered from this time period, there is no evidence, such as PNG pollen, to support inflow of the Fly River to the GoC (Reeves et al., 2008). High illite:smectite signatures from the GoP inner mid-shelf MIS 5a clinothem in JPC 36 suggest that Fly River sediment likely deposited in the Gulf of Papua during the MIS 5a highstand. With this consideration, any avulsion of the Fly River to the GoC would have occurred only from MIS 4 to MIS 2.

Of the three hypotheses, the preferred explanation is the Fly River sediment bypassed the inner shelf during MIS 3 time based on the clay mineralogy, geomorphological evidence of canyon incision offshore of the Fly River (Crockett et al., 2008), flume experiments (Bijkerk et al., 2016), and condensed deposits on other margins (Ridente et al., 2009). Below is a conceptual model of the response of the Fly and Purari Rivers and the evolution of the inner shelf clinothem and Pandora Trough from MIS 5a to the present.

3.6.4 Implications for Source-to-Sink Sediment Routing

Sediment routing through the last sea-level cycle appears to be highly dependent on shelf accommodation, which in turn affected connections between rivers and the incised valley heads as well as the establishment of oceanographic currents. In this study's conceptual model, it is

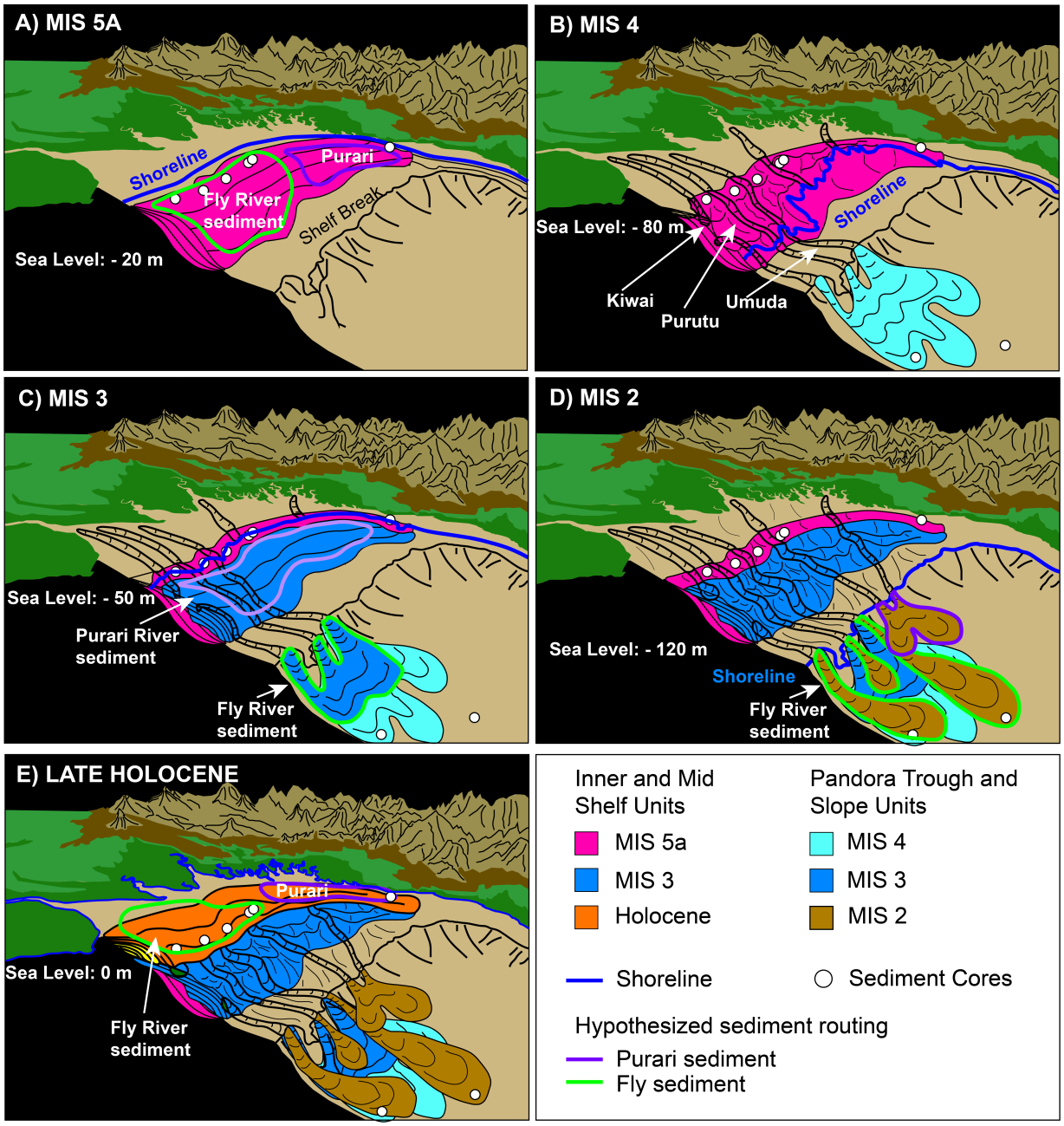

Figure 3.11: Conceptual model for the response of the Fly and Purari rivers during sea-level cycles from MIS 5a to the Holocene. A) During highstand conditions of MIS 5a, distribution of Fly and Purari sediment is on the inner shelf sediment similar to today. B) During the MIS 4 lowstand, there is incision of the three valleys offshore the Fly River. Fly River sediment bypasses to Pandora Trough. C) During MIS 3, Fly River sediment possibly bypassed the inner shelf through the incised valleys to Pandora Trough. Purari River sediment may have deposited on the inner shelf. D) During the MIS 2 lowstand, the inner shelf clinothem was incised and eroded. E) During Holocene highstand conditions, Fly River sediment is deposited in the SW inner shelf and Purari sediment is deposited in the NE inner shelf.

hypothesized that illite:smectite ratios on the inner mid-shelf clinothem during MIS 5a were similar to present-day conditions because these time periods were both highstands in sea-level (Figs. 3.9, 3.11A). Higher sea-level conditions may have allowed for the establishment of along-margin currents during MIS 5a; however, this hypothesis needs to be tested with oceanographic models. When sea-level fell to -80 m during MIS 4, the sediment eroded from river floodplains and inner mid-shelf MIS 5a clinothem (Unit D) was discharged to the outer shelf, slope, or possibly Pandora Trough (Fig. 3.11B). At this sea-level stage, it is possible that incised valley heads were directly connected to or separated by short distances from the Fly River mouth, based on the -80 m depth contour in Fig. 3.4. As a result of this short connection, Fly River sediment was likely routed through the incised valleys to PT during MIS 4. As the -50 m contour (in Fig. 3.4) intercepts the Kiwai, Purutu, and Umuda valleys, a connection between the Fly River and the incised valleys may have been maintained through MIS 3. Thus, sediment routing from the Fly River to PT may have persisted through MIS 3 (Fig. 3.11C). Bypassed Fly River sediment may have contributed to decreased illite:smectite ratios in the inner mid-shelf clinothem, as the low illite:smectite composition is consistent with the Purari River signature (Fig. 3.8B). Less extensive flooding of the shelf during MIS 3 may have inhibited the establishment of energetic oceanographic currents. In this low energy environment, the three-dimensional clinothem built by Purari River sediment may have prograded to the south by diffusion (sensu Driscoll & Karner, 1999) with the thickest MIS 3 deposits in the central and northeast GoP and thinner MIS 3 deposits in the southwest GoP. Diffusive transport of Purari sediment to the southwest may have allowed some low illite:smectite sediment to bypass to PT through incised valleys; however, this signal was likely drowned out by higher volumes of Fly River sediment traversing down incised valleys. Oceanographic models in future studies could test this hypothesis.

Lowstand conditions of 120 m below present sea-level during MIS 2 (Waelbroeck et al., 2002) incised and eroded the MIS 3 inner mid-shelf clinothem (Unit C) and deposited Fly River sediment with high illite:smectite in Pandora Trough, as evidenced in MVs 33 and 66 (Fig. 3.11D).

MV 66 sediment during MIS 2 lowstand was most likely recycled, as indicated by the high illite content and geochemical composition similar to shelf samples proximal to the Fly River. After MIS 2, sea-level rose in a nonlinear step like fashion (Waelbroeck et al., 2002). Transgressive deposits (Units B1 and B2) infilled incised valleys in the MIS 3 clinothem (Unit C), filling it with sand that was interpreted to have been reworked from the beach and shelf by Harris et al. (1996). The most recent deposits from the past 3.8 kyr are the late-Holocene clinothem, consisting of a prograding Unit A3 and aggrading Units A2 and A1. In the southest Gulf, the Holocene clinothem is composed mostly of sediment from the Fly River with high illite:smectite, whereas in the northeast Gulf, the Holocene clinothem has mineralogy characterized by low illite:smectite (Fig. 3.11E). During highstand conditions, river deposits are largely sequestered on the shelf with low accumulation rates in Pandora Trough (Walsh & Nittrouer, 2003; Muhammad et al., 2008). Thus, sequences in the inner mid-shelf clinothem are dominated by 20-kyr cyclicities that are likely preserved due to the interplay of shelf physiography created by foreland basin subsidence, the contrasting dynamics of large and small rivers throughout a sea-level cycle, and the incisional power of rivers.

Varying responses of small and large rivers to sea-level changes has been investigated in other margins such in the Gulf of Mexico (Anderson et al., 2016) and the South Yellow Sea (Xu et al., 2012; Hu et al., 2018). Large rivers draining into the Gulf of Mexico, such as the Brazos, Colorado, and Rio Grande rivers, fill accommodation created during lowstands differently than smaller rivers (Anderson et al., 2016). Anderson et al. (2016) suggested that stream power and the physiography of the shelf exert influences on the duration of a river's incision and morphology of the river's incised valley. Large rivers tended to overfill incised valleys during the sea-level transgression and highstand (Anderson et al., 2016). During the late Holocene, large rivers could no longer fill their floodplains, and as a result, sediment from the Brazos, Colorado, and Missisippi rivers supplied sediment to the Texas Mud Blanket starting 3.5 ka (Anderson et al., 2016). In contrast, small rivers tended to under-fill their valleys during

the early lowstand, sea-level transgression, and highstand (Anderson et al., 2016). In the South Yellow Sea, sediment discharged from the Yellow River is estimated to constitute 38% of the total sediment volume in the South Yellow Sea Holocene clinothem (Xu et al., 2012; Hu et al., 2018). The small rivers, the Min and Ou rivers, contribute sediment loads as high as 10 Mt/yr; however, this sediment appears to be trapped in the river deltas (Xu et al., 2012). These studies in the Gulf of Mexico and the Yellow Sea describe margins where sediment from small rivers are trapped within underfilled floodplains and large rivers build out Holocene deposits. Rivers in the Gulf of Mexico behave differently than those in the GoP to sea-level cycles; these behavioral differences could be attributed to the gradient and physiography of the Gulf of Mexico shelf (Anderson et al., 2016). In the GoP, inherited foreland basin physiography (Harris et al., 1996; Slingerland et al., 2008; Wei et al., 2019) and incisional power of the Fly River may contribute to bypass of Fly River sediment and sedimentation dynamics of the inner mid-shelf clinothem.

This suggests that the ability of rivers to incise valleys may contribute to the varying responses of small and large rivers to sea-level changes. Q_w:Q_s and shelf physiography (i.e., limited accommodation proximal to the Fly River) may exert influences on the Fly River's well-developed incised valleys and the routing of its sediment during intermediate sea-levels. The response of GoP rivers on timescales ranging from 7-29 kyr may also contribute to 20-kyr cyclicities along the inner mid-shelf clinothem sequences and compositional shifts. Thus, this study agrees with the hypotheses of Lobo & Ridente (2014) that 20-kyr cyclicities in shelf deposits are controlled by i) shelf physiography during highstands and intermediate stages in sea-level (Ridente et al., 2009) and ii) the incisional dynamics of rivers (e.g., Banfield & Anderson, 2004; Anderson et al., 2016).

3.7 Conclusion

This study tracks the dispersal of sediment from the Fly River, which has suspended sediment with high illite:smectite, and from the Purari River, which has low illite:smectite. Down-core changes in illite:smectite suggest that sediment source of the Gulf of Papua inner mid-shelf clinothem may have shifted from MIS 5a to Present in cycles of 20 kyr. The main control on the routing of Fly River sediment to the inner mid-shelf or to Pandora Trough is shelf physiography. Shelf physiography is affected by foreland basin tectonics that cause differential subsidence, with less accommodation in the southwest GoP and more accommodation in the northeast GoP (Pigram et al., 1989; Pigram & Symonds, 1991; Wei et al., 2019). The presence of three incised valleys offshore of the Fly River (Crockett et al., 2008) could be attributed to narrowing of the shelf in the southwest GoP or higher water:sediment discharge that may favor incision over deposition. Flooding of varying portions of the shelf during sea-level highstands and intermediate highstands may allow or inhibit the connections of the Fly River to incised valleys.

During the present-day and MIS 5a highstands, sediment from the inner mid-shelf clinothem has high illite:smectite ratios. Present-day sediment transport in the GoP is characterized by energetic along-margin currents that advect Fly River sediment to the northeast (Walsh et al., 2004; Slingerland et al., 2008) and it is possible that more shelf flooding during maximum highstands allows for the establishment of these currents. Highstand conditions during the present and MIS 5a drowned incised valleys and inhibited connections between valley heads and the Fly River. The MIS 3 intermediate highstand had paleo-depths of 50-80 mbsl (Waelbroeck et al., 2002; Septama & Bentley, 2017) and relict clinothem deposits dating to MIS 3 are characterized by low illite:smectite, or a Purari River signature. Less of the shelf was flooded during this intermediate highstand, and as a result, a connection between the Fly River and incised valleys may have been maintained. This study proposes that during MIS 3, such a connection allowed Fly River sediment to bypass the inner mid-shelf and deposit sediment in the deeper

Pandora Trough. During MIS 3, the inner mid-shelf clinothem may be largely sourced from the Purari River with low illite:smectite signatures. It is possible that oceanographic currents were not as energetic during MIS 3, and such conditions may have allowed the Purari River to build a three-dimensional clinothem through along-margin diffusion. The different response of large flood plain rivers versus small mountainous rivers throughout sea-level cycles has important implications world-wide for sediment yield, routing, as well as timing and location of deposition. Previous studies on other margins have also documented varying responses of small and large rivers to sea-level changes in the Gulf of Mexico (Anderson et al., 2016) and the South Yellow Sea (Xu et al., 2012; Hu et al., 2018). In these studies, shelf physiography plays a major role in controlling the behavior of rivers (Anderson et al., 2016; Xu et al., 2012). This study agrees with the findings of Lobo & Ridente (2014) that the 20-kyr cyclicities observed in the GoP are influenced by local basin factors, such as subsidence that preserves inner mid-shelf deposits, and variable incision of rivers throughout a sea-level cycle.

3.8 Acknowledgements

This work has been accepted for publication as **Wei, E.A. and Driscoll, N.W. Clay Mineralogy of Gulf of Papua Shelf and Pandora Trough Deposits Constrains Sediment Source and Routing During the Last Sea-Level Cycle,** ***Sedimentology***. The dissertation author was the primary investigator and author of this material. This research was funded by the National Science Foundation awards 0305699, 0305779, and 0305607 under the MARGINS Source to Sink program. Special thanks to the shipboard scientists and crew of the R/V Melville as their efforts allow scientists access to the sea. We also thank the Oregon State University Marine Sediment Sampling Group for core acquisition. Comments from J.P. Walsh, Erlangga Septama, and an anonymous reviewer greatly improved the manuscript. Rudy Slingerland, John Milliman, Miriam Kastner, James Day, Robert Rex, and Brian Oller provided helpful discussions that improved

the quality of the manuscript. Heather Webb and Joan Kimbrough at San Diego State University assisted us with running X-Ray Diffractometer. Larry Peterson provided assistance sampling Pandora Trough cores. Rachel Marcuson and Ana Martini aided in sampling benthic foraminifera for radiocarbon dating.

Chapter 4

Post-glacial stratigraphy offshore of the Oceano Dunes, Central California

4.1 Abstract

High-resolution CHIRP seismic, multibeam bathymetry and backscatter, and surficial sediment grabs were acquired to reconstruct post-glacial sediment dispersal offshore of the Oceano Dunes and the Santa Maria Dune Complex, California. The study area is located in a basin bounded by uplift to the south and convergence to the north. Uplift of the San Luis block to the north influences the depth of the transgressive surface and leads to deposition away from uplifted terrain. In the cross-shore direction, a change in slope of the transgressive surface at water depths of 85-90 m is interpreted as a shoreline cutoff. Seaward of the shoreline cutoff is a depocenter of postglacial sediment. Volumetric estimates of the healing-phase wedge are much higher than the most recent post-glacial sediment packages and a reduction in terrigenous sediment supply could be caused by El Niño climatic conditions. Shoaling of the transgressive surface in the northern survey area may cause sediment in this area to be preferentially reworked, causing subsequent sediment bypass to the central survey area. Extensive sediment reworking

also prevails in the southern survey area, where wind and wave energy are not in the lee of the San Luis headlands. Reworking of recent sediment in the northern and southern survey areas is supported by truncation of reflectors within recent post-glacial sediment units and surficial mineralogy. In the northern survey area, terrestrial input appears to be low with the bulk of the surficial sediment being composed of well-sorted shell and sand dollar fragments. The central survey area has the highest abundance of lithics and the southern survey area is dominated by well-sorted frosted quartz. Two samples at depths of 18 and 20 m in the southern survey area are anomalously coarse and may be relict sediment that has been reworked by wave orbitals. Thus, the largest controls on sediment depocenters in this region are tectonically-controlled morphology, preferential reworking of sediment in areas with shoaling bathymetry, and climate. This study has implications for the timing and formation of the Santa Maria Dune Complex as well as regional sediment supply to the dunes.

4.2 Introduction

Relative sea-level and sediment supply are considered by classic sequence stratigraphy studies to be the dominant controls on the geometry of continental shelf deposits (e.g., Mitchum Jr et al., 1977; Vail et al., 1977; Christie-Blick & Driscoll, 1995). Of the components that affect relative sea-level, eustasy is often considered the main driver that can be amplified or diminished by tectonic uplift or subsidence (e.g., Posamentier & Vail, 1988). This assumption is valid in settings where uplift or subsidence acts parallel to eustatic sea-level changes. Nevertheless, in active settings where deformation is at high angles to the margin, tectonic deformation can play a large role in shelf geometry (e.g., Le Dantec et al., 2010; Hogarth et al., 2012; Klotsko et al., 2015). In this study, CHIRP seismic profiles collected offshore of the Oceano Dunes constrain the location and relative rates of uplift of the San Luis Block. Such block uplift exerts strong influences on past and present depocenters and sediment dispersal. Defining a process-oriented

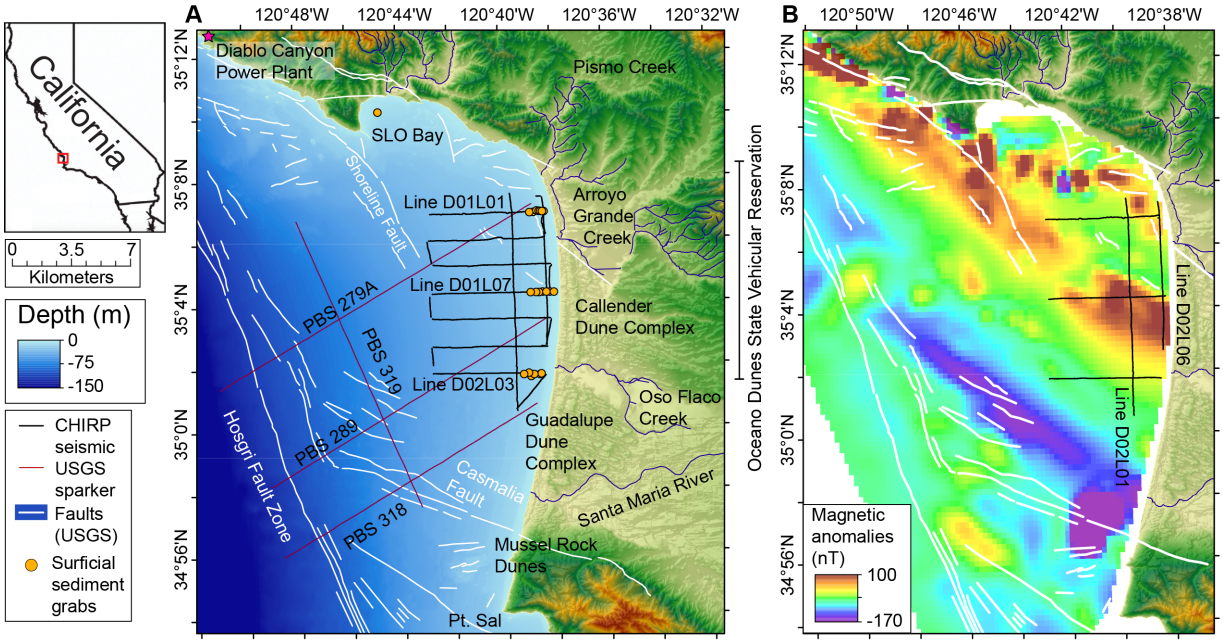

Figure 4.1: A) The seismic study area is located offshore of the Oceano Dunes State Vehicular Reservation. The location of the map area relative to the California coast is shown by the black box in the inset in the upper left corner. Black lines show the location of the CHIRP seismic profiles and red lines show the location of USGS single-channel sparker seismic lines. Yellow circles indicate the location of surficial sediment grabs. White lines show the location of the offshore Hosgri Fault Zone from Johnson & Watt (2012) and the USGS faults database (2010). The location of the Diablo Canyon Power Plant is indicated by a pink star. B) Faults and the CHIRP seismic survey are shown relative to magnetic anomaly data from Sliter et al. (2009), with warm colors showing positive anomalies and cool colors showing negative anomalies.

framework for marine deposits offshore of the Oceano Dunes is important to understand their sustainability in the wake of future climate change and sea-level rise.

The Oceano Dunes State Vehicular Reservation Area (ODSVRA) lies within the Callender Dune Complex and is one of the only coastal regions that allow vehicles to drive on the beach and dunes. Anthropogenic impacts on sediment dispersal are likely high in this reserve, as this area receives between 1.5-2 million visitors annually and 1,531 acres of the park allow access from street-legal and off-highway vehicles (TRA Environmental Sciences Inc, 2016). Within the past few years, there has been increasing concern about reducing emissions of PM_{10} particulates $<$10 μm in diameter and dust that potentially pose hazards to human health. The Callender Dune Complex is part of a greater Santa Maria Dune Complex (SMDC) that also contains the

Guadalupe and Mussel Rock Dune Complexes (Fig. 4.1a) that are protected from driving. The SMDC is one of the largest coastal dune landscapes in North America and serves as a U.S. Fish and Wildlife Service-designated critical habitat for the western snowy plover (*Charadrius nivosus nivosus*; federally listed as threatened), the California least tern, and other coastal birds (TRA Environmental Sciences Inc, 2016). Despite many studies on the timing of dune formation (e.g., Orme & Tchakerian, 1986; Orme, 1992; Peterson et al., 2018) and the processes that act upon them (e.g., Barrineau et al., 2012; Gillies & Etyemezian, 2014; Etyemezian et al., 2015; Crisp, 2017), no study has characterized the environment offshore of the dunes.

Coastal dune sediment in the SDMC is largely derived from beach sands (Patsch and Griggs, 2006) that are transported landward by prevailing winds from the northwest that are capable of exceeding the fluid threshold of 6 m s^{-1} (Gillies & Etyemezian, 2014) necessary to mobilize sediment (Bagnold, 1941). In turn, beaches along the coastal dunes are supplied by longshore transport that moves sand predominantly from north to south and fluvial discharge from the Santa Maria River, Pismo Creek, and the smaller Oso Flaco Creek (Patsch & Griggs, 2008; Fig. 4.1). The SDMC dunes are at risk and may be decreasing in areal extent due to decreased sediment supply from the dammed Santa Maria River (Crisp, 2017) and high coastal erosion rates (Hapke et al., 2006). Knowledge on the sedimentation history of post-glacial offshore deposits could yield sediment budgets, which are important inputs for future studies on anthropogenic impacts. Furthermore, understanding these deposits is important for illuminating the relationship between the relative sea level history of the California coast and sediment supply, which are both crucial for the development of dunes (Orme, 1992).

Past and ongoing tectonic deformation within the Santa Maria Basin creates and destroys available accommodation for sediment discharged from the Santa Maria River and smaller creeks. Seismic profiles collected as part of this study places constraints on recent uplift north of the Santa Maria Basin. Though onshore studies have calculated uplift rates by dating terraces (Lettis & Hanson, 1992; Lettis et al., 2004), recently-offset stratigraphic surfaces should have a

higher preservation potential in marine environments (Pacific Gas and Electric Company, 2013). Characterizing regional deformation is important, as the Diablo Canyon Nuclear Power Plant is in close proximity to the Hosgri and Shoreline Fault Zones (Fig. 4.1; Pacific Gas and Electric Company, 1988; Pacific Gas and Electric Company, 2013).

The SDMC has persisted since at least 2.6 Ma through multiple sea-level cycles and periods of tectonic deformation (McCrory et al., 1995). Such sea-level cycles exert influences on the geometry of continental shelf deposits and this study will focus on sediment deposited since the sea-level transgression postdating the Last Glacial Maximum (LGM). Lower sea-levels during the LGM subaerially exposed the continental shelf, and as a result, the shelf was incised and eroded by channelized flows (Posamentier et al., 1992). When sea-level rose during the subsequent transgression, accommodation could potentially outpace sediment supply and as a result, aggradationally stacking deposits may have developed (Vail et al., 1977; Van Wagoner et al., 1990; Christie-Blick & Driscoll, 1995). Local depressions formed by channelization may be preferentially infilled during the early stages of sea-level rise compared to adjacent zones (Thomas & Anderson, 1994; Zaitlin et al., 1994; Cattaneo et al., 2007). Sea-level rose in a non-linear step-like fashion with multiple periods of rapid rises, such as Meltwater Pulses (MWP) 1A and 1B that were punctuated by intervals with lower rates of sea-level rise (Fairbanks, 1989; Fairbanks et al., 1992; Bard et al., 1990). As sea-level rose, shoreface sediment was subject to wave-based erosion that may have been remobilized and transported landward and basinward (Christie-Blick & Driscoll, 1995; Posamentier & Allen, 1993). During periods with lower rates of sea-level rise, wave-based erosion may have acted upon certain water depths for an extended period of time and potentially formed abrasion platforms (Posamentier & Allen, 1993; Klotsko et al., 2015). The stacking patterns and distribution of post-glacial deposits that formed after the LGM appear to have been influenced by changes in the rate of relative sea-level rise and sediment supply (Posamentier & Allen, 1993; Cattaneo & Steel, 2003; Klotsko et al., 2015).

The goal of this study is to quantify post-glacial sediment volumes and characterize

surficial sediment in order to understand recent oceanographic and tectonic processes. Results from this dataset record interactions between Holocene sea level changes, block uplift, and climate that shape the shelf. This study hypothesizes that post-glacial sediment cover on the shelf offshore of the Santa-Maria Dunes is thin due to four main processes: i) regional deformation preferentially uplifts deposits in the Northern survey area and creates large-scale folding along the margin, ii) early Holocene units thicken to the south away from the northern shoals, iii) reworking of shelf sediment by wave orbitals occurs preferentially in areas with shoaling topography in the north and areas in the south not shielded by headlands, and iv) dispersal of sediment sourced from the Santa Maria River may be influenced by El Niño climatic conditions.

4.3 Geologic Background

4.3.1 Previous studies on basin architecture and stratigraphy

The ODSVRA and SDMC lie within a basin shaped by multiple tectonic events since the Miocene (McCrory et al., 1995). Based on backstripping analysis, the basin is marked by four major tectonic events: i) a period of volcanism, normal faulting, and rapid tectonic subsidence around 18-16 Ma; ii) an interval of slow subsidence from 16-6 Ma; iii) a period of shortening and bathymetric inversion from 6-4 Ma characterized by slow uplift; iv) a period of intense shortening that is ongoing today (McCrory et al., 1995). Recent uplift and subsidence patterns are a function of crustal shortening in the Los Osos domain that is characterized by northwest-trending reverse faults that divide the region into several blocks (Lettis et al., 2004). The entire area shown in Figure 4.1 lies within the Los Osos domain. Block uplift accommodated by reverse faults has formed the San Luis Range without deforming it and has uplifted marine terraces formed at 120 and 80 ka (Lettis & Hanson, 1992). Subsidence has produced the Santa Maria valley (Lettis & Hanson, 1992). Northwest-trending hills and valleys can be observed in the magnetic anomaly data from the USGS (Fig. 4.1b; Sliter et al., 2009). Abrupt changes in magnetic anomaly data can

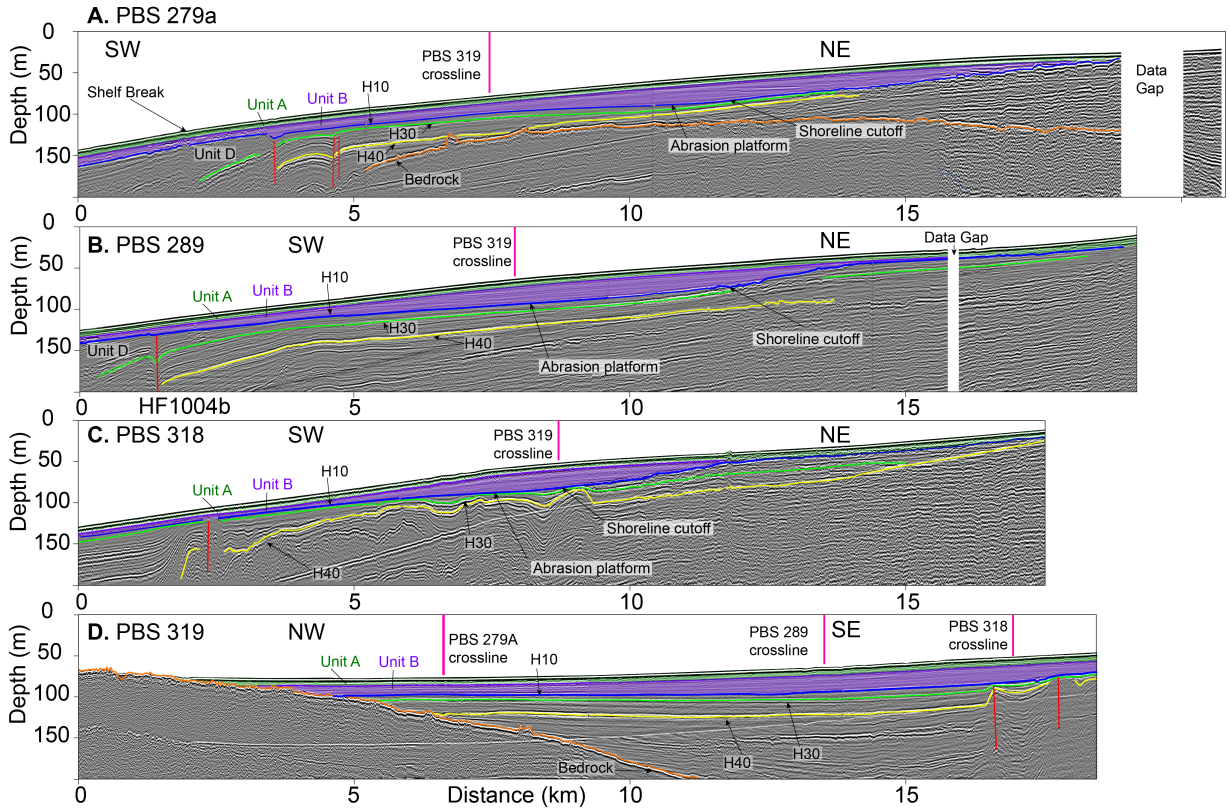

Figure 4.2: Reprocessed USGS single-channel sparker seismic dip profiles (A-C) and one strike profile (D). Interpretations of 3 regional unconformities, H40, H30, and H10 are from Pacific Gas and Electric Company (2013). Post-glacial sediment Units A, B, and C are labeled by color. Some horizons at the southwestern end of dip profiles are offset by strands of the Hosgri Fault Zone, shown by vertical red lines. Fault locations are from interpretations from Pacific Gas and Electric Company (2013). Vertical pink lines indicate crossline locations. Profile locations are shown on Figure 4.1.

be attributed to lithologic and structural boundaries, whereas high magnetic anomalies that may track the presence of serpentinite, mafic, or ultramafic rocks that produce intense signals (Sliter et al., 2009; Johnson & Watt, 2012). The western boundary of the Los Osos domain is delineated by the Hosgri Fault Zone (HFZ). It is suggested that since the Pliocene, lateral slip of the HFZ in the Santa Maria Basin has been on the order of 1-2 km (Namson & Davis, 1990). To the south, a restraining bend on the Hosgri fault uplifts a block of the Point Sal ophiolite (Johnson & Watt, 2012) as the the HFZ transitions from a single splay to multiple splays (Pacific Gas and Electric Company, 2014).

In order to characterize fault architecture along $\sim$94 km of the Hosgri Fault, Johnson & Watt (2012) and Pacific Gas and Electric Company (2013) employed deeper-penetrating Multi-Channel Seismics (MCS) from Sliter et al. (2009) to describe the sequence stratigraphic and faulting characteristics in the study area. Quaternary sediments onlap Mesozoic basement rocks or Neogene marine rocks. The package onlapping the bedrock was hypothesized to have been deposited during MIS 9 and is separated from the overlying package by the H40 transgressive surface that forms an angular unconformity and was hypothesized to have formed during the transgression between MIS 8 and 7 (Pacific Gas and Electric Company, 2013). Above this is a package deposited during the MIS 7 highstand that is separated from overlying sediment by the H30 transgressive surface, which is characterized as the most prominent angular conformity that planes underlying surfaces (Fig. 4.2; Pacific Gas and Electric Company, 2013). It is hypothesized that the H30 transgressive surface represents sea level rise between MIS 6 and 5 (Pacific Gas and Electric Company, 2013). The youngest unconformity and the one most relevant to this study is H10, the transgressive surface formed after the Last Glacial Maximum (LGM; Pacific Gas and Electric Company, 2013). H10 is time-transgressive and characterized by angular truncation of some underlying reflectors with an attendant change from high amplitude reflectors below to lower amplitude reflections above (Fig. 4.2; Johnson & Watt, 2012).

Deposits post-dating the marine transgression and H10 thicken towards the center of the

basin and display thicknesses ranging from 0-45 m (Pacific Gas and Electric Company, 2014). Post-transgressive deposits were interpreted to have been deposited in shelf, nearshore, and coastal floodplain environments, although none of this sediment was sampled by cores (Johnson & Watt, 2012). The continental shelf break is diffuse and not well-defined because of high volumes of sediment deposition by the Santa Maria River (Johnson & Watt, 2012) or because of deformation associated with the HFZ along the outer continental shelf (Pacific Gas and Electric Company, 2014).

Though long core samples have not been recovered on this margin, Nordstrom & Margolis (1972) characterized surficial sediment offshore of the ODSVRA. The study found that although grain size generally fines offshore, a band of coarser sand exists between the depths of 15-29 m. The authors observed three types of abrasions in quartz and hypothesized that the coarse sand was subjected to mechanical abrasion on a high energy environment and then subsequently submerged in a quiescent offshore environment with quartz dissolution (Nordstrom & Margolis, 1972). It is possible that strong bottom currents or storm induced wave surges could have caused abrasion of the quartz grains (Nordstrom & Margolis, 1972).

4.3.2 Oceanography and rivers

The southern end of the ODSVRA is located within the Santa Barbara Littoral Cell that extends from Santa Maria in the north to Ventura in the south (Patsch & Griggs, 2008). Within this littoral cell, four rivers and small streams contribute about 99.5% of sand to this cell despite dams upriver that have reduced sediment discharge by 40% (Patsch & Griggs, 2008). Material eroded from cliffs within the littoral cell likely are transported offshore, as the cliffs are composed of fine-grained Monterey Shale or silty shale from the Sisquoc Formation (Runyan & Griggs, 2003; Patsch & Griggs, 2008). An estimated 38,000 m^3 a^{-1} (Bowen & Inman, 1966) to 300,000 m^3 a^{-1} (Mulligan, 1985) of sand were lost from the littoral cell due to onshore transport to the Santa Maria dunes. This estimate is based off migration rates and cross-sectional areas of dunes.

Longshore currents in this littoral cell flow south with intermittent rip currents breaking seaward and southwesterly (Bowen & Inman, 1966).

It was hypothesized that the Santa Maria littoral cell may have been one of the earliest in the California Holocene coast to form, with ages from *Tivela stultorum* ranging between 10-8 ka (Masters et al., 2006). High abundances of *Tivela* dates around 6-5 ka and also 2-1 ka suggest that these times were periods of the most active sand beach accretion (Masters, 2006). The formation of wide beaches can be linked to favorable geomorphology in the Santa Maria cell such as abundant sand supply from the Santa Maria River, a gently sloping shelf, wave sheltering by the San Luis headlands, and the headlands of Point Sal acting as a natural groin (Masters, 2006). Beach formation may have coincided with a number of strong El Niño events that occurred between 12-8 ka and caused the establishment of southward-flowing littoral cells (Keefer et al., 2003; Carré et al., 2005; Masters, 2006).

The main tributaries discharging into the study area are the Arroyo Grande Creek in the north-central portion of the survey area, Oso Flaco Creek in the southern survey area, and the Santa Maria River located south of the survey area. Of these, the Santa Maria River has the largest discharge. Incision of the Santa Maria River into paleo-dune deposits during sea level lowstands has created a river valley that bisects the Santa Maria Dune Sheet (Peterson et al., 2018). Sediment discharged from the Santa Maria river is generally characterized by relatively high abundances (48-54%) of lithic fragments that are moderately angular (Peterson et al., 2018). It is hypothesized that the lithic fragments could be derived from recycled marine sandstones, meta-sedimentary rocks, and igneous rocks in the Coast Range and Transverse Range river drainages (Yancey & Lee, 1972; Scott & Williams, 1978; Peterson et al., 2018). Construction of the Lopez Dam in the 1950's controls the water discharge to Arroyo Grande Creek and as a result reduces winter peak flow downstream and increases summer base flow (Central Coast Salmon Enhancement, 2005). Prior to damming of the river, water discharge from the Arroyo Grande Creek was intermittent, especially in the summer and early fall. Arroyo Grande Creek drains unconsolidated and easily

eroded sediments (Central Coast Salmon Enhancement, 2005) that yield an average of 11.3 tons of sediment annually (Inman & Jenkins, 1999). However, trapping of sediment by the dam creates sediment-starved or "hungry water" that may exacerbate erosion of the main stem downstream (Central Coast Salmon Enhancement, 2005).

Table 4.1: Ages of the three stages of coastal dune deposits and the stage of presently-active dunes (Orme, 1990; Cousineau, 2012; Peterson et al., 2018).

Deposit	Expression	Maximum Age (years BP)	Study	Dune phase
Holocene	Active Dunes	<200	Orme (1992)	Dunes IV
Unweathered Holocene Dune deposits	Younger parabolic and lobate dunes	4100-370	Peterson et al. (2018)	Dunes III
Middle-Holocene uncemented weathered dunes	Older parabolic dunes	4100-7790	Peterson et al. (2018)	Dunes II
Late Pleistocene cemented dunes	Paleodunes	47,100-27,000	Orme (1990); Peterson et al. (2018)	Dunes I

4.3.3 Dunes

The Santa Maria Dune Sheet consists of marine terraces capped by three types of paledunes that are buried by the most recent Holocene active dunes. The underlying marine terrace could correspond to a similar low terrace that has been dated to 85-80 ka by $^{230}Th/^{234}U$ ages of the bivalve *Protothaca staminea* (Pacific Gas and Electric Company, 1988; Clark, 1990; Orme, 1992). The three types of paleodunes in order from oldest (bottom) to youngest (top) are late-Pleistocene cemented dunes with a thermoluminescence date of ∼47.1 ka, middle-Holocene uncemented weathered dunes with ages ranging from 7790 to 4100 years BP, and unweathered Holocene dune deposits with ages ranging from 4100 to 370 years BP (Peterson et al., 2018; Table 4.1). The presently active transverse dunes were probably activated within the past 200 years

(Orme, 1992; Table 4.1). The oldest late-Pleistocene paleo-dunes are associated with sea level lowstands and the two Holocene paleo-dunes are associated with marine transgressions (Orme & Tchakerian, 1986; Orme, 1992; Peterson et al., 2018). During the late-Pleistocene, the shelf was exposed during the sea level lowstand and net wind directions predicted at $\sim 143°$ supplied the dunes (Peterson et al., 2018). Middle Holocene uncemented weathered dunes coincide with the slowing of the Holocene marine transgression from 9-5 ka, and during this time, shoreward wave transport exceed shoreline retreat and signaled the onset of perennial beach development (Masters et al., 2006; Peterson et al., 2018). These observations led Orme (1992) to the conclusion that transverse dunes tend to form during periods of sea level fall and plentiful sand budgets, whereas parabolic dunes form during and after sea level rise with diminished sand budgets. Crisp (2017) hypothesized that in the Mussel Rock Dune Complex, decreases in areal extent of transverse dunes and increases in the areal extent of parabolic dunes are related to decreased sediment supply from damming of the Santa Maria River in 1959.

The ODSVRA are located within the youngest and most active sequence of beach and dune sands. Aerial imagery analyses reveal that the dunes migrate at variable rates and experience episodic migration during El Niño and La Niña periods, when westerly winds advance onshore (Barrineau et al., 2012). In recent years, the impact of airborne particulates in the ODSVRA that may be influenced by vehicular traffic has gained much attention. Airborne particulates <10 μm in diameter increase in concentration during wind events when the prevailing west-northwest winds (292°) surpass an average speed of 3.6 m/s (Etyemezian et al., 2015). Dust generated by wind is confined to a narrow range of wind directions, dominated by winds from 292° and secondly by winds from 315° (Etyemezian et al., 2015). Slight increases in wind can rapidly increase the amount of dust as wind shear and sand flux are related by a power-law (Etyemezian et al., 2015).

4.4 Methods

In July 2016, 79 km of CHIRP seismic data were acquired on the continental shelf offshore of the Oceano Dunes in Central California. The Scripps Institution of Oceanography EdgeTech X-Star CHIRP subbottom reflection sonar was towed a few meters below the surface. At the depth of the survey, the CHIRP unit used a 50 ms 1-15 kHz swept frequency acoustic source, which allows it to acquire sub-meter vertical resolution and seafloor penetration up to 50 meters. Data were recorded in SEG-Y format with real-time GPS navigation recorded with each shot for location accuracy. The data were processed and heave was removed using SIOSEIS (Henkart, 2003) and then imported into the Kingdom software package (Kingdom.IHS.com) for interpretation. Kingdom was used to calculate the depth to and thickness of interpreted surfaces. Generic Mapping Tools (GMT; gmt.soest.hawaii.edu) were used to apply continuous surface algorithm between points to convert to a gridded surface.

To examine shelf stratigraphy deeper than 50 m, we reprocessed USGS single-channel sparker data (Sliter et al., 2009). This dataset was collected in 2008 and 2009 with a 500 J mini-sparker source with a signal frequency ranging from 200-1600 Hz fired at 1/2 s shot interval and a 15-m long hydrophone streamer (Sliter et al., 2009). Since the original dataset has moderate levels of noise and strong amplitudes, processing of the data involved swell removal, multiple removal, coherency filtering to improve reflector continuity, and source wavelet shaping after the methods of Sargent et al. (2011), Klotsko et al. (2015), and Sahakian et al. (2017).

The bathymetry of the shelf was mapped from the 5-40 m depth contours using a RESON SeaBat 7125 multibeam system. This system uses a 200 kHz pulse to acquire swath bathymetry with $\sim$2 cm vertical resolution and 0.5 m pixel resolution. Bathymetry data were processed using QPS Qimera software by using the auto process function, applying sound velocity corrections to select areas, and applying the wobble analysis correction. The bathymetry and backscatter data were gridded at 2 m. Along with bathymetry, the RESON system also collects acoustic backscatter

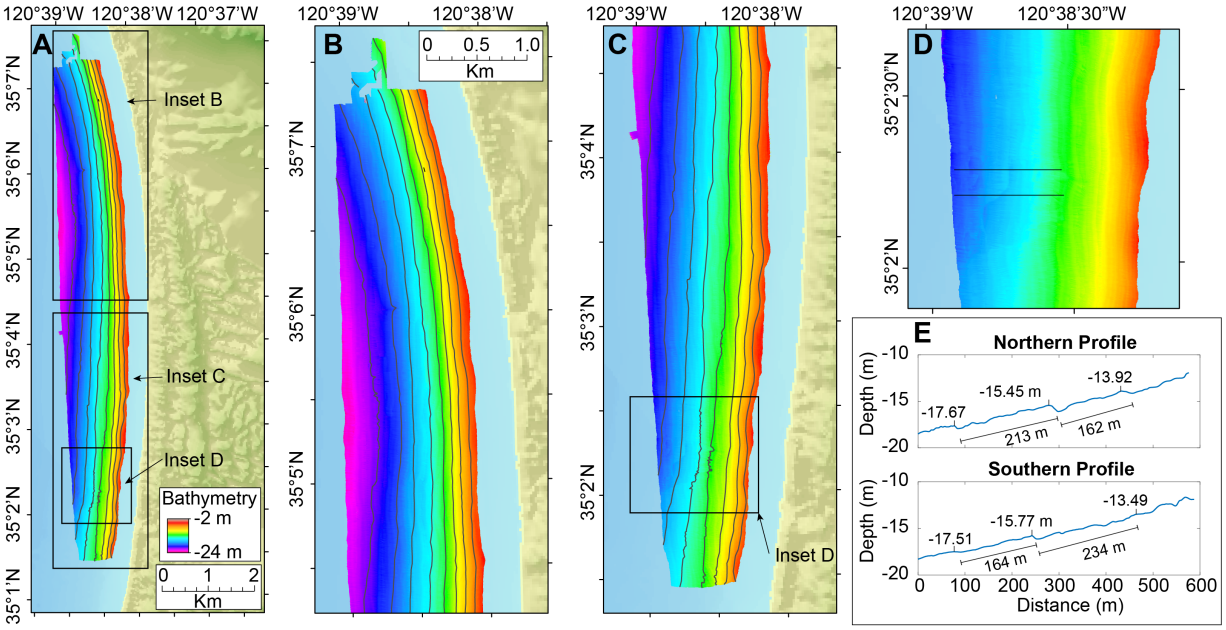

Figure 4.3: A) Multibeam bathymetry data are shown. Contours are at depth intervals of 2 m. Color depth scale is shown. B) Zoom of the northern half of the study area, C) zoom of the southern half, and D) zoom of the high-backscatter feature in the southern area (see Figure 4.4). E) two-dimensional dip profiles highlight roughness in this region.

data. Backscatter data were processed with QPS Fledermaus Geocoder Toolbox (FMGT) software. The FMGT software processing workflow involves application of filter processing, adjusting for angle varying gain, calculating statistics, building a mosaic, and Angle Range Analysis (ARA; Fonseca & Mayer, 2007; Rzhanov et al., 2012; Santos et al., 2018).

Surficial sediment grabs were collected with a van Veen sampler along three east-west transects in the northern, central, and southern CHIRP profiles. Sand dollars were removed from the samples before they were dried for grain size analysis. Grain size analysis involved dry-sieving the samples. Grain size sorting, skewness, and kurtosis were calculated using the methods described by Folk (1980). 100 grains in the 250-500 μm or 500-1000 μm fractions were visually sorted for quartz, authigenic carbonates, and lithics with replicates performed on each sample.

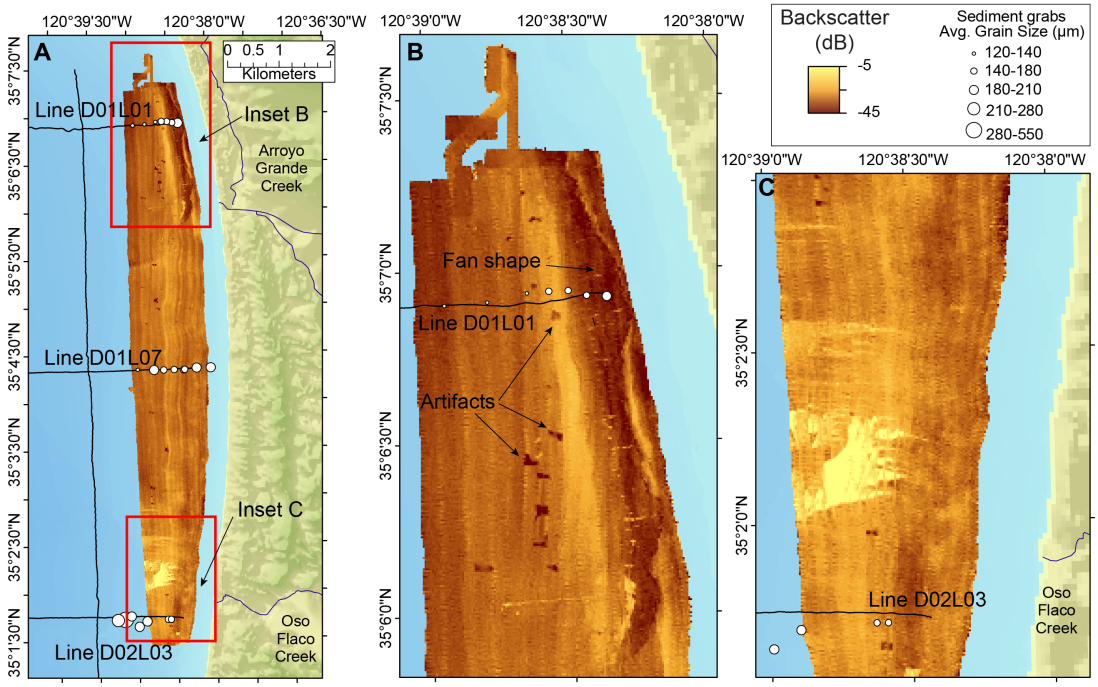

Figure 4.4: Reson Multibeam backscatter data are shown. A) Mean backscatter data for the survey. Note the range in backscatter intensity is low, with light colors being high backscatter. Notable features are a shore-parallel dark band in inset B and a bright feature in inset C. B) Inset B highlights the fan shape of the band with low backscatter. Arrows highlight artifacts in the backscatter data. C) Inset C shows high backscatter that correlates with increased surface roughness (See Figure 4.3).

4.5 Results

4.5.1 Multibeam bathymetry and backscatter

The bathymetry of the basin shoals in the northern and southern ends of the survey area (Fig. 4.3). Contours at 2 m intervals in the multibeam bathymetry data reveal that the shelf has a low-gradient slope. Closely-spaced contours in the northern part of the survey area indicate steep cross-shore slopes (Fig. 4.3). Within the basin there is low rugosity since the inner shelf is smoothed over by thick sediment deposits. The feature with the highest seafloor rugosity is located in the southern study area (Fig. 4.3d). Cross-sectional profiles through this rippled feature reveal a gentle stoss with an average slope of 0.6° and a steeper lee with an average slope of 2.2° (Fig. 4.3e). The amplitude of these features is very small, with a maximum amplitude of 64 cm and an average amplitude of 43 cm.

Backscatter throughout the shelf exhibits minor variance, as most of the values on the histogram range between -22 to -42 dB (Fig. 4.4). Lowest values are observed in the along-shore ribbon expanding from the northeast survey area and the band of low backscatter is highlighted in panel B of the backscatter mosaic (Fig. 4.4B). This band generally follows isobaths; however, at CHIRP line D01L01, the band also tapers landward, such that it resembles the shape of a fan. South of this fan-shaped pattern with low backscatter, the backscatter increases and the band becomes lighter. Highest backscatter values are observed in the southern survey area in the high-rugosity feature located at depths between 14-20 m (Fig. 4.4C).

Angular Range Analysis (ARA) predicts surficial sediment grain size phi could encompass a range from -1 to 8 phi, or 2000 to 4 μm (Fig. 4.5). The survey area is predicted to consist of 22% sediment between 1-2 phi, 47% sediment between 2-3 phi, and 29% sediment between 3-4 phi (250-500, 125-250 and 63-125 μm respectively). Sediment between -1 to 0 phi, 0-1 phi, and 4-8 phi is predicted to constitute $<$2% of the survey area. A band of medium sand (125-250 μm) is predicted to exist offshore of the Arroyo Grande Creek at depths greater than 12 m (Figs. 4.5a,

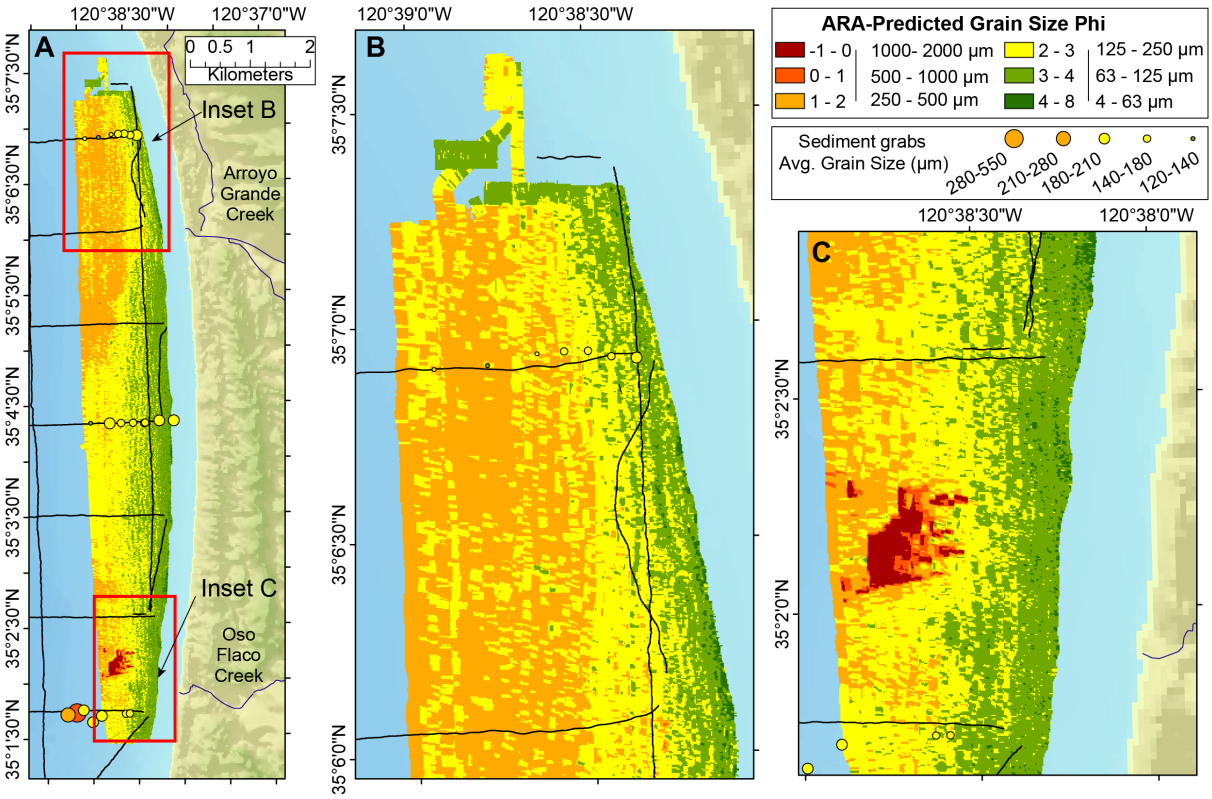

Figure 4.5: Angle Range Analysis (ARA) in QPS FMGT software predicted grain size phi. Circles show the locations of sediment grabs and circle size corresponds to average grain size as shown in Figure 4.4. Circle color corresponds to grain size phi shown in the map and legend, with red being coarser and green being finer. B) Zoom of the northern half of the survey area. C) Zoom of the southern half of the survey area.

b) and is spatially coincident with the band of low backscatter (Fig. 4.4b). Sediment samples shallower than 12 m are predicted by ARA are predicted to consist of fine sand (4-125 μm). The central survey area is predicted to consist of fine sand (125-250 μm; 2-3 phi) at depths greater than 12 m, which would be slightly finer than the medium sand (250-500 μm; 1-2 phi) predicted in the northern survey area. In the southern survey area, the seafloor has a patchy appearance and is predicted to consist of medium sand. The feature with high backscatter and rugosity offshore of Oso Flaco Creek is predicted to consist of coarse to very coarse sand from -1 to 1 phi (500-2000 μm). ARA predicted grain size does not necessarily correspond to average grain size of the surficial sediment grabs. The ARA predictions fail the most in the nearshore area, which have low backscatter but tend to have coarser grain sizes due to their proximity to the beach. The ARA map predicts landward fining of grain size in the northern survey even though landward coarsening is observed. Furthermore, most of the surficial sediment grabs are between 2-3 phi (125-250 μm) even though the ARA prediction map displays more variability in grain size.

4.5.2 Shelf stratigraphy

The deeper stratigraphic framework for this area is based off horizons identified by Johnson & Watt (2012) and Pacific Gas and Electric Company (2013) using USGS single-channel sparker data (Fig. 4.2). As the single-channel sparker dataset is lower-resolution and high penetration, the stratigraphic interpretations from Johnson & Watt (2012) and Pacific Gas and Electric Company (2013) focus largely on sequence boundaries and marine flooding surfaces, which helps identify potential piercing points to estimate strike-slip fault offset. CHIRP seismic profiles are designed to image the upper stratigraphic layers at unprecedented resolution; as such, CHIRP profiles only resolve the sediment package directly underlying the H10 horizon and overlying packages.

New high-resolution CHIRP seismic data reveal that the shelf is composed of two distinct sedimentary units separated by the regional H10 unconformity (Figs. 4.6, 4.7, 4.8, and 4.9).

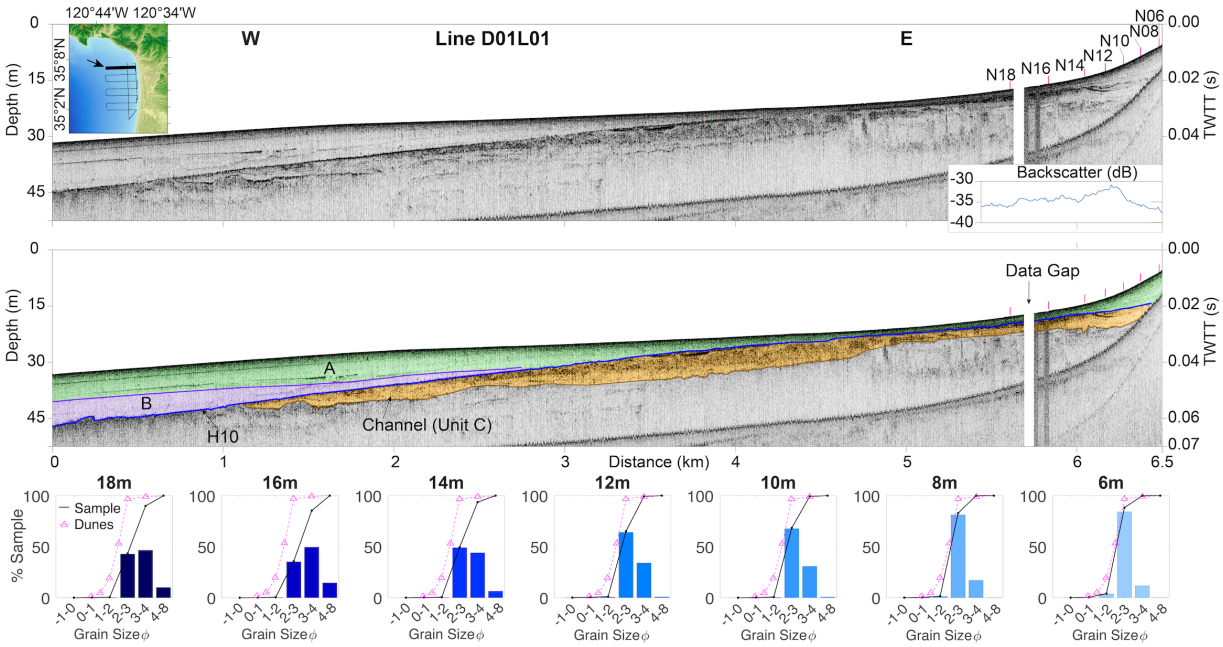

Figure 4.6: The northern dip profile with and without interpretation of units. Surficial sediment grabs were projected orthogonally onto the seismic profile. They are labeled with N for Northern transect and the numbers indicate the depth of the sample. The inset map shows the location of the profile. Below the uninterpreted profile is the backscatter through this transect plotted with the same distance scale. Note the low backscatter in the landward portion of the profile. The bottom panel shows grain size histograms for grab samples located on the profile. The pink line in the grain size histograms represents the grain size distribution of dune samples from Orme and Tchakerian (1986).

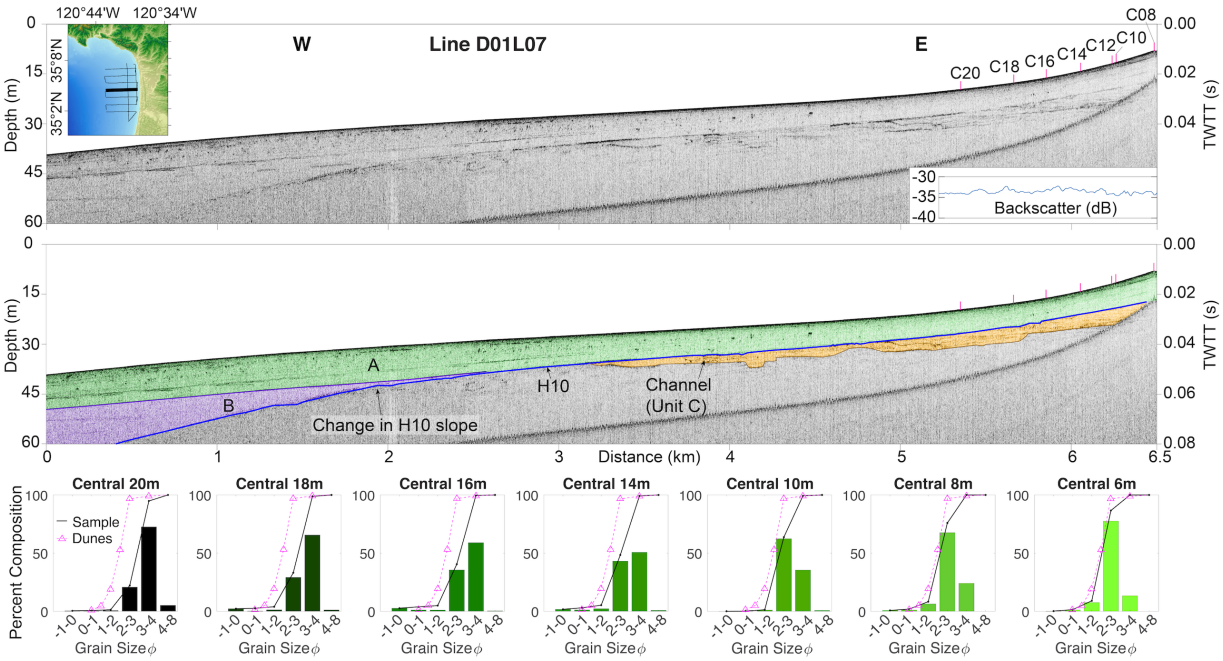

Figure 4.7: The central dip profile with and without interpretation of units. Surficial sediment grabs were projected orthogonally onto the seismic profile. They are labeled with C for Central transect and the numbers indicate the depth of the sample. The inset map shows the location of the profile. Below the uninterpreted profile is the backscatter through this transect plotted with the same distance scale. The bottom panel shows grain size histograms for grab samples located on the profile. The pink line in the grain size histograms represents the grain size distribution of dune samples from Orme and Tchakerian (1986).

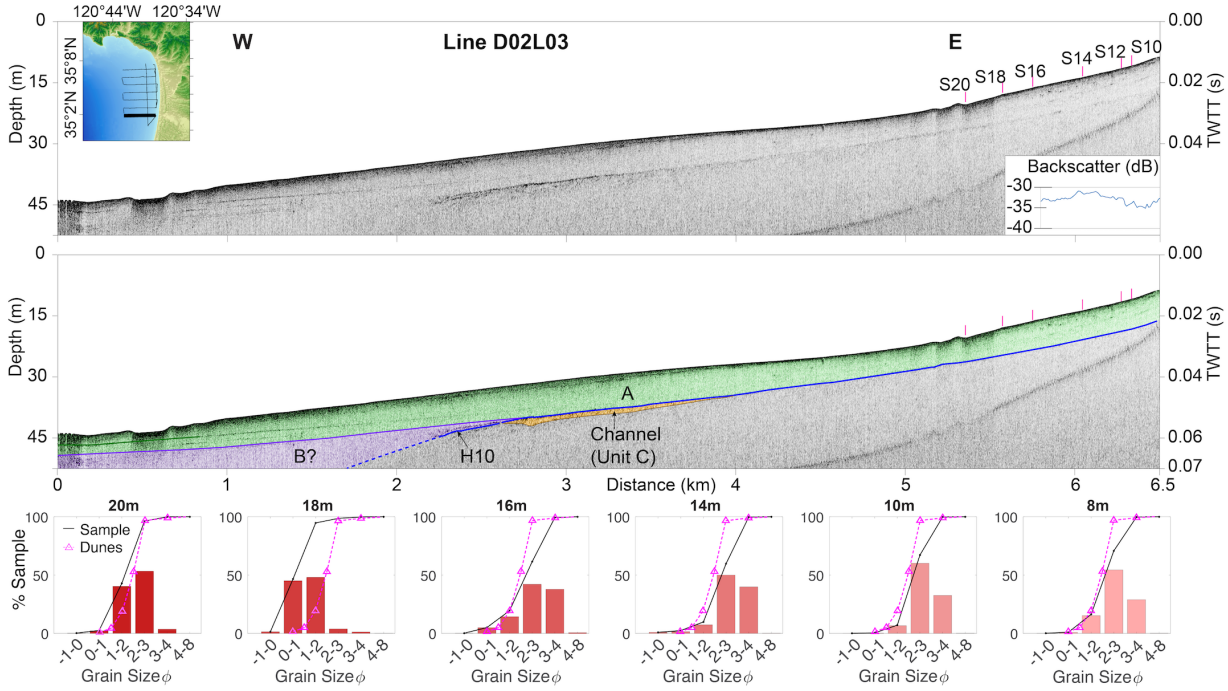

Figure 4.8: The southern dip profile with and without interpretation of units. Surficial sediment grabs were projected orthogonally onto the seismic profile. They are labeled with S for Southern transect and the numbers indicate the depth of the sample. The inset map shows the location of the profile. Below the uninterpreted profile is the backscatter through this transect plotted with the same distance scale. The bottom panel shows grain size histograms for grab samples located on the profile. The pink line in the grain size histograms represents the grain size distribution of dune samples from Orme and Tchakerian (1986).

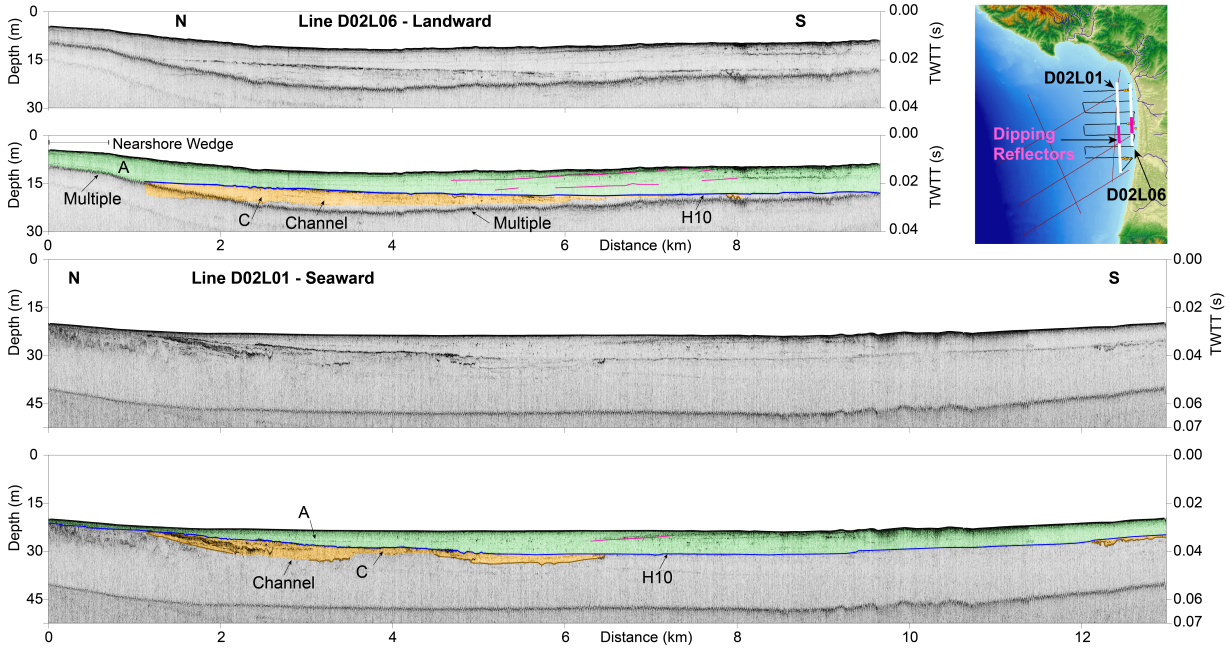

Figure 4.9: Two strike profiles with and without interpretation of units. The inset map shows the location of the two strike profiles. The locations of dipping reflectors traced in pink in the interpreted profile are also shown on the inset map. Note that the H10 reflector exhibits southward dip.

This study will focus mainly on the channels underlying the H10 surface, the H10 surface, and overlying sediment packages. The bottommost unit (Unit C) lies below the regional H10 unconformity and is the only unit with channel-like morphologic features (Figs. 4.6, 4.7 and 4.9). Sediment above the H10 surface has been subdivided into three packages based on their acoustic character, frequency and amplitude of reflectors, and stratal geometry. The stacking of these four units build the modern continental shelf, which is slightly broader in the southern study area caused by a southward thickening of the uppermost unit.

Regional unconformity H10 and the underlying Unit C

Observed throughout the survey area, the H10 reflector separates truncated reflectors below from flat-lying more acoustically transparent units above. The H10 reflector is often the highest-amplitude reflector in the entire survey area; however, the amplitude of this reflector does

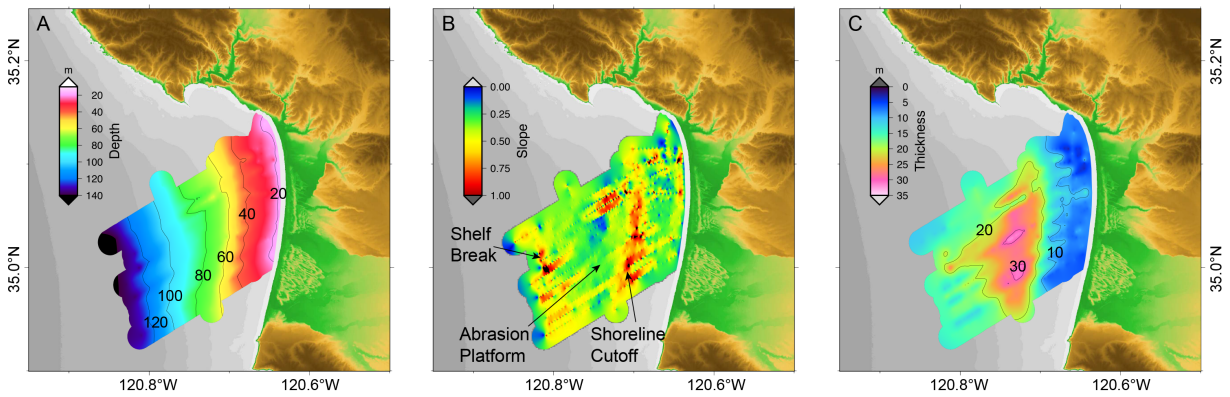

Figure 4.10: A) the depth of the H10 unconformity. B) the slope of the H10 surface. C) the thickness of sediment overlying the H10 unconformity. Contours are labeled with their corresponding depths/thickness.

display north-south variability. The amplitude of this reflector is strongest in the northern section of the survey (Figs. 4.6 and 4.9), decreases in acoustic amplitude in the central portion (Fig. 4.7), and exhibits a faint acoustic amplitude on the southernmost dip line (Fig. 4.8) and at the southern end of strike profiles (Fig. 4.9).

In reprocessed USGS sparker dip profiles, the gradient of the H10 unconformity varies downdip (Figs. 4.2, 4.10). The map of the H10 surface reveals that the 40 and 60 m depth contours are closely spaced (Fig. 4.10a). Upslope at depths of ∼40 m, the H10 unconformity exhibits a transition from shallow to slightly steeper gradients (Figs. 4.2a, b, c) with steep gradients ranging from 0.40-0.57°. The change in gradient of the H10 surface is also observed in the gradient map as a north-south trending swath with slopes approaching 0.8° (Fig. 4.10b). Following Grossman et al. (2006), we refer to the steeper gradient feature as a "stepped feature", which exhibits steeper gradients in southern dip profile PBS 319 (Fig. 4.2c) and shallower gradients in northern dip line PBS 279a (Fig. 4.2a). Between depths of 84-89 m, the gradient of the H10 unconformity flattens and maintains a gentle gradient (0.16-0.26°) until depths of 90-95 m. The gentle gradient feature in H10 between 84-114 m is best defined in the northern (PBS 279a; Fig. 4.2a) and southern (PBS 318; Fig. 4.2c) dip profiles and has diffuse boundaries in the central (PBS 289; Fig. 4.2b) dip profile. Below the gentle gradient feature, the slope of the H10 unconformity increases at

depth and is best observed on profile PBS 279a in the north (Fig. 4.2a) and also observed on the gradient map of H10 (Fig. 4.10b).

At depths shallower than 40 m, CHIRP seismic profiles and the depth map of the H10 unconformity shows that it generally mimics basin bathymetry (Figs. 4.9 and 4.10a). Strike profiles parallel to the margin reveal north-south variability in the depth of the H10 regional unconformity, with H10 shoaling toward the north in the seismic survey, deepening in the center of the survey, and again shallowing toward the south (Figs. 4.6, 4.7, 4.8, and 4.9). In the landward CHIRP strike profile (Fig. 4.9a), the regional unconformity dips to the south with a slope of 0.05° with a 4.5 m depth differential between the northern end of the profile and the center of the basin. The regional unconformity exhibits a steeper dip of 0.09° in the seaward strike profile (Fig. 4.9b), with a depth differential of 10.8 m between the northern end of the profile and the center of the basin.

Unit C, the basal sediment unit, is composed of a channel unit filled with continuous reflectors (Fig. 4.6). In the northern area, Unit C has reflectors with strong acoustic amplitudes (Fig. 4.6). The seaward strike profile images the channel infill, which is characterized by well-defined acoustically-strong reflectors that dip towards the south (Fig. 4.9). In the central survey area, flat-lying reflectors with slightly diminished acoustic reflectivity are observed in the channels (Fig. 4.6). Channels are not well imaged well in the two southernmost lines (Fig. 4.8).

Table 4.2: Mean thickness of sediment units, the area over which they were calculated, volume, and percent volume.

Sediment unit	Mean thickness (m)	Area (km^2)	Volume (km^3)	Percent of total volume
Unit A	4.2	315.5	1333	32.3
Unit B	8.2	315.5	2573	62.4
Unit C	2.4	90.3	217	5.3
Total			1544	

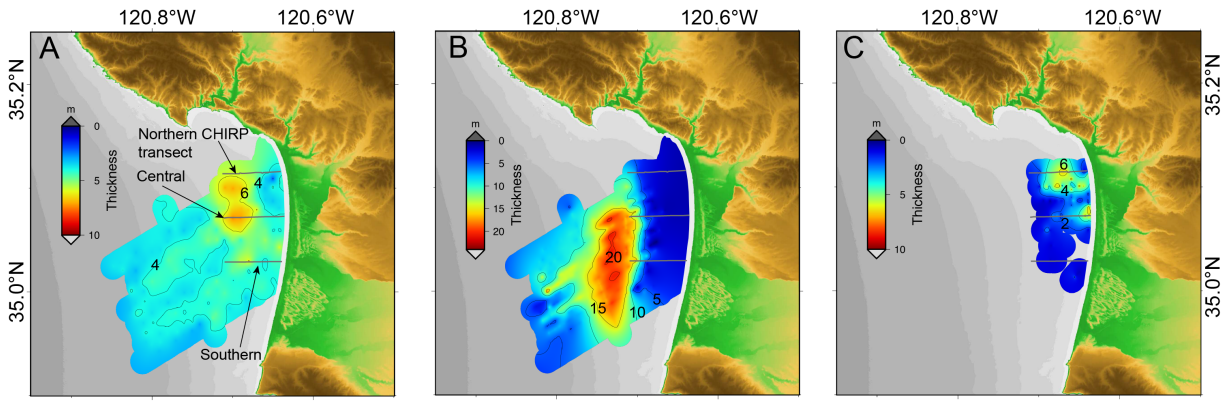

Figure 4.11: A) Thickness of Unit A, the most recent package, B) thickness of Unit B, and C) thickness of channel fill Unit C. Note that the color scale bars for the thicknesses of the packages are not the same. The location of the northern, central, and southern CHIRP dip profiles are shown in gray.

Post-glacial geometry and packages

The sediment overlying the regional H10 unconformity are divided into Units B and A based on their acoustic character and stratal geometry. The seafloor exhibits a slight change in gradient at 30-50 m depth (0-1 km of Figs. 4.6, 4.7, and 4.8), flattens in the middle portion of the survey area (2-5 km), and steepens in the nearshore sediment wedge (5.5-6.5 km in Fig. 4.6). Isopachs of sediment deposited above the H10 unconformity reveal that sediments are thickest in the central survey area and thinnest in the northern survey area (Fig. 4.10c).

Unit B, shown in figures as a purple sediment unit, exhibits landward onlap and seaward downlap onto the regional H10 unconformity and is present below the depths of 35 m (Figs. 4.2a, b, c). The upper boundary of this unit was delineated by a discontinuous seismic reflector with varying acoustic amplitude. Unit B contains few faint subhorizontal and discontinuous reflectors in both the CHIRP seismic and single-channel sparker profiles (Figs. 4.2, 4.6, 4.7, and 4.8). In single-channel sparker dip profiles, Unit B reflectors exhibit sigmoidal geometries below that transitions upsection into aggradational geometries. In CHIRP seismic profiles, the upper boundary of Unit B is imaged more clearly in the four most northerly strike profiles (Figs. 4.6 and 4.7). In the southernmost CHIRP profile, the seaward sediment is acoustically transparent,

making it difficult to identify the H10 unconformity; thus, the thickness of Unit B is more difficult to determine (Fig. 4.8). The isopach map of Unit B shows that most of the accommodation is located downdip of the 60 m contour (Fig. 4.10c). The thickest deposits of Unit B correspond to areas where the H10 surface is the steepest, suggesting that changes in gradient of the H10 surface may be linked to the location of the Unit B depocenter.

Unit A is the uppermost unit and is bounded below by the H10 unconformity and above by the seafloor. Unit A has thicknesses ranging from 2-6 m and thickens to the north, with depocenters at the seaward portion of the CHIRP profiles at seafloor depths greater than 25 m (Figs. 4.6, 4.7, 4.8, 4.11a). The thinnest Unit A deposits are in the northern dip profile at seafloor depths $<$20 m, where sediment cover is $<$1 m due to shoaling of the H10 regional unconformity (Fig. 4.6). Landward of the shoaling of H10 in the northern dip profile is a nearshore sediment wedge between seafloor depths of 6 and 16 m (Fig. 4.6). The nearshore wedge is too narrow to be imaged in the isopach map (Fig. 4.11a). Unit A exhibits slight thinning towards the south (Fig. 4.11a) and could be attributed to a slight shoaling of the H10 regional unconformity and thinner sediment cover (Fig. 4.9).

Within Unit A are reflectors with strong acoustic amplitudes that can be observed in the seaward portions of the northern and central dip profiles (Figs. 4.7 and 4.8). In the seaward strike line, the acoustic amplitude of reflectors within Unit A diminishes towards the south where the sediment is acoustically transparent (Fig. 4.9). The central portion of the survey area has high-amplitude reflectors that dips $\sim 0.08°$ to the north (between 5-7 km and highlighted in pink in Fig. 4.9a; between 6-8 km in Fig. 4.9b). In the south (Fig. 4.8) are acoustically-transparent mound-like features on the seafloor with relief ranging from 1-2 m at depths of $\sim$20 m. This line is south of the high-rugosity features that are identified from the multibeam bathymetry and backscatter.

Volumetric estimates within each sediment unit reveals that Unit B comprises $\sim$62% of the post-glacial sediment volume (Table 4.2). In comparison, younger Unit A comprises only 32%

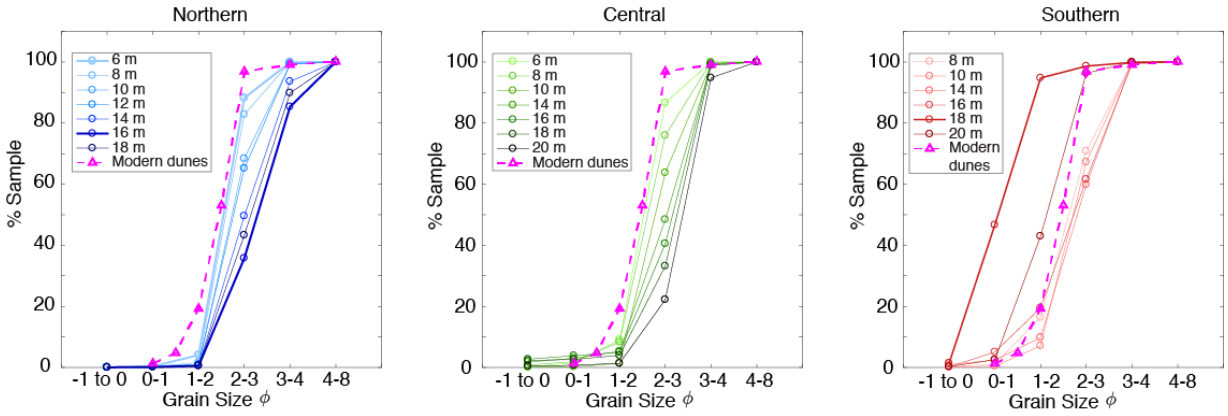

Figure 4.12: Cumulative grain size histograms for the northern (left), central (middle), and southern (right) transects of surficial sediment grabs. Lighter colors reflect shallow samples and darker colors reflect deeper samples. In all three plots, the cumulative grain size distribution of the modern dunes (from Orme and Tchakerian, 1986) is plotted alongside the surficial sediment grabs.

of the post-glacial volume respectively (Table 4.2). Unit C channel fill comprises an insignificant amount of margin sediment (Table 4.2). Volumetric estimates are generally consistent with isopach maps that illustrate greater thicknesses of Unit C (Fig. 4.11).

Table 4.3: Grain size parameters of the shallowest and deepest samples on each transect.

Sample	Mean grain size phi	Sorting (Folk, 1980)	Sorting (classification)	Percent silt
North (6 m)	2.58	0.15	Very well sorted	0.12
North (18 m)	3.31	0.78	Moderately sorted	10.14
Central (6 m)	2.53	0.30	Very well sorted	0.00
Central (20 m)	3.38	0.78	Moderately sorted	5.19
South (8 m)	2.62	0.80	Moderately sorted	0.19
South (20 m)	2.08	0.40	Well sorted	0.02

4.5.3 Grain size and mineralogy

Cumulative grain size plots of the northern and central transects show a general trend of seaward fining (Figs. 4.5, 4.6, 4.8, and 4.12). In the northern transect, there are three distinct

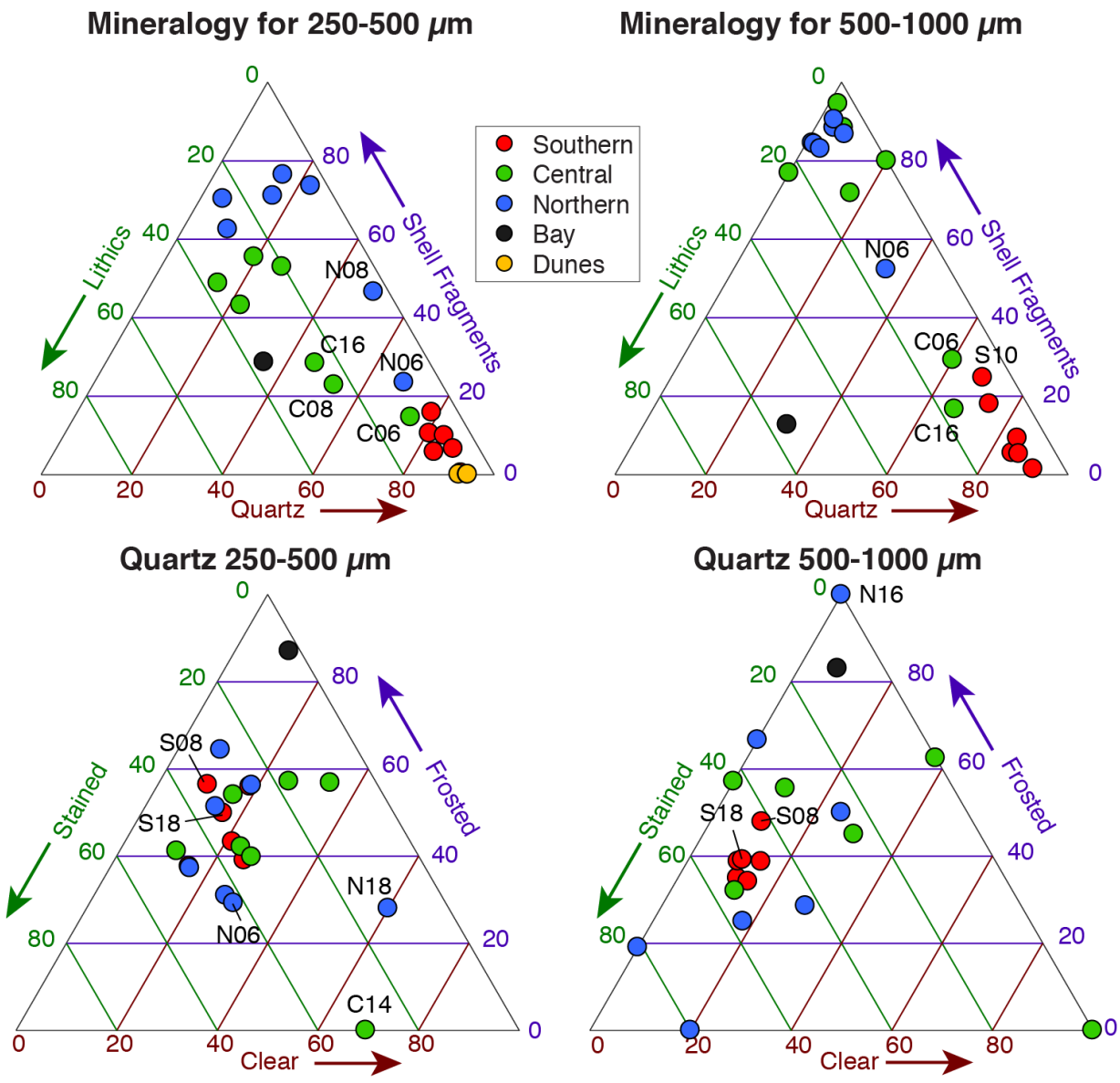

Figure 4.13: The top panel shows ternary diagrams describing the mineralogy of the surficial sediment grabs with relation to percent Lithics, percent Carbonate, and percent Quartz. The bottom panel shows the relative percent frosted, stained, and clear quartz. The diagrams on the left show these relations for the grain size fraction between 250-500 μm and the diagrams on the right show these relations for the grain size fraction between 500-1000 μm.

clusters of grain size, with the samples at 6-8 m being slightly finer than presently-active dunes (Dunes IV; Orme & Tchakerian, 1986), 10-12 m samples with decreasing proportions of 125-250 μm sand, and samples between 14-18 m having a higher proportion of 63-125 μm sand (Figs. 4.6 and 4.12). In the northern transect, the sample at 16 m has the finest grain size even though it is landward of the sample at 18 m. Northern transect samples from the shallow nearshore wedge (at 6 and 8 m) are very well sorted and exhibit a seaward progression to moderately sorted (Table 4.3). Similarly, nearshore samples in the central transect are very well sorted and transition to moderately sorted at depth (Table 4.3). The southern transect grain size samples exhibit seaward fining until 18 m; samples at 18 and 20 m are anomalously coarse; their grain size distributions are much coarser than that of the presently-active dunes, with the coarsest grain sizes in the 18 m sample (Figs. 4.8 and 4.12). Southern transect samples display opposite patterns of sorting than the northern or southern transects, as seaward samples in the southern transect from the acoustically-transparent mounded feature are well sorted (Table 4.3).

The mineralogy was classified for the grain size classes 500-1000 μm and 250-500 μm. Major constituents of these sand fractions include quartz, heavy minerals, shell fragments and shells, and benthic foraminifera. The greatest amounts of quartz within these size fractions were observed in the southern transect samples, comprising 78-92% of the samples (average 85%), followed by a range of 14-74% quartz in the central transect samples (average 37%), and 5-68% quartz in the northern transect (average 27%; Fig. 4.13). Southern transect samples are clustered in the bottom right of the ternary diagram, indicating that their composition is mostly quartz (Fig. 4.13). Shell fragments and shells are present in the following amounts for the transects: 0-16% in the southern transect, 14-55% in the central transect, and the most shell fragments in the northern transect with 23-76% (Fig. 4.13). Northern transect samples generally cluster in the top corner of the ternary diagram, suggesting that they are composed mostly of shell fragments, with the exception of samples N06 and N08 (Fig. 4.13). Lithics, including biotite, muscovite, chlorite, hematite, amphibole, volcanic glass, and garnet comprised 5-10% in the southern transect

(average 7%), 11-37% in the central transect (average 25%), and 3-27% (average 13%) in the northern transect. These results can be compared to the findings of the California Geologic Survey (California Geological Survey (CGS), 2011) that sampled disturbed and undisturbed portions of the dunes. This report found that quartz, plagioclase, and K-spar account for 75-89% of the unsieved sand samples and lithics comprise 1-14% of the unsieved sand (California Geological Survey (CGS), 2011).

In surficial sediment grabs, Western sand dollars (Dendraster excentricus) were recovered only in the central and southern transects and none were recovered in the northern transect. In the central transect, sand dollars were present at depths between 6-8 m and 12-18 m, whereas in the southern transect, sand dollars were recovered from depths of 8-16 m, with no sand dollars present in the 18 and 20 m sand samples. Due to poor penetration of the sediment grabber in areas with sand dollars present, it was difficult to quantify the abundance of sand dollars by volume.

4.6 Discussion

4.6.1 Stratigraphic framework for post-LGM sediment

The location of sediment depocenters may exert influences on the transfer of sediment to the SMDC and depocenters are influenced by eustasy in the across-margin direction and by tectonic deformation in the along-margin direction. As the rates of eustatic sea-level rise typically exceed rates of tectonic deformation, tectonic deformation may play a secondary control on shelf architecture in some settings (Hogarth et al., 2012). Nevertheless, on margins where tectonic deformation is very localized (e.g., Gerber et al., 2010) or exhibits alongshore rather than cross-shore variations (e.g., Hogarth et al., 2007; Le Dantec et al., 2010; Klotsko et al., 2015), eustatic signals can be more readily identified and separated from accommodation created by tectonic deformation. Defining the stratigraphic architecture of post-LGM sediment aids in our understanding of the rates of tectonic uplift of the San Luis Block, styles of wave-base erosion

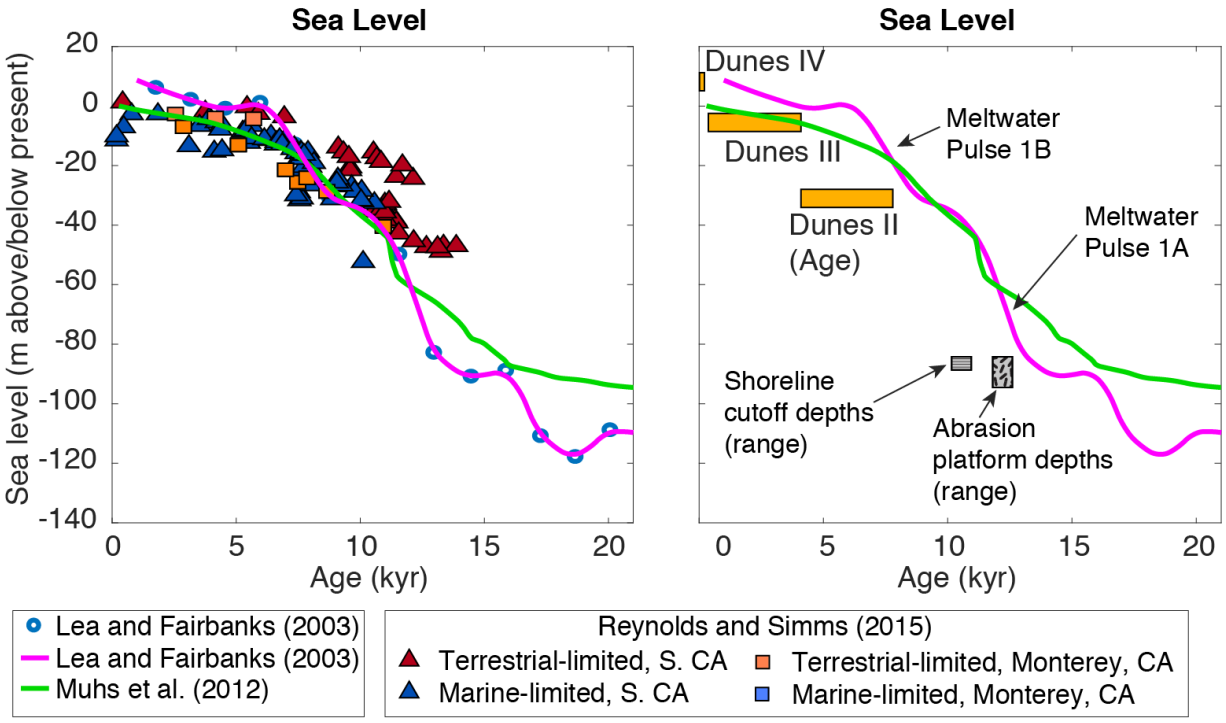

Figure 4.14: At left, Sea-level curves from Lea and Fairbanks (2003) are compared to local sea-level curves from Muhs et al. (2012) and sea-level data from Reynolds and Simms (2015). At right, the relative timing of dune deposition (from Orme, 1990, 1992; Peterson et al., 2018; see Table 4.1) are represented by yellow horizontal rectangles and juxtaposed on the Lea and Fairbanks (2003) and Muhs et al. (2012) sea-level curves. The ranges of depth for the shoreline cutoff and the abrasion platform in the H10 surface are shown by vertical rectangles.

during the transgression, past sediment transport and depositional regimes, and the timing and formation of the Santa Maria dunes. As the CHIRP and multibeam datasets collected for this study place important constraints on post-glacial and modern processes, they will be the focus of this study.

The most prominent reflector in CHIRP profiles, the H10 surface, is the regional unconformity and is interpreted as the transgressive surface formed by wave-base erosion during post-LGM sea level rise ($\sim$21 ka to present). The transgressive surface truncates underlying Unit C channel fill deposits and separates subaerially exposed deposits below from marine deposits above. Similar post-glacial deposits overlying the transgressive surface have been observed elsewhere along the California shelf (e.g., Grossman et al., 2006; Draut et al., 2009; Hogarth et al., 2012; Klotsko et al., 2015).

Wave-base erosion planed off and truncated Unit C. Channels are interpreted to represent incision during lower sea levels between Marine Isotope Stage 2 (MIS 2) and the sea level transgression. Therefore, Unit C may have formed during lowstand conditions that exposed the shelf subaerially. Channels are generally deeper and broader within the northern region of the study area (Fig. 4.11c) and are proximal to the Arroyo Grande and Pismo creeks. Our observations of channels in the northern survey area are consistent with observed channels within SLO Bay that were imaged by a deeper-penetrating 3-D multi-channel seismic dataset (Pacific Gas and Electric Company, 2014). Incised channels imaged in northern survey area seismic profiles are oriented in the same direction as Pismo Creek, which has a drainage pattern forming axial-parallel to deformation (Fig. 4.1b). We propose that in the north, higher topography and a higher concentration of streams (Fig. 4.1b) may favor extensive channel incision. Thinning of Unit C in the southern dip profile (Fig. 4.8) and isopach maps (Fig. 4.11c) suggest that channel incision does not appear to be as extensive in the central survey area, even though subaerial valleys could form adjacent to Oso Flaco Creek and separating the Callender and Guadalupe Dune Complexes. Less extensive channel incision in the south could be a result of subsidence

within the basin.

Cross-shelf changes in gradient of the H10 transgressive surface could reflect changes in the rate of post-glacial sea-level rise. Low rates of sea-level rise may result in the formation of terraces and notches (Sunamura, 1992), whereas high rates of sea-level rise rapidly submerge exposed surfaces and thus increases preservation (Fletcher & Sherman, 1995; Klotsko et al., 2015). The change in gradient of the H10 surface between the depths of 84-89 m is interpreted as the shoreline cutoff and the down-dip low-gradient portion of H10 located between 89-95 m is interpreted as an abrasion platform (e.g., Posamentier & Allen, 1993; Muhs et al., 1994; Klotsko et al., 2015; Fig. 4.14). Previous studies propose that the abrasion platform was cut during a period when the rate of sea level rise was slower, such as time periods preceding Meltwater Pulses (MWP) 1A and 1B (Bard et al., 1990; Fairbanks et al., 1992; Grossman et al., 2006; Hogarth et al., 2012; Klotsko et al., 2015). Offshore of Santa Cruz, Grossman et al. (2006) recovered dateable material from vibracores and found that the abrasion platform may have been eroded prior to 15 ka, or during the slow sea-level rise before MWP 1A. During MWP 1A, the steep shoreline cutoff may have been rapidly drowned, thus preserving the stepped feature (Grossman et al., 2006).

Following the interpretations of Grossman et al. (2006), Hogarth et al. (2012), and Klotsko et al. (2015), we hypothesize that the abrasion platform at depths of 89-95 m likely formed during a slower sea level rise following the LGM (Fig. 4.14). When comparing the depth of the abrasion platform to the global sea-level curve from Lea et al. (2002) and the San Nicholas Island sea-level curve from Muhs et al. (2012), this depth corresponds to the time period before MWP 1A (Fig. 4.14). As the Muhs et al. (2012) sea-level curve is best constrained before MIS 2, Fig. 4.14 also shows sea-level curves that captures post-glacial sea-level rise more accurately (e.g., Lea et al., 2002; Reynolds & Simms, 2015).

During a time of slower sea level rise, wave-based erosion would have more time to erode surfaces at a gentler gradient. The acceleration in the rate of sea-level rise during MWP 1A

may have drowned the shoreline cutoff and preserved it. We propose that Unit B was deposited seaward of the shoreline cutoff following MWP 1A; however, the exact timing of the formation of the shoreline cutoff, abrasion platform, and Unit B is uncertain. An alternative hypothesis posits that the shoreline cutoff at this location may have been formed by the minor high-sea stand of 62 m at ∼49 ka (MIS 3) and is observed in a submarine terrace near Santa Cruz Island (Chaytor et al., 2008; Muhs et al., 2014). If the abrasion platform was formed during MIS 3, it would likely have been overprinted by channel incision during the maximum lowstand of MIS 2. As the abrasion platform is well preserved without evidence of any subaerial erosion, we favor the hypothesis that the platform was eroded during a slower rate in sea-level rise during the last transgression. Vibracore collection with age-dating in the northern transect with thin post-glacial sediment cover would be required to determine the formation age of the shoreline cutoff. The seaward change in gradient around 120 m depth is likely the shelf break. It is more pronounced in the north and diminishes towards the south in proximity to the Santa Maria River (Fig. 4.2). The north-south variability in shelf break gradient could be due to thick sediment deposits sourced from the Santa Maria River that obscures the shelf break rollover (Johnson & Watt, 2012; Pacific Gas and Electric Company, 2014) or basin subsidence.

The shoreline cutoff and abrasion platform likely influenced the location of post-glacial depocenters, as postglacial sediment thickness and Unit B thickness is the greatest above the abrasion platform. As Unit B pinches out at the top of the shoreline cutoff, it is likely that deposition of this unit occurred below the wave base, in a style similar to post-glacial Unit I found offshore of San Onofre (Klotsko et al., 2015). Based on its geometry, we interpret Unit B as a healing-phase wedge that was deposited as part of a transgressive systems tract. The transgressive systems tract is characterized by backstepping beds that terminate landward by onlap and seaward by downlap (Posamentier & Vail, 1988). Healing phase wedges are deposited during sea-level transgressions when sediment eroded from the shoreface infills local lows and are often deposited seaward of notches such as the shoreline cutoff (Posamentier & Allen, 1993; Le Dantec et al.,

2010; Klotsko et al., 2015). North-south variability in the transgressive surface influences the location of depocenters for Unit B, as it thickens in the central survey area (Fig. 4.11b).

We propose that the north-south variability in depth of the H10 unconformity and the shoreline cutoff may reflect uplift of the San Luis block in the northern survey area. Previous studies proposed that San Luis block uplift has been continuous since the past 0.5-2 Myr and estimated uplift rates of 0.11-0.22 mm a^{-1} (Pacific Gas and Electric Company, 1988; Hanson et al., 1992). Our hypothesis is also supported by southward dipping reflectors within Unit A (Fig. 4.9). North-south variability in the depth of the shoreline cutoff, with the shallowest shoreline cutoff in the north and deeper cutoffs in the south (Fig. 4.2) is consistent with differential uplift. Based on the depth difference in the H10 surface from the two CHIRP strike profiles, we calculated uplift rates. In the center of the basin, the H10 surface has depths of 18.8 and 32.7 m in the landward and seaward strike profiles, respectively (Fig. 4.9). Given these depths, the landward strike profile would have been flooded at 7.8 ka and the seaward strike profile would have been flooded at 9.4 ka (Fig. 4.14). Differences in depth between the northern end of the strike line and the center of the basin (4.5 m in the landward profile, 10.8 m in the seaward profile) likely record both uplift to the north and basin subsidence to the south. Thus, dividing the depth differential by 2 captures the uplift signal more accurately. Dividing the uplifted height by two and by time yields uplift rates of 0.29 mm a^{-1} for the landward strike profile and 0.58 mm a^{-1} for the seaward strike profile, which is approximately 3 times greater than rates published in the literature. Our age constraints are poor as we used the sea-level curve to infer age-depth relationships. For more accuracy, calculations of uplift rates would require vibracores that recovered dateable material. Additionally, our rates may be greater than those in the literature because uplift rates within the literature represent time-averaged uplift rates from terraces dated at 75 or 125 ka (Pacific Gas and Electric Company, 1988; Hanson et al., 1992; Hanson & Lettis, 2013), whereas our uplift rates look at only the past 7-9 kyr.

Northward-dipping reflectors (shown by the pink line) in CHIRP profiles with Unit A

suggest that infilling of the basin was not entirely aggradational but also may have included a progradational component as well (Fig. 4.9). These northward dipping reflectors are observed north of Oso Flaco Creek and correspond to the middle of the dune field (Fig. 4.9 inset). The northward prograding reflectors coincide spatially with a deepening of the H10 surface in the central basin (Fig. 4.9), suggesting that sediment may have prograded into areas with more accommodation. Alternatively, these layers may be folded as a result of contractional deformation. As the seafloor along the two strike profiles (Lines D02L06 and D02L01; Fig. 4.9) are located at depths less than 20 m, it is possible that Unit A sediment in both profiles and Unit B in the landward strike profile was reworked by wave orbitals and advected north. An alternative hypothesis is that Units A and B prograded to the north as a result of along-margin diffusion (e.g., Driscoll & Karner, 1999) away from Oso Flaco Creek. This is supported by thickening Unit B deposits just offshore of Oso Flaco Creek (Figs. 4.9, 4.11b), suggesting that high discharge events from this creek may supply sediment to this unit. Whether wave orbitals and diffusive transport from creeks act in concert, prograding reflectors from Oso Flaco Creek are preserved by greater accommodation in the central basin.

The geometry, thickness, and volume of post-glacial sediment units (Table 4.2) suggest that terrigenous supply may have been greater during the formation of Unit B than A. Isopach maps show that Unit B deposits are thick and more uniform, whereas Unit A appears thinner and patchier (Fig. 4.11). In the Santa Maria Basin, progressive thinning of sediment units could be caused by changes in climate from the LGM through the sea-level transgression. Coastal lowlands on the Central California coast were 2-3 wetter during the LGM than present (Heusser, 1995) and pollen records from the Vandenberg Dune Sheet just south of Point Sal records regional drying from 9 ka to the late Holocene (Anderson et al., 2015). Such wetter conditions during the LGM may enable increased terrigenous sediment supply forming Unit B and decreased supply during accumulation of Unit A. Millennial variability in storm climate could also be responsible for dispersal of sediment sourced from the Santa Maria River. During the period from 12 to 8

ka, a number of strong El Niño events occurred (Keefer et al., 2003; Carré et al., 2005), that may have resulted in episodic, northward dispersal of Santa Maria River sediment that could supply sediment to the northern end of the littoral cell (Masters, 2006). The period from 8-5 ka is characterized by a La Niña-like climate (Keefer et al., 2003), during which southward littoral transport was restored and beaches were established (Masters, 2006). We propose that Unit B was deposited before or during 12-8 ka. At 12 ka, sea level was approximately 50 m below present and the abrasion platform may have been submerged by 25 m (Fig. 4.14). Strong El Niño events may have advected Santa Maria River sediment northward and offshore, resulting in thick Unit B deposits that onlap the H10 transgressive surface. Thus, we propose that Unit A was deposited from 8 ka to the present, during which time the establishment of the modern littoral cell may have preferentially retained sediment on beaches instead of forming marine deposits. This period is also coincident with significant periods of postglacial dune formation at 4 ka and 1.7 ka as well as the formation of active dunes $\sim$200 years BP (Table 4.1; Fig. 4.14; Orme, 1990; Orme, 1992; Orme & Tchakerian, 1986; Knott & Eley, 2006; Cousineau, 2012; Peterson et al., 2018). Thus, dune formation may have played a role governing the thickness and geometry of Unit A. As we do not have ages of the sediment units, it is difficult to constrain whether millennial climate variability could have affected sediment supply.

4.6.2 Zone of low backscatter and high backscatter feature

The multibeam backscatter dataset exhibit a narrow range of amplitudes throughout the survey area with two notable areas: a ribbon of low backscatter in the north and a high backscatter feature in the south (Fig. 4.4). As demonstrated from the ARA prediction map, backscatter may be able to predict overall patterns of grain size but still does not accurately predict small changes in grain size (Fig. 4.5). The failed prediction of the ARA algorithm suggests that grain size may not be a dominant control on backscatter, as ARA may also be affected by surface roughness and the volume contribution (Fonseca & Mayer, 2007). As the backscatter dataset has a horizontal

resolution ∼1.9 mm, we propose that the horizontal resolution is too coarse to resolve small changes in grain size. Instead, grain size may influence the formation of bedforms which in turn can increase seafloor roughness.

One notable feature in the backscatter dataset is the high backscatter feature in the southern survey area (Fig. 4.4). As there are no grab samples from this feature, the surficial sediment is possibly composed of medium to coarse sand based off the ARA prediction map (Fig. 4.5) and previous studies reveal that coarse sand typically displays a high and uniform backscatter (Eittreim et al., 2002; Ferrini & Flood, 2006). Based off the short amplitude of the feature at 43 cm and its distinct stoss and lee slopes (Fig. 4.3e), it is interpreted to be ripples with an adjacent patch of reworked sand. Such features have been documented on the Eel River margin to increase roughness and backscatter (e.g., Borgeld et al., 1999). The proximity of this deposit to the Oso Flaco Creek suggests that the sand could be derived from storm deposits. High-discharge events in the Oso Flaco Creek could be capable of transferring sand to the nearshore region with depths between 12-20 m and this sand could be subsequently reworked by wave orbitals. Similar flooding events on the Eel margin may have sufficiently increased orbital velocities that could form bedforms such as ripples and sand waves (Borgeld et al., 1999). Since the high backscatter features and the mounded features in the southernmost CHIRP lines are coincident at depths of 18-22 m, it is possible that these features have the same origin. 2-D profiles through the structures suggest that they are similar to ripples with a westward stoss and eastward lee. Sample S20 is located in a trough of one of these mounded features and sample S18 is located on a feature-less seafloor. Grab samples S18 and S20 have anomalously coarse grain sizes, suggesting that these features may also be reworked deposits that have been initially emplaced by storm events.

In the northern survey area, a band of low backscatter may be related to smooth surficial sediment in the nearshore wedge (Figs. 4.4b, 4.6). The fan shape that tapers towards the coast resembles a region of low backscatter observed on the Eel river margin that is also composed of well-sorted silt and fine sand of the Eel and Mad river prodeltas (Borgeld et al., 1999). Borgeld et

al. (1999) imply that the low backscatter may be related to the smoothness and lack of bedforms.

4.6.3 Grain size, sorting, and mineralogy: implications for sediment transport in the basin

Surficial sediment grabs reveal that tectonic uplift exposes northern transect samples to reworking by waves, littoral transport in the Santa Maria Basin may be limited to the upper 12 m, and extensive reworking by oceanographic currents occurs throughout the southern transect as the dominant wave and wind direction is not sheltered by the San Luis headlands. As present-day littoral transport in the Santa Maria cell is to the south, we expect littoral sediment to be sourced from SLO Bay and for sediment discharged from creeks to move southward. Sediment transported by littoral transport could be characterized by the SLO Bay sample, which has high lithic contents, especially within the 500-1000 μm grain size fraction (Fig. 4.13).

Properties of northern transect surficial sediment grabs suggest that these samples are reworked and that sediment transported by littoral currents may be retained within the nearshore wedge. Extensive reworking of shallower sediment in the northern transect could be due to tectonic uplift, which may also engender preservation of the nearshore wedge. Slightly higher lithic and quartz content in the N06 and N08 samples in the northern transect (Fig. 13) may have been sourced by southward littoral transport of SLO Bay sediment. Deeper samples in the northern transect are instead composed of 83-90% shell fragments and 6-14% lithics, thus serving as an endmember composition (Fig. 4.13). Much of the shell fragments within the northern transect appear to be fragments of Western sand dollars (*Dendraster excentricus*) that have experienced varying degrees of mechanical weathering. The high concentration of shell fragments and shells could be due to reduced terrigenous sediment supply to samples deeper than 8 m. Low terrigenous sediment supply to the Northern survey area is supported by thinning Unit A in the northern CHIRP profile D01L01 (Figs. 4.6, 4.11a, b). Post-glacial deposits in Unit A coincident with the locations of samples N16 and 18 are thin, suggesting that sediment

flux to the distal ends of the nearshore wedge is low. The lack of lithic minerals characteristic to SLO Bay in deeper northern transect samples also suggests that littoral currents carrying SLO Bay sediment may bypass the northern transect and instead emplace deposits in the central transect. Furthermore, the narrow range of grain sizes within shallow northern transect samples (Fig. 4.12) could suggest extensive reworking. Reworking by wave orbitals may be active only to 12 m and deeper than this, deeper samples are only moderately sorted (Table 4.3). Thus, we propose that in this region, most of the longshore transport appears to occur at depths of 12 m or shallower. Similarly, littoral transport is hypothesized to be limited to the upper 8 m offshore La Jolla (Le Dantec et al., 2010). Bypass and non-deposition within the northern transect could be caused by tectonic uplift and shoaling bathymetry, which decreases accommodation and allows seafloor shallower than 30 m to be reworked by wave orbitals. Such extensive reworking within the northern transect may explain the abundance of shell fragments. As reworked sediment is advected by littoral currents to the central basin, increasing depth may correspond to decreasing energy that may enable the deposition of SLO Bay sediment.

The mineralogic signature in the central transect reflects lithic abundances that approach that of SLO Bay and a range of shell and quartz abundances. As the central transect is located south of Arroyo Grande Creek, this addition of lithics and heavy minerals may be derived from Arroyo Grande Creek or from southward littoral transport from SLO Bay that bypassed the northern transect. If littoral transport is limited to the upper 12 m, deeper depths within the central transect may allow sediment carried by currents to fall out of suspension and be emplaced. As this study did not sample suspended or bedload sediment from Arroyo Grande Creek, we cannot definitively distinguish the source of the lithic fragments.

As the wind and waves in southern transect are not sheltered by the San Luis headlands, waves in the southern transect are larger and may rework surficial sediment the most extensively. Southern transect mineralogy is dominated by frosted and iron-stained quartz (Fig. 4.13) that suggests this sand may have experienced abrasion in a subaerial environment. The mineralogy

of the southern transect exhibit similarities with the mineralogy of dune samples from Orme & Tchakerian (1986) and California Geological Survey (CGS) (2011), suggesting that sediment from the central and southern survey area may supply sand to the beach and then to the dunes (Bowen & Inman, 1966; Patsch & Griggs, 2008). Little variability in grain size (Fig. 4.12) and sorting (Table 4.3) of southern transect samples suggests extensive reworking. We propose that the southern transect experiences the highest wave energy, as this area is outside of the lee of the San Luis headlands, whereas the northern and central transects may be shielded by headlands. Less sand within 4-8 phi (4-63 μm) could suggest that fine particles are transported landward to the beach and dunes. This exchange between the nearshore sand in the central and southern survey area and the dunes could explain why a nearshore wedge exists only in the northern survey area and is largely absent in the central and southern survey area.

The rippled feature with possibly high concentrations of coarse sand is located offshore of Oso Flaco Creek, suggesting that storm deposits from this creek supply sediment to this area. Of the grab samples in the southern transect, samples S18 and S20 have the coarsest grain size distributions. Sample S20 is located in the trough of a mounded feature that could be a ripple. These coarser sediments are likely "relict sediments" that are hypothesized to have been deposited during the Last Glacial Maximum (LGM) and subsequently reworked (Nordstrom & Margolis, 1972). Examinations of relict sediments by Nordstrom and Margolis (1972) under a scanning electron microscope revealed surface textures that suggest relict sediments were subject to mechanical abrasion in a subaerial environment and then later submerged long enough to develop etch pits. Based on the stratigraphic location of this sample and the interpretations of Nordstrom & Margolis (1972), this deposit may have been subaerially exposed during times of lower sea level and re-worked during the post-glacial transgression.

Estimations of dune deposit volumes in the north and south SMDC suggest shifting depocenters from the Late Pleistocene to the Late Holocene (Peterson et al., 2018) and our offshore study establishes a new stratigraphic framework that might explain depocenter shifts

through time. Peterson et al. (2018) used the Oso Flaco Creek to divide the SMDC into northern (Callender Dune Complex) and southern portions (Guadalupe Dune Complex; Fig. 4.1a). In the Late Pleistocene, northern SMDC volumes were 9 times greater than southern SMDC volumes, in the Middle Holocene, northern volumes were 2 times greater than southern volumes, and in the Late Holocene, southern volumes were 3 times greater than northern volumes (Peterson et al., 2018). Peterson et al. (2018) hypothesized that the north-south variability in dune volume could be attributed to switching from northern littoral transport prior to 6 ka to southern littoral transport after 3 ka. We propose that the shift in dune depocenters from north to south occurred due to a combination of Holocene climate changes and tectonic uplift. During the Middle-Late Holocene, establishment of southward-littoral cells (Masters, 2006) may have contributed to increased sediment transport to the shelf offshore the Guadalupe Dune Complex. Uplift of the San Luis block to the north likely decreased accommodation and caused depocenters to shift southward away from uplifted topography in the Late Holocene. This southward depocenter shift may have allowed the Guadalupe Dune Complex to accumulate more sediment in the Late Holocene. Again, a shift in littoral transport since the Late Pleistocene could be tested by acquiring long vibracores with organic material for age-dating.

4.7 Conclusion

Preexisting physiography and accommodation exert the largest influences on post-glacial stratigraphy on the continental shelf, as across-margin accommodation is created seaward of the shoreline cutoff and along-margin accommodation is diminished to the north by tectonic uplift. We observe evidence of block uplift that causes a shoaling of the H10 transgressive surface in the north, uplifts the shoreline cutoff in the northern sparker dip profile, and causes reflectors within Units C and A to dip to the south. Based on the dip of the transgressive surface, we calculated uplift rates that are three times greater than those reported in the literature. As deformation on this

margin is at high-angles to the shoreline, we can distinguish uplift signals from eustatic sea-level rise during periods when rates of sea-level rise exceed uplift rates. Quantifying these rates of uplift are important for understanding margin accommodation and tectonic hazards, as active faults are within close proximity of the Diablo Canyon Nuclear Power Plant.

In the cross-shore direction, the shoreline cutoff exerts the largest control on sediment depocenters. We propose that the shoreline cutoff was formed between the LGM and MWP 1A and that Unit B was deposited seaward of the shoreline cutoff following MWP 1A. Seaward of the shoreline cutoff, Unit B filled available accommodation, creating a healing-phase wedge that is thick and aggradational. The volume of Unit B is twice that of Unit A (Table 4.2) and may be related to millennial variability in ENSO.

Variable and patchy Unit A in the north could be due to block uplift, which limits accommodation seaward of the nearshore wedge. As a result of uplifted topography in the north, littoral currents may bypass the northern transect and instead deposit lithic-rich sediment in the central survey area. Thus, terrigenous supply to the northern survey may be reduced at depths $>$10 m, as surficial sediment is dominated by shell and sand dollar fragments. The central survey area has deeper antecedent relief and this area may allow for more quiescent conditions that could cause deposition from sediment transported by littoral currents. Shallow antecedent topography in the southern survey area may expose the seafloor to wave orbitals that can rework surficial sediment. Furthermore, wind in the southern survey area is not shielded by the headlands of the San Luis Range (longer fetch) and may be subject to more intense wave energy. Here, mineralogy of surficial sediment is dominated by frosted quartz and closely resembles mineralogy of the dunes. A notable feature in the southern survey area is a rippled feature with high backscatter with anomalously coarse sediment. This coarse sediment may be "relict sediment" that was subaerially exposed during lowstand conditions and reworked by currents during highstand conditions. Increased accommodation to the south relative to the north and the establishment of southward-flowing littoral currents during the Middle Holocene may

explain why dunes accumulated faster in the south (Guadalupe Dune Complex) than in the north (Callender Dune Complex). Thus, recent dune accumulation is dependent on the tectonic, eustatic, and climatic processes that control depocenters on the shelf.

4.8 Acknowledgements

This work is in preparation for publication as **Wei, E.A. and Driscoll, N.W. Post-glacial stratigraphy offshore of the Oceano Dunes, Central California.** The dissertation author was the primary investigator and author of this material. This study was funded by a grant from the CA State Parks. We would like to thank Ronnie Glick for assistance with this project. Alistair Harding offered a tremendous amount of assistance with processing the USGS sparker data. We would like to thank the crew of the R/V Point Loma: James Holmes, Boe Derosier, Brendon Mendenhall, Colby Nicholson, and Mackenzie Roberts for providing a safe platform to acquire the data.

Chapter 5

Strike-slip Transpressional Uplift Offshore San Onofre, California Inhibits Sediment Delivery to the Deep Sea

5.1 Abstract

The Inner California Borderlands is a complex margin where sediment delivery to the basin floor is largely routed through canyon-channel-gully systems. Using nested geophysical surveys, piston and gravity cores from the Eastern Gulf of Santa Catalina, this study compares two canyon systems and investigates how tectonics, shelf width, gradient, and autogenic processes influence turbidite emplacement timing and grain size. One end-member canyon is the Dana Point Canyon, which is proximal to the San Juan Creek drainage and has a concave-up channel profile. The other endmember system consists of the San Onofre North and South (SON and SOS) canyons that are detached from San Mateo Creek by a wide 10 km shelf and traverses a tectonically-deformed slope with multiple ponded basins. 53 radiocarbon ages sampled from 9 cores reveal that turbidite deposition at Dana Point persists during the sea-level lowstand of

Marine Isotope Stage (MIS) 2 through the subsequent transgression and highstand. On the contrary, turbidite emplacement adjacent to the SON and SOS canyons occurs mostly during MIS 2 and ceases around 8 ka. The main regional control on turbidite timing is the wide shelf adjacent to the SON and SOS canyons that consist of a broad uplifted anticline. This anticline separates the SON and SOS canyons from a riverine source during the sea-level transgression. Much of the tectonic deformation offshore of San Onofre was created by transpression along the right-lateral Newport Inglewood-Rose Canyon Fault Zone. Second-order controls on local turbidite emplacement include small synclines and anticlines that form ponded basins and accommodate deformation on the San Mateo Fault Zone. These basins engender deposition and intervening steep slopes promote sediment bypass. Complex bathymetry offshore San Onofre also affects channel gradient, which act to accelerate or decelerate flow. Turbidity flow dynamics modified by gradient changes offshore of San Onofre have the ability to modulate channel architecture and grain size. The implications of this work are that tectonically-deformed morphology complicates the timing of turbidite emplacement throughout a sea level cycle and thus the interpretation of turbidites as paleoseismic records in such regions will introduce much uncertainty.

5.2 Introduction

Studying submarine channels has both societal and scientific relevance. Not only do they serve as conduits for terrigenous material across margins to the deep oceans (Allen, 2008), but fan deposits at the base of the submarine channels can serve as significant hydrocarbon reservoirs when filled with sand- or silt-prone sequences (Mayall & Stewart, 2000; Stow & Mayall, 2000; Pettingill & Weimer, 2002; Mayall et al., 2006). Large castrostrophic flows through channels can be a significant geohazard to marine infrastructure (Paull et al., 2002; Xu et al., 2010). For these reasons, it is important to understand the evolutionary processes that shape channel morphology and stacking patterns through time in sedimentary basins.

The Inner California Borderlands (ICB) is a complex, tectonically active margin that is characterized by narrow continental shelves dissected by numerous canyon-channel systems. As the distance between river mouth and canyon heads are short, canyon-channel systems are effective conduits that funnel sediment to submarine fans on the basin. Thus, the ICB is an ideal place to study source-to-sink processes and sediment routing (Normark et al., 2009; Covault et al., 2010; Romans et al., 2016). These canyon-channel systems are so effective at funneling sediment that turbidites form the bulk of the basin fill (Normark et al., 2009).

Sediment flux to submarine canyons can occur either as particles that settle out of suspension or flows that move downslope as turbidites. Turbidites originate in canyon heads and are capable of traveling to the most distal parts of a deep-sea fan. Plausible triggers for turbidity currents include river floods, storm events, tsunami wave loading, sediment loading, internal tides, and earthquakes (Goldfinger et al., 2007; Xu et al., 2010). Storm waves can rework shelf sediment and advect it to canyon heads as a turbid layer in the Hueneme and Mugu Canyons (Xu et al., 2010). Since multiple causes are capable of producing turbidites, it can be difficult to distinguish seismo-turbidites from those produced by tsunamis, storms, and sediment loading. Hyperpycnal flows may be influenced by longshore currents (Sommerfield & Nittrouer, 1999; Wright et al., 2001; Goldfinger, 2011) or may also be triggered by floods; as a result, these deposits are commonly organic-rich (Shiki, 1996; Shiki et al., 2000; Mulder et al., 2001; Goldfinger, 2011). Some studies have argued that seismo-turbidites can be distinguished by wide areal extent, multiple coarse-fraction pulses, variable mineralogical provenance, greater depositional mass, and coarser texture than the storm-generated events (Nakajima & Kanai, 2000; Goldfinger et al., 2007; Goldfinger, 2011). Other studies cite concerns for using turbidites as records of paleoseismic activity, as geologic dating lacks the time resolution to determine whether a fault ruptured as a whole or whether it ruptured in segments over a time period of days, years, or even decades (Nelson et al., 1995; Atwater et al., 2014). As such, there is still debate as to whether deep-sea turbidites are reliable paleo-seismometers (Sumner et al., 2013; Atwater et al., 2014). As the

ICB is tectonically active, turbidite records have the potential to provide insight on earthquakes; however, many of the tests used to evaluate paleoseismic deposits have much uncertainty (Sumner et al., 2013).

In addition to hydrodynamic regimes, morphologic factors such as bathymetry and shelf width may exert important controls on sediment flux to canyons (Xu et al., 2010). Factors such as distance from a river source and shelf width may change throughout sea-level cycles. Sequence stratigraphic models predict that the greatest delivery of sediment to canyons and basin floor occurs during sea-level lowstands when rivers deposit directly into the canyon-channel system (e.g., Vail et al., 1977; Mitchum Jr, 1985; Posamentier et al., 1991). Nonetheless, many recent studies have proposed that sea-level is subordinate to the distance between the canyon head and shoreline (Covault et al., 2010; Blum et al., 2013; Gamberi et al., 2015) and proposed that distances $<$5 km result in canyons characterized by active sand transport (Sweet & Blum, 2016). In addition, secondary factors can exert controls on sediment flux to the deep sea, including strength and location of littoral cells and the presence of shelf clinothems that sequester sediment (Sweet & Blum, 2016).

Despite the postulation that shelf width exerts the largest control on sediment delivery to canyon-channel systems, few studies have sampled sediment offshore San Onofre where there is a wide shelf. This study presents extensive seismic surveys, density of sediment cores, and radiocarbon ages from this region and focuses on the San Onofre North (SON) and South (SOS) canyons. While much of the ICB margin, such as the shelf offshore of Dana Point, has widths $\sim$2 km, the shelf offshore of San Onofre has a maximum width $\sim$10 km (Fig. 5.1C). By comparing the Dana Point to the SON and SOS canyon systems, the overarching goal of this research is to test the hypothesis that the wide shelf formed by along-margin tectonic transpression at a left lateral stepover exerts the largest control on the timing of turbidite emplacement to the deep basins. Additionally, this study investigates the role of secondary controls such as across-margin deformation, changes in gradient, and autogenic processes on grain size and depositional timing.

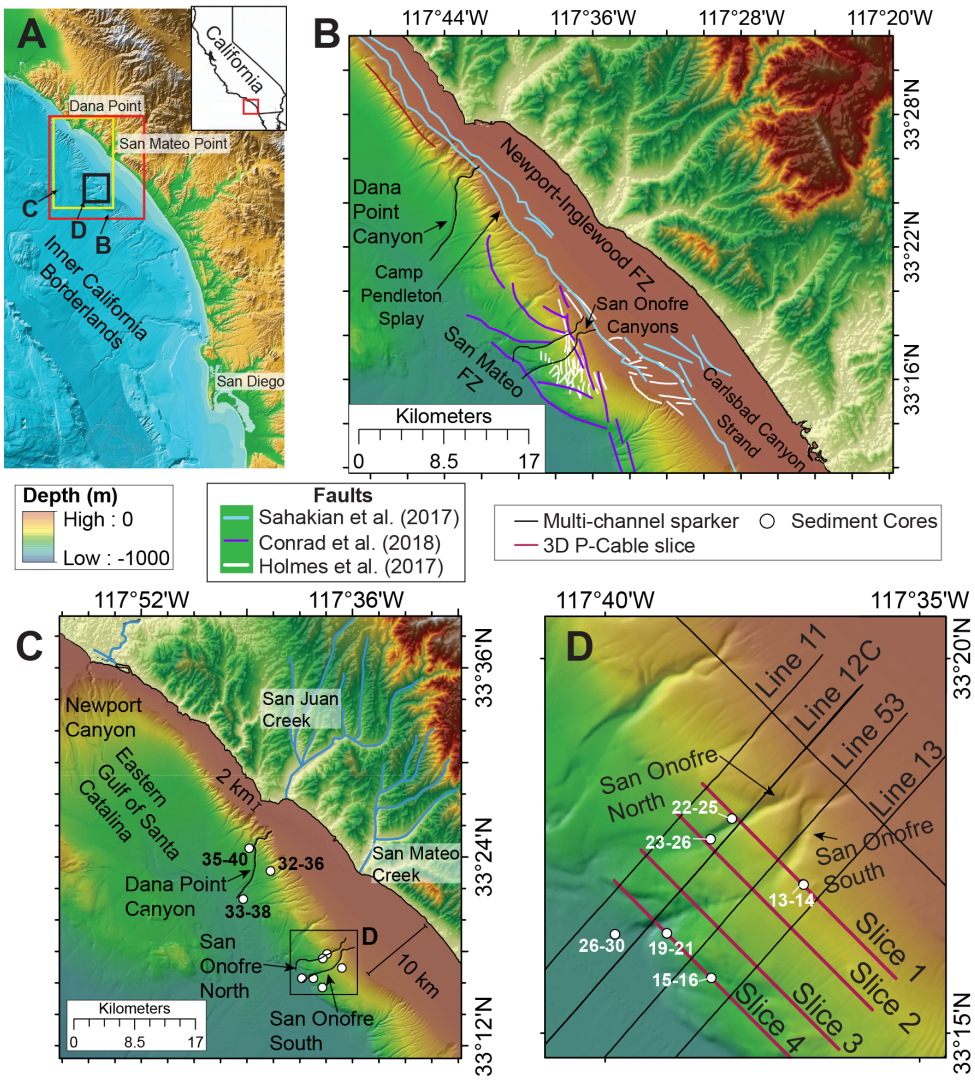

Figure 5.1: A) The Inner California Borderlands (ICB) is a tectonically active region located offshore of Southern California. This study focuses on the portion of the margin with the wide continental shelf. The locations of insets B, C, and D are shown. B) Known active faults within the study area are shown. Blue faults are from Sahakian et al. (2017), purple faults are from Conrad et al. (2018), and white faults are from Holmes et al. (2017). FZ = Fault Zone. C) Dana Point Canyon is located to the north of the San Onofre North and South canyons. The shelf offshore of Dana Point is 2 km wide. Cores adjacent to the Dana Point Canyon are shown. The area shown in inset D is outlined by the black box. D) The study area offshore of San Onofre. This study uses 2D Sparker Multi-channel seismics shown by the black lines and slices of 3D P-cable Sparker seismics shown by the red lines. Gravity Cores (GC) and Jumbo Piston Cores (JPC) are labeled with white circles. Bathymetry from Dartnell et al. (2015).

The main findings of this study are that Dana Point Canyon has remained active during lowstands, transgressions, and highstands in sea-level due to its short ∼2 km connection to San Juan Creek with little to no tectonic deformation along this portion of the margin. In contrast, the SON and SOS canyon-channel systems are complicated by jogs on the right-lateral strike-slip Newport-Inglewood/Rose Canyon (NIRC) Fault that create broad anticline uplift in the along-margin direction (Klotsko et al., 2015; Sahakian et al., 2017; Holmes et al., 2017). Smaller-scale anticlines and synclines in the across-margin direction may be deformed by crosscutting faults in the San Mateo Fault Zone (Holmes et al., 2017; Conrad et al., 2018). Much of this deformation pre-dates recent sediment deposition (Sahakian et al., 2017; Conrad et al., 2018). The broad along-margin anticline widens the shelf, which in turn caused sand delivery to the slope to cease around 8 ka during the last sea-level transgression. Most of the sand delivery to the deep offshore San Onofre occurred during sea-level lowstands such as Marine Isotope Stage (MIS) 2. Turbidity flows can be affected by allogenic and autogenic processes that cause spatial and temporal variability in turbidite emplacement. Allogenic processes that are inferred to be regional include across-margin deformation that creates the mid-slope ponded basin that captures sediment, disrupts the equilibrium profile of the channel, affects channel gradient and thus flow velocity, and increases roughness that can cause hydraulic jumps. Autogenic processes include flow stripping around meander bends.

5.3 Geologic Setting

5.3.1 Geomorphology of the Inner California Borderlands

The Inner California Borderlands is a complex seismically active region off Southern California that is highly deformed (Ehlig, 1977; Crouch, 1979; Legg, 1991; Crouch & Suppe, 1993; Magistrale, 1993; Nicholson et al., 1994; Bohannon & Geist, 1998; Meade & Hager, 2005; Ryan et al., 2009; Ryan et al., 2012; Maloney et al., 2016). Such deformation is responsible for

the characteristic basin and ridge basement structure observed in the ICB bathymetry. The main basins within the ICB are the Gulf of Santa Catalina (GoSC) and the San Diego Trough (SDT). Our coring locations focus on the Eastern GoSC (Fig. 5.1). Canyons that feed into the Eastern GoSC include Newport Canyon to the north, San Mateo Canyon, Oceanside Canyon, Carlsbad Canyon, and La Jolla Canyon (Normark et al., 2009).

5.3.2 Strike-slip tectonics offshore San Onofre

Much of the complex tectonic deformation in the ICB occurred during the Oligocene to the late Miocene, after which deformation in the ICB decreased dramatically in magnitude and changed in style (Maloney et al., 2016). During the Oligocene to late Miocene, the ICB underwent block rotation, extension, and transcurrent faulting associated with microplate capture and formation of the Transverse Ranges (Lonsdale, 1991; Nicholson et al., 1994; ten Brink et al., 2000t). As plate motion became more northerly during the late Miocene, deformation of this region created a vast system of basins and ridges that dominates ICB bathymetry (Atwater & Stock, 1998; Maloney et al., 2016).

Presently active faults in the ICB exhibit less extension in comparison to widespread deformation that occurred in the past and are recorded in Pliocene sediment packages (Bormann et al., in press). Two active faults that dominate the GoSC region are the Palos Verdes Fault in the western GoSC and the Newport-Inglewood/Rose-Canyon (NIRC) Fault along the eastern basin (Fig. 5.1B; Ryan et al., 2009). Sediment dispersal is affected most by the NIRC Fault, as the Palos Verdes Fault controls geomorphology to the west of the study area (Fig. 5.1B). The right-lateral strike-slip NIRC Fault trends northwest-southeast, has been active since at least the Miocene in the north, and it is estimated to accommodate 0.5-2 mm a^{-1} of Pacific-North American plate boundary motion (Freeman et al., 1992). The southern portion of the NIRC, the Rose Canyon Fault, formed in the late Pliocene (Ehlig, 1977; Grant et al., 1997) and its slip rates are estimated between 1-2 mm a^{-1} (Lindvall & Rockwell, 1995). The NIRC Fault transitions offshore south of

La Jolla Canyon, parallels the coast from Newport Beach to Seal Beach, and continues onshore into the Los Angeles Basin (Fig. 5.1B).

The NIRC fault exhibits much variability from south to north. The NIRC Fault Zone is characterized by compression offshore of San Onofre and to the south near La Jolla and Carlsbad, it is characterized by extensional deformation and divergence (Maloney et al., 2016). Where the shelf is wide, two segments of the NIRC fault are separated by a stepover of 1 km (Fig. 5.1B). The left lateral jog between these two segments engenders transpression and forms an anticlinal feature responsible for the widening of the shelf in this region (Sahakian et al., 2017; Holmes et al., 2017). The anticlinal feature is onlapped by younger sediment (Sahakian et al., 2017). Fault splays may be responsible for some geomorphic controls in this region and the Camp Pendleton splay may control the location of a paleochannel (Sahakian et al., 2017). The area offshore of San Onofre displays a large number of smaller splays of the NIRC fault to the east and these smaller splays may be responsible for distributing deformation associated with the NIRC fault (Sahakian et al., 2017). Deformation offshore San Onofre is older than on other locations to the north or south on the NIRC fault (Sahakian et al., 2017), as the transgressive surface is not displaced (Klotsko et al., 2015). It is hypothesized that this section of the fault has been inactive for a much longer time period than areas to the north or south and fault activity is estimated to pre-date 100 ka (Sahakian et al., 2017). Furthermore, it is possible that the central section of the NIRC fault has not experienced surface rupture in past events such as the 1933 M 6.4 Long Beach earthquake (Sahakian et al., 2017).

The study area on the slope offshore San Onofre coincides with the San Mateo (SM) Fault Zone, which consists of steeply to moderately northeast-dipping fault strands (Maloney et al., 2016; Conrad et al., 2018). Deformation within the SM Fault Zone includes strike-slip, normal, and reverse offset, with the greatest amount of deformation on the lower slope (Conrad et al., 2018). Many of these faults exhibit crosscutting relationships and are difficult to resolve, which explains differing interpretations of faults across this region (Holmes et al., 2017; Conrad et al.,

2018).

5.3.3 Canyon Systems in the ICB

Three drainages contribute to sediment flux to the margin. The Santa Ana River is located north of Dana Point, has a mean annual suspended sediment flux of 450 Mt a^{-1} (Warrick & Farnsworth, 2009), and feeds directly into Newport Canyon. The Santa Ana River is the largest contributor of sediment in the study area. South of Dana Point, the San Juan Creek has an annual sediment discharge of 98 Mt a^{-1} (Warrick & Farnsworth, 2009) and contributes to the Dana Point Canyon. Just north of San Onofre, the San Mateo Creek discharges 2.7 Mt a^{-1} of sediment (Warrick & Farnsworth, 2009) and is detached from the head of San Mateo Canyon. Previous studies speculate that sediment discharge from the San Mateo Creek were higher in the past, as evidenced by the creek's construction of a subaerial delta (Kennedy & Tan, 2007). Sediment discharge to canyons in the ICB likely increased during the Last Glacial Maximum, when creeks would directly discharge sediment to the canyon head (Covault & Romans, 2009).

Canyons that discharge into the Eastern Gulf of Santa Catalina include the Newport, Oceanside, Carlsbad, San Mateo, and La Jolla canyon-channel systems as well as numerous small gullies (Prins & Postma, 2000; Covault et al., 2007; Covault & Romans, 2009; Normark et al., 2009; Covault & Graham, 2010). It is estimated that about half of the canyons and most of the small gullies were active during the LGM but became inactive during the post-glacial transgression when canyon heads were stranded on the upper slope (Normark et al., 2009). Of these systems, Newport Canyon has been extensively studied by sediment cores in the channel, in the canyon, on the overbank, and at splay elements (Covault et al., 2010). One head on the eastern end of the Newport Canyon remains active as it is fed directly by the Santa Ana River and the San Diego Creek and indirectly by littoral drift from other rivers (Warrick & Farnsworth, 2009; Normark et al., 2009). As the canyon is active, cores recovered near the channel recover recently-deposited turbidites and they lack a hemipelagic drape (Normark et al., 2009). Another

canyon that is presently active is the La Jolla Canyon, which lacks a fluvial source but is instead sourced by littoral drift (Normark et al., 2009). The La Jolla Canyon represents the end of the littoral cell, as it is bounded to the south by resistant Cretaceous rocks that trap sediment (Inman & Brush, 1973; Normark et al., 2009; Le Dantec et al., 2010). During the post-glacial transgression, erosion of the La Jolla Canyon head kept pace with sea-level rise (Normark et al., 2009). Both the Oceanside and Carlsbad canyons were active during the LGM but were drowned during the post-glacial transgression (Normark et al., 2009). Nonetheless, during lowstand intervals such as MIS 2, the Oceanside Canyon may have potentially intercepted littoral drift before it could reach the Carlsbad or La Jolla canyons (Normark et al., 2009). Carlsbad Canyon is not fed directly by any river system and as a result contributed less sediment to the seafloor than the Newport or Oceanside canyons when it was active during MIS 2 (Normark et al., 2009). Its location on a relatively narrow portion of the shelf may have allowed the Carlsbad Canyon to keep pace with shoreline transgression during the early stages of the MIS 2-1 transition (Normark et al., 2009). Gullies on the margin do not appear to correspond to the position of distributary mouths (Piper et al., 1990) and it is proposed that they could form where coastal geomorphology focuses rip currents during storms (Normark et al., 2009). Denudation rates from river catchments illustrated that catchment erosion is much less than the rate of fan deposition (Covault et al., 2011). To account for additional sources of sediment to fans, the authors proposed that additional contributors are littoral transport, sea cliff erosion, and mass wasting of shelf and slope deposits (Covault et al., 2011).

Even though previous studies (e.g., Covault et al., 2011) propose that shelf width is an important control on sediment delivery through submarine canyons, few studies have examined the timing of deposition offshore of San Onofre, a wide shelf in the ICB. Since the publication of Covault et al. (2007, 2011), additional marine seismic surveys have investigated the complex sedimentation and tectonic regimes offshore of San Onofre (e.g., Klotsko et al., 2015; Maloney et al., 2016; Sahakian et al., 2017; Holmes et al., 2017; Conrad et al., 2018; Bormann et al., in

press). Neither the San Onofre North and South canyons nor the Dana Point canyons have been studied in detail; the goal of this study is to understand how deformation on varying spatial scales modulates the timing of sand delivery to the deep sea.

Table 5.1: Radiocarbon ages used in this study.

Core	Depth (m)	Calibrated Age	Uncalibrated Age	Age Error	Type of Foraminifera
GC 13-14	0.19	42860	40000	960	Planktonic
	0.19	45880	44600	1700	Benthic
GC 22-25	1.35	23250	21050	50	Benthic
	2.58	40660	38300	880	Benthic
	2.58	41880	38700	910	Planktonic
GC 23-26	1.29	12810	13100	40	Benthic
	1.29	9460	9180	25	Planktonic
	2.12	8850	10050	30	Benthic
	2.12	10300	9480	30	Planktonic
JPC 15-16	1.87	13400	13700	45	Benthic
	2.04	13360	13650	55	Benthic
	2.10	16530	14800	60	Planktonic
	2.16	14270	14450	45	Benthic
	2.30	13880	14150	60	Benthic
	3.18	17670	15600	55	Planktonic
	3.18	17670	16650	65	Benthic
	3.32	18170	17100	65	Benthic
	3.32	18060	15950	60	Planktonic
	4.09	17480	16500	50	Benthic

Table 5.1 (continued): Radiocarbon ages

Core	Depth (m)	Calibrated Age	Uncalibrated Age	Age Error	Type of Foraminifera
JPC 19-21	3.48	13450	13750	45	Benthic
	3.59	13880	14150	40	Benthic
	5.32	18890	17800	80	Benthic
	5.48	19300	18150	75	Benthic
	7.29	25830	23700	150	Benthic
	7.39	26270	24200	160	Benthic
	7.68	27620	25600	200	Benthic
	7.74	27840	25900	200	Benthic
	7.74	33140	30100	320	Planktonic
JPC 26-30	2.10	13160	13015	40	Benthic
	4.30	20260	18540	60	Benthic
	7.20	27500	25400	140	Benthic
	7.38	28780	26900	150	Benthic
	7.38	28930	26000	130	Planktonic
	8.43	33870	31900	390	Benthic
	8.51	34200	32300	410	Benthic
	9.15	35450	33700	490	Benthic
GC 35-40	0.78	570	2730	20	Benthic
	0.96	820	3030	20	Benthic
	1.41	1680	3850	20	Benthic
	1.94	2790	4760	20	Benthic
	2.13	3180	5080	25	Benthic

Table 5.1 (continued): Radiocarbon ages

Core	Depth (m)	Calibrated Age	Uncalibrated Age	Age Error	Type of Foraminifera
GC 35-40	2.83	5260	6680	30	Benthic
	2.98	5760	7140	25	Benthic
JPC 32-36	0.44	1030	3230	20	Benthic
	5.22	15540	15150	45	Benthic
	5.37	15990	15450	50	Benthic
	7.94	18890	17800	85	Benthic
JPC 33-38	4.00	10770	10230	25	Planktonic
	6.10	13960	13180	45	Planktonic
	7.22	18010	16950	210	Benthic
	7.60	16320	15700	70	Benthic
	7.77	15860	15350	60	Benthic

5.4 Methods

2D multi-channel seismic reflection data were collected in August 2013 on the R/V New Horizon and R/V Melville using a 2 kJ three-tip EG&G sparker source and 48-channel streamer. Group spacing of 6.25 m and 6.25 m shot spacing allows reflectors to be resolved to approximately 1.5 s two-way travel time (Sahakian et al., 2017). Data were stacked at 1500 m/s and processing included poststack f-k migration using a water velocity of 1500 m/s (Driscoll et al., 2018; Sahakian et al., 2017). Based on observations from the 2D dataset, a high-resolution 3D data set was acquired using a 3D P-Cable system with 14 streamers with 8 channels per streamer, 6.25 m group spacing, 3.125 m shot spacing, and a 2 kJ three-tip EG&G sparker source (Holmes

et al., 2017). This study uses a data grid of 39 km^2 collected over the continental slope and the data are published in Driscoll et al. (2018) and Sahakian et al. (2017). 3D data were processed by Geotrace Technologies, a petroleum services company, due to the large size of the data volume. Additionally, 546 km of Compressed High Intensity Radar Pulse (CHIRP) data were collected in 2016.

In January 2016, 64 Gravity (GC) and Jumbo-piston cores (JPC) were collected onboard the R/V Thompson as part of a study designed to evaluate hazards such as recent faulting. The survey and coring targets were designed to image faults and paleochannels that could potentially serve as piercing points. Trigger cores were deployed with the JPCs. GC and JPC targets were selected from previously-collected Sparker and Boomer Multichannel as well as CHIRP seismic profiles. In some cases, drift in ship position caused the cores to be offset from the profiles, in which case the core locations were projected orthogonally onto the profile. On board, whole intact cores were scanned for magnetic susceptibility, gamma density, P-wave velocity, and resistivity using a GeoTek Core-logger. Cores were split and observations of color, grain size, sediment structures, and general lithology were recorded.

A total of 116 samples at 96 unique depths were collected for radiocarbon dating, preferentially from planktonic foraminifera (Table 5.1). As some samples did not contain sufficient planktonic foraminifera for age dating, mixed benthic foraminifera were used in these samples. Fragmented foraminifera and foraminifera that showed signs of diagenesis were avoided. For 20 samples, both planktonic and benthic samples were collected in order to define a reservoir age. 110 samples were analyzed at the National Ocean Sciences Accelerator Mass Spectrometry facility at the Woods Hole Oceanographic Institution and produced an age using the Libby half-life of 5568 years and following the convention of Stuiver & Polach (1977). 6 samples were analyzed at the WM Keck Carbon Cycle Accelerator Mass Spectrometry facility at the University of California Irvine following the same conventions. The ^{14}C ages were converted using the CALIB program version 7.0.4 (Stuiver & Reimer (1993)) with a reservoir age of 800

for planktonic foraminifera <12,000 yr and a reservoir age of 1100 for planktonic foraminifera >12,000 yr (Southon et al., 1990; Kienast & McKay, 2001; Kovanen & Easterbrook, 2002). Based off the 20 samples that acquired ages for both benthic and planktonic foraminifera, we calculated an average difference in reservoir age of 900 years. For this difference in reservoir age, benthic foraminifera <12,000 year would have a reservoir age of 1700 yr, which is comparable to the reservoir age of 1750 for benthic foraminifera used by Mix et al. (1999), Covault et al. (2010), Brothers et al. (2015), and others. Thus, we used this value of 1750 years for a benthic reservoir age. Radiocarbon ages were sampled from fine-grained sediment above and/or below sand layers so that the age of the sand layer represented an average of these bracketing ages. Age-depth models for cores containing more than 2 dates were constructed using the Bacon software version 2.3.3 (Blaauw & Christen, 2011) using the same reservoir ages as mentioned above and calibration using the Marine 13 curve. This version of the Bacon software allows users to input abrupt events of sedimentation such as slumps and turbidites (Blaauw & Christen, 2011). The bounding depths of sand layers with abrupt basal contacts were inputted into the software as rapid periods of deposition in the age-depth models. If sand layers were bound by radiocarbon dates, the date of the sand layer was taken as an average of the corrected dates. If the sand layers were lacking bracketing radiocarbon ages, the age-depth model produced by the Bacon software was employed to determine the age of the middle of the sand layer.

5.5 Results

5.5.1 San Onofre North and South (SON and SOS) Canyon-Channel Geomorphology

Bathymetric profiles through the SON and SOS canyons reveal the marked variability in dip (Figs. 5.2A and B). The SON Canyon is characterized by a steep concave-up profile (average

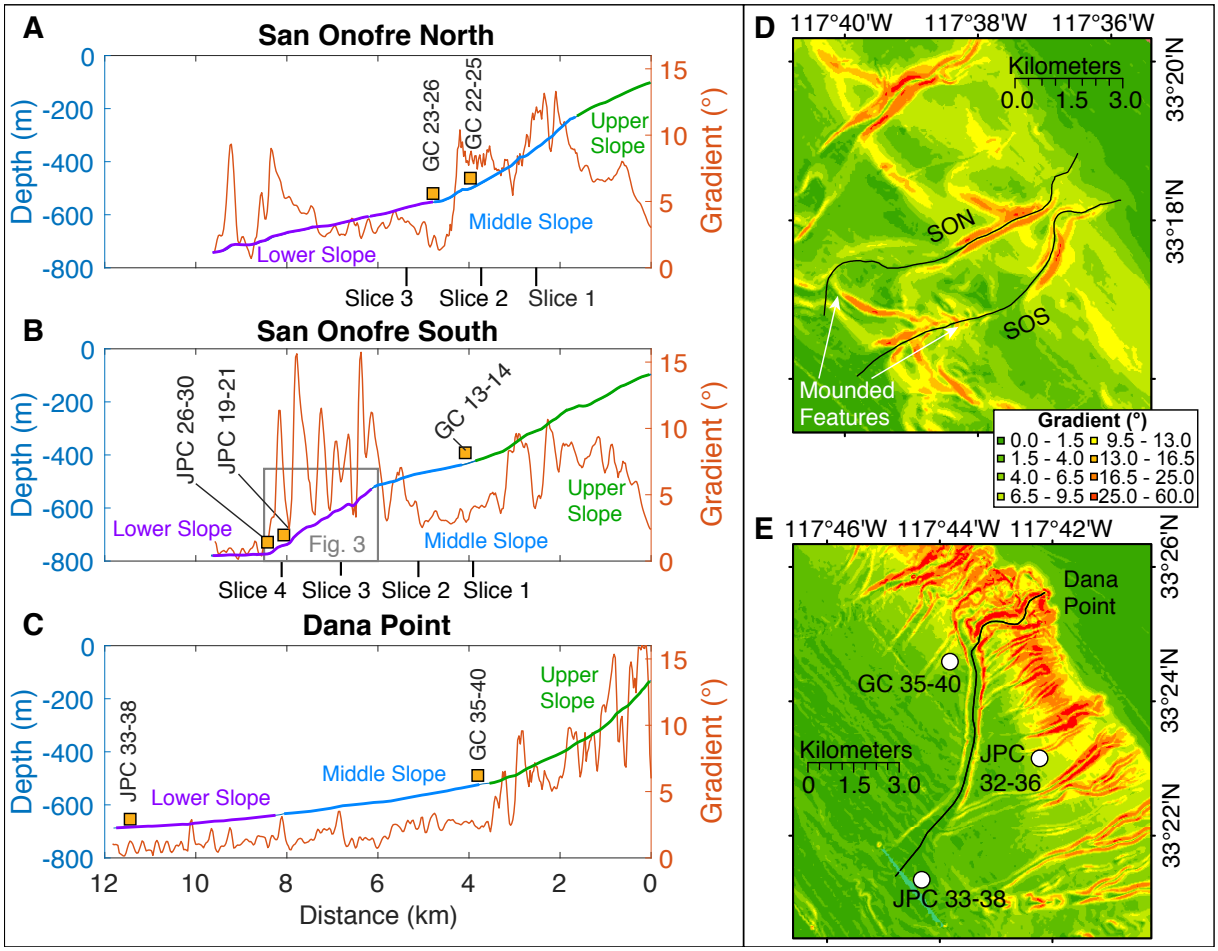

Figure 5.2: A, B, C) Bathymetric profiles of the San Onofre North, San Onofre South, and Dana Point Canyons are juxtaposed on the channel gradient. The channel profiles are subdivided into the Upper, Middle, and Lower slope. The location of sediment cores are highlighted by the yellow squares. The intersections of Sparker 3D seismic slices are shown by the vertical black lines. In B, the location of Figure 3 is highlighted. D, E) Maps of the slopes offshore of San Onofre and Dana Point SON = San Onofre North, SOS = San Onofre South. Green colors represent gentler slopes and red colors represent steeper slopes. The bathymetric profile through the channel is shown by the black line.

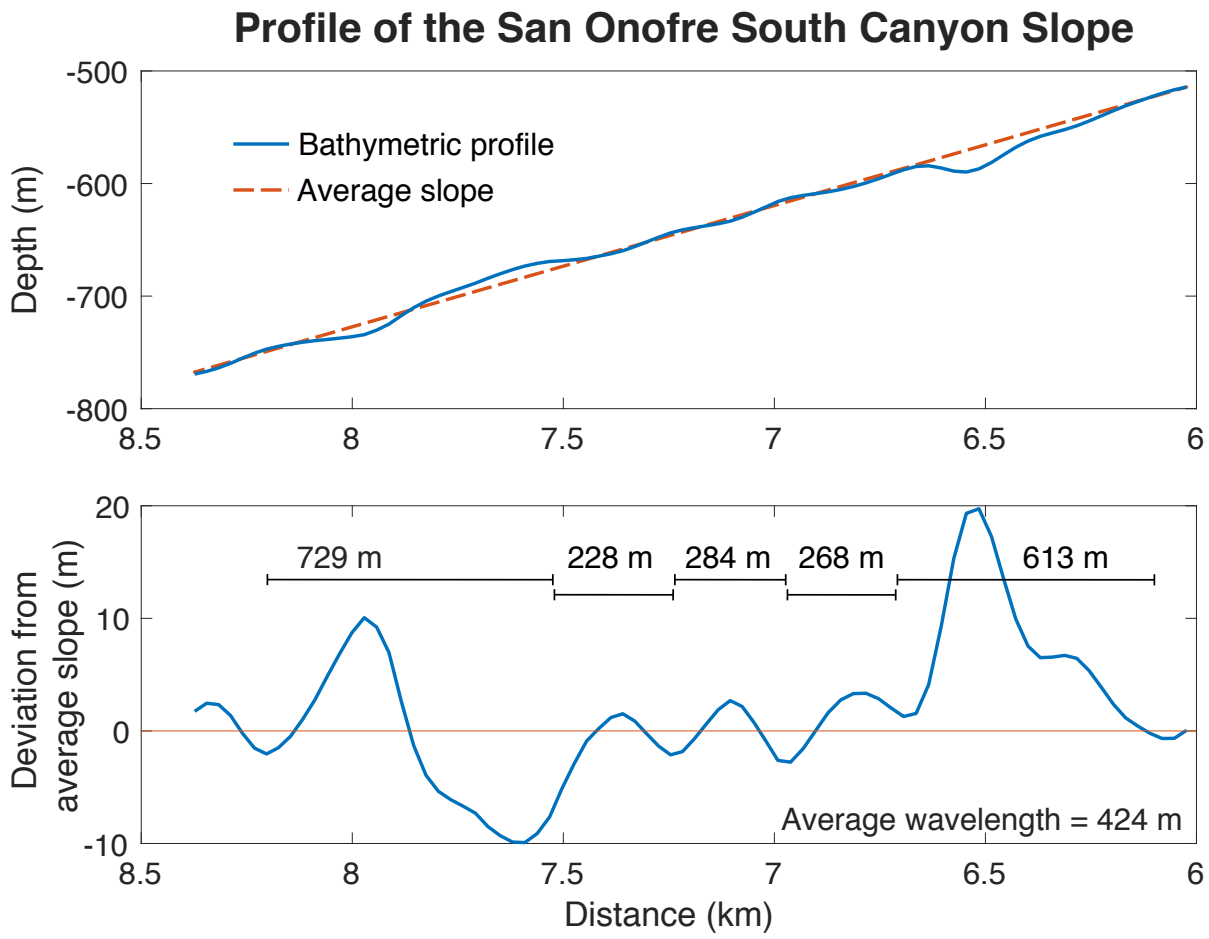

Figure 5.3: Top: the bathymetric profile from the lower slope of the San Onofre South Canyon is plotted in blue and has undulatory features. The dashed orange line is the average slope for this length of the canyon. Bottom: Subtracting the average slope from the bathymetric profile reveals undulatory features with amplitudes ranging from 2-15 m and wavelengths ranging from 228-729 m.

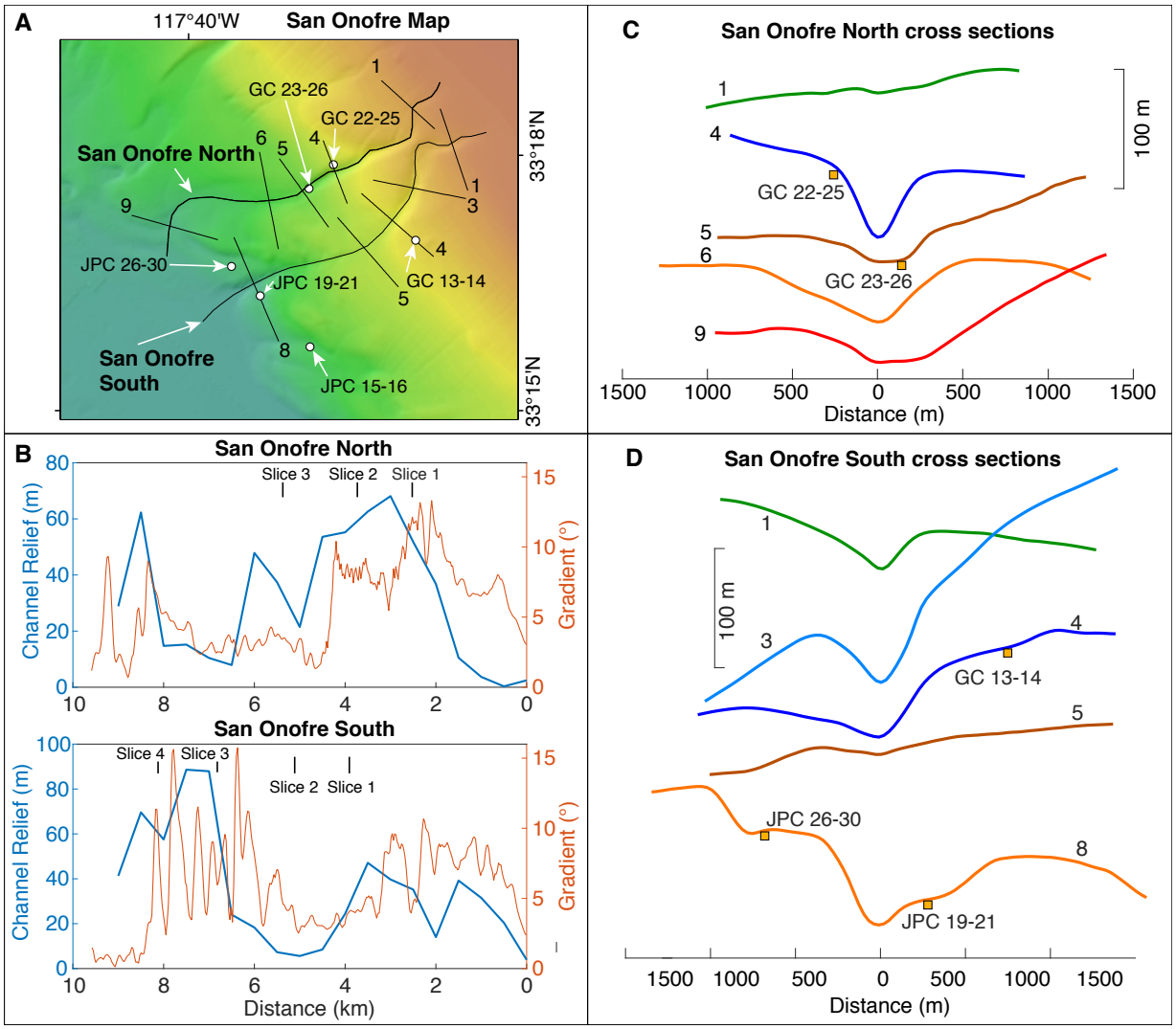

Figure 5.4: A) Map of the San Onofre North (SON) and South (SOS) Canyons. Cross-sections numbers correspond to their distance from the start of the bathymetric profile and are shown in C and D. Sediment cores are labeled. B) Channel relief is plotted relative to channel slope for the two canyons. The intersections of the 3D Multichannel Sparker slices with the canyons are indicated at the top of the plots. C and D) Cross sections through the SON and SOS canyon-channels are plotted. Horizontal and vertical scales are shown. Yellow boxes indicate the location of sediment cores along the cross-section.

$\sim$ 13°) in the middle slope between the depths of 240-680 m (Fig. 5.2A). Within the middle slope, gradient increases to as high as 13°. The lower slope has a gentler gradient of 4.4° with a few irregularities in the last 8-10 km of the channel that increase the slope to $\sim$9° for short distances (Fig. 5.2A). The characteristic feature of the SOS Canyon is the gently-sloping and smooth terraced feature (average $\sim$4.5°) in the middle slope between the depths of 430-480 m (Fig. 5.2B). Above the terraced feature, the average gradient of the upper slope is $\sim$7.7° and below the terraced feature, the average gradient of the lower slope is $\sim$7.4°. The upper slope has a few mounded features that cause the channel gradient to increase to $\sim$12° (Fig. 5.2B). The lower slope has higher rugosity than the upper or middle slopes and reveals undulatory bathymetric features between 500-800 m that increase channel gradient for short distances (Figs. 5.2B and 5.3). On the slope map, these appear as crescentic features that are perpendicular to the SOS canyon and exhibit higher slopes (Fig. 5.2D). Subtracting the average slope from the bathymetric profile reveals five mounded features, with two high-amplitude mounds of 10-20 m and three low-amplitude mounds of $\sim$2m (Fig. 5.3). The average wavelength of the three low-amplitude mounds is $\sim$260 m, whereas the two larger mounds have higher wavelengths (Fig. 5.3).

The SON and SOS channels exhibit changes in channel depth, shape, and gradient downslope, with narrow v-shaped channels in the middle slope and wider valleys in the lower slope (Fig. 5.4). This finding is consistent with other canyon-channel systems on the California margin and worldwide (e.g., Menard Jr, 1955; Normark, 1970; Covault et al., 2011). Both canyon-channels exhibit a linkage between deeper channel depths and steeper channel gradients (Fig. 5.4B). The shape of the channels also varies downslope, with an evolution from narrow v-shaped in the upper slope to broad valleys in the lower slope as exhibited in bathymetric cross sections (Figs. 5.4C and D). At 4 km, the SON channel is v-shaped and its channel depth of $\sim$55 m corresponds to increases in channel slope between 2-4 km (Figs. 5.4B and C). The shift from v-shaped channels to broader valleys occurs around 5 km for the SON channel and corresponds to decreasing slope (Fig. 5.4B and C). In the lower slope from 8-10 km, both channel depths and

valley width increase (Fig. 5.4B). The transition from narrow v-shape to broader valleys for the SOS channel occurs between 3-4 km, as the cross-section at 3 km has a v-shape with steep limbs and the cross-section at 4 km has asymmetrical limbs with gentler-sloping limbs (Fig. 5.4D). The SOS cross-section at 5 km is shallow and narrow. In the lower slope, an increase in channel gradient appears to correspond to deeper and wider channels, as evidenced at the cross-section at 8 km (Figs. 5.4B and D).

5.5.2 Stratigraphy of the San Onofre slope

Sparker dip profiles through the study area reveal the internal structure of sediment packages along the slope. Four sediment units were delineated based on sequence stratigraphic principles (e.g., Vail et al., 1977; Mitchum Jr et al., 1977; Christie-Blick & Driscoll, 1995). The upper boundaries of many of the packages can be defined by toplapping reflectors against the base of the overlying unit. The uppermost sediment package on the slope is the Pink Unit that infills local bathymetric lows in all dip profiles and pinches out where there are local bathymetric highs (Fig. 5.5). In strike profiles, the Pink Unit exhibits continuous high-amplitude reflectors that distinguish it from the underlying Blue Unit (Figs. 5.6A and B). In dip profiles, the underlying Blue Unit also infills local bathymetric lows and is not present everywhere on the slope (Fig. 5.5). Its discontinuous, low-amplitude reflectors in strike profiles exhibit toplap, especially over bathymetric highs (Figs. 5.6A and B). Orange Unit reflectors exhibit toplap in dip Line 11 against the Blue Unit (Fig. 5.5A), and in dip Line 53, flat-lying reflectors in the Blue Unit terminate against the Orange Unit (Fig. 5.5C). Green Unit reflectors exhibit some toplap against the overlying Orange Unit around 5 km in dip Line 53 and around 7 km in dip Line 13 (Figs. 5.5C and D). The lower boundary of the Green Unit is a high-amplitude reflector that can be traced throughout strike and dip profiles (Figs. 5.5 and 5.6). As this survey is focused on recent channel dynamics and slope processes, sediment packages below the Green Unit were not interpreted.

Dip profiles through the survey area (Fig. 5.5) reveal that in general, portions of the

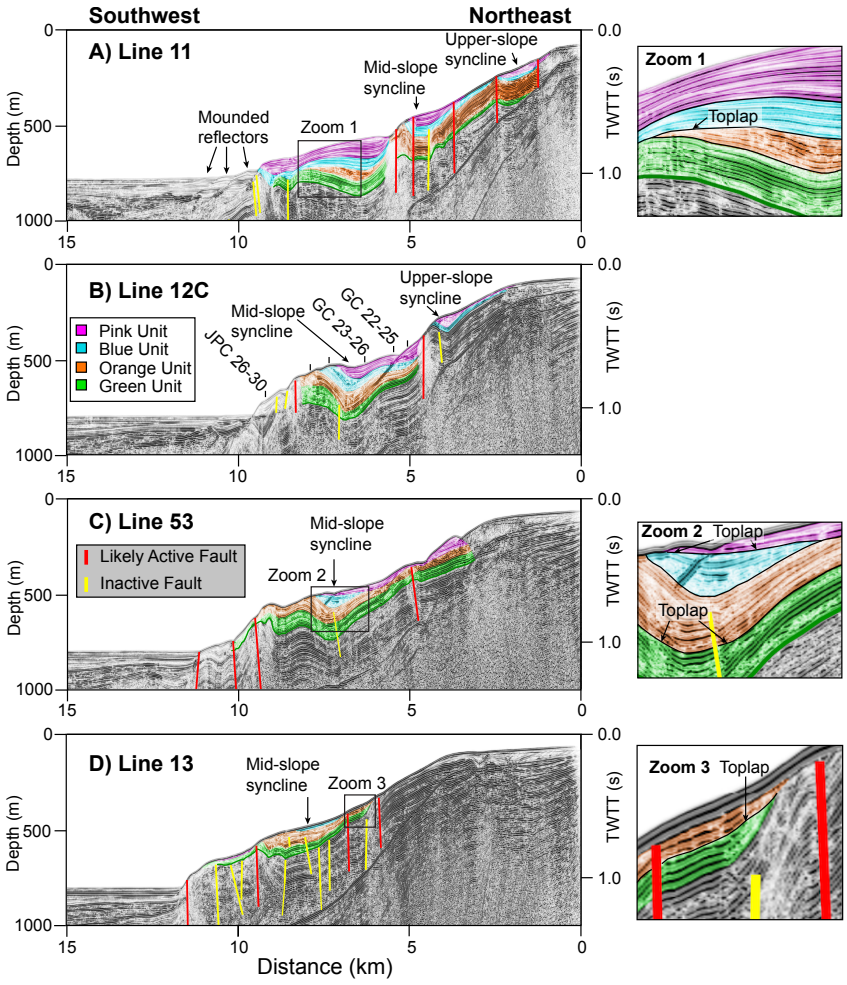

Figure 5.5: Sparker seismic dip profiles offshore San Onofre reveal the internal structure of the slope and are organized with the northernmost profile at the top and southernmost profile at the bottom. Colors of Units are shown in panel A. Active faults are shown in red and Inactive faults are shown in yellow. Locations of lines are shown in Figure 5.1. At right are enlargements of areas that show toplapping relationships. Vertical Exaggeration = 5.6.

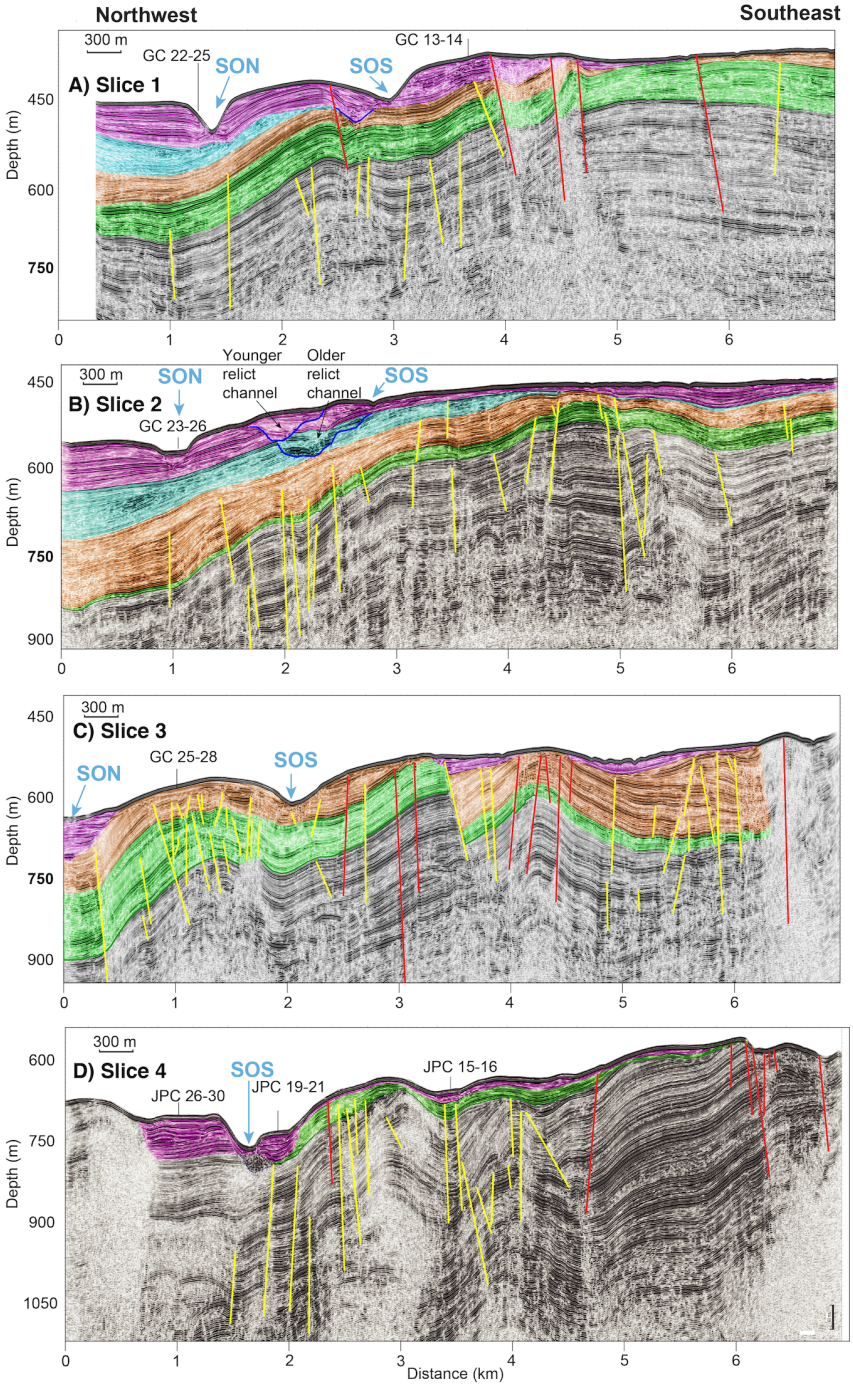

Figure 5.6: Strike slices along the San Onofre margin reveal the internal architecture of the slope and channel elements. The shallowest (easternmost) slice is at the top and the deepest slice (westernmost) is at the bottom. Locations of lines are shown in Figure 5.1. Vertical Exaggeration = 5.1.

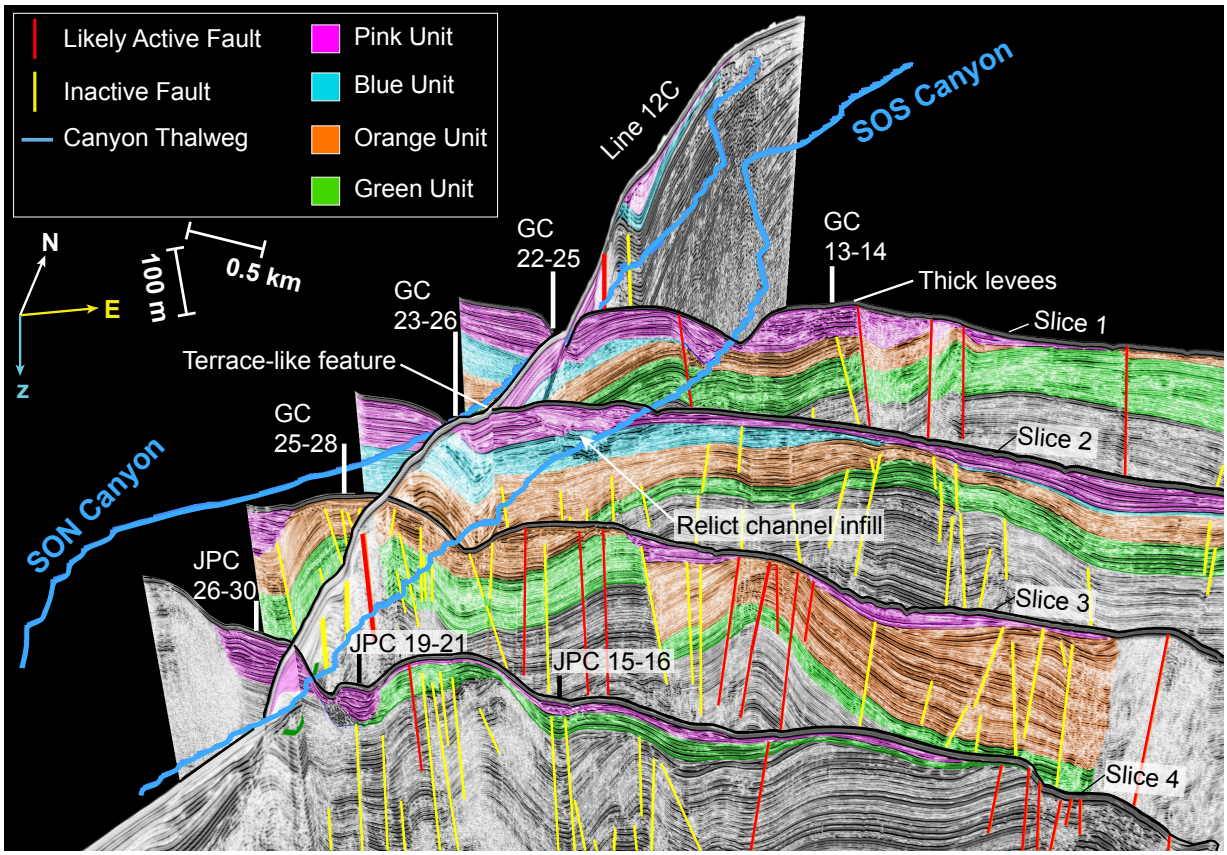

Figure 5.7: A 3D seismic fence diagram with a Sparker 2-D seismic profile and Sparker 3D slices. The locations of the two canyons are traced in blue. Colors denote sediment units, with the Pink unit as the youngest and the Green unit as the oldest. Likely active faults are shown in red and inactive faults are shown in yellow. Locations of cores are plotted as white or black lines. Vertical Exaggeration = 6.

slope with steep gradients are along anticline limbs. Portions of the slope with gentler gradients correspond to infilled local synclines. Upper slope synclines with a NW-SE trend appear only in the two northern dip profiles (Fig. 5.5A and B). Two faults bounding the upper-slope syncline in Line 11 appear to deform Orange, Blue, and Pink Units. Both faults appear to have a bathymetric expression, with transtension across the northeastern fault causing extension and transpression across the southwestern fault causing slight uplift (Fig. 5.5A). Older reflectors within the Orange Unit appear to be conformable; however, younger reflectors within the Orange and Blue Units thicken towards the western fault (Fig. 5.5A). Younger Pink Unit sediment progrades into the upper-slope syncline in Line 11 (Fig. 5.5A). The upper-slope syncline in Line 12C does not appear to have been deformed by recent faulting and a fault on the southwestern side of the syncline deforms sediment underlying the Blue Unit (Fig. 5.5B). Blue Unit reflectors within the Line 12C upper-slope syncline are conformable, whereas Pink Unit reflectors thicken towards the southwest limb of the syncline (Fig. 5.5B). These upper-slope synclines are separated from a mid-slope syncline by an anticlinal structure that is cross-cut by a recent fault and obscured by gas-wipeout (Figs. 5.5A and B). In contrast to the upper-slope syncline, the mid-slope syncline is observed in all dip profiles and coincides with a reduction in seafloor gradient (Fig. 5.5). Note that the local mid-slope and upper-slope synclines are completely infilled by sediment (Fig. 5.5). Deformation within the mid-slope syncline appears to have along-margin variability. In Line 11, reflectors within the Green, Orange, Blue, and Pink units are offset by recent faults (Fig. 5.5A) and reflectors within the Pink and Blue Units appear to thicken towards the southwestward fault (Fig. 5.5A). Active faults bound the syncline in lines 12C, 53, and 13; nevertheless, faults cross-cutting the mid-slope syncline appear to have deformed only the Green and Orange units (Figs. 5.5A, B, and C). In these three lines, only Green and Orange units exhibit sediment thickening towards cross-cutting faults in the mid-slope syncline (Figs. 5.5A, B, and C).

The southwestern side of the mid-slope syncline is bounded by an anticline with steeply dipping limbs; this anticline is best imaged in Lines 12C and 53 (Fig. 5.5B and C). Reflectors pinch

out upslope of the anticline and recent sediment cover thins downslope. The southwestern limb of this anticline contributes to the steep gradient of the lower slope. At the slope-basin transition, recent sediment onlap slope deposits (Fig. 5.5B). This recent sediment has an undulatory bathymetric expression and appears to step northeast through time (Fig. 5.5A). The most seaward undulatory feature is onlapped by aggrading reflectors (Fig. 5.5A).

Four slices from 3D P-Cable data oriented along-strike to the margin reveal that the most prominent feature shaping the slope offshore of San Onofre is a prominent NW-SE trending anticline that is clearly imaged in Slice 2 (Fig. 5.6B). The anticline crest is located to the southeast of the SON and SOS canyons and sediment thins across the crest (Fig. 5.6B). Away from the crest, sediment units thicken to the northwest. The Green and Orange units are cross-cut by numerous faults that offset seismic reflectors and create localized deformation. Downslope in Slice 3, faulting and deformation may extend to the seafloor, and the southeast flank of the SOS canyon-channel appears to have seafloor expression of uplift (Fig. 5.6C). Blue and Pink Units are thicker in the middle slopes in Slices 1 and 2, and the Blue Unit is not present in Slices 3 and 4 (Fig. 5.6).

Variations in slope may exert influences not only on channel shape but also whether there is aggradation or incision into recent Pink Unit deposits. Pink Unit deposits adjacent to the SON channel have aggradational reflector character in Slices 1-3 (Figs. 5.6A, B, and C). The SON channel is perched, with over 16 m of aggradational Pink Unit deposits in Slice 1 and the channel truncates horizontal reflectors within the upper Pink Unit (Fig. 5.6A). In Slice 2, the SON channel is perched over 18 m of Pink Unit deposits, above which a u-shaped feature is infilled with chaotic reflectors (Fig. 5.6B). Aggradational Pink Units bounding the SON channel to the northwest have maximum thicknesses of 82 m in Slice 1 and 87 m in Slice 2, and diminish in thickness to the southeast adjacent to the SOS channel (Fig. 5.6B). Broadening in Slice 3, the SON channel has a base of a thick Pink Unit deposit that unconformably aggrades into a NW-SE trending synform (Fig. 5.6C). The SON channel is not present in Slice 4 (Fig. 5.6D). Reflectors in the Pink

Unit surrounding the SOS channel exhibit more variability. In Slice 1, the SOS channel has an asymmetric v-shape that is adjacent to dipping wavy reflectors in the Pink Unit to the northwest and conformable reflectors to the southeast (Fig. 5.6A). In Slice 2, the SOS channel is extremely narrow and shallow, and is bordered to the northwest by chaotic deposits (Fig. 6B). The SOS channel width and floor width broaden downslope in Slice 3, where the channel appears to be located in a local syncline and truncates reflectors in the Orange Unit (Fig. 5.6C). In Slice 3, note the lack of Pink Unit deposits adjacent to the channel. In the lower slope Slice 4, the SOS channel exhibits asymmetry, with thick aggradational deposits to the northwest and thinner aggradational deposits to the southeast that form a bench-like feature (Fig. 5.6D).

Deformation on this margin is complex, as evidenced by the multiple NW-SE trending synclines that create local accommodation (Fig. 5.5), NW-SE trending anticlines that correspond to increases in slope gradient (Fig. 5.5), and a prominent NW-SE trending anticline that appears to exert control on SON and SOS locations as well as Pink Unit thickness (Fig. 5.6). 3-dimensional seismic fence diagrams provide an unprecedented view of the synclines and anticlines (Fig. 5.7). Overall, the SON and SOS channels are located on the flank of the broad NW-SE trending antiform in Slices 1 and 2 in the middle slope (Figs. 5.6A, B, and 5.7). The SON channel is located at deeper depths than the SOS channel and in Slices 1-2, the Pink, Blue, Orange, and Green Units thicken (Figs. 5.6A, B, and 5.7). In contrast, accommodation for the SOS channel is limited, as it is located proximal to the antiform. The lack of accumulation adjacent to the SOS channel in Slices 1-2 is coincident with its v-shape and as the SOS channel moves into a synform in Slices 3-4, channel width increases (Figs. 5.6A, B, and 5.7).

5.5.3 San Onofre Sediment Core Facies and Chronology

Cores offshore of San Onofre can be grouped by their depth on the middle slope (300-600 m) or on the lower slope (600-1000 m). Note that few cores were recovered on the upper slope due to high sand content. Most of the cores are composed of clay or silty clay that are punctuated

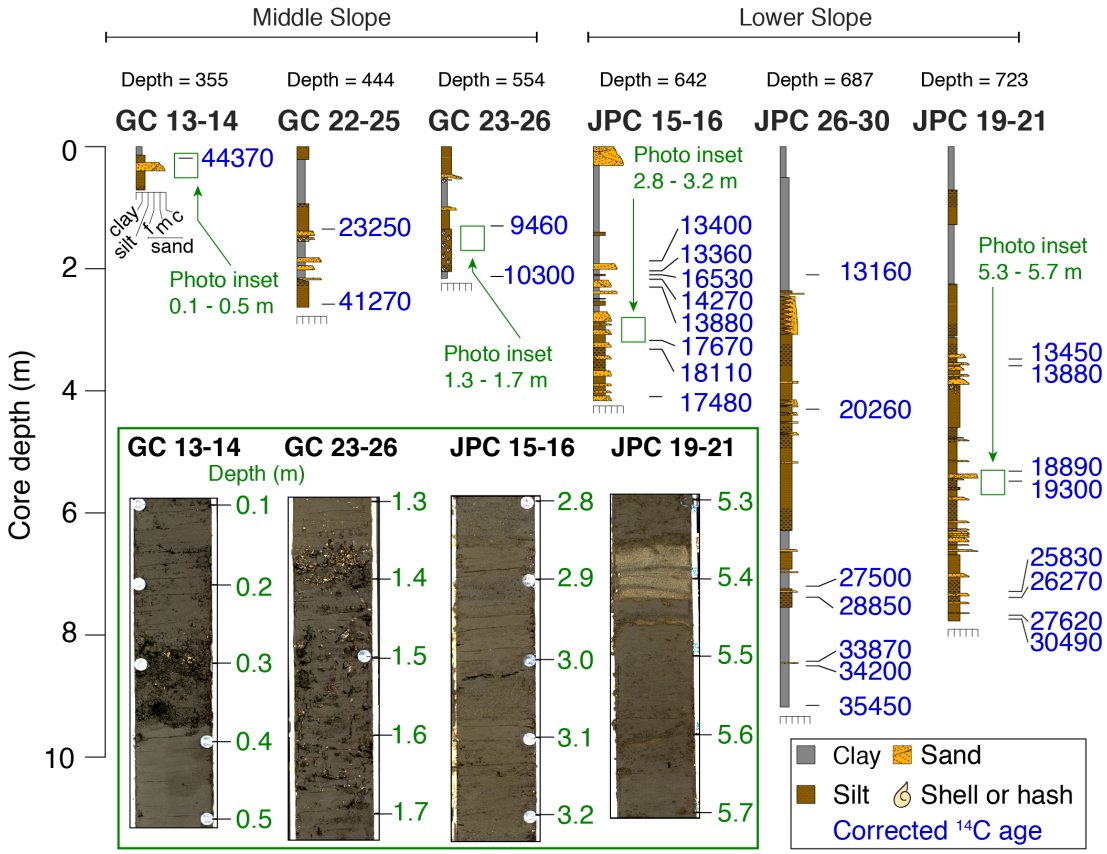

Figure 5.8: Schematic diagrams of San Onofre cores. Labeled grain size scale is shown under GC 13-14 and unlabeled scales are shown under all other cores. Corrected radiocarbon ages are shown to the right of the cores. At the bottom left, photo insets of select cores are plotted with their depth. The locations of the photo insets are shown relative to core diagrams by the outlined green rectangles.

by thin (<1 cm) to thick (10's of cm) sand layers. With the exception of JPC 15-16, most of the cores offshore of San Onofre are capped by tens of cm to meters of clay or silty clay (Fig. 5.8). In JPC 26-30, the base of the upper clay section is dated to approximately 12.9 kyr, 22.9 kyr in GC 22-25, and 44.5 kyr in GC 13-14 (Fig. 5.8). Underlying these caps of clay or silty clay are interbedded muds and sands. Sand layers in the cores are commonly observed to have sharp, erosive basal boundaries and gradational upper boundaries; however, the basal boundary was occasionally diffuse. Often, sand layers are characterized by color changes, as noted by the change from olive green to tan in the photo of JPC 19-21 (Fig. 5.8 photo inset). Some of the sand layers also contained shell hash in GCs 22-25 and 23-26 from the middle slope (Fig. 5.8). Cores from the middle slope generally contain fewer and thinner sand layers than cores recovered from the lower slope (Fig. 5.8).

GC 13-14 on the middle slope contains only one sand layer composed of sandy silt with gravel and shell hash (Fig. 5.8 photo inset). The sandy silt and shell hash were likely deposited before the overlying layer with a radiocarbon age of 44.5 ka. Approximately 90 m downslope, the middle portion of GC 22-25 contains 5 sand layers that fine upward with grain sizes ranging from fine to coarse sand. Radiocarbon dates bracketing the five sand layers suggest that they were deposited between 22.3-41.3 ka (Fig. 5.8). GC 23-26, recovered from the SOS channel thalweg (Fig. 5.5B), is composed of an upper silt cap, two sand layers composed of fine sand that are separated by 40 cm of clay, and blocky silt with shell hash in the lower sections of the core. Shell hash is interbedded with silt in GC 23-26 and the concentration of shell hash decreases downsection beginning at 1.4 m (Fig. 5.8 photo inset). The silt with shell hash is dated between 9.5 and 10.3 ka.

JPCs 15-16, 26-30, and 19-21 were recovered from the lower slope (Figs. 5.6D and 5.8) and are longer cores that contain 13, 14, and 23 sand layers respectively. The upper 30 cm of JPC 15-16 contains an upward-fining sand layer with coarse sand at the base. Below that is $\sim$ 160 cm of clay and silt. The lower 2.5 m of JPC 15-16 is characterized by sand layers with fine

to medium sand that are interbedded with silt and clay. Sand layers in the middle of the core tend to be thinner and were deposited between 13.5-14 ka. Sand layers increase in frequency and thickness in the lower 1.5 m in the core with ages ranging between 17.8 and 18.2 ka. Constraining the exact timing of sand layer deposition is difficult in this core, as ages are inverted. As such, dating of the layers was conducted using age models calculated by the R Bacon package. The upper 2.5 m of JPC 26-30 is capped by clay. Below this, fine sand is interbedded with silt. In the lower portion of the core, thin layers of fine sand predate MIS 2. Overall, sand layers in JPC 26-30 are less frequent and separated by longer intervals than those in JPCs 15-16 or 19-21. Sand layers within JPC 19-21 at 5.3 m depth have a lighter color than the surrounding silt and exhibit sharp basal and upper contacts (Fig. 5.8 photo inset). The upper 3.4 m of JPC 19-21 consists of silt and clay and between 3.4-3.9 m is a cluster of 5 sand layers. Around 6 m, sand layers are closer together and thicken until the bottom of JPC 19-21, where sand layers are spaced farther apart and consist of fine sand (Fig. 5.8).

5.5.4 Dana Point Canyon-Channel and Core Stratigraphy

The narrow shelf ($\sim$ 2 km) offshore of Dana Point separates the head of Dana Point Canyon from San Juan Creek (Fig. 5.1C). Dana Point Canyon has two branches at the head of the canyon and one broad meander before it joins Newport Canyon in the basin (Figs. 5.2E and 5.9A). Three cores, GCs 35-40, and JPCs 32-36 and 33-38 were collected adjacent to the Dana Point Canyon (Fig. 5.1C and 5.9A). Sparker seismic surveys do not extend into this area and therefore, most of our interpretations on geomorphology are based off limited CHIRP seismic coverage and multibeam bathymetry.

The bathymetric profile of the Dana Point Canyon is generally concave-up with a steep upper slope (5-15°), and gentler gradients on the middle and lower slopes (0-3°; Fig. 5.2C). Steep gradients in the upper slope coincide with greater channel relief and canyon-channel depth dramatically decreases between 3-4 km as gradient decreases (Fig. 5.9B). This transition occurs

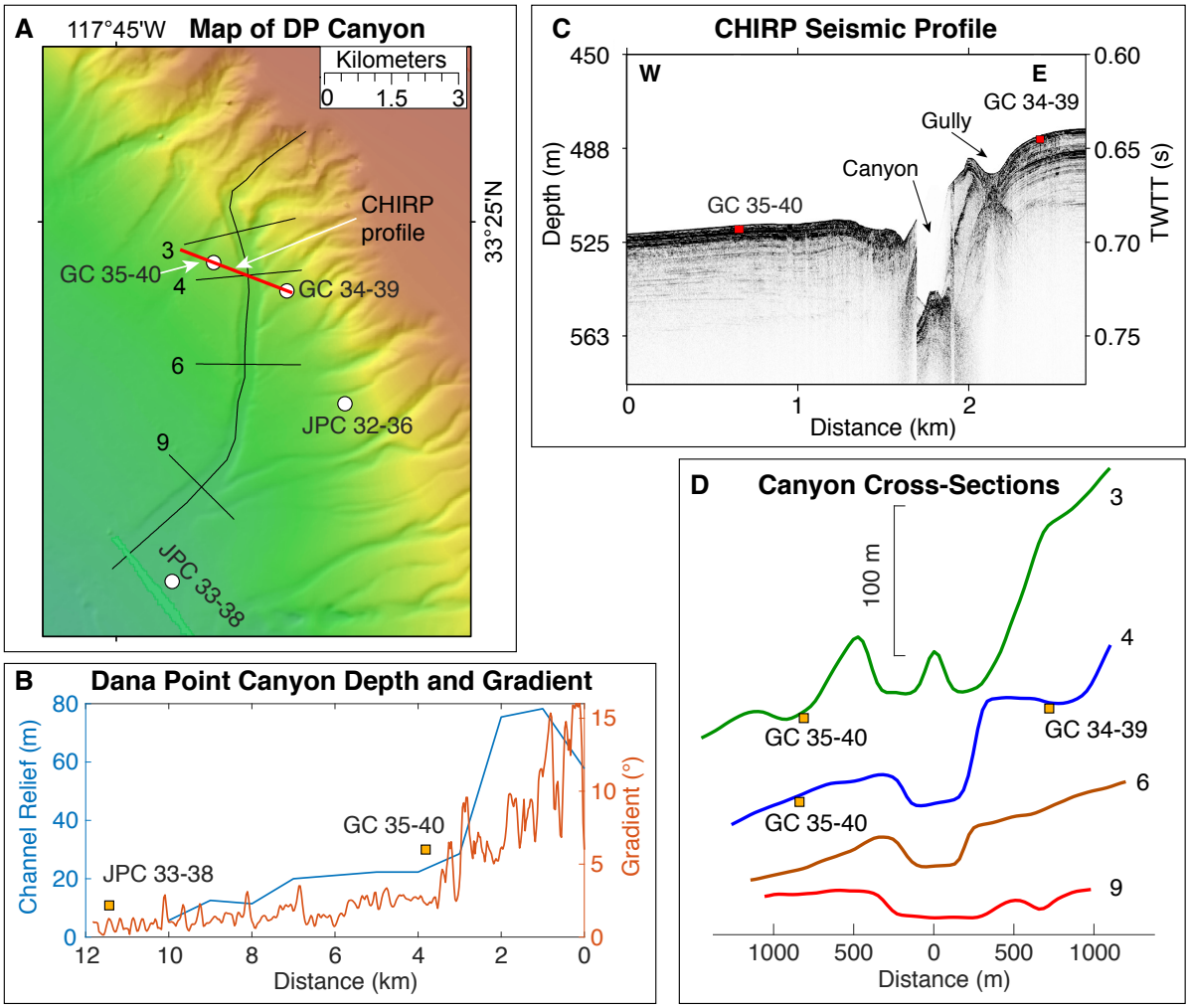

Figure 5.9: A) Map of the Dana Point Canyon. The location of the CHIRP profile shown in B is highlighted in red. Cross-sections numbers correspond to their distance from the start of the bathymetric profile and are shown in D. Sediment cores used in this study are also labeled. B) Channel relief is plotted relative to channel gradient. Yellow boxes indicate the location of sediment cores along the bathymetric profile. C) CHIRP seismic profile through GCs 35-40 and 34-39. D) Cross sections through the DP canyon-channel are plotted. Numbers at right correspond to the distance along the bathymetric profile. Horizontal and vertical scales are shown. Yellow boxes indicate the location of sediment cores along the cross-section.

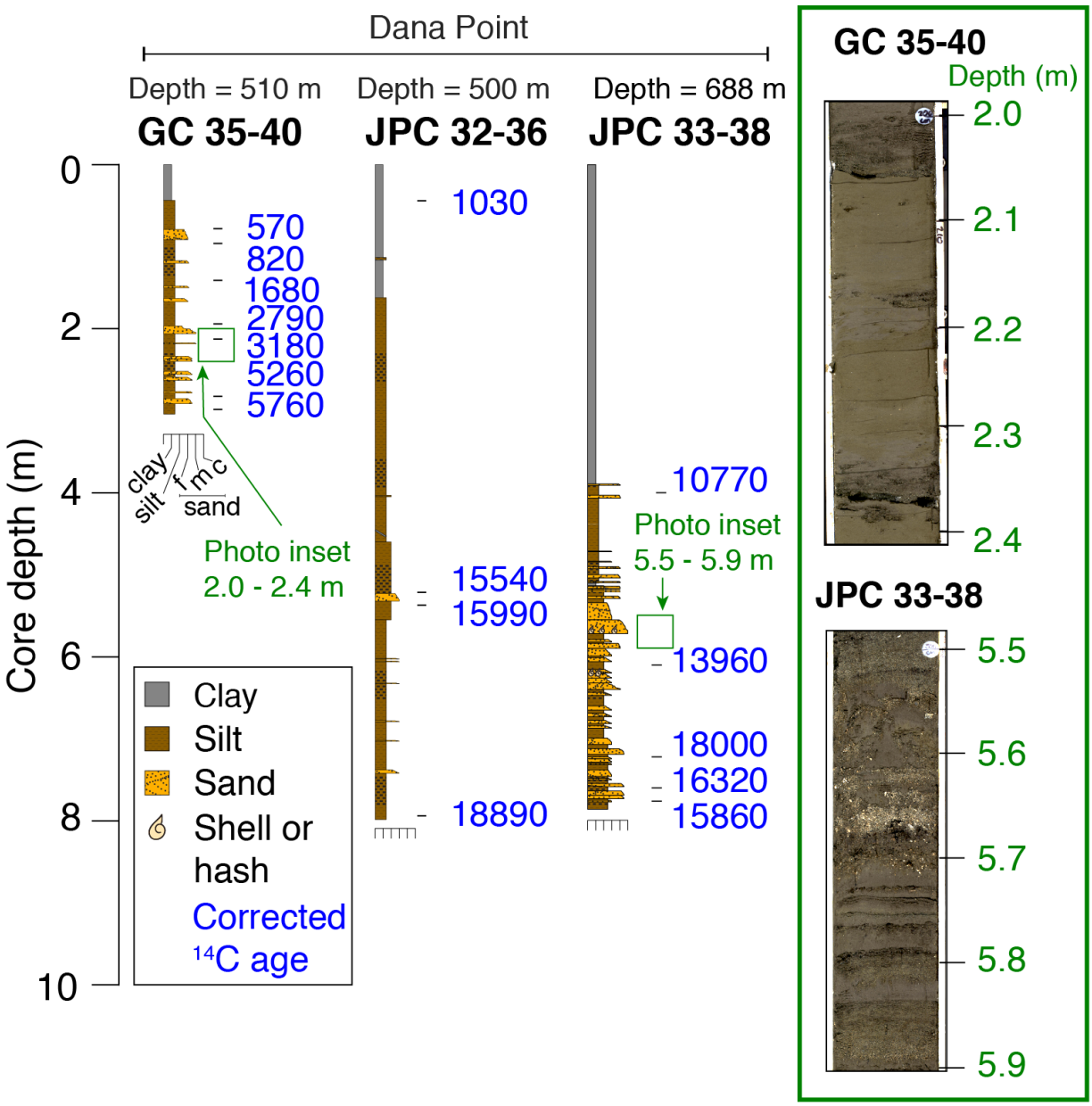

Figure 5.10: Schematic diagrams of Dana Point cores. Grain size scale is shown under GC 35-40. Unlabeled grain size scales are shown below all other cores. Corrected radiocarbon ages are shown to the right of the cores. At right, photo insets of select cores are plotted with their depth. The location of the photo insets are shown relative to core diagrams by the outlined green rectangles.

at the intersection of the canyon head branches and at the inner bend of the canyon's only meander (Figs. 5.9A and B). A CHIRP seismic profile through this transition reveals that the canyon has higher walls to the east (Fig. 5.9C). Unlike the SON and SOS canyons, the Dana Point Canyon maintains a u-shaped channel with a wide valley floor throughout the slope (Fig. 5.9D).

JPC 32-36 and GC 35-40 are located on the middle slope at depths of 500 and 510 m, whereas JPC 33-38 is located on the lower slope at depths of 688 m. GC 35-40 was recovered from the Dana Point channel flank and is located at the transition from higher to lower channel gradient (Figs. 5.9B and C). JPC 33-38 is located at the slope-basin transition where the canyon widens (Fig. 5.9A). Cores in Dana Point are capped by an upper layer of clay and silt that varies from $<$1 to 4 m thick (Fig. 5.10). In GC 35-40, the age of the clay and silt cap is $<$570 years BP, $<$10.8 ka in JPC 33-38, and cannot be constrained by available ages in JPC 32-36 (Fig. 5.10). Below this, silty clay and sandy silt are interbedded with fine sand. Sand layers in GC 35-40 are a few cm's thick, whereas sand layers in JPC 32-36 are thin and most are $<$1 cm (Fig. 5.10). The 12 sand layers in GC 35-40 exhibit ages between 570-5760 years BP and this range of ages is limited by the short core recovery. JPC 32-36, which is farthest core from the Dana Point Canyon, has the thinnest and fewest sand layers (7) that are dated between 15.5-18.9 ka (Fig. 5.10). Thick and thin sand layers in JPC 33-38 are amalgamated and can be distinguished by erosive lower boundaries (Fig. 5.10). JPC 33-38 has the most abundant (37) and thickest sand layers that range in age from 10.7 to 15.9 ka (Fig. 5.10). Sand color ranges from olive-gray in the photo of GC 35-40 to light tan in the photo of JPC 33-38 (Fig. 5.10). Some sand layers in JPC 33-38 contain shell hash, which can be observed between 5.6-5.7 m in this core's photo inset (Fig. 5.10).

5.6 Discussion

Comparisons of the SON and SOS canyons to the Dana Point Canyon draw similarities to studies that contrast coast-disconnected canyons versus connected canyons along the same active

margin (sensu Gamberi et al., 2015). A study on the Sicilian margin observed that canyons with heads close to the coast are active during the present highstand and are sourced by hyperpycnal flows or longshore currents that rework shelf sands (Gamberi et al., 2015). On the contrary, sediment supply to coast-disconnected canyons ceased during the post-glacial transgression (Gamberi et al., 2015). We propose that terrigenous sand supply to the coast-disconnected SON and SOS canyons was shut off around 8 kyr, as evidenced by thick Holocene mud caps overlying sand deposits (Fig. 5.8). Conversely, Dana Point Canyon has its head close to the coastline and can still receive recent sand deposition from littoral transport or hyperpycnal flows.

Deposition on the continental slope can occur by two main modes: gravity-driven turbidites during intervals with high terrigenous supply or pelagic sedimentation when terrigenous supply is low. Turbidites were identified in sediment cores by fining-upward sand layers (i.e., graded beds) with erosional bases. While many of the turbidites have sharp, erosive basal contacts and gradational upper contacts, some basal boundaries were occasionally diffuse. Pelagic deposition occurs predominantly as the upper clay section found in most of the cores (Figs. 5.8 and 5.10) and was identified in cores based off interpretations by Normark et al. (2009). Such deposits are also observed draping inactive canyons that halted deposition $\sim$ 15-20 kyr ago (Sweet & Blum, 2016), such as the Mississippi (Normark et al., 1986), Amazon (Milliman et al., 1975; Normark et al., 1997), and Nile (Ducassou et al., 2009).

The morphology and stratigraphy of deposits flanking the canyon-channel systems can reveal the relative timing of active channel-forming processes. After terrigenous supply to the canyon-channel was shut off, pelagic mud draped the canyon-channel system. Under this pelagic drape are interbedded sands and muds that compose the sets of aggradational reflectors flanking the SON and SOS channels. These deposits are interpreted to be levee deposits that represent the tops of the flows that spilled over the channel as a result of flow-stripping processes (e.g., Piper & Normark, 1983).

Our coring dataset allows us to investigate broad patterns that distinguish the San Onofre

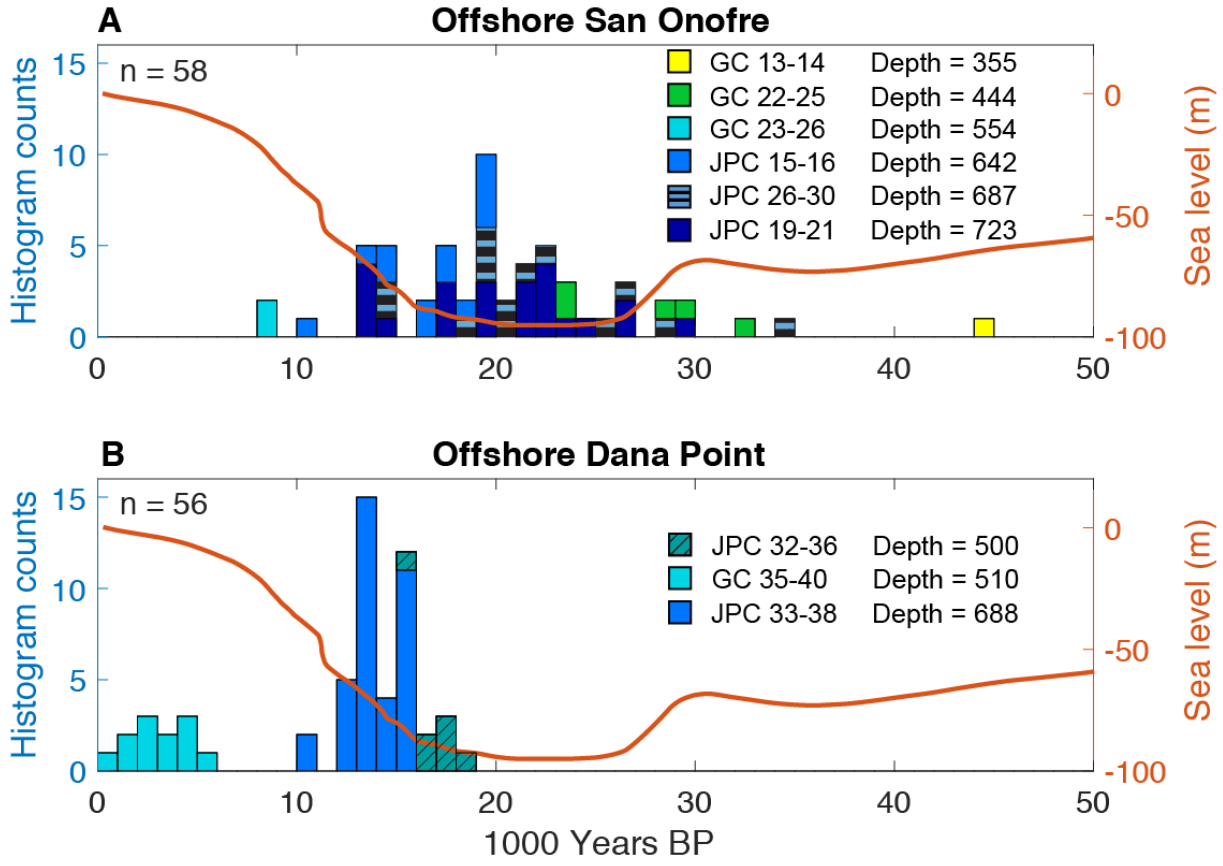

Figure 5.11: A) Histograms of sand layer depositional timing offshore San Onofre and Dana Point. A) The number of sand layers recovered from cores offshore San Onofre. B) The number of sand layers recovered from cores offshore Dana Point. In orange, the Southern California sea level curve from Muhs et al. (2012) versus time.

Canyons (SON and SOS) from the Dana Point Canyon in addition to patterns that distinguish middle slope canyon morphology from lower slope morphology. The recovery of cores from levee and thalweg deposits can facilitate investigations of autogenic turbidite flow processes, such as flow stripping. We propose that large-scale shelf-width differences and ponded basins constructed by strike-slip tectonics affect sediment supply and hence the *timing* of turbidite emplacement, whereas flow dynamics and channel geomorphology influence the *relative grain size* of turbidites.

5.6.1 Shelf width controls regional timing of turbidite deposition

This paper addresses multiple scales of the SON, SOS, and Dana Point canyons. Large-scale features such as shelf width and slope gradient are predominantly controlled by tectonic deformation. The broad anticline along the outer shelf imaged by Sahakian et al. (2017) and Holmes et al. (2017) is a first-order tectonic feature that has increased shelf width offshore of San Onofre. Second-order features include the NW-SE trending anticlines and synclines imaged in dip and strike profiles along the slope (Figs. 5.5 and 5.6). The NW-SE trending ponded basins and anticlines as well as the NW-SE trending anticlines and synclines are related to transpression and transtension along faults in the SM Fault Zone (Maloney et al., 2016; Holmes et al., 2017; Conrad et al., 2018; Bormann et al., in press). Third-order features such as channel levees are geomorphic features that are influenced by properties of turbidity flows, such as flow velocity and entrainment.

The San Onofre and Dana Point canyons have three main differences that may affect the emplacement of turbidites, namely i) shelf width is $\sim$ 10 km offshore San Onofre versus $\sim$ 2 km offshore of Dana Point (Fig. 5.1C); ii) Dana Point was likely attached to San Juan Creek during the sea-level lowstand and during the ensuing transgression, whereas the San Onofre canyons were likely not attached to a creek source during the post-glacial transgression; and iii) the slope offshore Dana Point is relatively smooth and concave-up in comparison to a more rugose slope offshore of San Onofre. As shelf width is known to be an important control on sediment supply to the slope and basin, widening of the shelf caused by the NW-SE trending anticline may contribute to decreased sediment supply to the slope in that region (Covault et al., 2007; 2010). We propose that broad tectonic and structural controls influence the timing of turbidite deposition *regionally* (San Onofre versus Dana Point). In section 5.6.2, we discuss why there are *local* variances in the timing turbidite emplacement (e.g., different depths on the slope and distances from the channel) that are affected most by ponded basins and channel geomorphology.

Histograms for turbidite ages offshore of San Onofre and offshore of Dana Point reveal

that the timing of turbidite deposition in these two environments exhibits marked differences (Fig. 5.11). Turbidites are emplaced to the Dana Point slope throughout lowstands and highstands in sea-level (Fig. 5.11). On the contrary, turbidites transported to the slope offshore of San Onofre show a marked decreased around 12-13 ka with the last few emplacements at approximately 8 ka (Fig. 5.11).

The lack of turbidites offshore San Onofre that are younger than 8 ka suggests that the most favorable conditions for turbidite deposition offshore of San Onofre are sea-level lowstands and the early transgression (Fig. 5.11). Older turbidites within the San Onofre cores dating back to 40 ka may have a high potential for recovery within JPCs because sedimentation rates in this area are lower than in Dana Point and therefore the overlying sediment is thinner. It appears that the cores located on the middle slope, GC 13-14 and GC 22-25, have the oldest turbidite ages whereas cores on the middle and lower slopes have slightly younger turbidite ages (Fig. 5.11). This may be related to ponded basins, channel gradient, and geomorphology, which will be discussed in Sections 5.6.2 and 5.6.3.

The narrower shelf width at Dana Point and its potential connection to San Juan Creek may facilitate the emplacement of turbidites during sea level lowstands, transgressions, and highstands. JPC 33-38 recovered from 688 m depth recovered turbidites spanning the interval from 13-18 ka, whereas GC 35-40 from slightly shallower depths of 510 m recovered turbidites spanning the interval from 1-6 ka (Figs. 5.10 and 5.11). Thick clay deposits in the upper 4 m of JPC 33-38 are interpreted as hemipelagic sediment deposited during the sea-level transgression and highstand when terrigenous supply was lower. This contrasts with the timing of turbidite deposition in GC 35-40, where most of the core is characterized by turbidites interbedded with silt. Only the upper 0.5 m of GC 35-40 is capped by clay. This difference between highstand turbidite deposition in GC 35-40 and lowstand deposition in JPC 33-38 may be related to channel dynamics and core location explored in Section 5.3. Turbidites within JPC 32-36 span the interval of 15-19 ka (Fig. 5.10). This suggests that Dana Point Canyon remained active during the lowstand, subsequent

transgression, and highstand. Timing differences between core locations are likely due to local variability in turbidity flow discussed in Section 5.6.3.

5.6.2 Across-margin deformation controls local turbidite emplacement

Deformation across the San Onofre slope exerts three main influences on turbidite emplacement: i) NW-SE trending anticlines and synclines form ponded basins that either trap sediment or cause bypass (Figs. 5.5 and 5.7), ii) NW-SE trending anticlines and synclines dictate the morphology of SON and SOS channel levees, and iii) structural controls influence slope gradient, which in turn affect canyon-channel dynamics and geomorphology (discussed further in Section 5.3). Ponded basins models predict they exert controls on grain size, as they are predicted to fill with thick, sand-rich deposits, whereas slopes tend to have deposits containing less sand (Prather, 2000). This model may explain why GCs 22-25 and 23-26 recovered $\sim$ 4-5 turbidites from the mid-slope syncline/ponded basin (Figs. 5.7 and 5.8).

On the slope, the only method of generating basins/synclines may be tectonic deformation (Covault et al., 2012) such as right jogs on the right-lateral strike-slip NIRC and SM Fault Zone that form transtensional basins (Ryan et al., 2009; Maloney et al., 2016). Recent deformation of the middle slope ponded basin may be observed in Line 11 (Fig. 5.5A); however, recent deformation of Blue and Pink unit sediment is not observed south of Line 11 (Fig. 5.5). Thus, it appears that deformation within the ICB occurred on timescales much longer than the timescales of recent deposition; on this margin, there was no recent renewal of accommodation in local ponded basins. Thick Pink, Blue, and Orange units within the mid-slope ponded basin suggests that it is completely infilled, which has in turn diminished depth and width of the SON and SOS channels (Slice 2; Fig. 5.5B). Supporting evidence for this comes from infilling of the relict SOS channel in Slice 2 (Fig. 5.6B and 5.7), which intersects the middle slope ponded basin. U-shaped reflectors that are infilled with aggrading Blue and Pink units are suggestive of relict channels (Fig. 5.6B). The older and deeper relict channel was infilled and this aggradational

sediment was subsequently truncated by a younger relict channel located to the northwest with shallower channel depths (Fig. 5.6B). After the complete infilling of the younger relict channel, the present-day SOS channel is deflected to the southeast of the relict channels and maintains a shallow depth (Fig. 5.6B). The infilled relict channels serve as an example of how the formation of such ponded basins affect the flow dynamics of channels and channel element architecture.

When ponded basins in the upper, middle, and lower San Onofre slope became completely infilled with thick sediment, sediment likely bypassed these basins and deposited turbidites on the lower slope and basin floor (Figs. 5.5, 5.6, 5.7). The lower age of the mud cap in GC 22-25 could imply that turbidite emplacement to the ponded basin ceased before 23.25 ka as the basin infilled. Shortly after, bypass of the ponded basin and pelagic sedimentation may have commenced. This hypothesis is supported by abundant turbidites on lower slope JPCs 15-16, 19-21, and 26-30 that post-date 23 ka (Fig. 5.11). The formation of ponded basins and intervening anticlines influences the channel profile and channel gradients, as discussed below.

The NW-SE trending anticlines and synclines imaged in the dip and strike profiles (Figs. 5.5 and 5.6) exert controls on the levee morphology adjacent to the SON and SOS canyon-channels. On the middle slope, levees thin towards the anticline crest adjacent to the SOS canyon-channel and thicken away from the anticline crest (Figs. 5.6A and B). Levees located closer to the anticline crest may have less frequent deposition than those located at deeper depths away from the anticline. For example, GC 13-14 has one turbidite that is $\sim$20 kyr older than multiple turbidites in GC 22-25. While GC 13-14 is located on a shallower levee close to the anticline crest, GC 22-25 is located in deeper water away from the anticline crest. On the lower slope, the SOS channel migrates into a NW-SE trending syncline as the channel widens (Figs. 5.6C and D). Thus, deformation on the San Mateo Fault Zone appears to influence turbidite emplacement and timing on scales $<$1 km by creating ponded basins that trap sediment, forming anticlines that cause sediment bypass in the cross-margin direction, and affecting levee architecture in the along-margin direction.

5.6.3 Channel gradient controls morphology and localized differences in turbidite timing

Channel gradient exerts controls on turbidity flow behavior and morphology, as the force of turbidity flows is proportional to gradient (McHargue et al., 2011). Therefore, steep gradients along broader scales are often related to greater incision, whereas gentler gradients are related to deposition (Prather, 2000; McHargue et al., 2011; Brothers et al., 2015; Maier et al., 2017). Without tectonic deformation, canyon-channel systems on a continental slope would trend towards an equilibrium profile just like fluvial systems (McHargue et al., 2011). A smooth concave-up profile is observed through the Dana Point Canyon, whereas tectonic deformation offshore of San Onofre has created bathymetric irregularities that disrupt the equilibrium profile for the SON and SOS canyons (Fig. 5.2). In this manner, the SON and SOS canyons exhibit similarities to the Palos Verdes Channel, where strike-slip tectonics that create local uplift or pull-apart basins that have prohibited channels from developing an equilibrium profile (Maier et al., 2017). In the Palos Verdes Channel, local uplift abruptly increases channel gradient, leading to hydraulic jumps that can cause subsequent scouring or bypass; breaks in gradient may lead to deposition (Maier et al., 2017).

Turbidity current flow dynamics influence architectural elements of channel systems such as width, depth, and confinement by levees or erosion (Piper & Normark, 2009; McHargue et al., 2011; Talling et al., 2013; Talling et al., 2015). In the Palos Verdes Canyon, regions of steep gradients and sediment bypass are characterized by overbank deposits, whereas regions characterized by breaks in gradient are characterized by depocenters (Maier et al., 2017). Variability of channel flow throughout the lengths of the SON, SOS, and Dana Point canyons may control grain size of overbank deposits, thus complicating the turbidite record from cores. Nevertheless, deposits cannot be used to unambiguously characterize the nature of turbidity flows, as different processes can form similar deposits (Talling et al., 2012).

Though the gradient of the Dana Point Canyon is not complicated by tectonic deformation, changes in gradient downslope can cause local variances in the timing of turbidite emplacement. The gradient changes from 5-15° in the upper slope to <5° in the middle slope (Fig. 5.2C); GC 35-40 is located at this break in gradient and here deposition may be favored over bypass. As a result, it records recent turbidites within the past 600 years (Fig. 5.10). In contrast, JPC 33-38 is located at the slope-basin transition where the channel levees decrease in height and the channel becomes unconfined (Fig. 5.9B). This transition to an unconfined channel may explain why turbidites have not been emplaced in JPC 33-38 within the past 10 kyr. JPC 32-36 recovered fewer turbidites and may be related to its location farther from the channel axis (Fig. 5.9A).

Of the San Onofre canyons, the SON canyon profile trends the most towards equilibrium whereas the SOS canyon profile is punctuated by the mid-slope ponded basin (Figs. 5.2A and B). The recency of turbidite emplacement and the SON and SOS channel gradient do not exhibit a one-to-one relationship. This could be due to complex geomorphic features that are constructed in response to accelerating or decelerating turbidity flow.

Offshore San Onofre, breaks in channel gradient are observed at the transitions from the upper to middle and middle to lower slopes (Fig. 5.2). Where these breaks occur, thick, aggradational channel levees flank the SON and SOS channels (Fig. 5.7). These breaks coincide with GC 23-26 on the SON canyon mid-slope, at GC 13-14 on the SOS canyon mid-slope, and JPC 26-30 on the SOS canyon lower slope (Figs. 5.2A and B). While GC 23-26 exhibits recent turbidite emplacement as young as 8 ka, JPC 26-30 exhibits turbidite emplacement as recent as 14 ka, and there was no turbidite emplacement at GC 13-14 since >44 ka (Figs. 5.8 and 5.11).

Steep gradients in the lower slope facilitates faster turbidity currents that potentially caused bypass and thinning sediment cover. In Slice 3, a small NE-SW trending anticline separating the SON and SOS canyons appears to have no Pink or Blue unit sediment cover and the SOS channel appears to incise the southwest flank of the anticline (Figs. 5.6C and 5.7). The only core recovered from a portion of the slope with a steep gradient is GC 22-25, and a lack of turbidites

<23.3 ka in this core (Figs. 5.8 and 5.11) may be indicative of either bypass due to steep channel gradient or sediment starvation caused by infilling of the upslope ponded basin.

On the lower slope, deformation on short length scales (<1 km) may trigger hydraulic jumps that produce the mounded bathymetry shown in Fig. 5.3 and also observed in the slope map in Fig. 5.2D. These mounds are similar to crescentic bedforms located at the channel-lobe transition zone in the adjacent San Mateo Canyon and have been interpreted as cyclic steps (Kostic, 2011; Covault et al., 2014; Covault et al., 2017). Cyclic steps are large-scale, upstream-migrating, wave-like bedforms with wavelengths of 100's to 1000's of m and are typically observed in unconfined submarine environments (Covault et al., 2017). In the San Mateo Canyon (Covault et al., 2014) and in model simulations (Kostic, 2011), cyclic steps are located at the decrease in gradient at the channel-lobe transition zone (Covault et al., 2017). Cyclic steps that are oriented orthogonal to the canyon, such as the ones observed here, are typically initiated by large turbidity currents (Normark et al., 2002; Covault et al., 2017). In this study area, cyclic steps are observed in the lower kilometer of the SON profile (Fig. 5.2A), as the SON channel widens (Fig. 5.2D). Cyclic steps can be observed in seismic dip Line 11 as landward-migrating mounded reflectors (Fig. 5.5A). Note that the cyclic step is observed just landward of the basin deposits. In contrast, cyclic steps are observed throughout the steep lower slope in the SOS profile (Figs. 5.2B and 5.3) and the gradient map of the SOS lower slope exhibits much more variability in downslope gradient (Fig. 5.2D). In a manner similar to the San Mateo Canyon, subsurface folding observed in dip Line 12C (Fig. 5.5B) caused by deformation along the San Mateo Fault Zone (Conrad et al., 2018) may create rugose bathymetry that causes turbidity currents to undergo hydraulic jumps necessary for the formation of cyclic steps (e.g., Ryan et al., 2009; Covault et al., 2017).

In addition to gradient, flows moving down a canyon-channel system are also affected by autogenic processes such as flow filtering and flow stripping, both of which are commonly observed in deepwater channels. Flow stripping occurs when the top of a turbidity flow becomes elevated above channel confinement and the unconfined flow top spreads out and detaches from

the confined flow (Piper & Normark, 1983). This results in the deposition of the uppermost mud-rich fraction in overbank deposits and thus contributes to levee construction (McHargue et al., 2011). Flow filtering is the process by which overbank deposition contributes to the loss of mud and the increase in relative sand concentration downslope. Thus, channelized flows become thinner and sandier as they progress downslope and the resulting overbank deposits become progressively sandier and less cohesive with time (McHargue et al., 2011). Flow filtering processes that affect levee grain size are observed in our suite of levee cores consisting of GCs 22-25 and 13-14 from 440-560 m depth (Figs. 5.6A and 5.8) and JPCs 26-30 and 19-21 from 680-730 m depth (Figs. 5.6D and 5.8). In these levee cores, we observe an increase in sand content in the lower slope JPCs compared to the middle slope GCs. Likewise, this relationship is manifested in the Dana Point Canyon, where the lower slope JPC 33-38 has thicker turbidites with medium to coarse sand, whereas middle slope GC 35-40 has thinner turbidites with fine to medium sand (Figs. 5.9 and 5.10).

When autogenic processes such as flow filtering are complicated by allogenic elements such as gradient, ponded basins, and wide shelves, the record of turbidite emplacement becomes increasingly difficult to disentangle. As such, paleoseismology studies that rely on turbidite emplacement records (e.g., Goldfinger et al., 2003; Goldfinger et al., 2007) should be approached with caution. The most conclusive results of this study confirm findings of regional scales from Covault et al. (2007, 2010) and Normark et al. (2009). The wide shelf offshore San Onofre prevents terrigenous supply to the deep sea during the post-glacial transgression and highstand, whereas the narrow shelf offshore Dana Point remains connected to sediment sources and has allowed for the recent emplacement of turbidites within the past 1000 years. On scales finer than 1 km, the dynamics of tectonic deformation, gradient, and autogenic processes can explain variances in depositional timing from individual cores. Despite studies that attempt to link flow processes to the sedimentary record (e.g., Xu et al., 2010; Symons et al., 2017; Maier et al., 2019), we still do not completely understand down-canyon variability in turbidity current flow and the

preservation of facies adjacent to canyons. The concave-up profile of the Dana Point Canyon could theoretically provide an idealized record of turbidites and sand delivery to the deep sea. Nevertheless, cores adjacent to Dana Point Canyon illustrate that grain size and the emplacement of turbidites are complicated by gradient and flow filtering. Thus, individual core records from the much more complex margin offshore of San Onofre are imperfect records that show how turbidity currents dynamically respond to changes in gradient imposed by tectonic deformation. Turbidites offshore this tectonically active margin could theoretically record recent deformation. Nevertheless, turbidites offshore of San Onofre are $>$8 ka and fail to record historical earthquakes such as the 1933 Long Beach earthquake. This also supports the hypothesis of Sahakian et al. (2017) that this region has deformed less recently than other strands on the NIRC Fault Zone.

A disconnect persists between the ages of the cores, the recovered length of the cores, and the resolution of the Sparker 2D and 3D profiles. Despite advances in coring technology, piston cores and gravity cores are still not able to recover cores long enough to resolve sediment packages older than the Pink Unit or sediment offset by faulting. Without deeper cores, it is difficult to constrain margin evolution on the timescales imaged in the seismic reflection data.

5.7 Conclusion

This study draws comparisons between small end-member canyons within the ICB. Dana Point Canyon can be considered a shore-proximal canyon with an ideal concave-up profile and minimal tectonic deformation on the continental slope. As evidenced from dated turbidite deposits, this canyon has remained active during the most recent lowstand, sea-level transgression, and highstand. In contrast, the San Onofre North and South canyons are separated from the coast by a wide $\sim$ 10 km shelf that is characterized by extensive deformation. Shelf widening offshore of San Onofre is caused by a left step along the right-lateral Newport Inglewood/Rose Canyon Fault (e.g., Maloney et al., 2016; Sahakian et al., 2017; Holmes et al., 2017). This broad feature inhibits

sand supply to the SON and SOS canyons after 8 ka and these canyons are predominantly active during MIS 2. On scales $<$1 km, variability in turbidite emplacement timing can be attributed to ponded basins, small anticlines that promote bypass, and increases in gradient. These basins were likely formed by crosscutting faults in the San Mateo Fault Zone. Gradient and autogenic processes of turbidity flows may play an important role controlling the grain size of turbidites. Thus, allogenic processes acting on a range of scales muddies interpretations of the turbidite record as paleoclimate or paleoseismic indicators.

5.8 Acknowledgements

This work has been submitted for publication as **Wei, E.A., Holmes, J.J., and Driscoll, N.W. Strike-slip Transpressional Uplift Offshore San Onofre, California Inhibits Sediment Delivery to the Deep Sea, *Frontiers in Earth Science.*** The dissertation author was the primary investigator and author of this material. This project was funded by the California Public Utility Commission through Southern California Edison. Many thanks to the crew of the R/V Thompson and core technicians at Oregon State University for assisting with the collection of these cores, the crew of the R/V New Horizon and R/V Melville for assisting with the acquisition of seismic profiles and swath bathymetry, Geotrace Technologies and NCS Subsea Inc. for processing seismic data, and Alex Hangsterfer at Scripps for aiding with core curation. Mackenzie Roberts, Leanne Hirsch, and Lana Graves processed the cores and sampled benthic and planktonic foraminifera for radiocarbon age dating. Funding for six radiocarbon ages was provided by the Scripps Institution of Oceanography Department Graduate Student Excellence Research Award.

Chapter 6

Conclusion

The research presented in the preceding chapters sheds light on tectonic processes that affect shelf width. Central to this research is the concept that shelf width exerts important controls on sediment storage on inner mid-shelf clinothems and routing of sediment through incised valleys to the deep sea (e.g., Covault et al., 2010). In order to improve our understanding of the timescales of sediment storage and routing, nested geophysical methods, such as CHIRP seismic, sparker seismic, were paired with chronological and geochemical datasets extracted from sediment cores.

An expanded scope of the seismic study area and newly-acquired chronological constraints from sediment cores shed light on the major processes that control Holocene clinothem architecture in the Gulf of Papua (GoP). Radiocarbon ages from benthic foraminifera illustrate that the late Holocene clinothem is younger than previously proposed by Slingerland et al. (2008a). In this chronostratigraphic framework, surfaces of lap separating sediment units are not controlled by eustatic sea-level fluctuations but instead may be influenced by accommodation and oceanographic currents. Expanding the geographic scope of the seismic survey area allowed us to examine the influence of foreland basin tectonics on accommodation, as the northeast GoP is subsiding at rates of 1 mm/yr and the southwest GoP has limited accommodation due to peripheral bulge

uplift. Such differential subsidence causes aggradational clinothem geometries in the central and northern GoP and toplap and bypass in the southern GoP. Progradation of the late Holocene clinothem into bathymetric lows illustrates that along-margin bottom currents observed during the Trade Wind season by Walsh et al. (2004) and modeled by Slingerland et al. (2008b) have built the late Holocene clinothem obliquely to the northeast. Such currents have persisted for the past 2000 years.

Clay mineralogy of shelf and deepwater deposits elucidate sediment routing throughout the past 120 kyr. Sediment sourced from the Fly River can be distinguished by high illite:smectite >5 whereas sediment sourced from the Purari River has a signature with low illite:smectite <5. Sediment from the inner mid-shelf clinothem exhibits shifts in illite:smetite through time, with high illite:smectite during the Holocene, low illite:smectite during the MIS 3 intermediate lowstand, and high illite:smectite during the MIS 5a highstand. In Pandora Trough, high illite:smectite corresponds to MIS 2 lowstand deposits or turbidite sediment. Such shifts in mineralogy are interpreted to reflect how contributions of the Fly and Purari rivers to the inner mid-shelf clinothem have changed throughout the sea-level cycle. We hypothesize that during the MIS 3 intermediate lowstand, Fly River sediment bypassed the inner mid-shelf clinothem through three-incised valleys and deposited sediment in Pandora Trough. During the intermediate lowstands, incised valley heads and the Fly River were possibly connected. Peripheral bulge uplift permits the persistence of incised valleys offshore of the Fly River, whereas foreland basin subsidence offshore of the Purari River has widened the shelf.

Recent uplift of the San Luis block to the north of the Santa Maria Basin can be constrained by the transgressive surface that dips 0.05-0.08° to the south. This study calculated uplift rates of 0.3-0.6 mm/yr, which are 3 times greater than those calculated by PG&E (1988) and Hanson et al. (1992). Contractional deformation in the north-south direction and uplift of the transgressive surface causes depocenters of post-glacial sediment to shift southward to the center of the basin. In the across-margin deformation, depocenters are located seaward of the shoreline

cutoff. By relating the depth of the shoreline cutoff to the regional sea-level curve from Muhs et al. (2012), we estimate that the shoreline cutoff was formed before Meltwater Pulse 1A. Block uplift and shoaling bathymetry to the north may influence the degree of sediment reworking by wave orbitals, as surficial sediment grabs from the northern and southern transects are very-well sorted, whereas surficial sediment from the center of the basin may be too deep to be affected by wave orbitals. The location of depocenters and subsequent reworking by oceanographic currents have implications for estimating sediment budgets in this area, which are crucial for understanding the sustainability of the Santa Maria Dunes.

In the Inner California Borderlands, shelf width is a dominant control that determines whether canyon-channel systems remain active during sea-level highstands (Covault et al., 2007; Normark et al., 2009; Covault et al., 2010). This study is novel because it uses multiple sediment cores to constrain the timing of turbidite deposition in shore-proximal and detached canyons. By recovering cores in the upper, middle, and lower slopes, this study examines both autogenic and allogenic processes affecting sediment gravity flows. Dana Point Canyon is detached from San Juan Creek by a narrow 2-km shelf and actively deposited turbidites within the past 1000 years. The San Onofre North and South (SON and SOS) canyons are located offshore of the widest part of the shelf in the ICB, are detached from San Mateo Creek by 10 km, and turbidite deposition ceased in the past 8 kyr. Nested geophysical surveys reveal the structurally complex geometry beneath the San Onofre slope that is characterized by a broad east-west trending anticline and multiple north-south trending anticlines and synclines. The broad east-west trending anticline was formed by transpression along the right-lateral Newport-Inglewood Rose-Canyon Fault Zone (Sahakian et al., 2017). This broad anticline may inhibit the SON and SOS canyons from intercepting sediment transported by littoral currents to the south. North-south trending synclines are infilled with trapped ponded sediment whereas anticlines increase channel gradient and may accelerate sediment gravity flows. These north-south trending anticlines accommodate deformation from the San Mateo Fault Zone (Conrad et al., 2018). Thus, shelf width controls

turbidite depositional timing regionally, whereas ponded basins and changes in gradient may affect local turbidite depositional timing.

Appendix A

A 2000 Year Geomagnetic Field Record from the Gulf of Papua

A.1 Abstract

A high resolution Holocene record of geomagnetic field direction and intensity in the Gulf of Papua was con- structed using paleomagnetic data from eight piston cores collected in the region. The chronology of the cores was based largely on radiocarbon dates from benthic foraminifera. Correlation of seismic reflectors imaged in subbottom data between nearby cores was consistent with the chronostratigraphic framework based on radio- carbon dates and provided additional confidence of the age model. In other regions, where cores sampled dif- ferent depositional settings associated with the three-dimensional prograding lobes, reflectors could not be confidently correlated between cores. Furthermore, radiocarbon ages from the bottoms of trigger cores and tops of co-located piston cores revealed varying amounts of overpenetration of the piston core below the seafloor. The relative paleointensity, and a general eastward trend in the declination and steepening of the inclination in our new record are generally compatible with the closest (¿ 4300 km) existing records. Our record does not agree well with global field models

CALS3k and pfm9k, likely reflecting the lack of existing data contributing to field models in the region.

A.2 Introduction

Sediment records are key contributors to our knowledge of the global variability of the geomagnetic field. For the past 50 years sediments have proven to be useful recorders of magnetic field direction (e.g., Harrison & Somayajulu, 1966; Opdyke & Henry, 1969; Mackereth, 1971) and relative intensity (e.g., Levi & Banerjee, 1976; King et al., 1983; Tauxe, 1993). In addition, deep sea sediment sequences have been successfully used to construct long term (a few million years) records of relative paleointensity (dipole strength) (e.g., Ziegler et al., 2011; Channell et al., 2009; Valet et al., 2005) and to recognize excursions or polarity reversals in marine sequences (e.g., Clement & Kent, 1987;Ohneiser et al., 2013; Wu et al., 2014). Similarities between various regional stacks (e.g., Barletta et al., 2010; Barletta et al., 2010; Stoner et al., 2002; Yamamoto et al., 2007) and consistency with ^{10}Be records (Christl et al., 2003) provide increasing confidence in the reliability of these sedimentary records. High accumulation rate sediment records can also provide information on directional and intensity variations over shorter time scales that are used to construct Holocene global field models (e.g., Korte & Constable, 2011; Nilsson et al., 2014). These models aim to analyze global and regional field variations and provide insight into the dynamics of the core. Records with high sediment accumulation rates are preferred over those with lower rates, and the ideal data for these models will have measures of geomagnetic inclination, declination and intensity.

Holocene field models are based primarily on archeomagnetic data and high accumulation rate sedimentary records from lakes, as relatively few deep-sea sedimentary records have the required time resolution. Sedimentation rates in the open ocean are typically low (up to 5 cm/kyr for carbonate (Milliman, 1993), up to 1 cm/kyr for biogenic silica (Nelson et al., 1995), and $<$0.5

cm/kyr for pelagic clays (Zhou & Kyte, 1992)) and provide insufficient temporal resolution to record the Holocene geomagnetic field with much detail. Continental margin sediments offer the possibility of obtaining high-resolution Holocene records and studies have been conducted in the Arctic (Barletta et al., 2008; Barletta et al., 2010; Lisé-Pronovost et al., 2009), North Atlantic (Stoner et al., 2007) and Antarctic (Brachfeld et al., 2000). The current distribution of marine and lacustrine Holocene paleomagnetic sediment records is heavily biased towards the northern hemisphere and Europe, with very few records in the southern hemisphere (e.g., Nilsson et al., 2014), and fewer than 100 records globally. Continental margin sediments can potentially expand this sparse global coverage of Holocene records for paleomagnetic studies, but the more complex sedimentary environments of margins compared to lakes requires more scrutiny while correlating multiple cores. These complexities can include variations in accumulation rates that may differ by an order of magnitude over small spatial scales and hiatuses that can introduce data gaps.

The reliability of sedimentary geomagnetic records can be enhanced by using multiple local records. If there are sufficient age constraints on each core, combining the geomagnetic records from multiple cores at a single location into a single record can average out some of the variability in the sedimentary recording process. In practice, independent age constraints are not always available for each core and a composite record may be constructed by matching peaks in magnetic susceptibility (e.g., Gogorza et al., 2002; Constable & McElhinny, 1985) or by matching features in the inclination and declination (e.g., Lund et al., 2016). Both of these approaches may present challenges; magnetic susceptibility variations may be too small to identify correlatable features, and remanence directions may have spurious features that should not be used for correlation. Additionally, the justification for using either remanence or susceptibility variations for correlation is based on the assumption that variations must represent the same time period. Whether this is true depends on the spatial scale over which the correlation is made as well as variation in accumulation rates. For this reason, it is important to use independent (not related to magnetics) ways to establish correlation between cores. Some examples of lithologic

features that characterize units that can be identified in each core are color changes (Verosub et al., 1986) representing oxic and anoxic sediments (Frank et al., 2007), rapidly deposited layers (Turner et al., 2015), and dated tephra layers (Ali et al., 1999). Radiocarbon dating, of wood, shells and foraminifera can be used to establish an age model, as can ^{210}Pb, which can be used to determine the sediment accumulation rates in cores, and environmental markers such as pollen that can help identify known, dated horizons (Brachfeld & Banerjee, 2000).

In this study, we examine the feasibility of using sediments from margins with very high sedimentation rates to get a high resolution, late Holocene field record from the continental margin of Papua New Guinea. Generating a composite record from the Gulf of Papua is challenging due to the complexity of the margin (Walsh et al., 2004; Harris et al., 1993; Slingerland et al., 2008, 2008b), so we explore whether using seismic reflectors can help in establishing correlations between cores. The Gulf of Papua offers a distinct advantage for this test of using seismic reflectors because it was the focus of a multidisciplinary effort to understand source to sink properties of margin environments and, as a result, over 6800 km of seismic data (Slingerland et al., 2008, 2008b), as well as fifty piston and gravity cores with companion trigger cores were collected. This site also represents a location where there is a distinct lack of recent paleomagnetic data. Although there are some nearby study sites, few cover the last 2000 years with good resolution. Constable (1985) and Constable & McElhinny (1985) studied two lakes in northeastern Australia, about 600km away, but these lake sediments are missing approximately the last 1500 years. Lund et al. (2006) studied four cores from a transect in the western Equatorial Pacific Ocean but these too are missing the most recent Holocene, as are the box cores from the Ontong-Java Plateau measured by Constable & Tauxe (1987). More complete records were established by Richter et al. (2006), who provided a high resolution (400 cm/kyr) inclination and relative paleointensity record from the Western Pacific, and the Haberzettl et al. (2013) study of relative paleointensity and paleosecular variation for the past 1300 years in an Indonesian Lake (up to 900 cm/kyr sedimentation rate). The next closest southern hemisphere Holocene records that span 0–2000

years are found about 4000 km away in southern Australia (Barton & McElhinny, 1981) and New Zealand (Turner & Lillis, 1994; Turner et al., 2015).

Here we present a high-resolution composite record of geomagnetic field variations over the last 2000 years that included measurements from cores with accumulation rates up to 500 cm/kyr. The addition of this new record from the Gulf of Papua should complement existing studies and enhance our understanding of regional field variations in this area, specifically addressing whether the large inclination varia- tions ($\sim$30° in 500 years) predicted by the CALS3k.4 (Korte & Constable, 2011) model are representative of this site, or whether those variations are due to the lack of regional data. Seismic and core data help constrain the offsets between trigger and piston cores. Local correlations between cores are consistent with radiocarbon data; however, regional seismic correlation is difficult along the Papua New Guinea margin because of the numerous river inputs.

A.3 Regional setting

The setting for this study is the Gulf of Papua, located off the southeast coast of Papua New Guinea (Fig. A.1). This tropical region receives 2-9 m of rain per year (Harris et al., 1993). As a result, 3.84×10^8 tons (Milliman et al., 1999) of sediment is delivered to the gulf each year, with half of that transported mainly through three rivers, the Fly River in the south, and the Kikori and Purari rivers in the north (Milliman, 1995). The Gulf of Papua has a broad, low gradient shelf (Walsh et al., 2004). The margin is built up of clinoforms (Walsh et al., 2004; Harris, 1994; Harris et al., 1993; Harris et al., 1996; Slingerland et al., 2008; Slingerland et al., 2008), consisting of topsets, foresets, and bottomsets. The topset is the gently sloped portion located shoreward that rolls over to the steeper dipping foreset at depths of 25-40 m and the bottomset (or pro delta) is the gently sloped portion located basinward of the foreset (Walsh et al., 2004 and references

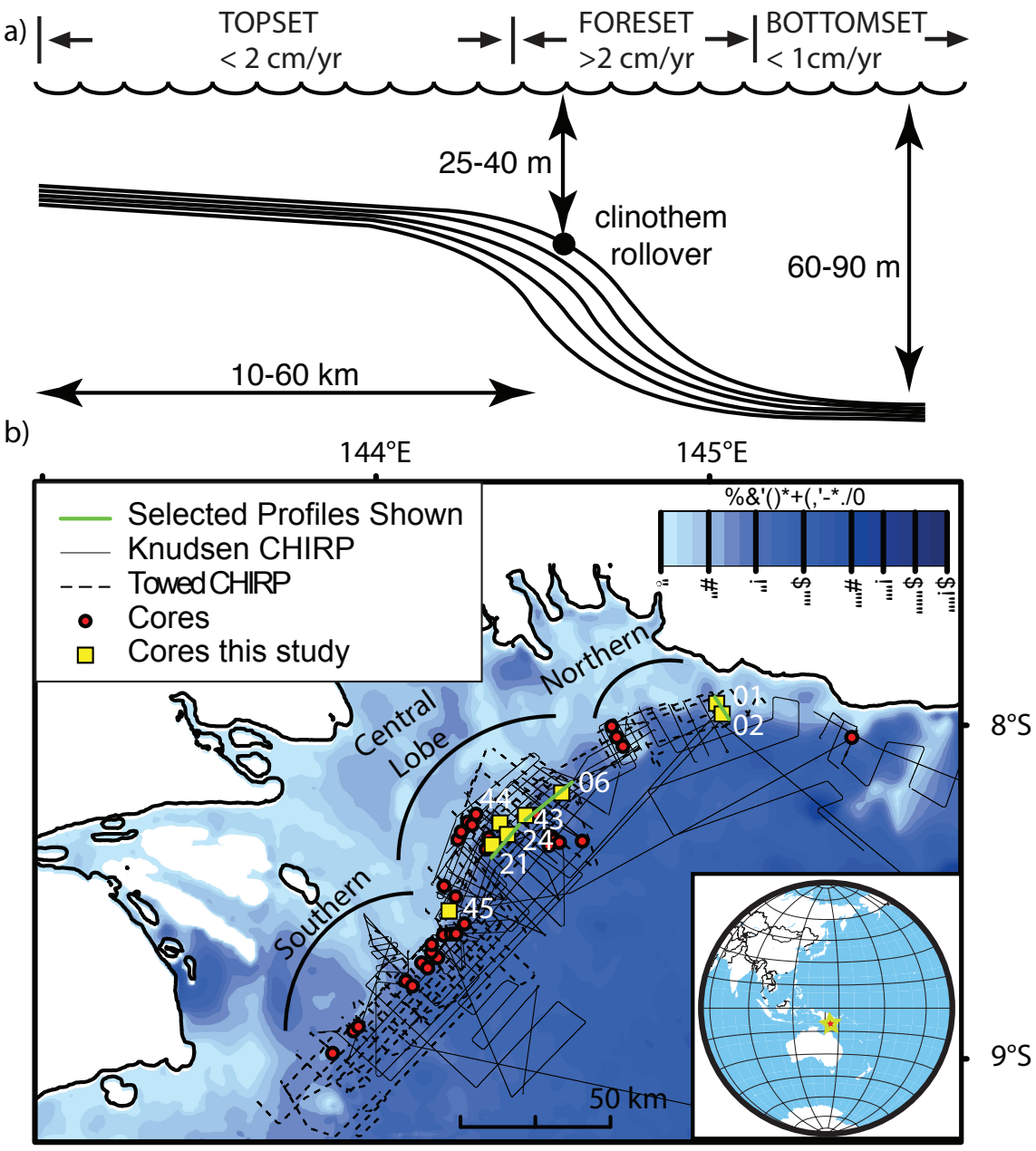

Figure A.1: a) A cartoon of a clinoform showing typical distances, depths and values for sedimentation in the Gulf of Papua based on Walsh et al., 2004. b) A bathymetric map of the GoP showing location of the cores collected (red), cores used in this study (yellow squares), towed CHIRP lines (black dashes), Knudsen CHIRP lines (solid black) and interpreted seismic profiles used in this study (green lines). The inset shows the location of Papua New Guinea.

Table A.1: Cores used in this study. Jumbo piston cores (JPC) and companion trigger cores (TC) are listed along with their recovered length, latitude/longitude location, water depth, and a description of their location on the clinoform. The seismic line from cruise VANC22MV that most closely corresponds to each core's location is listed.

Core Name	Length (m)	Lattitude	Longitude	Water depth (m)	Location on clinothem	Seismic line
JPC 01	8.190	-7.9565	145.03517	53.9	Northern lobe; foreset	mv22-0402-3.5_LF_003
TC 01	2.130					
JPC 02	9.900	-7.9780	145.04967	62.6	Northern lobe; bottomset	mv22-0402-3.5_LF_008
TC 02	1.940					
JPC 06	11.13	-8.198	144.57	55.1	Central lobe; bottomset	mv22-0402-3.5a_LF_025 (Line 07 in Wei et al., 2019)
TC 06	2.030					
JPC 21	9.400	-8.37467	144.37317	52.5	Central lobe; bottomset	mv22-0402-3.5a_LF_025 (Line 07 in Wei et al., 2019)
TC 21	1.97					
JPC 24	9.560	-8.33950	144.39183	48.6	Central lobe; bottomset	mv22-0402-3.5a_LF_025 (Line 07 in Wei et al., 2019)
TC 24	1.830					
JPC 43	7.800	-8.28383	144.45817	50.8	Central lobe; bottomset	mv22-0402-3.5a_LF_025 (Line 07 in Wei et al., 2019)
TC 43	2.060					
JPC 44	6.320	-8.30750	144.38117	38.6	Central lobe; foreset	png2L04; png2L05; png2L06
TC 44	1.990					
JPC 45	6.890	-8.63550	144.23317	47.0	Southern lobe; bottomset	mv22-0402-3.5a_LF_034 (Line 03 in Wei et al., 2019)
TC 45	2.000					

therein). This study uses sediment cores mainly from the bottomset of the Holocene clinothem with depths ranging from 47 to 63 m and two cores from the foreset ranging in depth from 39 to 54 m (Table A.1; Fig. A.1a).

The Gulf of Papua clinothem is a three-dimensional feature composed of three main lobes: the Southern, Central, and Northern lobes (Fig. A.1b; Wei et al., 2019). The three lobes are depocenters of the Holocene clinothem as defined by Holocene sediment thickness and stratal geometry (Slingerland et al., 2008; Wei et al., 2019). Clinothem geometry observed in the Gulf of Papua records longshore transport as well as infilling of pre-existing morphology. In addition, there are seasonal variations with sediment input during the monsoon and sediment reworking during the tradewind seasons (Walsh et al., 2004; Slingerland et al., 2008) These processes combine to result in variations in accumulation over short spatial and temporal scales and the possibility of large, event-driven deposits.

A large number of studies have aimed to quantify the sedimentation rates in the area (Harris et al., 1993; Walsh et al., 2004), using sediment traps, ^{210}Pb and radiocarbon. Studies from areas closest to our cores provide evidence for highly variable and sometimes very large sedimentation rates. Walsh et al. (2004) and Harris et al. (1993) show sedimentation rates varying from 0.6 cm/yr up to 5 cm/yr, and show a single large event where sedimentation was as high as 12 cm/yr and lasted 4-5 years. Sedimentation rates vary across the clinothem, as the foreset is the area of fastest sediment accumulation. Additionally, sedimentation rates vary parallel to the margin, with the highest sedimentation rates observed in the Central lobe of the clinothem (Walsh et al., 2004).

A.4 Materials and methods

A.4.1 Seismic data and coring sites

Swept-frequency CHIRP seismic data, both from a surface-towed Edgetech system (500 Hz-6 kHz with a 50 ms sweep) and a hull-mounted Knudsen system (3.5kHz center frequency) (Fig. A.1), were collected along both strike- and dip-parallel lines between September 2003 and March 2004. They show subsurface layers and reflectors in the sediment 50-100 m below the seafloor with sub-meter resolution (Slingerland et al., 2008). These were used to identify the stacked clinoforms that make up the margin and to understand the depositional history of the region.

The coring sites and seismic lines from the R/V Melville cruises are shown in Fig. A.1b. The cores used in this study are mainly from the bottomset of the clinothem (Table A.1) and were chosen to span the length of the margin, which is useful in assessing the internal consistency of the geomagnetic record over tens of kilometers. Most of the cores in this study were collected from the Central lobe of the clinothem, with the exception of jumbo piston cores (JPCs) 01 and 02, which were collected from the Northern lobe, and JPC 45 from the Southern lobe. The tight spacing of seismic data ensures that variations of the clinoform margin can be mapped in the along-shore and down-slope directions and additionally ensures that there is detailed contextual information for each collected core. Due to drift during coring operations, some cores were not located precisely on a seismic line but were projected to the nearest line, and in most cases can be reliably projected onto more than a single line.

A.4.2 Physical analysis and sedimentology

Whole core multi-sensor track (MST) data were collected at Oregon State University prior to splitting the cores. This included P-wave amplitude, resistivity, density, temperature and magnetic susceptibility. Although insufficient calibration information was stored to provide

useful estimates of P-wave velocity, resistivity or density, we were able to use the MST to provide reliable magnetic susceptibility data as these data require only a simple volume correction. The cores were later split into halves with a router blade to cut the plastic core liner and a piece of piano wire separated the sediment. One half was kept as a pristine archive half, used for visual core descriptions, and photographs, and the other half was used for sampling for paleomagnetic measurements and radiocarbon dating. The cores were stored in D-tubes and kept refrigerated at the core repository at Scripps Institution of Oceanography. All cores consist mainly of a homogeneous olive grey to dark grey silty clay that sometimes includes very fine, discontinuous sand layers. Cores JPC21 and JPC24 contain a large (30-60 cm) sand layer with a mud matrix and shell fragments that was determined to be an erosional unconformity that represents a transgressive lag deposit formed during sea level rise after the Last Glacial Maximum (Harris et al., 1996; Wei et al., 2019). Sediments below this are thought to have been deposited from 50,000-20,000 years BP (Harris et al., 1996; Slingerland et al., 2008) and are not a focus of this study.

A.4.3 Paleomagnetic procedures

The eight cores used in this study visually had many sections of homogeneous, fine-grained material. The jumbo piston cores (JPC) and trigger cores (TC) are 12cm in diameter and were sampled with a combination of U-channels (inner dimensions 1.8 cm by 2.1 cm) and continuous discrete samples collected in $7cm^3$ plastic cubes. The cubes were used for measurements of the anisotropy of magnetic susceptibility (AMS) and for directional measurements of all trigger cores as well as JPC21 and JPC45. Samples were taken from the middle of the core to avoid core disturbance near the edges. In a few cases the entire length of the core was not sampled, either due to flow-in at the bottom of the core or because the sediment was too coarse-grained to be sampled.

Anisotropy of magnetic susceptibility (AMS) as well as bulk susceptibility was measured using the Kappabridge KLY-4S and the AMSspin program (Gee et al., 2008). AMS results are

described in detail in a future paper. The bulk susceptibility measurements from the Kappabridge show good agreement with the MST whole core susceptibility measurements, for cores where both types of data are available. So for cores where we were unable to collect discrete samples we rely on the MST measurements for susceptibility.

For a small number of representative samples from each core thermomagnetic curves were measured (50°C/min, 100 mT field, up to 700°C) to characterize their magnetic mineralogy and material from these samples was measured on the alternating gradient force magnetometer (AGFM) at SIO paleomagnetic laboratory to characterize the domain state. The remanence of discrete samples was measured using a 2G magnetometer at the SIO paleomagnetic laboratory, and U-channel measurements were made at the Institute for Rock Magnetism at University of Minnesota. After measuring the natural remanent magnetization (NRM), the samples were progressively demagnetized using stepwise alternating field demagnetization. This was done at steps of 5, 10, 15, 20, 25, 30, 40, 50 and 70 mT, at which point the sample had reached about 10% of its initial magnetization. The characteristic remanent magnetizations were determined with principal component analysis (Kirschvink, 1980, with the UPMag program of Xuan & Channell (2009) for analysis of U-channel data) using measurements from all steps 10-70 mT. Samples were also given an anhysteretic remanent magnetization (ARM) in an 80mT alternating field with a 100 μT bias field. Pilot samples were fully demagnetized to compare the ARM and NRM and demagnetizations. Based on the results of these pilot samples, ARMs of all samples were demagnetized at 5 and 10 mT and this partially demagnetized ARM was used as the normalizer for relative intensity estimates.

To orient different sections of the cores that were not oriented relative to one another during acquisition with a fiducial mark on the liner (for both the piston and trigger cores), we determined the Fisher average of the 10-70 mT PCA directions of the bottommost five points and uppermost five points of each section. The position of the upper most section was held fixed, and the next section was rotated by the average difference in declination between base of the

upper section and the top of the next section to ensure that the core declination values aligned at section breaks. This process was repeated until reaching the lowermost core section. The average declination of the trigger core was set to the average declination (5.6°) predicted from the gufm global field model (Jackson et al., 2000) over the past 400 years.

Table A.2: Lab results from AMS dating provided conventional radiocarbon ages (years before 1950) and standard deviation in age for samples. Calibrated radiocarbon ages from Calib 7.1 (Stuiver & Reimer, 1993).

Core	Average sample depth in core (cm)	Conventional radiocarbon age	Standard deviation in age	Calibrated radiocarbon age	1-σ	2-σ
TC 01	9	Modern				
TC 01	205	1175	40	715	660-757	626-845
JPC 01	38	1220	30	753	686-794	665-873
JPC 01	413	1440	30	979	924-1029	885-1108
JPC 01	598	1495	40	1036	960-1097	922-1165
JPC 01	805	1825	40	1361	1291-1406	1266-1496
TC 02	5	>Modern				
TC 02	188	860	35	477	441-515	339-556
JPC 02	21	1655	35	1207	1165-1265	1079-1265
JPC 02	123	2835	35	2580	2507-2677	2408-2717
JPC 02	283	2445	30	2075	2000-2135	1941-2244
JPC 02	463	6140	30	6561	6498-6623	6431-6675
JPC 02	943	9480	100	10,333	10,206-10,445	10,107-10,598
TC 06	10	>Modern				

Table A.2 (continued): AMS radiocarbon ages

Core	Average sample depth in core (cm)	Conventional radiocarbon age	Standard deviation in age	Calibrated radiocarbon age	1-σ	2-σ
TC 06	198	785	30	414	365-474	305-492
JPC 06	13	830	30	455	421-498	333-522
JPC 06	253	1460	80	1005	909-1103	803-1203
JPC 06	523	1710	30	1257	1212-1301	1162-1348
JPC 06	1073	2015	40	1570	1506-1647	1414-1703
TC 21	8	>Modern				
TC 21	188	630	30	265	148-317	129-396
JPC 21	7	585	25	204	145-268	68-301
JPC 21	69	4185	30	4259	4180-4340	4115-4401
JPC 21	90	5165	30	5518	5474-5569	5410-5625
TC 24	15	>Modern				
TC 24	176	500	30	112	0-173	0-234
JPC 24	7	390	30	Post AD 1950	6	7
JPC 24	243	950	35	544	499-595	475-631
JPC 24	390	3880	30	3835	3760-3907	3688-3968
TC 43	7	>Modern				
TC 43	198	645	30	382	237-359	142-405
JPC 43	13	995	30	576	535-616	504-646
JPC 43	373	1820	30	1353	1294-1394	1267-1478

Table A.2 (continued): AMS radiocarbon ages

Core	Average sample depth in core (cm)	Conventional radiocarbon age	Standard deviation in age	Calibrated radiocarbon age	1-σ	2-σ
JPC 43	548	2400	90	2027	1894-2138	1810-2288
JPC 43	723	2070	35	1633	1561-1691	1514-1774
JPC 44	26	710	35	351	293-401	261-453
JPC 44	163	900	35	506	467-539	430-608
JPC 44	313	775	30	404	337-462	301-486
TC 45	163	>Modern				
JPC 45	53	555	30	175	124-256	0-279
JPC 45	103	370	70	Post AD 1950		
JPC 45	153	620	35	251	147-303	106-396
JPC 45	203	640	30	277	230-359	138-402
JPC 45	253	600	30	222	146-282	65-330
JPC 45	303	565	30	184	133-258	0-287
JPC 45	353	640	30	277	230-359	138-402
JPC 45	403	640	30	277	230-359	138-402
JPC 45	453	675	30	318	265-372	151-144
JPC 45	503	665	35	306	256-372	146-430
JPC 45	553	645	25	283	237-356	145-401
JPC 45	603	600	30	222	146-282	65-330
JPC 45	653	620	35	251	147-303	106-396

A.4.4 Radiocarbon dating

Samples of mixed benthic foraminifera were picked from all cores to be used for AMS radiocarbon dating (Table A.2). In most cases, a large quantity (about 200 g) of sediment spanning a depth of $\sim$5 cm provided sufficient material ($>$2 mg) for dating. Most samples were sent to the Center for Accelerator Mass Spectrometry at Lawrence Livermore National Laboratory; two samples were sent to National Ocean Sciences Accelerator Mass Spectrometry (NOSAMS) facility at Woods Hole Oceanographic Institution. Where possible, a sample was picked from the top and bottom of the trigger core, as well as from the top, middle and bottom of the piston core. This strategy was employed to evaluate whether the trigger and piston cores had recovered the sediment/water interface, and to give a way, independent of magnetic measurements, to determine the offset/overlap between the trigger and piston cores.

This approach was largely successful, with the exception of JPC44, where there was not sufficient dateable material in the bottom of the trigger core, and the sample from the top of the piston core that did not successfully graphitize during the conversion of CO_2 to graphite necessary for radiocarbon dating (T. Guilderson, pers. comm.). This may have been caused by sulfur in the sample, which would likely indicate a reducing environment. Unfortunately, we could not obtain another sample to determine the source of the problem, and as a result JPC44 has poor age constraints.

We initially collected 13 samples of foraminifera at 50 cm spacing from JPC45 to be dated and to ensure we had at least one well-dated core. The calibrated radiocarbon ages for this core, however, had a narrow range from modern to 351 years BP. Two additional samples, from 355 and 605 cm were picked and sent to NOSAMS to rule out the possibility of lab error. The ages came back identical to those previously determined. The conventional radiocarbon ages were calibrated using Calib 7.1 (Stuiver & Reimer, 1993) and the Marine13 (Reimer et al., 2013) curve with an estimated Delta R of 10. Although using the CHRONO marine reservoir database and selecting many nearby records will not give this estimate of reservoir age (the seven closest

records will give an estimate of Delta R = -3, Gillespie & Polach (1979), McGregor et al. (2008), Rhodes et al. (1980), Chappell & Polach (1976)) we determined that the highest quality and most representative data to use for determining Delta R came from Burr et al. (2009) which used precisely dated corals from the South Pacific ∼950 km away. Previous radiocarbon ages collected from the Gulf of Papua cores (Harris et al., 1996; Johnstone, 2012) sampled material other than forams (peat, ooids, mollusk shells, bulk carbonate for example) and obtained anomalously old ages compared to our results, as well as dates out of stratigraphic order. Some of this material was likely reworked and these earlier radiocarbon ages are not used for establishing our age scale.

A.5 Results

A.5.1 Alignment of the piston and trigger cores

In ideal circumstances, the piston coring system has a trigger core that is designed to capture the uppermost sediment and duplicate the upper few meters of sediment captured by the piston core. The trigger core is a short (∼2 m) weighted gravity core that is suspended adjacent to the piston core, at some length (approximately 20 ft) below it. The impact of the trigger core with the seafloor releases the piston core, and a length of wire will ideally stop the piston at the seafloor, while the piston core barrel penetrates beyond the piston. However, there are many problems associated with this process of piston coring. The problems are common but complex (Lunne & Long, 2006 provide a review of seabed samplers that discusses many of these problems) and can include over penetration of the piston core, potentially caused by poor placement of the piston or incorrect estimates for the length of slack wire (Buckley et al., 1994) or rebound of the wire due to releasing the piston core. The amount of over penetration may be significant and some paleomagnetic studies (Lisé-Pronovost et al., 2009; Barletta et al., 2008, Peck et al., 1996) have estimated the over penetration by comparing the susceptibilities of piston core top to the trigger core and finding the best fit. These studies reveal that over penetration of up to

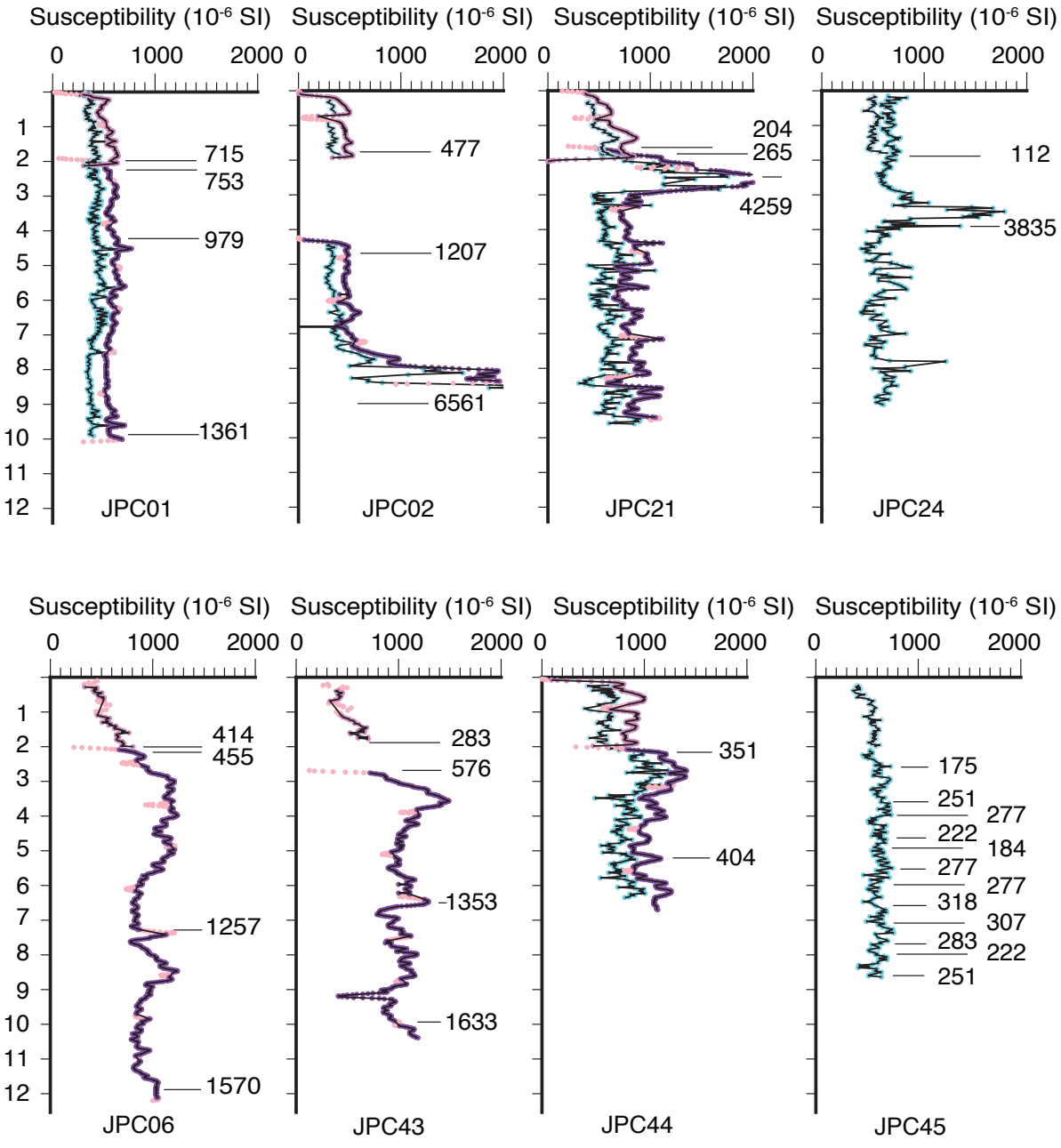

Figure A.2: Magnetic susceptibility for all cores used in this study plotted against depth below seafloor. Susceptibility data collected using cubes is shown in light blue (cyan) for the trigger core (piston core). Multi-sensor track susceptibility data is shown in deep pink (purple) for the trigger core (piston core), with light pink to show data from the ends of sections. Black lines indicate depths where samples were collected for radiocarbon dating (including the piston core offset), and the calibrated radiocarbon age in years BP rounded to the nearest decade is noted.

400cm may occur (Peck et al., 1996). Here we employ a similar strategy but, before comparing magnetic susceptibilities, we use ^{14}C dates from the trigger core bottom and piston core top to restrict the possible offset, only allowing the range of possible offsets to fit within the one sigma error of the radiocarbon dates, assuming a linear sedimentation rate. We determine the best fit of the magnetic susceptibilities using the root mean square error after linear interpolation between measured points. Because the tops of trigger cores had recent ages, data from the piston core is moved in 1 cm increments relative to the trigger core, within the range of predicted offsets and we determined the offset by minimizing the misfit of the susceptibility profiles. For cores where there was no overlap, the offset was determined using the linear sedimentation rate of the trigger core as it has less potential deformation.

After determining the offset for the piston core, the average declination of the trigger core was set to the present-day declination at the site (5.6°) and a rotation was applied to the entire piston core so that the averages of overlapping points agreed. For cases where there was no overlap, the average declination of the top 50 cm of the piston core was aligned to the bottom 50 cm of the trigger core. There was a single core (JPC44) where we could not obtain an age from the bottom of the trigger core. To determine the offset of this core, we used the following methods. The magnetic susceptibility of the trigger and piston cores differ by almost a factor of two, so there is likely no overlap. If the two dates from within JPC44 represent a constant sedimentation rate (5.4 cm/yr), and we employ this sedimentation rate to calculate the offset distance from a recent age at the top of the trigger core, the calculated offset of the piston core would be 16.7 m. This unrealistic offset, however, is subject to uncertainties because sedimentation rates calculated from two dates with a short time span between them (at the tops of cores where both dates are recent, for example) are oftentimes higher than rates calculated from dates with a long time span between them (using an older date from the middle of the core along with a recent date, for example) (Sadler, 1981). A minimum possible offset of 200 cm is assumed, which is reasonable considering the offsets found in other cores (range from 0 to 268 cm for seven of the cores, and

426 cm for a single core). Refinement of the offset depth for JPC44 would affect how the trigger core and upper 226 cm of the piston core are mapped to age, but the effect of these changes will be minimized when stacked due to the number of cores that have data in the 0-350 year range.

The radiocarbon age collected from the top of JPC24 piston core was the only piston core age (aside from a single age in JPC45) that had a modern age. Using this information, the offset of the piston core was assumed to be 0 cm, meaning the upper 200 cm captured the same time period as the companion trigger core. The declinations of these two do not appear compatible with each other, as they trend in opposite directions, but there is not sufficient evidence from either set of measurements to regard one as more reliable than the other.

The calculated offsets ranged from 426cm (JPC02) to no offset (JPC24) and are shown with the susceptibilities (Fig. A.2) to illustrate the goodness of fit for the reader. In the figure, the susceptibility values collected from discrete cubes (acquired assuming a nominal 10 cm^3 volume) and are left uncorrected for the true volume to allow a slight offset between the MST data and cube data. The volume-corrected bulk susceptibility data for the 7 cm^3 discrete samples brings the two sets of susceptibility data to nearly identical values.

A.5.2 Remanence directions

The remanence directions are all nearly univectorial, with a small overprint that is typically removed by 10 mT (Fig. A.3). The median destructive field (MDF, the alternating field (AF) value at which the remanence is reduced by half) values show little variation, and 95% are between 21 and 30 mT. Cores that were measured using discrete cubes (all trigger cores and the JPC45 and JPC21 piston cores) were demagnetized using +X, +Y, +Z and -X, -Y, -Z on alternating steps to allow identification of any spurious remanence due to a non-zero field in demagnetizer. Remanence directions from these alternate steps generally show no detectable difference in direction. A small number of samples have less ideal demagnetization behavior. For example, JPC21 (Fig. A.3c) represents a coarse-grained sample from the transgressive surface.

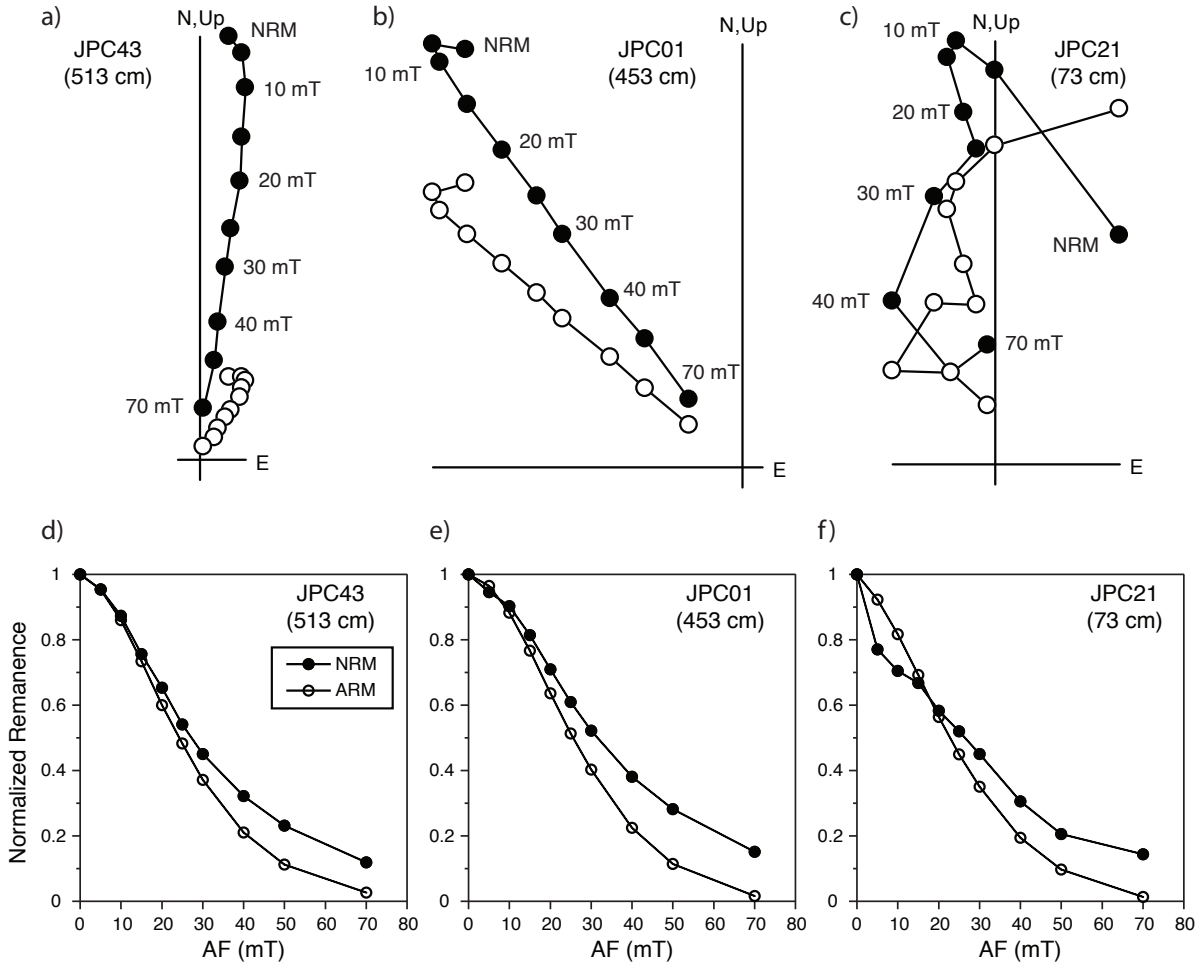

Figure A.3: Representative vector end-point orthogonal projections for typical samples (a,b) and a sample from the coarse-grained transgressive surface (c). Corresponding normalized demagnetiztion curves are shown in d,e,f.

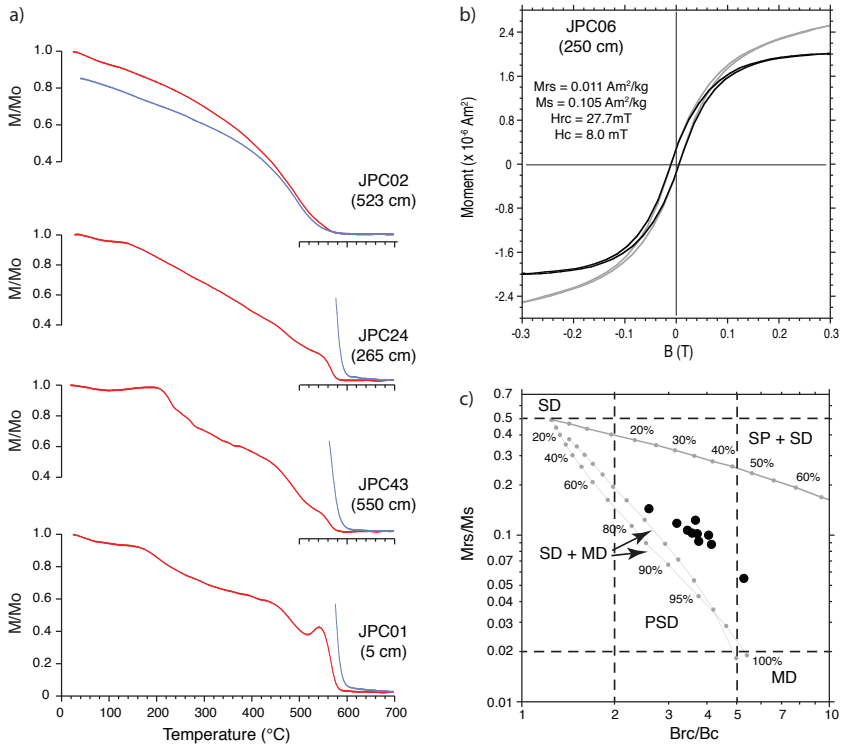

Figure A.4: a) Representative heating (red) and cooling (blue) curves. b) Typical hysteresis curve and derived parameters. The coercivity of magnetic minerals (Hc), the coercivity of remanence (Hcr) the saturation remanence (Mrs), and the saturation magnetization (Ms) are indicated. c) Day plot (Day et al., 1977) of samples from all eight cores. Most fall in the pseudo-single domain (PSD) region.

These coarse-grained samples were excluded from our study. Generally, the maximum angular deviation (MAD) of the principal eigenvector values were very low (<3°) although some points near section breaks or in portions of the less consolidated trigger cores exhibited higher MAD values, though still <5°. For U-channel samples, the response functions of the magnetometer coils result in smoothing of the data and edge effects at the ends of sections (Jackson et al., 2010). Measurements within approximately 5 cm of each section end were not used due to these edge effects. In a few cases (mainly the transgressive surfaces found in cores JPC21 and JPC24, and the base of JPC02) the MAD values were very high (>15°).

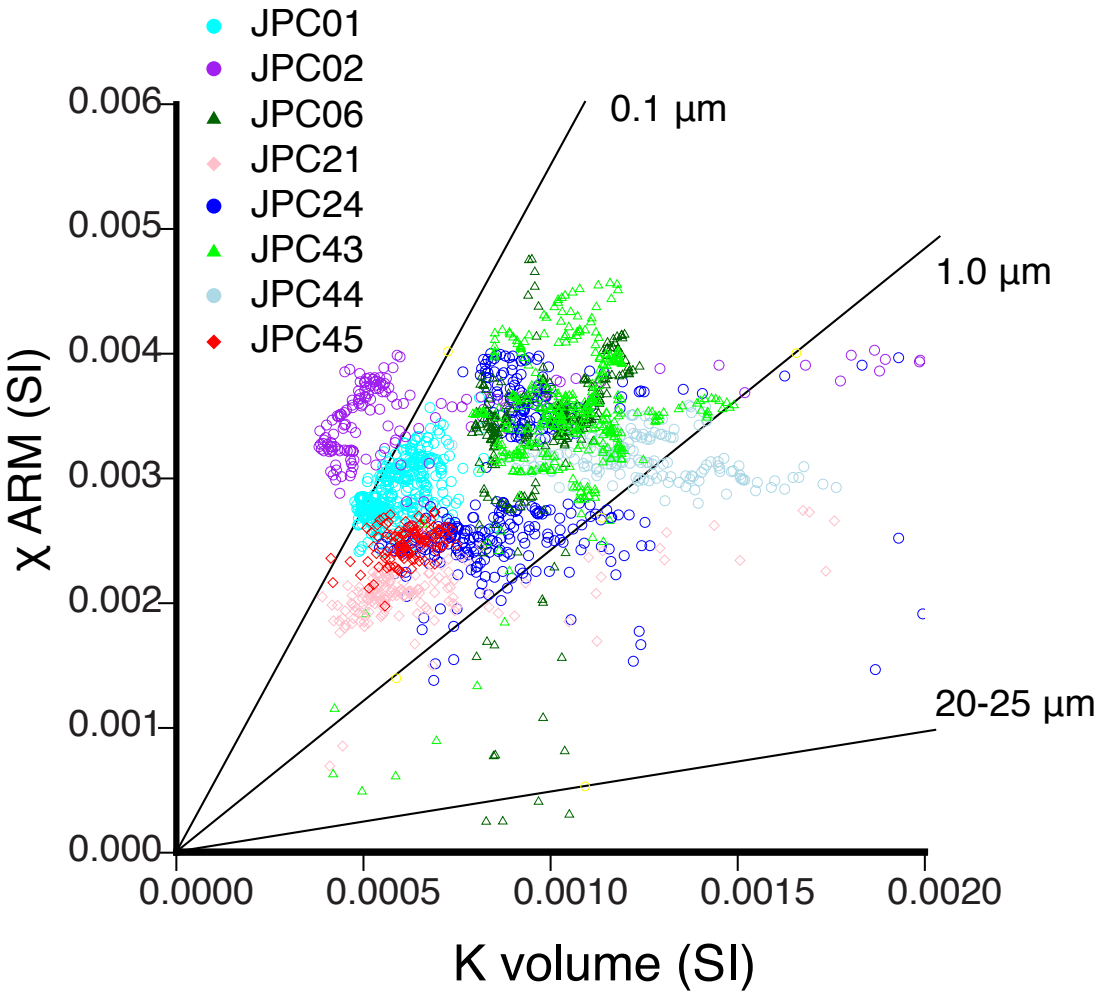

Figure A.5: Anhysteretic susceptibility (χARM) versus volume normalized low field susceptibility (K) after King et al (1982) to show relative grain size variations in magnetite. Idealized model from King et al (1983) is shown with black lines. Circles indicateχARM from U-channels and K from cubes measured, Triangles indicate χARM from U-channels and K from multi-sensor track, diamonds indicate χARM and K from cubes. K from cubes is normalized to the correct 7cc volume.

A.5.3 Magnetic mineralogy and suitability for paleointensity

The use of sediments for relative paleointensity determinations relies on the assumption that the remanence acquired is proportional to the field value and that variations in concentration of the magnetic minerals can be adequately accounted for by the normalization. Criteria aimed at establishing this are 1) the magnetization should be carried by magnetite in the 1-15 μm single domain/pseudo-single domain (SD/ PSD) range (King et al., 1983), 2) the concentration of magnetite should not vary down core by more than a factor of 10 (Tauxe, 1993), 3) the NRM should be defined by a single component of magnetization with MAD $<5°$ (Stoner & St-Onge, 2007), and 4) the normalizer should have a similar demagnetization curve to that of the NRM (Levi & Banerjee, 1976).

Thermomagnetic curves (Fig. A.4) in all cases reveal a discernible Curie point on the heating curves (575°C) that is compatible with the presence of low-Ti titanomagnetite. The curves range from nearly reversible with a single high Curie point to curves with more distributed Curie temperatures, suggestive of a range of magnetic minerals, and significant increases on cooling. The irreversibility of most curves, together with an increase in magnetization above 500°C on some heating curves, suggests that additional magnetite is formed during heating. Notably, none of the curves display a significant magnetization decrease over the interval (280-430°C) expected for the breakdown of griegite (e.g., Bol'shakov & Dolotov, 2012; Ron et al., 2007; Brachfeld et al., 2009). We suggest that the thermomagnetic data are most compatible with a range of titanomagnetite compositions, including low-Ti titanomagnetite, which should be suitable for relative intensity determinations. The volcanic source rocks (Slingerland et al., 2008) supplying material to the Gulf of Papua are consistent with this interpretation of a range of titanomagnetite compositions.

The shape of the hysteresis curves is characteristic of the pseudo-single domain region on a Day plot and most samples plot in the PSD region (Day et al., 1977) that should be suitable for relative intensity studies. Despite the color of the sediments, which might suggest the possible

presence of greigite, the hysteresis parameters for measured samples also do not indicate the presence of greigite (Mrs/Ms $\approx$ 0.5 and Bcr/Bc $\approx$ 1.5, Roberts, 1995), nor do the heating curves, but these were not measured exhaustively. Other studies have shown that greigite may be identified by an increase in the median destructive field of the NRM (Brachfeld et al., 2009) or by an acquisition of a gyromagnetic remanent magnetization (GRM) exhibited as an intensity increase and acquisition along the last axis of demagnetization (e.g. Snowball, 1997; Frank et al., 2007). Neither of these features were noted in our cores from the Gulf of Papua and so we conclude that variable amounts of PSD (titano)magnetite carry the remanence in these cores.

The concentration variations of pseudo-single domain (titano) magnetite in the Gulf of Papua cores also appears to be well within the range accepted for determining sedimentary relative intensity, shown by the minimal variations in susceptibility (Fig. A.5). Following King et al. (1983) we have plotted anhysteretic susceptibility (ARM, the anhysteretic magnetization acquired per unit bias field, Tauxe, 1993) versus low-field susceptibility (K) and compared it with the simple phenomenological model of King et al. (1983) as a measure of magnetite grain size and concentration. ARM is more sensitive to single domain and pseudo-single domain grains, whereas K will be more sensitive to large pseudo single domain or multi-domain grains and the ratio of the two can thus be used to give an estimate of relative particle size. The comparison to the phenomenological model based on sized magnetite data (King et al., 1982) provides an estimate of magnetite grain size and all cores fall generally below the upper 15 μm range limit. Individual cores plot in a cluster (Fig. A.5), indicating a consistent grain size. JPC24 has two distinct grain size and concentration clusters, and these correspond to the samples from above (lower cluster) and below (upper cluster) the transgressive surface.

The consistent grain sizes, minimal changes in susceptibility, and single component NRM with low MAD values satisfy the criteria outlined for suitable paleointensity studies. The overall similarity of the demagnetization curves of NRM and ARM (Fig. A.3) illustrate the suitability of ARM as a normalizer, and the relative paleointensity, calculated using NRM intensity at 10

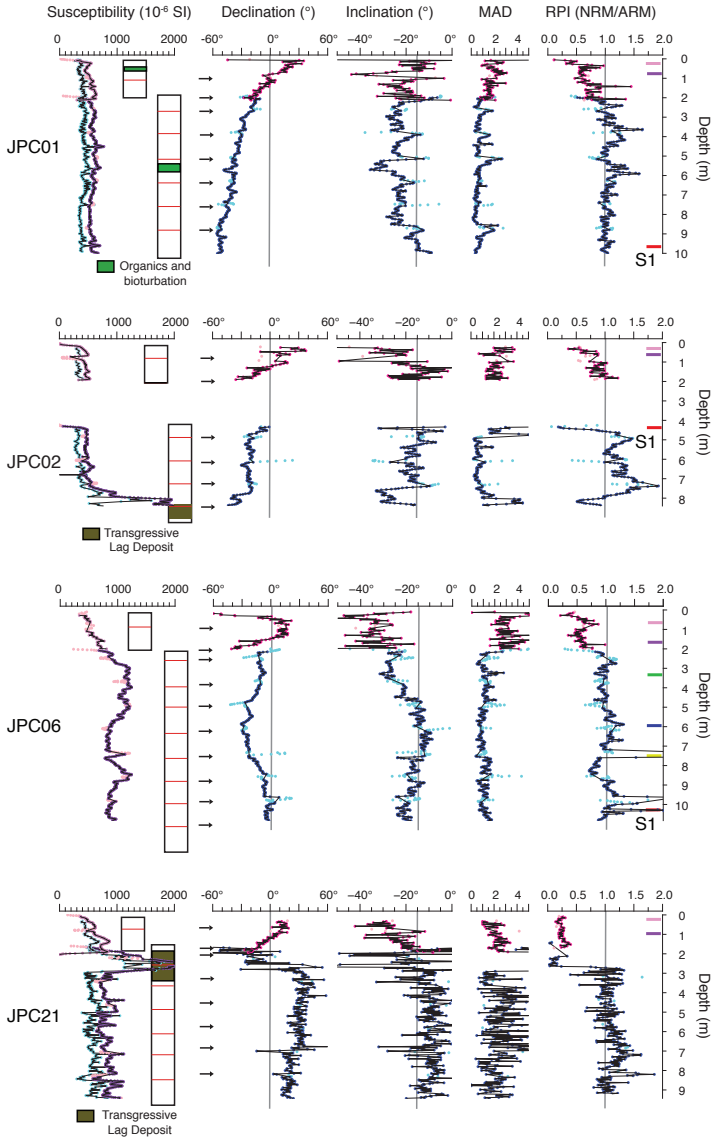

Figure A.6: Magnetic susceptibility and directional data for all cores used in this study plotted against depth below seafloor, with piston core offsets included. Susceptibility data collected using cubes is shown in light blue (cyan) for the trigger core (piston core). Multi-sensor track susceptibility data is shown in deep pink (purple) for the trigger core (piston core), with light pink to show data from the ends of sections. Representations of the visual core descriptions are depicted with the trigger core and piston core offset and red lines and arrows indicating the section boundaries. Cores that appear blank had no visual features of note. Relative declination, inclination, maximum angle of deviation (MAD) and relative paleointensity (RPI) are plotted in deep pink (blue) for the trigger (piston) core. Light pink (cyan) represents points from the ends of trigger (piston) core sections that were not used due to disturbance and/or response function of the magnetometer. The expected dipole inclination at the site is shown with a grey line. Colored bars at the far right indicate seismic reflector depths and correspond to Figure A.7.

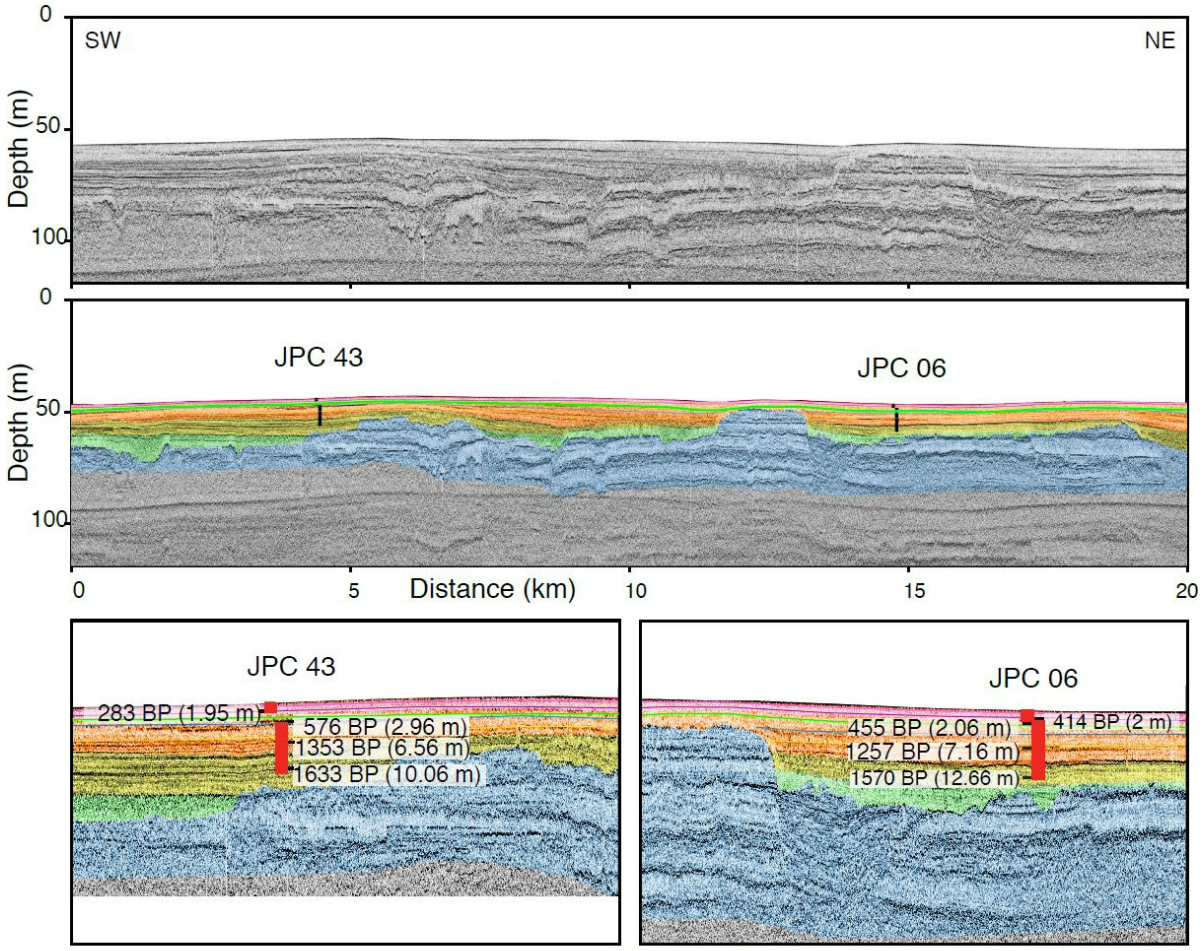

Figure A.7: The top panel shows an uninterpreted Knudsen seismic profile. The middle panel shows the same profile with interpretations of the sediment packages (colors, see text). Seismic reflectors have been traced between cores JPC06 and JPC43 and are shown in thin colored lines. The bottom panel shows the two cores in detail with the reflectors and calibrated radiocarbon ages marked. "a" indicates the calibrated radiocarbon age, and "d" indicates the depth below seafloor of that radiocarbon age.

divided by ARM intensity at 10 mT and the normalized to the mean, is shown in Fig. A.6.

Fig. A.6 shows relative declination, inclination and relative paleointensity (NRM_{10mT}/ ARM_{10mT} normalized to the mean) as a function of depth below seafloor. It is evident from this figure that the cores are very homogeneous, with few features to note on the lithological section, and mainly small variations in susceptibility, except for some very large increases related to the transgressive lag deposit in JPC02, JPC21 and JPC24. The MAD values are very small and there is little variation in the MDF values. There are similar inclination values in most cores, near $-20°$ and shallower than the present day inclination at the site ($\sim -30°$ from the IGRF). The declination values in the piston cores are less consistent and seem to exhibit signs of twisting (JPC01 and JPC44 for example), but the declination values in trigger cores show eastward trends. The transgressive lag deposit is evident in JPC21 and JPC24 and is accompanied by a large change in inclination. This large inclination is not evident in JPC02 and this is likely age related - at a depth of 9.46 m in JPC 02, the age is $\sim$ 10,000 BP, while the age of the sediment below this surface in JPC 21 and JPC24 is much older. It is apparent in some cores, JPC06 and JPC44 for example, that the inclination is discontinuous across section boundaries, indicating some physical deformation that likely occurred during the sectioning process.

A.5.4 Seismic correlation

One of the goals motivating this study was to determine whether the abundant seismic data from the Gulf of Papua margin could provide complementary information to radiocarbon ages in establishing the correlations between cores. The seismic data allow recognition of four distinct sedimentary sequences described by Slingerland et al. (2008a, 2008b) and Wei et al. (2019; Fig. A.7). At the base of the section is an older clinothem that has been incised and eroded (Unit C; shown in blue), mantled by a transgressive deposit (Unit B1; shown in green). The Holocene clinothem progrades out across this surface with the Yellow package (Unit A1) being more progradational and the Orange package (Unit A2) having more aggradational geometry

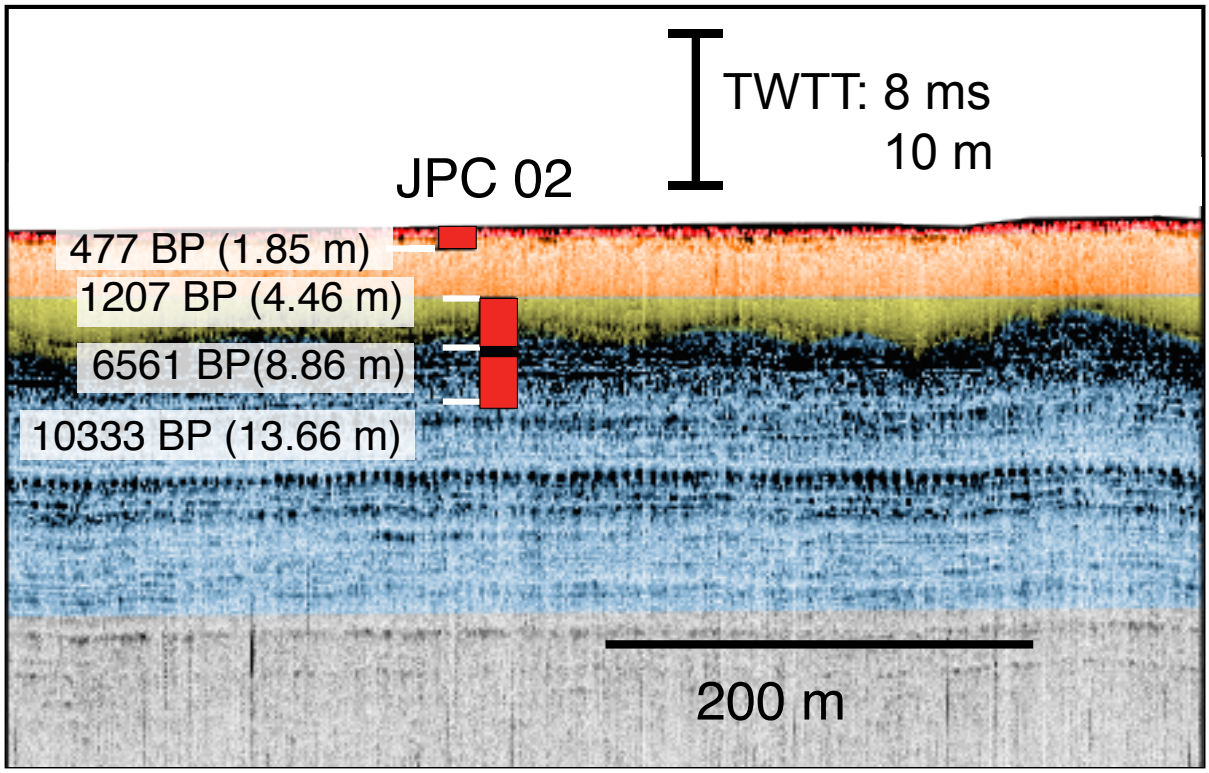

Figure 8

Figure A.8: An interpreted seismic CHIRP profile for JPC02. Depths of radiocarbon ages, and calibrated ages in years BP are noted. The 14C age of the trigger core sample is labeled "tc", "d" corresponds to the depth in the core of the radiocarbon age, and "a" corresponds to the 14C age of the sediment in the piston. Yellow, Orange and Red packages in the Holocene clinothem consist of fine-grained mud, Green (too thin to show in the seismic profile) represents transgressive deposits composed of shell fragments and sand in a mud matrix and the older relict Blue clinothem.

than Yellow. Separating the Yellow and overlying Orange package is a surface of lap, called S1 (Slingerland et al., 2008a, 2008b). Above Orange is an aggradational Red unit (A3) that is characterized by two reflectors (pink and purple) that can be observed in all lobes of the clinoform. The boundary between Orange and the most recent Red package is another surface of lap, called S2 (Slingerland et al., 2008a, 2008b). Distinctive reflectors within the Orange and Red seismic packages were traced, whenever possible, between the locations of the cores. A seismic reflector is an impedance contrast and in the Gulf of Papua it could represent an event, such as an erosional surface or changes in the sediment characteristics (e.g., a deposit during trade winds season). After picking two-way travel times for the reflectors, we converted these travel times to depth below seafloor using a velocity of 1300 m/s. Although this is low compared to literature values that commonly use a two-way travel time velocity of 1500m/s, lower values for seismic velocity have been used successfully in Fallen Leaf Lake matching reflector depths to identifiable features in cores (Maloney et al., 2013), and east of the MacKenzie River, where P wave velocity of the core logged at sea was 1333 m/s (Keigwin et al., 2018).

Additionally, the 4.26 m offset determined from radiocarbon ages for JPC02 is consistent with the location of the transgressive surface identified in the seismic data (Fig. A.8). With this 4.26 m offset, the top of the erosional surface (shown as shaded region of the core), which was identified in the core by ooids and coarse sediment, approximately coincides with the high amplitude reflector that we recognize as a regional erosional surface.

Fig. A.7 shows an uninterpreted and interpreted seismic profile (the location of the line shown is highlighted in Fig. A.1) and the locations of two cores (JPC06 and JPC43) on this strike-parallel seismic line. The two cores are located about 10 km apart, and the majority of the reflectors can be traced laterally between the core sites (Fig. A.7). The radiocarbon ages obtained from each core (Table A.2) indicate similar sedimentation rates at the two coring sites. The compatibility of the seismic reflectors with the radiocarbon ages (bottom panel Fig. A.7) indicates that these two cores likely have similar depositional history.

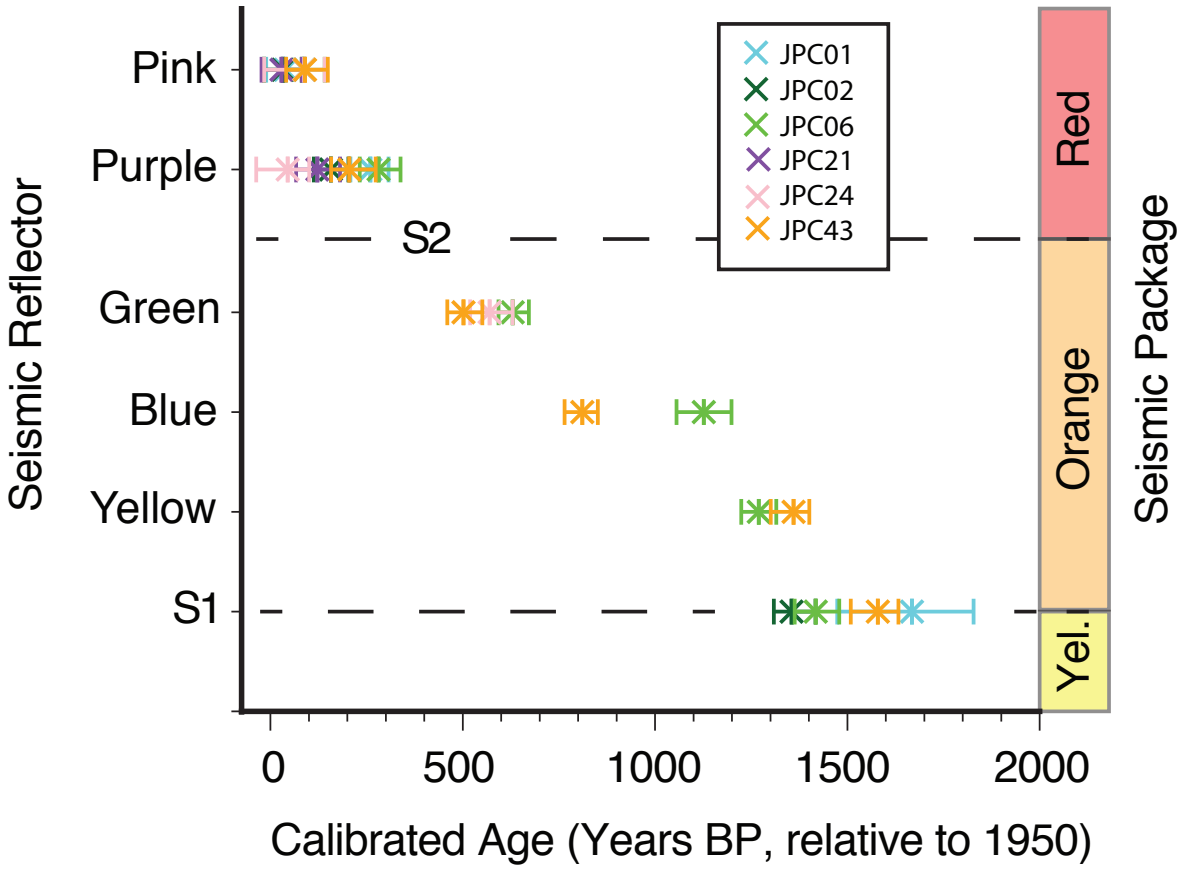

Figure A.9: Apparent ages of seismic reflectors in each core, determined using calibrated radiocarbon dates above and below each reflector. Reflectors were identified within the Orange and Red seismic packages and additionally at the S1 surface (Slingerland et al., 2008a) separating the Yellow and Orange packages. S2 represents the surface separating the Orange and Red seismic packages. Star represents best age, and the whiskers represent maximum and minimum estimates on the age from the 1-sigma error on the radiocarbon dates.

Although the overall consistency of the apparent ages of reflectors between cores JPC06 and JPC43 is encouraging (Fig. A.7), the large distances between cores and differences in sediment source along the margin make using seismic reflectors as temporal markers between lobes impossible. The reflectors within these sequences were identified based on acoustic character and stratal relationships. It is difficult to trace these reflectors between the lobes due to pinchout and truncation due to toplap, but within a lobe our preferred interpretation is that the reflectors have time significance. However, these reflectors are not identifiable everywhere. For example, high accumulation rate cores JPC44 and JCP45 nominally correspond with the Red seismic package but lack the Pink and Purple reflectors characteristic of this unit elsewhere. JPC 45 is located in the southern lobe and in a broad topographic low defined by the topography of the underlying blue sequence. It is possible that the high accumulation rates in this location are due to gravity flows. Reflectors were not continuously traced between lobes but nonetheless it is plausible that the changes in geometry may have a general time significance. The systematic increase in age with depth shown in Fig. A.9 generally supports such a relationship and is encouraging from a paleomagnetic perspective, because it suggests that the sedimentation was continuous, with few large gaps in the data.

A.5.5 Age model

Radiocarbon ages document significant variation in sediment ac- cumulation rates (Fig. A.10) and the eight cores display various degrees of continuity (Fig. A.7), due to both piston core offsets and hiatuses in the record. JPC01, JPC06, and JPC43 appear to span approximately 1500years with relatively continuous sedimentation. All the trigger cores also appear to represent continuous sedimentation, but the trigger cores for JPC01 and JPC02 appear to have a much lower sedimentation rate than cores farther southwest in the Gulf of Papua.

JPC44 and JPC45 are two cores that have extremely high sedimentation rates. Two dates within JPC44 gave a sedimentation rate of 5.4 cm/year. In JPC45, 680 cm of sediment accumu-

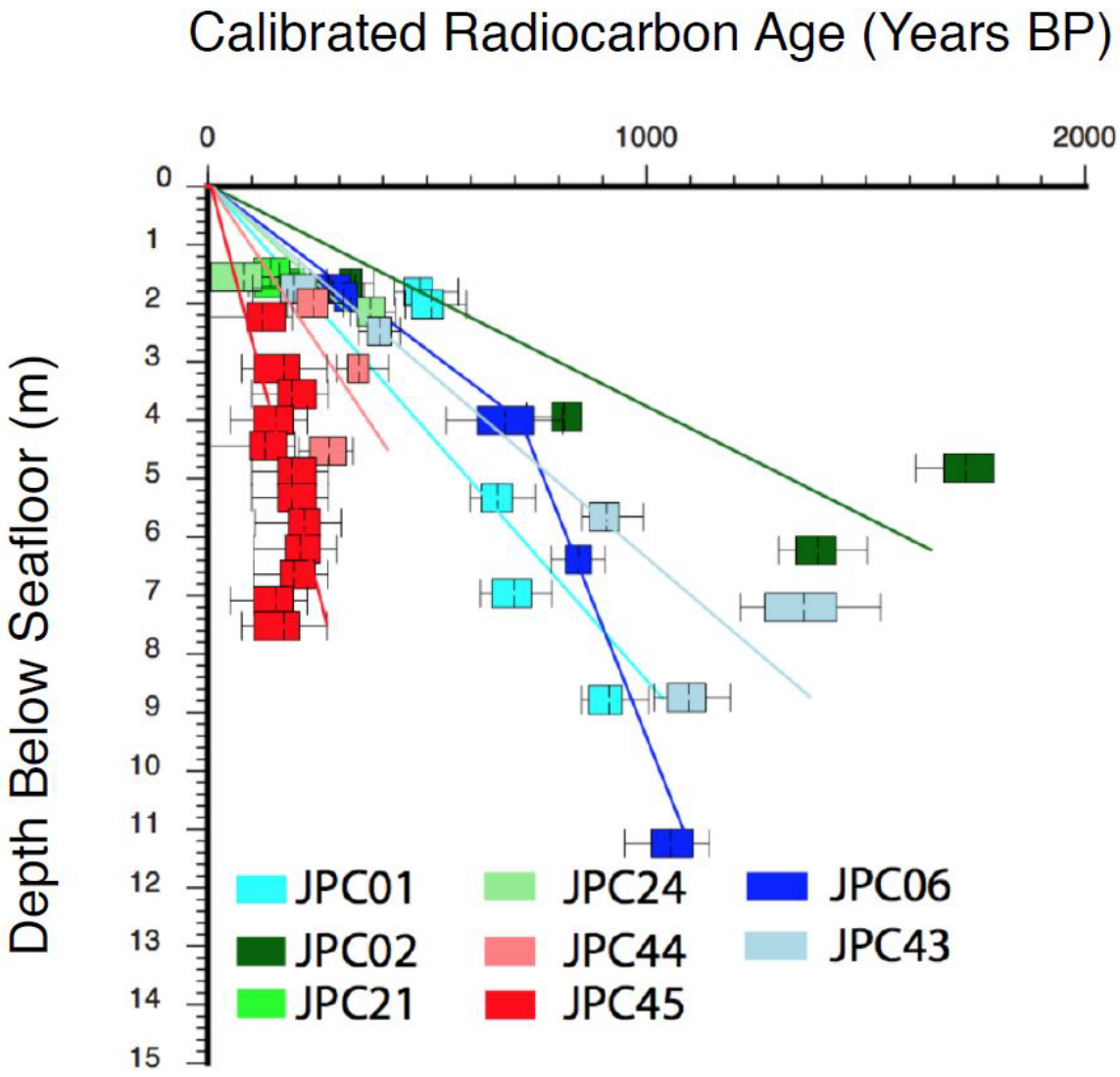

Figure A.10: Calibrated radiocarbon ages and best fit line with one sigma (box) and 2 sigma (whisker) error bars plotted against depth.

lated in the last 350 years BP. These variable and sometimes extremely large sedimentation rates are not a surprise (see Walsh et al., 2004 and Harris et al., 1993), but they can be used to make a strong case for converting measurements from depth to age using a core's own chronology.

The only hiatus that can be confidently identified is that associated with the transgressive surface; there is no visual evidence of other discrete events though they could be present. JPC02 extends back about 2000 years before encountering this hiatus, below which ages are significantly older (>6000 years BP). JPC21 and JPC24 have high sedimentation rates in the sections above the transgressive surface, but below the surface there were insufficient benthic foraminifera to perform radiocarbon dating. Samples from within the transgressive deposit were dated and yield ages >3500 years BP that may be used for estimating timing of the deposit, but this is not the focus of this study. The ages predating the transgressive deposit from JPC02, JPC21 and JPC24 (Table A.2) are not plotted or used in establishing an age-depth model because they span a hiatus or are obtained from potentially reworked material overlying an erosional unconformity.

While some studies do not use radiocarbon ages directly, but instead transfer age information from one core to another using correlations based on susceptibility or remanence, in this complex depositional setting that method is not appropriate. All cores are converted to age using a linear regression to find a best fitting line that passes through the origin, because the tops of all cores gave greater than modern radiocarbon ages. We do this for all cores, except JPC06 which is best represented by two straight line segments fit to the radiocarbon ages.

A.5.6 Stacking

Although the cores measured in this study collectively cover a time back to 2000 years BP, few cores cover that span continuously (Fig. A.11). The most recent 300 years are recorded in every core as all cores have present-day radiocarbon ages at the tops of the trigger cores. JPC01, JPC06 and JPC43 provide records back to approximately 1600 years, and JPC02 extends back approximately 2000 years; however, it is missing approximately 600 years of time between the

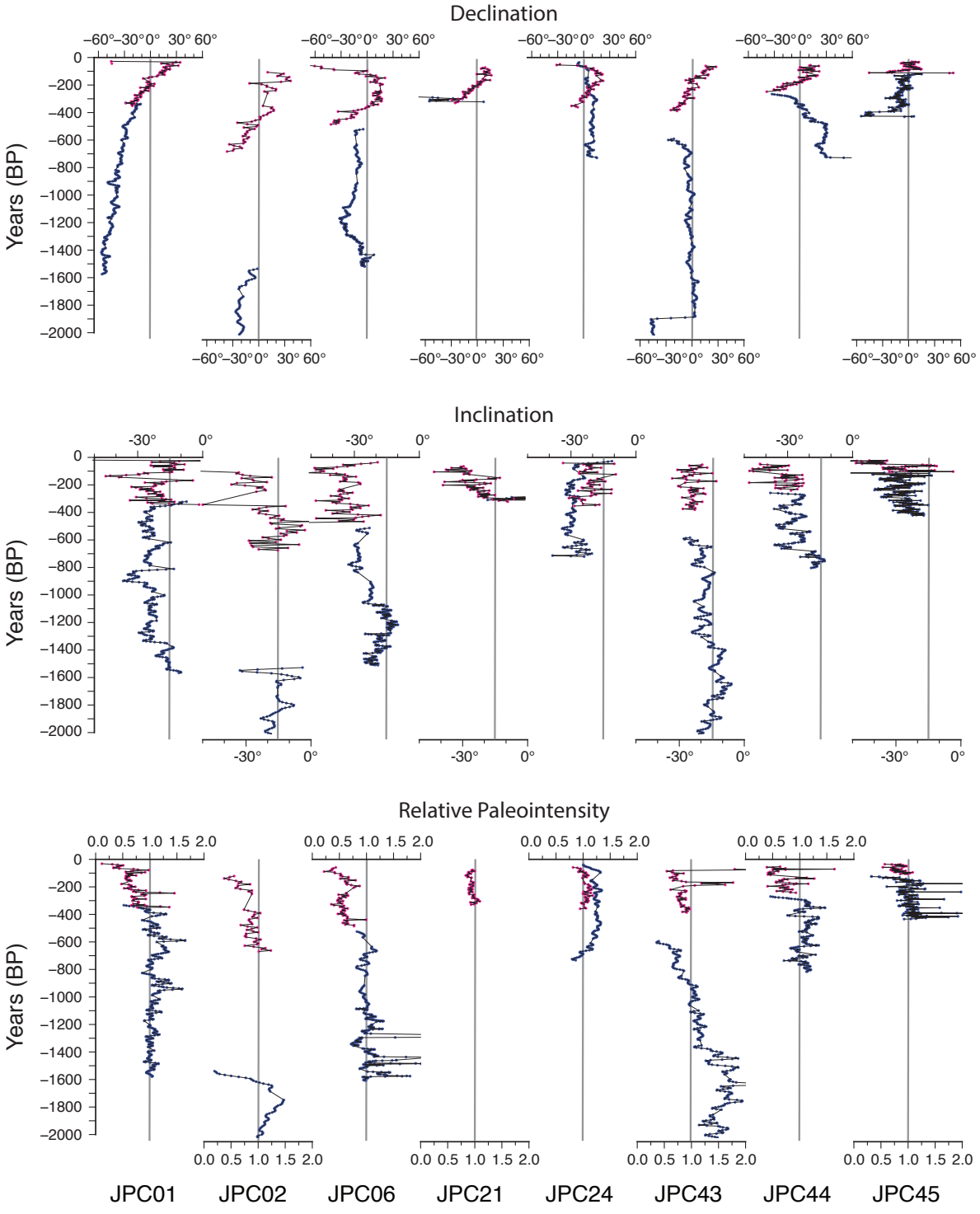

Figure A.11: Relative declination, inclination, and relative paleointensity for each core. Trigger core is shown in deep pink and piston core is shown in blue. GAD inclination predicted at this site is shown with a grey line.

trigger and piston cores due to the over penetration of the piston core. JPC44 and JPC45 cover the most recent 300 years with extremely high resolution, but provide minimal coverage before then. All trigger cores exhibit a consistent declination change, showing an easterly drift from approximately 500 years BP to present. However, piston cores that cover that same interval do not necessarily replicate that change. Of particular note is JPC24, where the piston core and trigger core appear to overlap completely in time but do not show the same trend in declination. JPC44 also shows an opposite trend in declination between the piston core and trigger core. Most of the cores have inclinations that get less steep, and closer to the geocentric axial dipole (GAD) value expected at the site, deeper in the core, although JPC24 is an exception, with inclinations in the trigger core lying close to the GAD value.

The high accumulation rates of JPC44 and JPC45 mean that the resolution of the first 300 years is better compared to the resolution in cores with lower sedimentation rates over the last 300 years. The differences in accumulation rates change our approach to stacking. While previous studies (e.g., Constable & McElhinny, 1985) interpolate a single value of inclination, declination and relative paleointensity to evenly spaced depths for each core, this approach would not translate well to this study. For example, a single interpolation scheme based on the lower resolution cores would eliminate data from the higher resolution ones. Conversely, an interpolation based on the higher sedimentation rate cores would result in a substantial fraction of interpolated data in the more slowly accumulated cores. We take a Fisher average of the inclination and declination data after binning into 20 year non-overlapping intervals, as a compromise between the low and high sedimentation rate cores, and calculate an alpha 95 confidence interval. A small amount of data was not included in the stack - the section of JPC44 that had a nearly instantaneous 100° shift in declination was removed prior to binning and averaging data.

To plot relative paleointensity versus depth in Fig. A.6, the values of $\mathrm{NRM}_{10mT}/\mathrm{ARM}_{10mT}$ were divided by the mean of the entire core. The result of this in JPC21 and JPC24 is a very low relative paleointensity in the section above the transgressive surface and a larger value for the

sections below the surface. The only conclusions that can be drawn from this are that the intensity of the field in the last 300 years is lower than the intensity of the field at some prior, unknown time. Therefore, in Fig. A.11, the values for JPC21 and JPC24 have been divided by the mean of the only the data from above the transgressive surface in these cores.

A.6 Discussion

The Gulf of Papua cores collectively provide a high-accumulation rate record of geomagnetic field from 2000 to present, helping to fill a major gap in the current global sedimentary field data. High resolution studies like this one are essential for refining our current Holocene field models. In this study, the broad inclination record is probably the most robust feature of the data, and an apparent trend for the past 2000 years observed in Fig. A.12 is a steepening in inclination from $-20°$ to the present-day value at the site of $-30°$. The declination has an eastward trend since 1400 years BP, and the relative paleointensity has been decreasing. Although data from the past 2000 years are shown, 1600-2000 years BP should be treated with caution, as it represents only one or two cores from the region. The abrupt change in inclination, declination, and paleointensity near 1600 years is due to the lower portion of the stack being calculated from only a single core and is not robust.

There are few complete, high-resolution records for 0-2000 years in this region. In addition to comparing our results to ODP Hole 1202B (4360 km away, Richter et al., 2006), and Lake Pounui (4780 km away, Turner & Lillis, 1994), we plot predictions at this site from the CALS3k.4 (Korte & Constable, 2011) and pfm9k (Nilsson et al., 2014) field models. The Holocene sedimentary paleofield record closest to the Gulf of Papua is the record from Lake Kailampaa (Haberzettl et al., 2013). The age model from this record is difficult to evaluate since all the dates were on bulk sediment and repeat analyses from multiple labs gave discrepant results. Given this poorly constrained age model, we have made no comparisons to this nearby record.

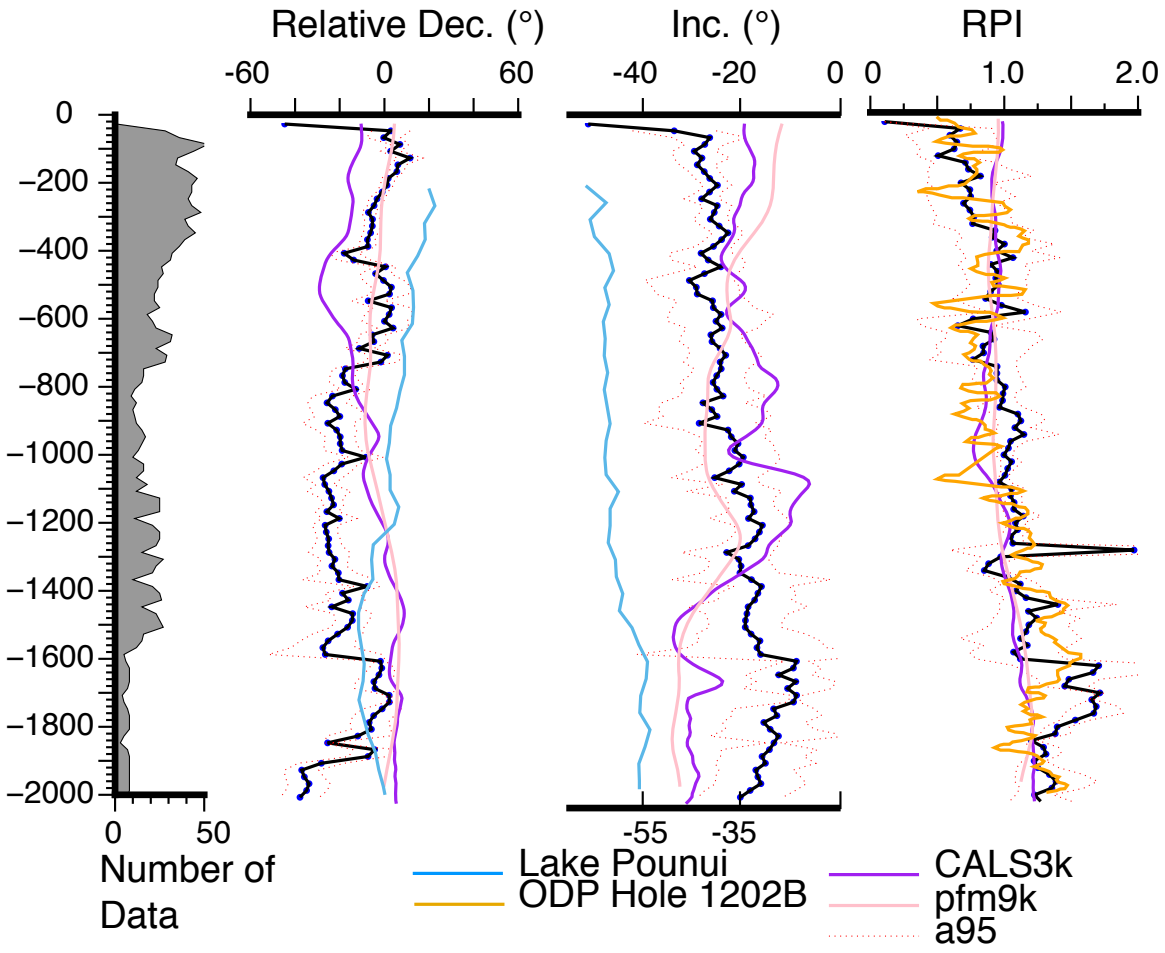

Figure A.12: Stacked record using 20 year age bins. Fisher mean is plotted in blue for declination and inclination with alpha 95 confidence interval (dotted red) and RPI mean (blue) and standard deviation (dotted red). Grey bars at left indicate number of points used to average. Model predictions from CALS3k and pfm9k are shown in purple and light pink. Results from Lake Pounui (Turner & Lillis, 1994), with inclination scale shown at bottom, and ODP Hole 1202B (Richter et al., 2006) are plotted for comparison.

Our record and the ODP Hole 1202B show a decrease in paleointensity over the last 2000 years (Fig. A.12). The long-term trends of these two records is remarkably similar and potentially even smaller-scale features may correlate - see for example 1800-1300 years BP or 600-200 years BP. The Lake Pounui record of declination shows a similar long-term trend to this study with a steady eastward trending portion from 1600 years BP to present.

Both inclination records exhibit the same pattern of steepening inclination. Generally, the records shown here exhibit better agreement amongst themselves than with predictions from the models. For example, the inclination of the models exhibits a shallowing from 1440 to present day compared to the two records, and the relative intensity of the models shows very little variation compared to the records shown. The addition of more sediment directional and paleointensity data as well as archeomagnetic data should help to refine the models in these areas.

Although early studies had concluded that westward drift was the dominant movement of non-dipolar parts of the field (e.g., Bullard et al., 1950; Vestine, 1953; Nagata, 1965), further studies showed more complex motions of the non-dipolar part of the field, including episodes of eastward drift. Westward drift was initially explained by Bullard et al. (1950) using dynamo theory that required the outer part of the core to rotate less rapidly than the inner part. This uniform view of the magnetic field coupled the solid mantle to the core as a whole, and features of the field moved westward with the motion of the outer part of the core Analysis of the global field model CALS7k.2 (Korte & Constable, 2005) by Wardinski & Korte (08) and Dumberry & Finlay (2007) showed both eastward and westward drift. While westward drift of high latitude flux patches and features in the Atlantic appear to be real (Nilsson et al., 2014), confirmation of westward drift in the southern hemisphere is limited due to the lack of data and limited resolution of the models in that region. The trend in declination from our new record does not suggest westward drift in this time period.

As noted previously, there are a number of different techniques that can be used to establish tie points between cores. The most suitable features to use as tie points should have

a well-known date and be continuous over the region of study, which usually requires a good understanding of the process or mechanism by which that feature is generated. There are examples of this, such as susceptibility changes related to glacial/interglacial variations, where the origin of the variations has a satisfying physical explanation (e.g., Lean & McCave, 1998; Sakai et al., 2000). Nevertheless, poor theoretical understanding of how sediments record the geomagnetic field should discourage one from attempting to match multiple inclination and declination features that appear on very short time scales or over large distances.

Susceptibility can be useful for establishing tie points, but it also can suffer from the same problems as matching inclination and declination changes in susceptibility and are not unique to specific causes or processes. It could be related to a time transgressive deposit, as was seen in this study, or it could be due to natural variation in sedimentation that is not necessarily continuous across the spatial scale of the study. In both cases of susceptibility and inclination/declination matching, matches should be made only if there is some level of coherence at the scale of interest. In our study we chose to combine cores based on their own chronology based on radiocarbon data and are consistent with stratigraphic correlation, because the complexities in the environment were simply too great to assume that variations in susceptibility had a relevant time association.

One of the more puzzling aspects of the Papua New Guinea records is the presence of apparent rapid (approximately instantaneous) changes in the declination within a core section. Several cores had sections where there were large ($>30°$) abrupt changes in relative declination. They are visible in JPC43, JPC44 and JPC45, occur at three different times (1800 BP, 400 BP and 300 BP), and do not swing in the same direction in all three cores (Fig. A.11). Cores JPC43 and JPC44 were measured with both U-channels and discrete samples across the swing in declination to verify that there was no error in the sampling or measurement of the U-channel. These swings in declination occurred in the middle of sections, away from any deformation evident at section ends. The MAD values and inclination values at these points do not deviate from the typical values, there are no visible changes in lithology, and the near vertical alignment of the minimum

susceptibility axes give us confidence that these cores represented an environment that has been relatively undisturbed since deposition. These swings occur near the bottoms of the cores but are well above the depth where flow-in occurs, which can be observed visibly and is also readily identified by the off-vertical minimum susceptibility axis with high MAD values.

It is also difficult to conceive how half a section of core could be rotated in the process of sectioning, capping, or splitting the cores, since the clay is very cohesive and there was no visible evidence of such a rotation, that is no break or gap in the core was observed. Another possibility is that these declination shifts represent a slump or fluid mud flow. The cores are far enough apart and sedimentation in the area is varied enough that these three declination shifts could represent three different events, with no requirement that the event be present in all cores, but with a slump or mudflow there should be some difference in magnetic fabric - more triaxial instead of oblate fabric, a change in the direction of Kmax, or an off-vertical minimum axis (Schwehr et al., 2006). In all three cores, there is no distinct change in fabric type or systematic variation in Kmax.

A final possibility is that these swings represent true changes in the geomagnetic field. This seems unlikely as the swings trend in different directions, are not visible in every core, and are not accompanied by a significant increase or decrease in intensity or inclination. Additionally, the rate at which these apparent shifts occur are significantly faster than anything predicted by gufm/IGRF at the location or even at similar latitudes. Rates predicted by these models are on the order of 0.05° per year - a factor of twenty smaller than the directional change observed (>50° of declination change over less than fifty years). Although we don't believe these represent true changes in the field, with a sufficient number of records, these large swings will have minimal effect on the resulting stack. Similar observations of abrupt changes in declination have been made previously (Barletta et al., 2010; Barletta et al., 2010) with no viable explanation.

A.7 Conclusions

We presented a high resolution paleosecular variation and relative paleointensity stacked record from a set of cores collected in the Gulf of Papua. Dating was performed on all cores using AMS radiocarbon, and showed that sedimentation was up to 500 cm/kyr in some locations, but also extremely variable. This high sedimentation rate allows for identification of features on short time scales. The main magnetic carrier was determined to be PSD (titano)magnetite, and the similar character of demagnetization curves for NRM and ARM as well as minimal grain size variation suggest that ARM is a suitable normalizer when determining paleointensity.

Our results from dating both the bottoms of the trigger cores and tops of the piston cores allowed us to determine the offset of the piston core with tools other than matching density or susceptibility. This approach revealed that in many cores there was no overlap of the two and the piston core had penetrated the seafloor much deeper than the trigger core before acquiring sediment.

Seismic data collected in the area were able to place additional constraints on the offsets calculated for the piston cores using sedimentation rates and correlation of reflectors between cores is consistent with the radiocarbon dates (Fig. A.8). Seismic data is very useful for aiding in paleomagnetic correlation, but it should be employed with caution because of the three dimensional variability of depositional packages. Correlations often break down across large distances where the assumption that a horizon is an isochron is less likely to be valid. Regardless of which parameter one chooses to aid in correlation of cores, there should be careful consideration before making the assumption that variations are time equivalent.

There are many challenges involved with separating true variations in the magnetic field from uncertainties in the coring process and from complexities in depositional environment. To create an ideal stack and minimize uncertainties, there is a need for multiple cores from the same site (meaning identical geographic coordinates) and multiple sets from a small region. An

excellent way to sample a site is with a companion gravity core, which will ensure there is no data gap (from piston core over penetration), and will provide a means of validating data from the upper portion of the piston core. A second piston core at a site would be labor and time intensive, but would allow one to isolate variations due to the coring process from variations due to the environment. Multiple radiocarbon dates from sets of cores in the region should be employed to establish an age model and highlight any regional variations in sedimentation.

Despite these limitations, our stacked record from this region shows a steepening in inclination over the past 2000 years and an eastward trend in declination, which is in good agreement with other nearby results, including ODP Hole 1202B (Richter et al., 2006), and Lake Pounui (Turner & Lillis, 1994). The stacked record based on these cores is inconsistent with both CALS3k and pfm9k. The poor agreement with these models is not unexpected since the models are poorly constrained by data in this region. This agreement with nearby records gives a good indication that the marine sediments in the Gulf of Papua are a reliable recorder of the magnetic field, but more data from the region would help improve Holocene field models.

A.8 Acknowledgements

This work is published in **Marcuson, R., Gee, J., Wei, E.A., and Driscoll, N.W., 2019. A 2000 year geomagnetic field record from the Gulf of Papua.** ***Marine Geology*** **408, 48-66**. The dissertation author was a co-author of this material. Core acquisition was funded by the National Science Foundation award 0305699 under the MARGINS Source to Sink program. We also would like to thank the crew of the R/V Melville, and Alex Hangsterfer who helped with cores. Carl Richter kindly provided us with data from ODP 1202.

Bibliography

Aalto, R. (2015). Quaternary morphodynamics of fluvial dispersal systems revealed: The Fly River, PNG, and the Sunda Shelf, SE Asia, simulated with the massively parallel GPU-based model 'GULLEM'. In *AGU Fall Meeting Abstracts*. AGU.

Aalto, R., Lauer, J., Darby, S., Goni, M., & Dietrich, W. (2014). Quaternary morphodynamics for two large rivers: the Fly River, PNG, and the Mekong River, Cambodia. In *AGU Fall Meeting Abstracts*, volume 1.

Aalto, R., Lauer, J. W., & Dietrich, W. E. (2008). Spatial and temporal dynamics of sediment accumulation and exchange along Strickland River floodplains (Papua New Guinea) over decadal-to-centennial timescales. *Journal of Geophysical Research*, *113*(F1).

Ali, M., Oda, H., Hayashida, A., Takemura, K., & Torii, M. (1999). Holocene palaeomagnetic secular variation at Lake Biwa, central Japan. *Geophysical Journal International*, *136*(1), 218–228.

Allen, G. P. & Posamentier, H. W. (1994). Transgressive facies and sequence architecture in mixed tide-and wave-dominated incised valleys: example from the Gironde Estuary, France.

Allen, P. A. (2008). Time scales of tectonic landscapes and their sediment routing systems. *Geological Society, London, Special Publications*, *296*(1), 7–28.

Anderson, J. B., Wallace, D. J., Simms, A. R., Rodriguez, A. B., Weight, R. W., & Taha, Z. P. (2016). Recycling sediments between source and sink during a eustatic cycle: Systems of late Quaternary northwestern Gulf of Mexico Basin. *Earth-Science Reviews*, *153*, 111–138.

Anderson, R. S., Ejarque, A., Rice, J., Smith, S. J., & Lebow, C. G. (2015). Historic and Holocene environmental change in the San Antonio Creek Basin, mid-coastal California. *Quaternary Research*, *83*(2), 273–286.

Andrews, J. T. & Vogt, C. (2014). Source to sink: Statistical identification of regional variations in the mineralogy of surface sediments in the western Nordic Seas (58°n–75°n; 10°w–40°w). *Marine Geology*, *357*, 151–162.

Atwater, B. F., Carson, B., Griggs, G. B., Johnson, H. P., & Salmi, M. S. (2014). Rethinking turbidite paleoseismology along the Cascadia subduction zone. *Geology*, *42*(9), 827–830.

Atwater, T. & Stock, J. (1998). Pacific-North America plate tectonics of the Neogene southwestern United States: an update. *International Geology Review*, *40*(5), 375–402.

Bagnold, R. (1941). *The physics of blown sand and desert dunes*. Methuen.

Banfield, L. A. & Anderson, J. B. (2004). Late Quaternary evolution of the Rio Grande delta: complex response to eustasy and climate change.

Bard, E., Hamelin, B., & Fairbanks, R. G. (1990). U-Th ages obtained by mass spectrometry in corals from Barbados: sea level during the past 130,000 years. *Nature*, *346*(6283), 456.

Barletta, F., St-Onge, G., Channell, J., & Rochon, A. (2010). Dating of Holocene western Canadian Arctic sediments by matching paleomagnetic secular variation to a geomagnetic field model. *Quaternary Science Reviews*, *29*(17-18), 2315–2324.

Barletta, F., St-Onge, G., Channell, J. E., Rochon, A., Polyak, L., & Darby, D. (2008). High-resolution paleomagnetic secular variation and relative paleointensity records from the western Canadian Arctic: implication for Holocene stratigraphy and geomagnetic field behaviour. *Canadian Journal of Earth Sciences*, *45*(11), 1265–1281.

Barletta, F., St-Onge, G., Stoner, J., Lajeunesse, P., & Locat, J. (2010). A high-resolution holocene paleomagnetic secular variation and relative paleointensity stack from eastern Canada. *Earth and Planetary Science Letters*, *298*(1-2), 162–174.

Barrineau, C., Tchakerian, V., & Houser, C. (2012). Aeolian processes of the Pismo-Oceano Dune Complex, California. In *AGU Fall Meeting Abstracts*.

Barton, C. & McElhinny, M. (1981). A 10,000 yr geomagnetic secular variation record from three Australian maars. *Geophysical Journal International*, *67*(2), 465–485.

Bijkerk, J. F., Eggenhuisen, J. T., Kane, I. A., Meijer, N., Waters, C. N., Wignall, P. B., & McCaffrey, W. D. (2016). Fluvio-marine sediment partitioning as a function of basin water depth. *Journal of Sedimentary Research*, *86*(3), 217–235.

Biscaye, P. E. (1965). Mineralogy and sedimentation of recent deep-sea clay in the Atlantic Ocean and adjacent seas and oceans. *Geological Society of America Bulletin*, *76*(7), 803–832.

Blaauw, M. & Christen, J. A. (2011). Flexible paleoclimate age-depth models using an autoregressive gamma process. *Bayesian analysis*, *6*(3), 457–474.

Blake, D. & Ollier, C. (1969). Geomorphological evidence of Quaternary tectonics in southwestern Papua. *Revue de Géomorphologie Dynamique*, *19*, 28–32.

Blum, M., Martin, J., Milliken, K., & Garvin, M. (2013). Paleovalley systems: insights from Quaternary analogs and experiments. *Earth-Science Reviews*, *116*, 128–169.

Bohannon, R. G. & Geist, E. (1998). Upper crustal structure and Neogene tectonic development of the California continental borderland. *Geological Society of America Bulletin*, *110*(6), 779–800.

Bol'shakov, V. & Dolotov, A. (2012). Magnetic properties of greigite in the Late Pleistocene sediments of the North Caspian. *Izvestiya Physics of the Solid Earth*, *48*(6), 516–531.

Bolton, B. R., Pile, J. L., & Kundapen, H. (2008). Texture, geochemistry, and mineralogy of sediments of the Fly River System. *Developments in Earth and Environmental Sciences*, *9*, 51–112.

Borgeld, J. C., Clarke, J. E. H., Goff, J. A., Mayer, L. A., & Curtis, J. A. (1999). Acoustic backscatter of the 1995 flood deposit on the Eel shelf. *Marine Geology*, *154*(1-4), 197–210.

Bowen, A. J. & Inman, D. L. (1966). Budget of littoral sands in the vicinity of Point Arguello, California. Report, US Army Corps of Engineers.

Brachfeld, S., Acton, G. D., Guyodo, Y., & Banerjee, S. K. (2000). High-resolution paleomagnetic records from Holocene sediments from the Palmer Deep, Western Antartic Peninsula. *Earth and Planetary Science Letters*, *181*(3), 429–441.

Brachfeld, S., Barletta, F., St-Onge, G., Darby, D., & Ortiz, J. D. (2009). Impact of diagenesis on the environmental magnetic record from a Holocene sedimentary sequence from the Chukchi-Alaskan margin, Arctic Ocean. *Global and Planetary Change*, *68*(1-2), 100–114.

Brachfeld, S. A. & Banerjee, S. K. (2000). A new high-resolution geomagnetic relative paleointensity record for the North American Holocene: A comparison of sedimentary and absolute intensity data. *Journal of Geophysical Research: Solid Earth*, *105*(B1), 821–834.

Brothers, D. S., Conrad, J. E., Maier, K. L., Paull, C. K., McGann, M., & Caress, D. W. (2015). The Palos Verdes fault offshore southern California: Late Pleistocene to present tectonic geomorphology, seascape evolution, and slip rate estimate based on AUV and ROV surveys. *Journal of Geophysical Research: Solid Earth*, *120*(7), 4734–4758.

Buckley, D., MacKinnon, W., Cranston, R., & Christian, H. (1994). Problems with piston core sampling: Mechanical and geochemical diagnosis. *Marine Geology*, *117*(1-4), 95–106.

Bullard, E. C., Freedman, C., Gellman, H., & Nixon, J. (1950). The westward drift of the Earth's magnetic field. *Philosophical Transactions of the Royal Society of London. Series A, Mathematical and Physical Sciences*, *243*(859), 67–92.

Burr, G., Beck, J., Corrège, T., Cabioch, G., Taylor, F. W., & Donahue, D. (2009). Modern and Pleistocene reservoir ages inferred from South Pacific corals. *Radiocarbon*, *51*(1), 319–335.

California Geological Survey (CGS) (2011). Oceano Dunes SVRA - sand grain size analyses, part 2: Microprobe analyses of grain size and mineral composition. Report, California Geological Survey.

Carré, M., Bentaleb, I., Fontugne, M., & Lavallée, D. (2005). Strong El Niño events during the early Holocene: stable isotope evidence from Peruvian sea shells. *The Holocene*.

Castelltort, S. & Van Den Driessche, J. (2003). How plausible are high-frequency sediment supply-driven cycles in the stratigraphic record? *Sedimentary geology*, *157*(1-2), 3–13.

Cattaneo, A. & Steel, R. J. (2003). Transgressive deposits: a review of their variability. *Earth-Science Reviews*, *62*(3-4), 187–228.

Cattaneo, A., Trincardi, F., Asioli, A., & Correggiari, A. (2007). The Western Adriatic shelf clinoform: energy-limited bottomset. *Continental Shelf Research*, *27*(3-4), 506–525.

Central Coast Salmon Enhancement (2005). Arroyo Grande Creek watershed management plan. Report, Prepared for The Department of Fish and Game State of California.

Channell, J., Xuan, C., & Hodell, D. (2009). Stacking paleointensity and oxygen isotope data for the last 1.5 Myr (PISO-1500). *Earth and Planetary Science Letters*, *283*(1-4), 14–23.

Chappell, J. & Polach, H. (1976). Holocene sea-level change and coral-reef growth at Huon Peninsula, Papua New Guinea. *Geological Society of America Bulletin*, *87*(2), 235–240.

Chaytor, J. D., Goldfinger, C., Meiner, M. A., Huftile, G. J., Romsos, C. G., & Legg, M. R. (2008). Measuring vertical tectonic motion at the intersection of the Santa Cruz-Catalina Ridge and Northern Channel Islands platform, California Continental Borderland, using submerged paleoshorelines. *Geological Society of America Bulletin*, *120*(7-8), 1053–1071.

Christie-Blick, N. & Driscoll, N. W. (1995). Sequence stratigraphy. *Annual Review of Earth and Planetary Sciences*, *23*(1), 451–478.

Christl, M., Strobl, C., & Mangini, A. (2003). Beryllium-10 in deep-sea sediments: a tracer for the Earth's magnetic field intensity during the last 200,000 years. *Quaternary Science Reviews*, *22*(5-7), 725–739.

Clark, D. (1990). Late Quaternary tectonic deformation in the Casmalia range, coastal south-central California. In W. Lettis, K. Hanson, K. Kelson, & J. Wesling (Eds.), *Neotectonics of south-central coastal California, Friends of the Pleistocene, Pacific Cell* (pp. 349–383).

Clement, B. M. & Kent, D. V. (1987). Short polarity intervals within the Matuyama: transitional field records from hydraulic piston cored sediments from the North Atlantic. *Earth and Planetary Science Letters*, *81*(2-3), 253–264.

Cohen, J. & Stockwell Jr, J. (2001). Cwp/su: Seismic unix release 35: a free package for seismic research and processing. *Center for wave phenomena, Colorado school of Mines*.

Conrad, J. E., Brothers, D. S., Maier, K. L., Ryan, H. F., Dartnell, P., & Sliter, R. (2018). Right-lateral fault motion along the slope-basin transition, Gulf of Santa Catalina, southern California. In K. M. Marsaglia, J. R. Schwalbach, & R. J. Behl (Eds.), *From the Mountains to the Abyss:*

The California Borderland as an Archive of Southern California Geologic Evolution, SEPM Special Publication, volume 110.

Constable, C. (1985). Eastern Australian geomagnetic field intensity over the past 14000 yr. *Geophysical Journal International*, *81*(1), 121–130.

Constable, C. & McElhinny, M. (1985). Holocene geomagnetic secular variation records from north-eastern Australian lake sediments. *Geophysical Journal International*, *81*(1), 103–120.

Constable, C. & Tauxe, L. (1987). Palaeointensity in the pelagic realm: marine sediment data compared with archaeomagnetic and lake sediment records. *Geophysical Journal International*, *90*(1), 43–59.

Cousineau, L. A. (2012). Stratigraphy of Quaternary dunes by sand mineralogy and pedogenic features, Los Osos, California. MS thesis, California Polytechnic State University, San Luis Obispo.

Covault, J. A. & Graham, S. A. (2010). Submarine fans at all sea-level stands: Tectono-morphologic and climatic controls on terrigenous sediment delivery to the deep sea. *Geology*, *38*(10), 939–942.

Covault, J. A., Kostic, S., Paull, C. K., Ryan, H. F., & Fildani, A. (2014). Submarine channel initiation, filling and maintenance from sea-floor geomorphology and morphodynamic modelling of cyclic steps. *Sedimentology*, *61*(4), 1031–1054.

Covault, J. A., Kostic, S., Paull, C. K., Sylvester, Z., & Fildani, A. (2017). Cyclic steps and related supercritical bedforms: building blocks of deep-water depositional systems, western North America. *Marine Geology*, *393*, 4–20.

Covault, J. A., Normark, W. R., Romans, B. W., & Graham, S. A. (2007). Highstand fans in the California borderland: The overlooked deep-water depositional systems. *Geology*, *35*(9), 783–786.

Covault, J. A. & Romans, B. W. (2009). Growth patterns of deep-sea fans revisited: Turbidite-system morphology in confined basins, examples from the California Borderland. *Marine Geology*, *265*(1-2), 51–66.

Covault, J. A., Romans, B. W., Fildani, A., McGann, M., & Graham, S. A. (2010). Rapid climatic signal propagation from source to sink in a southern California sediment-routing system. *The Journal of Geology*, *118*(3), 247–259.

Covault, J. A., Romans, B. W., Graham, S. A., Fildani, A., & Hilley, G. E. (2011). Terrestrial source to deep-sea sink sediment budgets at high and low sea levels: Insights from tectonically active Southern California. *Geology*, *39*(7), 619–622.

Covault, J. A., Shelef, E., Traer, M., Hubbard, S. M., Romans, B. W., & Fildani, A. (2012). Deep-water channel run-out length: Insights from seafloor geomorphology. *Journal of Sedimentary Research*, *82*(1), 21–36.

Crisp, D. (2017). Relationship of land use modification and sediment transportation to transverse and parabolic dune behavior in the Mussel Rock dunes complex, California. MS thesis, California State University Northridge.

Crockett, J. S., Nittrouer, C. A., Ogston, A. S., Naar, D. F., & Donahue, B. T. (2008). Morphology and filling of incised submarine valleys on the continental shelf near the mouth of the Fly River, Gulf of Papua. *Journal of Geophysical Research*, *113*(F01S12).

Crouch, J. (1979). Neogene tectonic evolution of the western Transverse Ranges and the California Continental Borderland. *Geological Society of America Bulletin*, *90*, 338–345.

Crouch, J. K. & Suppe, J. (1993). Late Cenozoic tectonic evolution of the Los Angeles basin and inner California borderland: A model for core complex-like crustal extension. *Geological Society of America Bulletin*, *105*(11), 1415–1434.

Dartnell, P., Driscoll, N. W., Brothers, D. S., Conrad, J. E., Kluesner, J., Kent, G., & Andrews, B. D. (2015). Colored shaded-relief bathymetry, acoustic backscatter, and selected perspective views of the Inner Continental Borderland, southern California. Technical report, US Geological Survey Scientific Investigations Map 3324.

Davies, H. L. (2012). The geology of New Guinea-the cordilleran margin of the Australian continent. *Episodes*, *35*(1), 87–102.

Davies, P. J., Symonds, P. A., Feary, D. A., & Pigram, C. J. (1989). The evolution of the carbonate platforms of northeast Australia. *44*, 26.

Day, G., Dietrich, W. E., Rowland, J. C., & Marshall, A. (2008). The depositional web on the floodplain of the Fly River, Papua New Guinea. *Journal of Geophysical Research*, *113*(F1).

Day, R., Fuller, M., & Schmidt, V. (1977). Hysteresis properties of titanomagnetites: grain-size and compositional dependence. *Physics of the Earth and planetary interiors*, *13*(4), 260–267.

Dietrich, W., Day, G., & Parker, G. (1999). The Fly River, Papua New Guinea: Inferences about river dynamics, floodplain sedimentation and fate of sediment. *Varieties of Fluvial Form*, 345–376.

Draut, A. E., Hart, P. E., Lorenson, T. D., Ryan, H. F., Wong, F. L., Sliter, R. W., & Conrad, J. E. (2009). Late Pleistocene to Holocene sedimentation and hydrocarbon seeps on the continental shelf of a steep, tectonically active margin, southern California, USA. *30*(3), 193–206.

Driscoll, N., Kent, G., & Bormann, J. (2018). Processed multi-channel seismic data (stacks and migrations) offshore California acquired during the R/V New Horizon expedition NH1320 (2013) using a sparker source. Technical report, Interdisciplinary Earth Data Alliance (IEDA).

Driscoll, N. W. & Karner, G. D. (1999). Three-dimensional quantitative modeling of clinoform development. *Marine Geology*, *154*, 15.

Driscoll, N. W. & Milliman, J. (2004a). Subbottom CHIRP active seismic data from the Gulf of Papua acquired during the R/V Melville expedition VANC22MV expedition (2004). Technical report, Rolling Deck to Repository, Marine Geoscience Data System.

Driscoll, N. W. & Milliman, J. (2004b). Subbottom CHIRP active seismic data from the Gulf of Papua acquired during the R/V Melville expedition VANC23MV expedition (2004). Technical report, Rolling Deck to Repository, Marine Geoscience Data System.

Droxler, A., Mallarino, G., Francis, J. M., Dickens, J., Beaufort, L., Bentley, S., Peterson, L., & Opdyke, B. Early part of last deglaciation: A short interval favorable for the building of coralgal edifices on the edges of modern siliciclastic shelves (Gulf of Papua and Gulf of Mexico). In *AAPG 2006 Annual Convention, Houston, Tex.*

Ducassou, E., Migeon, S., Mulder, T., Murat, A., Capotondi, L., Bernasconi, S. M., & Mascle, J. (2009). Evolution of the Nile deep-sea turbidite system during the Late Quaternary: influence of climate change on fan sedimentation. *Sedimentology*, *56*(7), 2061–2090.

Dumberry, M. & Finlay, C. C. (2007). Eastward and westward drift of the Earth's magnetic field for the last three millennia. *Earth and Planetary Science Letters*, *254*(1-2), 146–157.

Ehlig, P. (1977). Geologic report on the area adjacent to the San Onofre Nuclear Generating Station, Northwestern San Diego County, California. *Neotectonics and Coastal Instability: Orange and Northern San Diego Counties, California*, 113–132.

Eittreim, S. L., Anima, R. J., & Stevenson, A. J. (2002). Seafloor geology of the Monterey Bay area continental shelf. *Marine Geology*, *181*(1-3), 3–34.

Etyemezian, V., Gillies, J., Zhu, D., Plkharel, A., & Nikolich, G. (2015). 2013 intensive wind erodibility measurements at and near the Oceano Dunes Vehicular Recreation Area: Report of findings. Report, Prepared for California Department of Parks and Recreation.

Fairbanks, R. G. (1989). A 17,000-year glacio-eustatic sea level record: influence of glacial melting rates on the Younger Dryas event and deep-ocean circulation. *Nature*, *342*(6250), 637.

Fairbanks, R. G., Charles, C. D., & Wright, J. D. (1992). Origin of global meltwater pulses. In *Radiocarbon after four decades* (pp. 473–500). Springer.

Febo, L. A., Bentley, S. J., Wrenn, J. H., Droxler, A. W., Dickens, G. R., Peterson, L. C., & Opdyke, B. N. (2008). Late Pleistocene and Holocene sedimentation, organic-carbon delivery, and paleoclimatic inferences on the continental slope of the northern Pandora Trough, Gulf of Papua. *Journal of Geophysical Research*, *113*(F01S18).

Ferrini, V. L. & Flood, R. D. (2006). The effects of fine-scale surface roughness and grain size on 300 khz multibeam backscatter intensity in sandy marine sedimentary environments. *Marine Geology*, *228*(1-4), 153–172.

Fletcher, C. H. & Sherman, C. E. (1995). Submerged shorelines on O'ahu, Hawai'i: archive of episodic transgression during the deglaciation? *Journal of Coastal Research*, *17*, 141–152.

Folk, R. L. (1980). *Petrology of sedimentary rocks*. Hemphill Publishing Company.

Fonseca, L. & Mayer, L. (2007). Remote estimation of surficial seafloor properties through the application Angular Range Analysis to Multibeam sonar data. *28*(2), 119–126.

Francis, J. M., Daniell, J. J., Droxler, A. W., Dickens, G. R., Bentley, S. J., Peterson, L. C., Opdyke, B. N., & Beaufort, L. (2008). Deep water geomorphology of the mixed siliciclastic-carbonate system, Gulf of Papua. *Journal of Geophysical Research*, *113*(F01S16).

Frank, U., Nowaczyk, N. R., & Negendank, J. F. (2007). Rock magnetism of greigite bearing sediments from the Dead Sea, Israel. *Geophysical Journal International*, *168*(3), 921–934.

Freeman, S. T., Heath, E. G., Guptill, P. D., & Waggoner, J. T. (1992). Seismic hazard assessment, Newport-Inglewood fault zone. *Association of Engineering Geologists, Southern California Section, Special Publication*, *4*, 211–231.

Gamberi, F., Rovere, M., Marani, M. P., & Dykstra, M. (2015). Modern submarine canyon feeder-system and deep-sea fan growth in a tectonically active margin (northern Sicily). *Geosphere*, *11*(2), 307–319.

Gee, J. S., Tauxe, L., & Constable, C. (2008). Amsspin: A LabVIEW program for measuring the anisotropy of magnetic susceptibility with the Kappabridge KLY-4S. *Geochemistry, Geophysics, Geosystems*, *9*(8).

Gerber, T. P., Pratson, L. F., Kuehl, S., Walsh, J., Alexander, C., & Palmer, A. (2010). The influence of sea level and tectonics on Late Pleistocene through Holocene sediment storage along the high-sediment supply Waipaoa continental shelf. *Marine Geology*, *270*(1-4), 139–159.

Gillespie, R. & Polach, H. A. (1979). The suitability of marine shells for radiocarbon dating of Australian prehistory. In *Proceedings of the ninth international conference on radiocarbon dating*, (pp. 404–421). University of California Press.

Gillies, J. & Etyemezian, V. (2014). Wind and PM10 characteristics at the ODSVRA from the 2013 Assessment Monitoring Network. Report, Prepared for California State Parks, ODSVRA, Oceano, CA and OHMVR Division, Sacramento, CA.

Gogorza, C., Sinito, A., Lirio, J., Nuñez, H., Chaparro, M., & Vilas, J. (2002). Paleosecular variations 0-19,000 years recorded by sediments from Escondido Lake (Argentina). *Physics of the Earth and Planetary Interiors*, *133*(1-4), 35–55.

Goñi, M. A., Moore, E., Kurtz, A., Portier, E., Alleau, Y., & Merrell, D. (2014). Organic matter compositions and loadings in soils and sediments along the Fly River, Papua New Guinea. *Geochimica et Cosmochimica Acta*, *140*, 275–296.

Goldfinger, C. (2011). Submarine paleoseismology based on turbidite records. *Annual Review of Marine Science*, *3*, 35–66.

Goldfinger, C., Morey, A. E., Nelson, C. H., Gutiérrez-Pastor, J., Johnson, J. E., Karabanov, E., Chaytor, J., Eriksson, A., & Party, S. S. (2007). Rupture lengths and temporal history of significant earthquakes on the offshore and north coast segments of the Northern San Andreas Fault based on turbidite stratigraphy. *Earth and Planetary Science Letters*, *254*(1-2), 9–27.

Goldfinger, C., Nelson, C. H., Johnson, J. E., & Party, S. S. (2003). Holocene earthquake records from the Cascadia subduction zone and northern San Andreas fault based on precise dating of offshore turbidites. *Annual Review of Earth and Planetary Sciences*, *31*(1), 555–577.

Grant, L. B., Waggoner, J. T., Rockwell, T. K., & von Stein, C. (1997). Paleoseismicity of the north branch of the Newport-Inglewood fault zone in Huntington Beach, California, from cone penetrometer test data. *Bulletin of the Seismological Society of America*, *87*(2), 277–293.

Grossman, E., Eittreim, S., Field, M., & Wong, F. (2006). Shallow stratigraphy and sedimentation history during high-frequency sea-level changes on the central California shelf. *Continental Shelf Research*, *26*(10), 1217–1239.

Haberle, S. G. (1998). Late Quaternary vegetation change in the Tari Basin, Papua New Guinea. *Palaeogeography, Palaeoclimatology, Palaeoecology*, *137*(1-2), 1–24.

Haberzettl, T., St-Onge, G., Behling, H., & Kirleis, W. (2013). Evaluating Late Holocene radiocarbon-based chronologies by matching palaeomagnetic secular variations to geomagnetic field models: an example from Lake Kalimpaa (Sulawesi, Indonesia). *Geological Society, London, Special Publications*, *373*(1), 245–259.

Hanson, K. L. & Lettis, W. R. (2013). Application of multiple geochronologic methods to the dating of marine terraces in South-Central California. In J. S. Noller, J. M. Sowers, & W. R. Lettis (Eds.), *Quaternary Geochronology: Methods and Applications*, volume 4 (pp. 527–535). AGU Reference Shelf.

Hanson, K. L., Lettis, W. R., Wesling, J. R., Kelson, K. I., & Mezger, L. (1992). Quaternary marine terraces, south-central coastal California: implications for crustal deformation and coastal evolution. In C. H. Fletcher & J. F. Wehmer (Eds.), *Quaternary coasts of the United States: marine and lacustrine systems*, number 48 (pp. 323–332). Special Publications of SEPM.

Hapke, C. J., Reid, D., Richmond, B. M., Ruggiero, P., & List, J. (2006). National assessment of shoreline change part 3: Historical shoreline change and associated coastal land loss along sandy shorelines of the California coast. Technical report.

Harris, C. K., Sherwood, C. R., Signell, R. P., Bever, A. J., & Warner, J. C. (2008). Sediment dispersal in the northwestern Adriatic Sea. *Journal of Geophysical Research: Oceans*, *113*(C11).

Harris, P., Baker, E., Cole, A., & Short, S. (1993). A preliminary study of sedimentation in the tidally dominated Fly River Delta, Gulf of Papua. *Continental Shelf Research*, *13*(4), 32.

Harris, P., Pattiaratchi, C., Keene, J., Dalrymple, R., Gardner, J., Baker, E., Cole, A., Mitchell, D., Gibbs, P., & Schroeder, W. (1996). Late Quaternary deltaic and carbonate sedimentation in the Gulf of Papua foreland basin: response to sea-level change. *Journal of Sedimentary Research*, *66*(4).

Harris, P. T. (1994). Incised valleys and backstepping deltaic deposits in a foreland-basin setting, Torres Strait and Gulf of Papua, Australia. In R. W. Dalrymple, R. Boyd, & B. A. Zaitlin (Eds.), *Incised-Valley Systems: Origin and Sedimentary Sequences*, volume 51. Special Publications of SEPM.

Harris, P. T., Hughes, M. G., Baker, E. K., Dalrymple, R. W., & Keene, J. B. (2004). Sediment transport in distributary channels and its export to the pro-deltaic environment in a tidally dominated delta: Fly River, Papua New Guinea. *Continental Shelf Research*, *24*(19), 2431–2454.

Harrison, C. & Somayajulu, B. (1966). Behaviour of the earth's magnetic field during a reversal. *Nature*, *212*(5067), 1193.

Helland-Hansen, W. & Gjelberg, J. G. (1994). Conceptual basis and variability in sequence stratigraphy: a different perspective. *Sedimentary Geology*, *92*(1-2), 31–52.

Helland-Hansen, W. & Martinsen, O. J. (1996). Shoreline trajectories and sequences; description of variable depositional-dip scenarios. *Journal of Sedimentary Research*, *66*(4), 670–688.

Henkart, P. (2003). SIOSEIS software. Scripps Institution of Oceanography, La Jolla, California.

Heroy, D. C., Kuehl, S. A., & Goodbred, S. L. (2003). Mineralogy of the Ganges and Brahmaputra Rivers: implications for river switching and Late Quaternary climate change. *Sedimentary Geology*, *155*(3-4), 343–359.

Heusser, L. E. (1995). Pollen stratigraphy and paleoecologic interpretation of the 160-ky record from Santa Barbara Basin, Hole 893A1. In *Proceedings of the ocean drilling program, scientific results*, volume 146, (pp. 265–279).

Hill, K. C., Keetley, J. T., Kendrick, R. D., & Sutriyono, E. (2004). Structure and hydrocarbon potential of the New Guinea Fold Belt. In K. McClay (Ed.), *Thrust tectonics and hydrocarbon systems: AAPG Memoir*, volume 82 (pp. 494–594).

Hogarth, L. J., Babcock, J., Driscoll, N. W., Le Dantec, N., Haas, J. K., Inman, D. L., & Masters, P. M. (2007). Long-term tectonic control on Holocene shelf sedimentation offshore La Jolla, California. *Geology*, *35*(3), 275–278.

Hogarth, L. J., Driscoll, N. W., Babcock, J. M., & Orange, D. L. (2012). Transgressive deposits along the actively deforming Eel River Margin, Northern California. *Marine Geology*, *303*, 99–114.

Holmes, J. J., Driscoll, N. W., & Kent, G. M. (2017). 3d constraints on fault architecture and strain distribution of the Newport-Inglewood Rose Canyon and San Onofre trend fault systems. In *AGU Fall Meeting*.

Howell, A. L., Bentley, S. J., Xu, K., Ferrell, R. E., Muhammad, Z., & Septama, E. (2014). Fine sediment mineralogy as a tracer of latest Quaternary sediment delivery to a dynamic continental margin: Pandora Trough, Gulf of Papua, Papua New Guinea. *Marine Geology*, *357*, 108–122.

Hu, G., Xu, K., Clift, P. D., Zhang, Y., Li, Y., Qiu, J., Kong, X., & Bi, S. (2018). Textures, provenances and structures of sediment in the inner shelf south of Shandong Peninsula, western South Yellow Sea. *Estuarine, Coastal and Shelf Science*, *212*, 153–163.

Huang, J., Wan, S., Xiong, Z., Zhao, D., Liu, X., Li, A., & Li, T. (2016). Geochemical records of Taiwan-sourced sediments in the South China Sea linked to Holocene climate changes. *Palaeogeography, Palaeoclimatology, Palaeoecology*, *441*, 871–881.

Inman, D. L. & Brush, B. M. (1973). The coastal challenge. *Science*, *181*(4094), 20–32.

Inman, D. L. & Jenkins, S. A. (1999). Climate change and the episodicity of sediment flux of small California rivers. *The Journal of geology*, *107*(3), 251–270.

Irion, G. & Petr, T. (1983). *Clay mineralogy of selected soils and sediments of the Purari River basin*, (pp. 87–107). Springer.

Jackson, A., Jonkers, A. R., & Walker, M. R. (2000). Four centuries of geomagnetic secular variation from historical records. *Philosophical Transactions of the Royal Society of London. Series A: Mathematical, Physical and Engineering Sciences*, *358*(1768), 957–990.

Jackson, M., Bowles, J. A., Lascu, I., & Solheid, P. (2010). Deconvolution of u channel magnetometer data: experimental study of accuracy, resolution, and stability of different inversion methods. *Geochemistry, Geophysics, Geosystems*, *11*(7).

Johnson, S. Y. & Watt, J. T. (2012). Influence of fault trend, bends, and convergence on shallow structure and geomorphology of the Hosgri strike-slip fault, offshore central California. *Geosphere*, *8*(6), 1632–1656.

Johnsson, M. J. & Meade, R. H. (1990). Chemical weathering of fluvial sediments during alluvial storage: The Macuapanim Island point bar, Solimoes River, Brazil. *Journal of Sedimentary Research*, *60*(6).

Johnstone, E. A. C. (2012). *Geophysical constraints on sediment dispersal systems*. PhD thesis, University of California San Diego.

Jorry, S. J., Droxler, A. W., Mallarino, G., Dickens, G. R., Bentley, S. J., Beaufort, L., Peterson, L. C., & Opdyke, B. N. (2008). Bundled turbidite deposition in the central Pandora Trough (Gulf of Papua) since Last Glacial Maximum: Linking sediment nature and accumulation to sea level fluctuations at millennial timescale. *Journal of Geophysical Research*, *113*(F01S19).

Keefer, D. K., Moseley, M. E., & Defrance, S. D. (2003). A 38 000-year record of floods and debris flows in the Ilo region of southern Peru and its relation to El Niño events and great earthquakes. *194*(1-3), 41–77.

Keen, T. R., Ko, D. S., Slingerland, R. L., Riedlinger, S., & Flynn, P. (2006). Potential transport pathways of terrigenous material in the Gulf of Papua. *Geophysical Research Letters*, *33*(4).

Keigwin, L. D., Klotsko, S., Zhao, N., Reilly, B., Giosan, L., & Driscoll, N. W. (2018). Deglacial floods in the Beaufort Sea preceded Younger Dryas cooling. *Nature Geoscience*, *11*(8), 599–604.

Kennedy, M. P. & Tan, S. S. (2007). Geologic map of the Oceanside 30'x60' Quadrangle, California. Report, Department of Conservation, California Geological Survey.

Kienast, S. S. & McKay, J. L. (2001). Sea surface temperatures in the subarctic northeast Pacific reflect millennial-scale climate oscillations during the last 16 kyrs. *Geophysical Research Letters*, *28*(8), 1563–1566.

King, J., Banerjee, S. K., Marvin, J., & Özdemir, Ö. (1982). A comparison of different magnetic methods for determining the relative grain size of magnetite in natural materials: some results from lake sediments. *Earth and Planetary Science Letters*, *59*(2), 404–419.

King, J. W., Banerjee, S. K., & Marvin, J. (1983). A new rock-magnetic approach to selecting sediments for geomagnetic paleointensity studies: Application to paleointensity for the last 4000 years. *Journal of Geophysical Research: Solid Earth*, *88*(B7), 5911–5921.

Kirschvink, J. (1980). The least-squares line and plane and the analysis of palaeomagnetic data. *Geophysical Journal International*, *62*(3), 699–718.

Klotsko, S., Driscoll, N., Kent, G., & Brothers, D. (2015). Continental shelf morphology and stratigraphy offshore San Onofre, California: The interplay between rates of eustatic change and sediment supply. *Marine Geology*, *369*, 116–126.

Knott, J. R. & Eley, D. S. (2006). Early to middle Holocene coastal dune and estuarine deposition, Santa Maria Valley, California. *Physical Geography*, *27*(2), 127–136.

Kolla, V., Biondi, P., Long, B., & Fillon, R. (2000). Sequence stratigraphy and architecture of the late Pleistocene Lagniappe delta complex, northeast Gulf of Mexico. *Geological Society, London, Special Publications*, *172*(1), 291–327.

Korte, M. & Constable, C. (2005). The geomagnetic dipole moment over the last 7000 years—new results from a global model. *Earth and Planetary Science Letters*, *236*(1-2), 348–358.

Korte, M. & Constable, C. (2011). Improving geomagnetic field reconstructions for 0–3ka. *Physics of the Earth and Planetary Interiors*, *188*(3-4), 247–259.

Kostic, S. (2011). Modeling of submarine cyclic steps: Controls on their formation, migration, and architecture. *Geosphere*, *7*(2), 294–304.

Kovanen, D. J. & Easterbrook, D. J. (2002). Paleodeviations of radiocarbon marine reservoir values for the northeast Pacific. *Geology*, *30*(3), 243–246.

Kuehl, S. A., Levy, B. M., Moore, W. S., & Allison, M. A. (1997). Subaqueous delta of the Ganges-Brahmaputra river system. *Marine Geology*, *144*(1-3), 81–96.

Kuehl, S. A., Nittrouer, C. A., & DeMaster, D. J. (1986). Distribution of sedimentary structures in the Amazon subaqueous delta. *Continental Shelf Research*, *6*(1-2), 311–336.

Lauer, J. W., Parker, G., & Dietrich, W. E. (2008). Response of the strickland and fly river confluence to postglacial sea level rise. *Journal of Geophysical Research*, *113*(F1).

Le Dantec, N., Hogarth, L. J., Driscoll, N. W., Babcock, J. M., Barnhardt, W. A., & Schwab, W. C. (2010). Tectonic controls on nearshore sediment accumulation and submarine canyon morphology offshore La Jolla, Southern California. *Marine Geology*, *268*(1), 115–128.

Lea, D. W., Martin, P. A., Pak, D. K., & Spero, H. J. (2002). Reconstructing a 350ky history of sea level using planktonic Mg/Ca and oxygen isotope records from a Cocos Ridge core. *Quaternary Science Reviews*, *21*(1-3), 283–293.

Lean, C. & McCave, I. (1998). Glacial to interglacial mineral magnetic and palaeoceanographic changes at Chatham Rise, SW Pacific Ocean. *Earth and Planetary Science Letters*, *163*(1-4), 247–260.

Legg, M. R. (1991). Developments in understanding the tectonic evolution of the California Continental Borderland. In J. P. Dauphin & B. R. T. Simoneit (Eds.), *The Gulf and Peninsula Province of the Californias: American Association of Petroleum Geologists, Memoir*, volume 47 (pp. 145–177).

Lettis, W. R. & Hanson, K. L. (1992). Quaternary tectonic influences on coastal morphology, south-central california. *Quaternary International*, *15*, 135–148.

Lettis, W. R., Hanson, K. L., Unruh, J. R., McLaren, M., Savage, W. U., & Keller, M. A. (2004). Quaternary tectonic setting of south-central coastal California. In *Evolution of sedimentary basins/onshore oil and gas investigations: Santa Maria Province*. US Government Printing Office.

Levi, S. & Banerjee, S. K. (1976). On the possibility of obtaining relative paleointensities from lake sediments. *Earth and Planetary Science Letters*, *29*(1), 219–226.

Lindvall, S. C. & Rockwell, T. K. (1995). Holocene activity of the Rose Canyon fault zone in San Diego, California. *Journal of Geophysical Research: Solid Earth*, *100*(B12), 24121–24132.

Lisé-Pronovost, A., St-Onge, G., Brachfeld, S., Barletta, F., & Darby, D. (2009). Paleomagnetic constraints on the Holocene stratigraphy of the Arctic Alaskan margin. *Global and Planetary Change*, *68*(1-2), 85–99.

Liu, J., Xue, Z., Ross, K., Wang, H., Yang, Z., Li, A., & Gao, S. (2009). Fate of sediments delivered to the sea by Asian large rivers: long-distance transport and formation of remote alongshore clinothems. *The Sedimentary Record*, *7*(4), 4–9.

Lobo, F., Dias, J., González, R., Hernández-Molina, F., Morales, J., & Del Río, V. D. (2003). High-resolution seismic stratigraphy of a narrow, bedrock-controlled estuary: the Guadiana estuarine system, SW Iberia. *Journal of Sedimentary Research*, *73*(6), 973–986.

Lobo, F. J. & Ridente, D. (2014). Stratigraphic architecture and spatio-temporal variability of high-frequency (Milankovitch) depositional cycles on modern continental margins: An overview. *Marine Geology*, *352*, 215–247.

Lonsdale, P. (1991). Structural patterns of the Pacific floor offshore of peninsular California: Chapter 7: Part III. Regional geophysics and geology. *AAPG Memoir*, *47*, 87–125.

Lund, S., Platzman, E., & Johnson, T. (2016). Full-vector paleomagnetic secular variation records from latest quaternary sediments of Lake Malawi (10.0°S, 34.3°E). *Quaternary Science Reviews*, *144*, 16–27.

Lund, S., Stott, L., Schwartz, M., Thunell, R., & Chen, A. (2006). Holocene paleomagnetic secular variation records from the western Equatorial Pacific Ocean. *Earth and Planetary Science Letters*, *246*(3-4), 381–392.

Lunne, T. & Long, M. (2006). Review of long seabed samplers and criteria for new sampler design. *Marine Geology*, *226*(1-2), 145–165.

Mackereth, F. (1971). On the variation in direction of the horizontal component of remanent magnetisation in lake sediments. *Earth and Planetary Science Letters*, *12*(3), 332–338.

Magistrale, H. (1993). Seismicity of the Rose Canyon fault zone near San Diego, California. *Bulletin of the Seismological Society of America*, *83*(6), 1971–1978.

Maier, K. L., Brothers, D. S., Paull, C. K., McGann, M., Caress, D. W., & Conrad, J. E. (2017). Records of continental slope sediment flow morphodynamic responses to gradient and active faulting from integrated AUV and ROV data, offshore Palos Verdes, southern California Borderland. *Marine Geology*, *393*, 47–66.

Maier, K. L., Gales, J., Paull, C. K., Rosenberger, K., Talling, P. J., Simmons, S. M., Gwiazda, R. H., McGann, M., Cartigny, M. J., & Lundsten, E. (2019). Linking direct measurements of turbidity currents to submarine canyon-floor deposits. *Frontiers in Earth Science*, *7*, 144.

Maloney, J. M., Driscoll, N., Kent, G., Duke, S., Freeman, T., Bormann, J., Anderson, R., & Ferriz, H. (2016). Segmentation and step-overs along strike-slip fault systems in the inner California borderlands: Implications for fault architecture and basin formation. *Applied Geology in California, Environmental Engineering Geologists*, *26*, 655–677.

Maloney, J. M., Noble, P. J., Driscoll, N. W., Kent, G. M., Smith, S. B., Schmauder, G. C., Babcock, J. M., Baskin, R. L., Karlin, R., & Kell, A. M. (2013). Paleoseismic history of the Fallen Leaf segment of the West Tahoe–Dollar Point fault reconstructed from slide deposits in the Lake Tahoe Basin,California-Nevada. *Geosphere*, *9*(4), 1065–1090.

Marcuson, R., Gee, J., & Driscoll, N. (2014). An AMS Study of Gulf of Papua ocean sediment cores-evidence of deformation caused by piston coring. In *AGU Fall Meeting Abstracts*.

Marcuson, R., Gee, J., Wei, E., & Driscoll, N. (2019). A 2000 year geomagnetic field record from the Gulf of Papua. *Marine Geology*, *408*, 48–66.

Martin, D., Nittrouer, C., Ogston, A., & Crockett, J. (2008). Tidal and seasonal dynamics of a muddy inner shelf environment, Gulf of Papua. *Journal of Geophysical Research: Earth Surface*, *113*(F1).

Masters, P. M. (2006). Holocene sand beaches of southern California: ENSO forcing and coastal processes on millennial scales. *Palaeogeography, Palaeoclimatology, Palaeoecology*, *232*(1), 73–95.

Mayall, M., Jones, E., & Casey, M. (2006). Turbidite channel reservoirs—key elements in facies prediction and effective development. *Marine and Petroleum Geology*, *23*(8), 821–841.

Mayall, M. & Stewart, I. (2000). The architecture of turbidite slope channels. In *Deep-Water Reservoirs of the World: SEPM, Gulf Coast Section, 20th Annual Research Conference*, volume 578, (pp. 586).

McCrory, P. A., Wilson, D. S., Ingle, J. C., & Stanley, R. G. (1995). Neogene geohistory analysis of Santa Maria Basin, California, and its relationship to transfer of central California to the Pacific plate. In M. A. Keller (Ed.), *Evolution of sedimentary basins/onshore oil and gas investigations: Santa Maria Province*. US Government Printing Office.

McGregor, H., Gagan, M., McCulloch, M., Hodge, E., & Mortimer, G. (2008). Mid-Holocene variability in the marine 14c reservoir age for northern coastal Papua New Guinea. *Quaternary Geochronology*, *3*(3), 213–225.

McHargue, T., Pyrcz, M. J., Sullivan, M. D., Clark, J., Fildani, A., Romans, B., Covault, J., Levy, M., Posamentier, H., & Drinkwater, N. (2011). Architecture of turbidite channel systems on the continental slope: patterns and predictions. *Marine and Petroleum Geology*, *28*(3), 728–743.

McHugh, C. M., Fulthorpe, C. S., Hoyanagi, K., Blum, P., Mountain, G. S., & Miller, K. G. (2017). The sedimentary imprint of Pleistocene glacio-eustasy: Implications for global correlations of seismic sequences. *Geosphere*, *14*(1), 265–285.

McHugh, C. M., Hartin, C. A., Mountain, G. S., & Gould, H. M. (2010). The role of glacio-eustasy in sequence formation: Mid-Atlantic Continental Margin, USA. *Marine Geology*, *277*(1), 31–47.

Meade, B. J. & Hager, B. H. (2005). Block models of crustal motion in southern california constrained by GPS measurements. *Journal of Geophysical Research: Solid Earth*, *110*(B3).

Menard Jr, H. W. (1955). Deep-sea channels, topography, and sedimentation. *AAPG Bulletin*, *39*(2), 236–255.

Milliman, J., Driscoll, N., Slingerland, R., Babcock, J., & Walsh, J. (2004). Isotopic stage 3 deposition and stage 2 erosion of a clinoform in the Gulf of Papua: Regional tectonics versus eustatic sea-level change. In *AGU Fall Meeting Abstracts*, volume 85.

Milliman, J. & Farnsworth, K. (2011). Runoff, erosion, and delivery to the coastal ocean. *River discharge to the coastal ocean: a global synthesis, Cambridge University Press, Cambridge, UK*, 13–69.

Milliman, J. D. (1993). Production and accumulation of calcium carbonate in the ocean: Budget of a nonsteady state. *Global Biogeochemical Cycles*, *7*(4), 927–957.

Milliman, J. D. (1995). Sediment discharge to the ocean from small mountainous rivers: The New Guinea example. *Geo-Marine Letters*, *15*(3), 127–133.

Milliman, J. D., Farnsworth, K. L., & Albertin, C. S. (1999). Flux and fate of fluvial sediments leaving large islands in the East Indies. *Journal of Sea Research*, *41*(1-2), 97–107.

Milliman, J. D., Summerhayes, C. P., & Barretto, H. T. (1975). Quaternary sedimentation on the Amazon continental margin: a model. *Geological Society of America Bulletin*, *86*(5), 610–614.

Mitchum Jr, R., Vail, P., & Sangree, J. (1977). Seismic stratigraphy and global changes of sea level: Part 6. stratigraphic interpretation of seismic reflection patterns in depositional sequences. In C. Payton (Ed.), *Seismic Stratigraphy: Application of seismic reflection configuration to stratigraphic interpretation. Memoir 26. American Association of Petroleum Geologists, Tulsa*.

Mitchum Jr, R., Vail, P., & Thompson III, S. (1977). Seismic stratigraphy and global changes of sea level: Part 2. the depositional sequence as a basic unit for stratigraphic analysis: Section 2. In C. Payton (Ed.), *Seismic Stratigraphy: Application of seismic reflection configuration to stratigraphic interpretation. Memoir 26. American Association of Petroleum Geologists, Tulsa* (pp. 53–62).

Mitchum Jr, R. M. (1985). Seismic stratigraphic expression of submarine fans: chapter 7. *American Association of Petroleum Geologists Memoir*, *39*, 117–138.

Mix, A. C., Lund, D. C., Pisias, N. G., Bodén, P., Bornmalm, L., Lyle, M., & Pike, J. (1999). Rapid climate oscillations in the northeast Pacific during the last deglaciation reflect Northern and Southern Hemisphere sources. In P. U. Clark, R. S. Webb, & L. D. Keigwin (Eds.), *Mechanisms of Global Climate Change at Millennial Time Scales*, volume 112 (pp. 127–148). American Geophysical Union.

Montero-Serrano, J. C., Bout-Roumazeilles, V., Sionneau, T., Tribovillard, N., Bory, A., Flower, B. P., Riboulleau, A., Martinez, P., & Billy, I. (2010). Changes in precipitation regimes over North America during the Holocene as recorded by mineralogy and geochemistry of Gulf of Mexico sediments. *Global and Planetary Change*, *74*(3-4), 132–143.

Moore, D. M. & Reynolds, R. C. (1989). *X-ray Diffraction and the Identification and Analysis of Clay Minerals*, volume 378. Oxford university press Oxford.

Moore, E. A. (2011). *Chemical weathering and organic carbon fluxes from the Fly River, Papua New Guinea*. PhD thesis, Boston University.

Métivier, F. & Gaudemer, Y. (1999). Stability of output fluxes of large rivers in South and East Asia during the last 2 million years: implications on floodplain processes. *Basin Research*, *11*(4), 293–303.

Muhammad, Z., Bentley, S. J., Febo, L. A., Droxler, A. W., Dickens, G. R., Peterson, L. C., & Opdyke, B. N. (2008). Excess 210Pb inventories and fluxes along the continental slope and basins of the Gulf of Papua. *Journal of Geophysical Research*, *113*(F01S17).

Muhs, D. R., Kennedy, G. L., & Rockwell, T. K. (1994). Uranium-series ages of marine terrace corals from the Pacific coast of North America and implications for last-interglacial sea level history. *Quaternary Research*, *42*(1), 72–87.

Muhs, D. R., Simmons, K. R., Schumann, R. R., Groves, L. T., DeVogel, S. B., Minor, S. A., & Laurel, D. (2014). Coastal tectonics on the eastern margin of the Pacific Rim: late Quaternary sea-level history and uplift rates, Channel Islands National Park, California, USA. *Quaternary Science Reviews*, *105*, 209–238.

Muhs, D. R., Simmons, K. R., Schumann, R. R., Groves, L. T., Mitrovica, J. X., & Laurel, D. (2012). Sea-level history during the last interglacial complex on San Nicolas Island, California: implications for glacial isostatic adjustment processes, paleozoogeography and tectonics. *Quaternary Science Reviews*, *37*, 1–25.

Mulder, T., Migeon, S., Savoye, B., & Jouanneau, J. M. (2001). Twentieth century floods recorded in the deep Mediterranean sediments. *Geology*, *29*(11), 1011–1014.

Mulligan, K. (1985). The movement of transverse coastal dunes, Pismo Beach, California, 1982-1983. MS thesis, University of California Los Angeles.

Nagata, T. (1965). Main characteristics of recent geomagnetic secular variation. *Journal of geomagnetism and geoelectricity*, *17*(3-4), 263–276.

Nakajima, T. & Kanai, Y. (2000). Sedimentary features of seismoturbidites triggered by the 1983 and older historical earthquakes in the eastern margin of the Japan Sea. *Sedimentary Geology*, *135*(1-4), 1–19.

Namson, J. & Davis, T. L. (1990). Late Cenozoic fold and thrust belt of the Southern Coast Ranges and Santa Maria Basin, California. *AAPG Bulletin*, *74*(4), 467–492.

Neill, C. F. & Allison, M. A. (2005). Subaqueous deltaic formation on the Atchafalaya Shelf, Louisiana. *Marine Geology*, *214*(4), 411–430.

Nelson, D. M., Tréguer, P., Brzezinski, M. A., Leynaert, A., & Quéguiner, B. (1995). Production and dissolution of biogenic silica in the ocean: Revised global estimates, comparison with regional data and relationship to biogenic sedimentation. *Global Biogeochemical Cycles*, *9*(3), 359–372.

Nguyen, V. L., Ta, T. K. O., & Tateishi, M. (2000). Late Holocene depositional environments and coastal evolution of the Mekong River Delta, Southern Vietnam. *Journal of Asian Earth Sciences*, *18*(4), 427–439.

Nicholson, C., Sorlien, C. C., Atwater, T., Crowell, J. C., & Luyendyk, B. P. (1994). Microplate capture, rotation of the western Transverse Ranges, and initiation of the San Andreas transform as a low-angle fault system. *Geology*, *22*(6), 491–495.

Nilsson, A., Holme, R., Korte, M., Suttie, N., & Hill, M. (2014). Reconstructing Holocene geomagnetic field variation: new methods, models and implications. *Geophysical Journal International*, *198*(1), 229–248.

Nittrouer, C., Curtin, T., & DeMaster, D. (1986). Concentration and flux of suspended sediment on the Amazon continental shelf. *Continental Shelf Research*, *6*(1-2), 151–174.

Nittrouer, C. A., Austin, J. A., Field, M. E., Kravitz, J. H., Syvitski, J. P., & Wiberg, P. L. (2007). Writing a Rosetta stone: insights into continental-margin sedimentary processes and strata. *Special Publication*, *37*.

Nittrouer, C. A. & DeMaster, D. J. (1996). The Amazon shelf setting: tropical, energetic, and influenced by a large river. *Continental Shelf Research*, *16*(5/6), 21.

Nittrouer, C. A. & Wright, L. D. (1994). Transport of particles across continental shelves. *Reviews of Geophysics*, *32*(1), 85–113.

Nordstrom, C. E. & Margolis, S. V. (1972). Sedimentary history of central California shelf sands as revealed by scanning electron microscopy. *Journal of Sedimentary Research*, *42*(3).

Normark, W., Damuth, J., & Scientific Drilling Party (1997). Sedimentary facies and associated depositional elements of the Amazon Fan. In *Proceedings of the Ocean Drilling Program, 155 Scientific Results*. Ocean Drilling Program.

Normark, W., Meyer, A., Cremer, M., Droz, L., O'Connell, S., Pickering, K., Stelting, C., Stow, D., Brooks, G., Mazzullo, J., Roberts, H., & Thayer, P. (1986). Summary of drilling results for the Mississippi Fan and considerations for application to other turbidite systems. In *Initial Reports of the Deep Sea Drilling Project*, volume 96. U.S. Government Printing Office.

Normark, W. R. (1970). Growth patterns of deep-sea fans. *AAPG bulletin*, *54*(11), 2170–2195.

Normark, W. R., Piper, D. J., Posamentier, H., Pirmez, C., & Migeon, S. (2002). Variability in form and growth of sediment waves on turbidite channel levees. *Marine Geology*, *192*(1-3), 23–58.

Normark, W. R., Piper, D. J., Romans, B. W., Covault, J. A., Dartnell, P., & Sliter, R. W. (2009). Submarine canyon and fan systems of the California Continental Borderland. In H. J. Lee, , & W. R. Normark (Eds.), *Earth Science in the Urban Ocean: The Southern California Continental Borderland: Geological Society of America Special Paper*, volume 454 (pp. 69–87). Geological Society of America.

Ogston, A. S., Sternberg, R. W., Nittrouer, C. A., Martin, D. P., Goñi, M. A., & Crockett, J. S. (2008). Sediment delivery from the Fly River tidally dominated delta to the nearshore marine environment and the impact of El Niño. *Journal of Geophysical Research*, *113*(F1).

Ohneiser, C., Acton, G., Channell, J. E., Wilson, G. S., Yamamoto, Y., & Yamazaki, T. (2013). A middle Miocene relative paleointensity record from the Equatorial Pacific. *Earth and Planetary Science Letters*, *374*, 227–238.

Opdyke, N. & Henry, K. (1969). A test of the dipole hypothesis. *Earth and Planetary Science Letters*, *6*(2), 139–151.

Orme, A. & Tchakerian, V. (1986). Quaternary dunes of the pacific coast of the californias. In *Aeolian Geomorphology Proceedings of the 17th Annual Binghamton Geomorphology Symposium, September 1986*, (pp. 149–175). Allen and Unwin.

Orme, A. R. (1990). The instability of holocene coastal dunes: the case of the morro dunes, california. In K. F. Nordstrom, N. P. Psuty, & R. W. G. Carter (Eds.), *Coastal Dunes: Form and Process* (pp. 317–338). Wiley New York and Chichester.

Orme, A. R. (1992). Late Quaternary Deposits near Point Sal, south central California: A time frame for coastal-dune emplacement. In *Quaternary coasts of the United States: Marine and Lacustrine Systems. Society for Sedimentary Geology Special Publication* (pp. 309–315).

Pacific Gas and Electric Company (1988). Final report of the Diablo Canyon long term seismic program, US Nuclear Regulatory Commission. Technical report.

Pacific Gas and Electric Company (2013). Stratigraphic framework for assessment of fault activity offshore of the central california coast between point san simeon and point sal. Quality related technical report.

Pacific Gas and Electric Company (2014). Offshore low-energy seismic-reflection studies in estero bay, san luis obispo bay, and point sal areas. Report, Pacific Gas and Electric Company.

Pain, C. (1983). Volcanic rocks and surfaces as indicators of landform age: The Astrolabe Agglomerate, Papua New Guinea. *Australian Geographer*, *15*(6), 376–381.

Pain, C. & Blong, R. (1976). Late quaternary tephras around mt. hagen and mt. giluwe, papua new guinea. *Volcanism in Australasia*, 239.

Palinkas, C., Nittrouer, C., & Walsh, J. (2006). Inner-shelf sedimentation in the Gulf of Papua, New Guinea: A mud-rich shallow shelf setting. *Journal of Coastal Research*, 760–772.

Patruno, S., Hampson, G. J., & Jackson, C. A. (2015). Quantitative characterisation of deltaic and subaqueous clinoforms. *Earth-Science Reviews*, *142*, 79–119.

Patruno, S. & Helland-Hansen, W. (2018). Clinoform systems: Review and dynamic classification scheme for shorelines, subaqueous deltas, shelf edges and continental margins. *Earth-Science Reviews*.

Patsch, K. & Griggs, G. (2008). A sand budget for the Santa Barbara littoral cell, California. *Marine Geology*, *252*(1), 50–61.

Patterson, L. J. (2006). Petrological and geochemical investigations of deep sea turbidite sands in the Pandora and Moresby Troughs: Source to sink Papua New Guinea focus area. MS thesis, Louisiana State University, Baton Rouge, Louisiana.

Paull, C., Ussler, W., Greene, H., Keaten, R., Mitts, P., & Barry, J. (2002). Caught in the act: the 20 December 2001 gravity flow event in Monterey Canyon. *Geo-Marine Letters*, *22*(4), 227–232.

Peck, J. A., King, J. W., Colman, S. M., & Kravchinsky, V. A. (1996). An 84-kyr paleomagnetic record from the sediments of Lake Baikal, Siberia. *Journal of Geophysical Research: Solid Earth*, *101*(B5), 11365–11385.

Peterson, C. D., Ryan, C., Meyer, J., Price, D. M., & Hostetler, S. W. (2018). Origins of the Santa Maria and Vandenberg coastal dune sheets (100-0 ka) under changing sea levels, shoreline orientations and wave directions: Long-term records of coastal sand supply in south-central California, USA. *Journal of Geography and Geology*, *10*(1).

Petschick, R. (2000). Macdiff 4.2.2. Powder and clay diffraction software. http://servermac.geologie.uni-frankfurt.de/Homepages?Petschick?RainerE.html.

Pettingill, H. S. & Weimer, P. (2002). Worlwide deepwater exploration and production: Past, present, and future. *The Leading Edge*, *21*(4), 371–376.

Pickup, G. (1983). Sedimentation processes in the Purari River upstream of the delta. In *The Purari—tropical environment of a high rainfall river basin* (pp. 205–225). Springer.

Pigram, C. & Symonds, P. (1991). A review of the timing of the major tectonic events in the New Guinea Orogen. *Journal of Southeast Asian Earth Sciences*, *6*(3-4), 307–318.

Pigram, C. J., Davies, P. J., Feary, D. A., & Symonds, P. A. (1989). Tectonic controls on carbonate platform evolution in southern Papua New Guinea: passive margin to foreland basin. *Geology*, *17*(3), 199–202.

Piper, D. J., Kontopoulos, N., Anagnostou, C., Chronis, G., & Panagos, A. (1990). Modern fan deltas in the western Gulf of Corinth, Greece. *Geo-Marine Letters*, *10*(1), 5–12.

Piper, D. J. & Normark, W. R. (1983). Turbidite depositional patterns and flow characteristics, Navy submarine fan, California Borderland. *Sedimentology*, *30*(5), 681–694.

Piper, D. J. & Normark, W. R. (2009). Processes that initiate turbidity currents and their influence on turbidites: a marine geology perspective. *Journal of Sedimentary Research*, *79*(6), 347–362.

Posamentier, H. & Vail, P. (1988). Eustatic controls on clastic deposition II—sequence and systems tract models. In C. Wilgus, B. Hastings, C. Kendall, H. Posamentier, C. Ross, & J. Van Wagoner (Eds.), *Sea Level Changes–An Integrated Approach. SEPM Special Publication*, volume 42 (pp. 125–154).

Posamentier, H. W. & Allen, G. P. (1993). Variability of the sequence stratigraphic model: effects of local basin factors. *Sedimentary geology*, *86*(1-2), 91–109.

Posamentier, H. W., Allen, G. P., James, D. P., & Tesson, M. (1992). Forced regressions in a sequence stratigraphic framework: concepts, examples, and exploration significance. *AAPG bulletin*, *76*(11), 1687–1709.

Posamentier, H. W., Erskine, R. D., & Mitchum, R. M. (1991). Models for submarine-fan deposition within a sequence-stratigraphic framework. In P. Weimer & M. H. Link (Eds.), *Seismic Facies and Sedimentary Processes of Submarine Fans and Turbidite Systems. Frontiers in Sedimentary Geology* (pp. 127–136). Springer New York.

Prather, B. (2000). Calibration and visualization of depositional process models for above-grade slopes: a case study from the Gulf of Mexico. *Marine and Petroleum Geology*, *17*(5), 619–638.

Prins, M. A. & Postma, G. (2000). Effects of climate, sea level, and tectonics unraveled for last deglaciation turbidite records of the Arabian Sea. *Geology*, *28*(4), 375–378.

Puig, P., Ogston, A. S., Guillén, J., Fain, A., & Palanques, A. (2007). Sediment transport processes from the topset to the foreset of a crenulated clinoform (Adriatic Sea). *Continental Shelf Research*, *27*(3-4), 452–474.

Reeves, J. M., Chivas, A. R., García, A., Holt, S., Couapel, M. J. J., Jones, B. G., Cendón, D. I., & Fink, D. (2008). The sedimentary record of palaeoenvironments and sea-level change in the Gulf of Carpentaria, Australia, through the last glacial cycle. *Quaternary International*, *183*(1), 3–22.

Reimer, P. J., Bard, E., Bayliss, A., Beck, J. W., Blackwell, P. G., Bronk Ramsey, C., Buck, C. E., Cheng, H., Edwards, R. L., & Friedrich, M. (2013). Intcal13 and Marine13 radiocarbon age calibration curves 0-50,000 years cal BP. *Radiocarbon*, *55*(4), 1869–1887.

Reis, A. T., Maia, R. M. C., Silva, C. G., Rabineau, M., Guerra, J. V., Gorini, C., Ayres, A., Arantes-Oliveira, R., Benabdellouahed, M., Simões, I., & Tardin, R. (2013). Origin of step-like and lobate seafloor features along the continental shelf off Rio de Janeiro State, Santos basin-Brazil. *Geomorphology*, *203*, 25–45.

Reynolds, L. C. & Simms, A. R. (2015). Late Quaternary relative sea level in Southern California and Monterey Bay. *Quaternary Science Reviews*, *126*, 57–66.

Rhodes, E. G., Polach, H. A., Thom, B. G., & Wilson, S. R. (1980). Age structure of Holocene coastal sediments: Gulf of Carpentaria, Australia. *Radiocarbon*, *22*(3), 718–727.

Richter, C., Venuti, A., Verosub, K. L., & Wei, K.-Y. (2006). Variations of the geomagnetic field during the Holocene: Relative paleointensity and inclination record from the West Pacific (ODP hole 1202b). *Physics of the Earth and Planetary Interiors*, *156*(3-4), 179–193.

Ridente, D., Trincardi, F., Piva, A., & Asioli, A. (2009). The combined effect of sea level and supply during Milankovitch cyclicity: Evidence from shallow-marine ^{18}O records and sequence architecture (Adriatic margin). *Geology*, *37*(11), 1003–1006.

Ritchie, B. D., Gawthorpe, R. L., & Hardy, S. (2004). Three-dimensional numberical modeling of deltaic depositional sequences 1: Influence of the rate and magnitude of sea-level change. *Journal of Sedimentary Research*, *74*(2), 17.

Roberts, A. P. (1995). Magnetic properties of sedimentary greigite (Fe3S4). *Earth and Planetary Science Letters*, *134*(3-4), 227–236.

Romans, B. W., Castelltort, S., Covault, J. A., Fildani, A., & Walsh, J. (2016). Environmental signal propagation in sedimentary systems across timescales. *Earth-Science Reviews*, *153*, 7–29.

Ron, H., Nowaczyk, N. R., Frank, U., Schwab, M. J., Naumann, R., Striewski, B., & Agnon, A. (2007). Greigite detected as dominating remanence carrier in Late Pleistocene sediments, Lisan formation, from Lake Kinneret (Sea of Galilee), Israel. *Geophysical Journal International*, *170*(1), 117–131.

Runyan, K. & Griggs, G. B. (2003). The effects of armoring seacliffs on the natural sand supply to the beaches of California. *Journal of Coastal Research*, 336–347.

Ryan, H. F., Conrad, J. E., Paull, C., & McGann, M. (2012). Slip rate on the San Diego trough fault zone, inner California Borderland, and the 1986 Oceanside earthquake swarm revisited. *Bulletin of the Seismological Society of America*, *102*(6), 2300–2312.

Ryan, H. F., Legg, M. R., Conrad, J. E., Sliter, R. W., Lee, H., & Normark, W. (2009). Recent faulting in the Gulf of santa catalina: San diego to dana point. *454*, 291–315.

Rzhanov, Y., Fonseca, L., & Mayer, L. (2012). Construction of seafloor thematic maps from multibeam acoustic backscatter angular response data. *Computers & Geosciences*, *41*, 181–187.

Sadler, P. M. (1981). Sediment accumulation rates and the completeness of stratigraphic sections. *The Journal of Geology*, *89*(5), 569–584.

Sahakian, V., Bormann, J., Driscoll, N., Harding, A., Kent, G., & Wesnousky, S. (2017). Seismic constraints on the architecture of the Newport-Inglewood/Rose Canyon fault: Implications for the length and magnitude of future earthquake ruptures. *Journal of Geophysical Research: Solid Earth*, *122*(3), 2085–2105.

Sakai, H., Nomura, S., Horii, M., Kashiwaya, K., Tanaka, A., Kawai, T., Kravchinsky, V., & Peck, J. (2000). Paleomagnetic and rock-magnetic studies on Lake Baikal sediments -BDP96 borehole at Academician Ridge, Lake Baikal. In K. Minoura (Ed.), *A Mirror in Time and Space for Understanding Global Change Processes* (pp. 35–52). Elsevier.

Salomons, W. & Eagle, A. (1990). Hydrology, sedimentology and the fate and distribution of copper in mine-related discharges in the Fly River system, Papua New Guinea. *Science of the Total Environment*, *97*, 315–334.

Santos, R., Rodrigues, A., & Quartau, R. (2018). Acoustic remote characterization of seabed sediments using the Angular Range Analysis technique: The inlet channel of Tagus River estuary (Portugal). *Marine Geology*, *400*, 60–75.

Sargent, C., Hobbs, R. W., & Gröcke, D. R. (2011). Improving the interpretability of air-gun seismic reflection data using deterministic filters: A case history from offshore Cape Leeuwin, southwest Australia. *Geophysics*, *76*(3), B113–B125.

Schwehr, K., Tauxe, L., Driscoll, N., & Lee, H. (2006). Detecting compaction disequilibrium with anisotropy of magnetic susceptibility. *Geochemistry, Geophysics, Geosystems*, *7*(11).

Scott, K. M. & Williams, R. P. (1978). Erosion and sediment yields in the Transverse Ranges, southern California. *US Geological Survey Professional Paper*, *1030*.

Septama, E. & Bentley, S. J. (2017). Source-to-sink sediment delivery in the Gulf of Papua from scanning electron microscopy and mineral liberation analysis–aided provenance analysis of deep-sea turbidite sands. *AAPG Bulletin*, *101*(06), 907–936.

Septama, E., Bentley, S. J., & Droxler, A. W. (2016). Conduits, timing and processes of sediment delivery across a high-relief continental margin: Continental shelf to basin in Late Quaternary, Gulf of Papua. *Marine and Petroleum Geology*, *72*, 447–462.

Shiki, T. (1996). Reading of the trigger records of sedimentary events-a problem for future studies. *Sedimentary Geology*, *104*(1-4), 249–255.

Shiki, T., Kumon, F., Inouchi, Y., Kontani, Y., Sakamoto, T., Tateishi, M., Matsubara, H., & Fukuyama, K. (2000). Sedimentary features of the seismo-turbidites, Lake Biwa, Japan. *Sedimentary Geology*, *135*(1-4), 37–50.

Slingerland, R., Driscoll, N. W., Milliman, J. D., Miller, S. R., & Johnstone, E. A. (2008). Anatomy and growth of a Holocene clinothem in the Gulf of Papua. *Journal of Geophysical Research*, *113*(F1).

Slingerland, R., Selover, R. W., Ogston, A. S., Keen, T. R., Driscoll, N. W., & Milliman, J. D. (2008). Building the Holocene clinothem in the Gulf of Papua: An ocean circulation study. *Journal of Geophysical Research*, *113*(F1).

Sliter, R. W., Triezenberg, P. J., Hart, P. E., Watt, J. T., Johnson, S. Y., & Scheirer, D. S. (2009). High-resolution seismic-reflection and marine magnetic data along the Hosgri fault zone, central California. Technical report, US Geological Survey.

Snowball, I. F. (1997). Gyroremanent magnetization and the magnetic properties of greigite-bearing clays in southern Sweden. *Geophysical Journal International*, *129*(3), 624–636.

Sommerfield, C. K. & Nittrouer, C. A. (1999). Modern accumulation rates and a sediment budget for the Eel shelf: a flood-dominated depositional environment. *Marine Geology*, *154*(1-4), 227–241.

Southon, J. R., Nelson, D. E., & Vogel, J. S. (1990). A record of past ocean-atmosphere radiocarbon differences from the northeast pacific. *Paleoceanography*, *5*(2), 197–206.

Stoner, J., Laj, C., Channell, J., & Kissel, C. (2002). South Atlantic and North Atlantic geomagnetic paleointensity stacks (0–80ka): implications for inter-hemispheric correlation. *Quaternary Science Reviews*, *21*(10), 1141–1151.

Stoner, J. S., Jennings, A., Kristjánsdóttir, G. B., Dunhill, G., Andrews, J. T., & Hardardóttir, J. (2007). A paleomagnetic approach toward refining Holocene radiocarbon-based chronologies: Paleoceanographic records from the north Iceland (MD99-2269) and east greenland (MD99-2322) margins. *Paleoceanography*, *22*(1).

Stoner, J. S. & St-Onge, G. (2007). Chapter three magnetic stratigraphy in paleoceanography: Reversals, excursions, paleointensity, and secular variation. In *Developments in Marine Geology*, volume 1 (pp. 99–138). Elsevier.

Stow, D. A. & Mayall, M. (2000). Deep-water sedimentary systems: new models for the 21st century. *Marine and Petroleum Geology*, *17*(2), 125–135.

Stuiver, M. & Polach, H. A. (1977). Discussion reporting of 14 c data. *Radiocarbon*, *19*(03), 355–363.

Stuiver, M. & Reimer, P. J. (1993). Extended 14c data base and revised CALIB 3.0 14C age calibration program. *Radiocarbon*, *35*(1), 215–230.

Sumner, E. J., Siti, M. I., McNeill, L. C., Talling, P. J., Henstock, T. J., Wynn, R. B., Djajadihardja, Y. S., & Permana, H. (2013). Can turbidites be used to reconstruct a paleoearthquake record for the central Sumatran margin? *Geology*, *41*(7), 763–766.

Sunamura, T. (1992). *Geomorphology of rocky coasts*, volume 3. Oxford University Press, Trenhaile.

Swanson, K. M., Watson, E., Aalto, R., Lauer, J. W., Bera, M. T., Marshall, A., Taylor, M. P., Apte, S. C., & Dietrich, W. E. (2008). Sediment load and floodplain deposition rates: Comparison of the Fly and Strickland rivers, Papua New Guinea. *Journal of Geophysical Research*, *113*(F01S03).

Sweet, M. L. & Blum, M. D. (2016). Connections between fluvial to shallow marine environments and submarine canyons: Implications for sediment transfer to deep water. *Journal of Sedimentary Research*, *86*(10), 1147–1162.

Swenson, J. B., Paola, C., Pratson, L., Voller, V. R., & Murray, A. B. (2005). Fluvial and marine controls on combined subaerial and subaqueous delta progradation: Morphodynamic modeling of compound-clinoform development. *Journal of Geophysical Research: Earth Surface*, *110*(F2).

Symons, W. O., Sumner, E. J., Paull, C. K., Cartigny, M. J., Xu, J., Maier, K. L., Lorenson, T. D., & Talling, P. J. (2017). A new model for turbidity current behavior based on integration of flow monitoring and precision coring in a submarine canyon. *Geology*, *45*(4), 367–370.

Szczuciński, W., Jagodziński, R., Hanebuth, T. J. J., Stattegger, K., Wetzel, A., Mitrega, M., Unverricht, D., & Van Phach, P. (2013). Modern sedimentation and sediment dispersal pattern on the continental shelf off the Mekong River delta, South China Sea. *Global and Planetary Change*, *110*, 195–213.

Talling, P. J., Allin, J., Armitage, D. A., Arnott, R. W., Cartigny, M. J., Clare, M. A., Felletti, F., Covault, J. A., Girardclos, S., & Hansen, E. (2015). Key future directions for research on turbidity currents and their deposits. *Journal of Sedimentary Research*, *85*(2), 153–169.

Talling, P. J., Masson, D. G., Sumner, E. J., & Malgesini, G. (2012). Subaqueous sediment density flows: Depositional processes and deposit types. *Sedimentology*, *59*(7), 1937–2003.

Talling, P. J., Paull, C. K., & Piper, D. J. (2013). How are subaqueous sediment density flows triggered, what is their internal structure and how does it evolve? Direct observations from monitoring of active flows. *Earth-Science Reviews*, *125*, 244–287.

Tauxe, L. (1993). Sedimentary records of relative paleointensity of the geomagnetic field: Theory and practice. *Reviews of Geophysics*, *31*(3), 319.

Tcherepanov, E. N., Droxler, A. W., Lapointe, P., Dickens, G. R., Bentley, S. J., Beaufort, L., Peterson, L. C., Daniell, J., & Opdyke, B. N. (2008). Neogene evolution of the mixed carbonate-siliciclastic system in the Gulf of Papua, Papua New Guinea. *Journal of Geophysical Research*, *113*(F1).

ten Brink, U. S., Zhang, J., Brocher, T. M., Okaya, D. A., Klitgord, K. D., & Fuis, G. S. (2000). Geophysical evidence for the evolution of the California Inner Continental Borderland as a metamorphic core complex. *Journal of Geophysical Research: Solid Earth*, *105*(B3), 5835–5857.

Thiry, M. (2000). Palaeoclimatic interpretation of clay minerals in marine deposits: an outlook from the continental origin. *Earth-Science Reviews*, *49*(1-4), 201–221.

Thomas, M. A. & Anderson, J. B. (1994). Sea-level controls on the facies architecture of the Trinity/Sabine incised-valley system, Texas continental shelf. In R. Dalrymple, R. Boyd, & B. Zaitlin (Eds.), *Incised Valley Systems: Origin and Sedimentary Sequences: Society for Economic Paleontologists and Mineralogists Special Publication*, volume 51.

Torgersen, T., Luly, J., De Deckker, P., Jones, M., Searle, D., Chivas, A., & Ullman, W. (1988). Late Quaternary environments of the Carpentaria basin, Australia. *Palaeogeography, Palaeoclimatology, Palaeoecology*, *67*(3-4), 245–261.

TRA Environmental Sciences Inc (2016). Oceano Dunes SVRA dust control program: Draft program environmental impact report. Environmental impact report.

Turner, G., Howarth, J., de Gelder, G., & Fitzsimons, S. (2015). A new high-resolution record of holocene geomagnetic secular variation from New Zealand. *Earth and Planetary Science Letters*, *430*, 296–307.

Turner, G. M. & Lillis, D. A. (1994). A palaeomagnetic secular variation record for New Zealand during the past 2500 years. *Physics of the Earth and Planetary Interiors*, *83*(3-4), 265–282.

Vail, P. R., Mitchum Jr, R., & Thompson III, S. (1977). Seismic stratigraphy and global changes of sea level: Part 3. relative changes of sea level from coastal onlap: section 2. application of seismic reflection configuration to stratigrapic interpretation. In C. Payton (Ed.), *Seismic Stratigraphy: Application of seismic reflection configuration to stratigraphic interpretation. Memoir 26. American Association of Petroleum Geologists, Tulsa*.

Valet, J.-P., Meynadier, L., & Guyodo, Y. (2005). Geomagnetic dipole strength and reversal rate over the past two million years. *Nature*, *435*(7043), 802–805.

Van Wagoner, J. C., Mitchum, R., Campion, K., & Rahmanian, V. (1990). Siliciclastic sequence stratigraphy in well logs, cores, and outcrops: concepts for high-resolution correlation of time and facies. *American Association of Petroleum Geologists, Methods Exploration Series*, *7*.

Varela, A. N., Gomez-Peral, L. E., Richiano, S., & Poire, D. G. (2013). Distinguishing similar volcanic source areas from an integrated provenance analysis: Implications for foreland Andean basins. *Journal of Sedimentary Research*, *83*(3), 258–276.

Verosub, K. L., Mehringer, P. J., & Waterstraat, P. (1986). Holocene secular variation in western North America: Paleomagnetic record from Fish Lake, Harney County, Oregon. *Journal of Geophysical Research: Solid Earth*, *91*(B3), 3609–3623.

Vestine, E. H. (1953). On variations of the geomagnetic field, fluid motions, and the rate of the Earth's rotation. *Journal of Geophysical Research*, *58*(2), 127–145.

Villaseñor, T., Jaeger, J. M., Marsaglia, K. M., Browne, G. H., & Hampson, G. (2015). Evaluation of the relative roles of global versus local sedimentary controls on Middle to Late Pleistocene formation of continental margin strata, Canterbury Basin, New Zealand. *Sedimentology*, *62*(4), 1118–1148.

Vital, H., Stattegger, K., & Garbe-Schonberg, C.-D. (1999). Composition and trace-element geochemistry of detrital clay and heavy-mineral suites of the lowermost Amazon River: a provenance study. *Journal of Sedimentary Research*, *69*(3).

Waelbroeck, C., Labeyrie, L., Michel, E., Duplessy, J. C., McManus, J., Lambeck, K., Balbon, E., & Labracherie, M. (2002). Sea-level and deep water temperature changes derived from benthic foraminifera isotopic records. *Quaternary Science Reviews*, *21*(1-3), 295–305.

Walsh, J., Corbett, D., Kiker, J., Orpin, A., Hale, R., & Ogston, A. (2014). Spatial and temporal variability in sediment deposition and seabed character on the Waipaoa River margin, New Zealand. *Continental Shelf Research*, *86*, 85–102.

Walsh, J. & Nittrouer, C. (2003). Contrasting styles of off-shelf sediment accumulation in New Guinea. *Marine Geology*, *196*(3-4), 105–125.

Walsh, J. P., Nittrouer, C. A., Palinkas, C. M., Ogston, A. S., Sternberg, R. W., & Brunskill, G. J. (2004). Clinoform mechanics in the Gulf of Papua, New Guinea. *Continental Shelf Research*, *24*(19), 2487–2510.

Wan, S., Li, A., Clift, P. D., & Stuut, J.-B. W. (2007). Development of the East Asian monsoon: Mineralogical and sedimentologic records in the northern South China Sea since 20 Ma. *Palaeogeography, Palaeoclimatology, Palaeoecology*, *254*(3-4), 561–582.

Wardinski, I. & Korte, M. (08). The evolution of the core-surface flow over the last seven thousands years. *Journal of Geophysical Research*, *113*(B5).

Warrick, J. A. & Farnsworth, K. L. (2009). Sources of sediment to the coastal waters of the Southern California Bight. In H. J. Lee, , & W. R. Normark (Eds.), *Earth Science in the Urban Ocean: The Southern California Continental Borderland: Geological Society of America Special Paper*, volume 454 (pp. 39–52). Geological Society of America.

Warrick, J. A., Mertes, L. A. K., Washburn, L., & Siegel, D. A. (2004). Dispersal forcing of southern California river plumes, based on field and remote sensing observations. *Geo-Marine Letters*, *24*(1), 46–52.

Wei, E. A., Driscoll, N. W., & Slingerland, R. L. (2019). Oceanographic currents, differential subsidence, and physiography control three-dimensional clinothem growth in the Gulf of Papua, Papua New Guinea. *Marine Geology*, *407*, 164–180.

Wheatcroft, R. A., Wiberg, P. L., Alexander, C. R., Bentley, S. J., Drake, D. E., Harris, C. K., & Ogston, A. S. (2007). Post-depositional alteration and preservation of sedimentary strata. In C. A. Nittrouer, J. A. Austin, M. E. Field, J. H. Kravitz, J. P. M. Syvitski, & P. L. Wiberb (Eds.), *Continental Margin Sedimentation: From Sediment Transport to Sequence Stratigraphy* (pp. 101–155).

Wolanski, E. & Alongi, D. (1995). A hypothesis for the formation of a mud bank in the Gulf of Papua. *Geo-Marine Letters*, *15*(3-4), 166–171.

Wolanski, E., Norro, A., & King, B. (1995). Water circulation in the Gulf of Papua. *Continental Shelf Research*, *15*(2), 185–212.

Wright, L., Friedrichs, C., Kim, S., & Scully, M. (2001). The effects of ambient currents and waves on the behavior of turbid hyperpycnal plumes on continental shelves. *Marine Geology*, *175*, 25–45.

Wu, H., Zhao, X., Shi, M., Zhang, S., Li, H., & Yang, T. (2014). A 23 Myr magnetostratigraphic time framework for Site 1148, ODP Leg 184 in South China Sea and its geological implications. *Marine and Petroleum Geology*, *58*, 749–759.

Wu, J., Liu, Z., & Zhou, C. (2012). Late quaternary glacial cycle and precessional period of clay mineral assemblages in the western pacific warm pool. *Chinese Science Bulletin*, *57*(28-29), 3748–3760.

Xu, J., Swarzenski, P. W., Noble, M., & Li, A.-C. (2010). Event-driven sediment flux in Hueneme and Mugu submarine canyons, southern California. *Marine Geology*, *269*(1-2), 74–88.

Xu, K., Li, A., Liu, J. P., Milliman, J. D., Yang, Z., Liu, C.-S., Kao, S.-J., Wan, S., & Xu, F. (2012). Provenance, structure, and formation of the mud wedge along inner continental shelf of the East China Sea: a synthesis of the Yangtze dispersal system. *Marine Geology*, *291*, 176–191.

Xu, K., Milliman, J. D., Li, A., Paul Liu, J., Kao, S.-J., & Wan, S. (2009). Yangtze- and Taiwan-derived sediments on the inner shelf of East China Sea. *Continental Shelf Research*, *29*(18), 2240–2256.

Xuan, C. & Channell, J. E. T. (2009). UPmag: MATLAB software for viewing and processing u channel or other pass-through paleomagnetic data. *Geochemistry, Geophysics, Geosystems*, *10*(10).

Yamamoto, Y., Yamazaki, T., Kanamatsu, T., Ioka, N., & Mishima, T. (2007). Relative paleointensity stack during the last 250 kyr in the Northwest Pacific. *Journal of Geophysical Research*, *112*(B1).

Yancey, T. E. & Lee, J. W. (1972). Major heavy mineral assemblages and heavy mineral provinces of the central California coast region. *Geological Society of America Bulletin*, *83*(7), 2099–2104.

Zaitlin, B. A., Dalrymple, R. W., & Boyd, R. (1994). The stratigraphic organization of incised-valley systems associated with relative sea-level change. In R. Dalrymple, R. Boyd, & B. Zaitlin (Eds.), *Incised Valley Systems: Origin and Sedimentary Sequences: Society for Economic Paleontologists and Mineralogists Special Publication*, volume 51 (pp. 63–82).

Zhou, L. & Kyte, F. T. (1992). Sedimentation history of the South Pacific pelagic clay province over the last 85 million years inferred from the geochemistry of Deep Sea Drilling Project Hole 596. *Paleoceanography*, *7*(4), 441–465.

Ziegler, L. B., Constable, C. G., Johnson, C. L., & Tauxe, L. (2011). PADM2M: a penalized maximum likelihood model of the 0-2 Ma palaeomagnetic axial dipole moment. *Geophysical Journal International*, *184*(3), 1069–1089.